## Title

The Environments Around Nearby Supermassive Black Holes and the Upgrade of the OSIRIS Integral Field Spectrograph



## Author

Boehle, Anna Lee

## Publication Date

2017

Peer reviewed|Thesis/dissertation

UNIVERSITY OF CALIFORNIA

Los Angeles

# The Environments Around Nearby Supermassive Black Holes and the Upgrade of the OSIRIS Integral Field Spectrograph

A dissertation submitted in partial satisfaction
of the requirements for the degree
Doctor of Philosophy in Astronomy

by

Anna Lee Boehle

2017

ABSTRACT OF THE DISSERTATION

The Environments Around Nearby Supermassive Black Holes and
the Upgrade of the OSIRIS Integral Field Spectrograph

by

Anna Lee Boehle
Doctor of Philosophy in Astronomy
University of California, Los Angeles, 2017
Professor James E. Larkin, Chair

In this thesis, I explore the environments around supermassive black holes (SMBHs) in the nearby universe. The thesis is divided into five chapters. I begin with an introduction to SMBHs in general and to the astronomical instrumentation that is used to study their direct environments in the highest possible detail. The second chapter focuses on the closest galactic nucleus to Earth: the center of our own Milky Way galaxy. The orbits of stars around the Milky Way SMBH, Sgr A*, can be used to determine the black hole mass and distance. I present a new method of analyzing images of the Galactic center to increase the time baseline for faint, short-period stars that orbit Sgr A*. I use this new analysis method to improve the constraints on the mass of the SMBH and the distance to the Galactic center by a factor of 2. The second chapter discusses the upgrade of the detector in the OSIRIS instrument at W.M. Keck Observatory. This adaptive-optics-fed instrument uses an array of small lenses to sample a rectangular section of the focal plane, producing up to 3,000 spectra simultaneously with a spectral resolution of 3,800 and diffraction-limited spatial resolution. I helped to upgrade the original near-infrared (NIR) Hawaii-2 detector to a Hawaii-2RG, which improved the raw sensitivity of OSIRIS by a factor of 2 at J-band wavelengths (1.2 - 1.4 $\mu$m) and 1.6 at H- and K-band wavelengths (1.5 - 2.4 microns). The third and fourth chapters discuss a NIR integral field spectroscopic survey of nearby LINER (low ionization nuclear emission line) galaxies, the lowest luminosity class of active galactic nuclei. LINERs are found at the centers of $\sim$1/3 of galaxies within 40 Mpc, but it is unclear whether accretion

onto a supermassive black hole or another mechanism such as shock excitation drives their emission. I use the OSIRIS instrument to map the strength and kinematics of singly ionized iron, molecular hydrogen, and hydrogen recombination lines at spatial scales of 1-10 pc in the nuclei of 11 nearby LINERs, in close proximity to their central SMBHs. The third chapter presents a detailed study of the closest LINER in the sample, NGC 404, in which I find that its LINER emission is likely excited by shocks, and the final chapter presents results from the survey sample as a whole.

The dissertation of Anna Lee Boehle is approved.

Abby Kavner

Matthew A. Malkan

Tommaso L. Treu

James E. Larkin, Committee Chair

University of California, Los Angeles

2017

*To Piotr Decowski*

TABLE OF CONTENTS

LIST OF FIGURES

LIST OF TABLES

# ACKNOWLEDGMENTS

Graduate school has been a very long journey and there are so many people that helped me along the way. I would like to first thank my family. Without their encouragement and support throughout all these years of school, I would never have made it to where I am today. Thanks to my Mom, for my worldly upbringing, for tea parties after school, and putting so much time into raising us. And thanks to my Dad, for working like crazy to support us and for sincerely wanting to read this thesis. (As an aside: my Dad was also an undergrad physics major, whose astronomy thesis is even listed on ADS as I once discovered by accident!) And thanks to Duncan for being an awesome and supportive brother throughout my life.

I also want to thank my partner, Gunther. Your support throughout this (sometimes really tough!) process of grad school has been so incredible. Thank you for making sure I didn't work late too often and encouraging me to really relax in the evenings and on the weekends, even when everything was at its most stressful point. And thank you for saying so often how proud of me you are, it means so much.

I would also like to thank my thesis advisor, James Larkin. I am so glad that the OSIRIS detector upgrade project was so well timed for my thesis, and I learned so much from you about infrared instrumentation and extragalactic astronomy. I especially appreciate your always taking the time to have a meeting with me, no matter how busy things were with other projects. Thank you also for saying that I am well-suited for instrumentation, one day in the midst of detector installation preparation as we walked towards the basement lab I honestly would not have seriously considered this field of astronomy as a career had you not said that, and I am so excited to have some time to pursue instrumentation in my postdoc.

I also want to thank all the members of the IR Lab. This lab has felt like family and I'm really glad I had the chance to be a part of it. I have had such a great time working with you all (and playing DnD, talking about bikes, etc.) and I will miss you. A special shout out to the amazing women grads that I have overlapped with in the IR Lab and the awesome support and laughter that you have all provided: Sarah, Emily, and Pauline.

Thank you also to my masters advisor, Andrea Ghez. The summer of working with you

and the Galactic Center Group as an REU student is what led me to apply to astronomy graduate programs, pursue observational astronomy research, and ultimately come to UCLA. I'm really thankful to have had the opportunity to work with you and to study the orbits of stars at the Galactic center.

Finally, I would like to thank all the amazing physics and astronomy teachers that I have had throughout my academic career. This journey all began in high school, when I took my first physics class with Mr. Shanks in my junior year and then took the calculus-based physics class with Mr. Cotts in my senior year. I fell in love with the subject right away, and it was in no small part thanks to these amazing teachers who cared so much about teaching their students. Mr. Cotts especially encouraged me to pursue physics in college, saying I had the knack for it. It's amazing how powerful a statement like that can be to a student (see above!), and I took it heart.

This thesis is dedicated to one of my teachers in particular: Professor Piotr Decowski of the Physics Department at Smith College. He was the first physics professor that I met at Smith, when I took his Modern Physics 1 class in my first semester. By the end of those 15 weeks, I was an officially declared physics major and I had started working on particle physics research in his lab. Piotr was always incredibly patient and encouraging as I learned my first programming language, ROOT, and tried to fit Gaussians to PMT data to determine its gain by measuring the number of electrons produced by single photons hitting the light sensitive surface. Piotr took me and his other undergraduate researcher at the time to Thomas Jefferson National Lab with him for my first physics summer internship, an amazing learning experience. He also sincerely cared about my life outside the department, often attending my chamber music concerts with his wife and, along with the rest of the department, really supporting my decision to study abroad in Italy. I just always felt so cared for and supported by him, both while I was there at Smith and after I had gone. Piotr passed away during my third year of graduate school and I would like to dedicate this thesis to him as a small thanks for his role in my development as a scientist.

Chapter 2 is a version of Boehle et al. (2016), ApJ, 830, 17 and is reproduced with permission from the AAS. I would like to thank my co-authors on this work: Andrea Ghez,

Rainer Schödel, Leo Meyer, Sylvana Yelda, Saundra Albers, Gregory Martinez, Eric Becklin, Tuan Do, Jessica Lu, Keith Matthews, Mark Morris, Breann Sitarski, and Gunther Witzel. We additionally thank the staff of the Keck Observatory, especially Randy Campbell, Jason Chin, Scott Dahm, Heather Hershey, Carolyn Jordan, Marc Kassis, Jim Lyke, Gary Puniwai, Julie Renaud-Kim, Luca Rizzi, Terry Stickel, Hien Tran, Peter Wizinowich, and former director Taft Armandroff for all their help in obtaining the new observations. Support for this work at UCLA was provided by NSF grants AST-0909218 and AST-1412615, the Levine-Leichtman Family Foundation, the Preston Family Graduate Fellowship (held by A. B. and B. N. S.), the Galactic Center Board of Advisors, the Janet Marott Student Travel Awards, the UCLA Graduate Division Dissertation Year Fellowship (held by B. N. S.), the Eugene V. Cota-Robles Fellowship (held by A. B.) and Janet Marott for her support of research on S0-38 through the Galactic Center Group's Stellar Patron Program. The research by R.S. leading to these results has received funding from the European Research Council under the European Union's Seventh Framework Programme (FP7/2007-2013) / ERC grant agreement n° [614922]. The W. M. Keck Observatory is operated as a scientific partnership among the California Institute of Technology, the University of California, and the National Aeronautics and Space Administration. The authors wish to recognize that the summit of Mauna Kea has always held a very significant cultural role for the indigenous Hawaiian community. We are most fortunate to have the opportunity to observe from this mountain. The Observatory was made possible by the generous financial support of the W. M. Keck Foundation.

Chapter 3 is a version of Boehle et al. (2016), Proc. SPIE, 9908, Ground-based and Airborne Instrumentation for Astronomy VI, 99082Q and is reproduced with permission from SPIE. I would like to thank my co-authors on this work: James Larkin, Sean Adkins, Theodore Aliado, Michael Fitzgerald, Christopher Johnson, Jim Lyke, Kenneth Magnone, Ji-Man Sohn, Eric Wang, Jason Weiss. Additional support for A. B. was provided by the Eugene V. Cota-Robles Fellowship.

Chapter 4 is a version of a paper that has been submitted for publication in the Astrophysical Journal and I would also like to thank my co-authors on this work: James Larkin, Lee Armus, and Shelley Wright. Additional support for A. B. for the research conducted in

this chapter and in Chapter 5 was provided by the UCLA Dissertation Year Fellowship.

# VITA

| | |
|---|---|
| 2011 | B.A. (Physics), summa cum laude<br>Smith College. |
| 2011–2014 | Graduate Student Researcher, Galactic Center Group,<br>Astronomy & Astrophysics Division, Physics and Astronomy Department,<br>University of California, Los Angeles.<br>Advisor: Professor Andrea Ghez. |
| 2011–2015 | Eugene V. Cota-Robles Fellowship |
| 2012–2014 | Preston Family Graduate Fellowship in Astrophysics |
| 2013 | M.S. (Astronomy),<br>University of California, Los Angeles. |
| 2013–2017 | Graduate Student Researcher, Infrared Lab,<br>Astronomy & Astrophysics Division, Physics and Astronomy Department,<br>University of California, Los Angeles.<br>Advisor: Professor James Larkin. |
| 2016–2017 | Dissertation Year Fellowship<br>University of California, Los Angeles. |

# PUBLICATIONS

Hees, A.; Do, T.; Ghez, A.M.; Martinez, G.D.; Naoz, S.; Becklin, E.E.; Boehle, A.; Chappell, S.; Dehghanfar, A.; Chu, D.; Kosmo, K.; Lu, J.R.; Matthews, K.; Morris, M.R.; Sakai, S.; Schödel, R.; Witzel, G., *Testing General Relativity with stellar orbits around the supermassive black hole in our Galactic center*, 2017, Phys. Rev. Lett., 118, 211101

Boehle, A.; Ghez, A.M.; Schödel, R.; Meyer, L.; Yelda, S.; Albers, S.; Martinez, G.D.; Becklin, E.E.; Do, T.; Lu, J.R.; Matthews, K.; Morris, M.R.; Sitarski, B.; Witzel, G., *An Improved Distance and Mass Estimate for Sgr A* from a Multistar Orbit Analysis*, 2016, ApJ, 830, 17

Boehle, A.; J. E. Larkin; S. M. Adkins; T. Aliado; M. P. Fitzgerald, C. A. Johnson; J. E. Lyke; K. G. Magnone; J. M. Sohn; E. Wang; J. L. Weiss, *Upgrade of the detector in the integral field spectrograph OSIRIS at the W. M. Keck Observatory*, 2016, Proc. SPIE, 9908, Ground-based and Airborne Instrumentation for Astronomy VI, 99082Q

Boehle, A.; Schödel, R.; Meyer, L.; & Ghez, A. M., 2014, *New orbital analysis of stars at the Galactic center using speckle holography and orbital priors* in IAU Symposium 303, The Galactic Center: Feeding and Feedback in a Normal Galactic Nucleus, ed. L. O. Sjouwerman, C. C. Lang, & J. Ott, 242

Witzel, G.; Ghez, A.M.; Morris, M.R.; Sitarski, B.N.; Boehle, A.; Naoz, S.; Campbell, R.; Becklin, E.E.; Canalizo, G.; Chappell, S.; Do, T.; Lu, J.R.; Matthews, K.; Meyer, L.; Stockton, A.; Wizinowich, P.; Yelda, S., *Detection of Galactic center source G2 at 3.8 $\mu$m during periapse passage*, 2014, ApJ, 796, L8

Phifer, K.; Do, T.; Meyer, L.; Ghez, A.M.; Witzel, G.; Yelda, S.; Boehle, A.; Lu, J.R.; Morris, M.R.; Becklin, E.E.; Matthews, K., *Keck Observations of the Galactic Center Source G2: Gas Cloud or Star?*, 2013, ApJ, 773, L13

Meyer, L.; Ghez, A.M.; Schödel, R.; Yelda, S.; Boehle, A.; Lu, J.R.; Do, T.; Morris, M.R.; Becklin, E.E.; Matthews, K., *The Shortest-Known-Period Star Orbiting Our Galaxy's Supermassive Black Hole*, 2012, Science, 338, 84

# CHAPTER 1

# Introduction

This thesis focuses on high spatial resolution studies of the centers of nearby galaxies and the development of astronomical instrumentation that makes these observations possible. As detailed below, the centers of galaxies (also known as "galactic nuclei") are extreme environments in many respects and require detailed observations to disentangle their physical conditions. Understanding the fundamental characteristics and the important physical processes in galactic nuclei can improve our understanding of how galaxies form and evolve over cosmic time. The work presented in this thesis is focused on local galactic nuclei, including our own Milky Way, since observations of these nuclei can probe the smallest possible spatial scales when employing the largest optical/near-infrared telescopes on Earth.

## 1.1 Supermassive Black Holes at the Centers of Galaxies

A black hole is an object whose mass is confined to such a small physical volume that nothing, not even light, can escape its gravitational pull. Black holes are predicted by Albert Einstein's theory of general relativity (Schwarzschild, 1916); in this theory's framework, they are gravitational singularities that have zero volume and therefore infinite density. The closest distance that light or matter can reach before it becomes impossible to escape the black hole is known as the event horizon and is related to the mass of the black hole, among other properties. Since no light can be observed from beyond the event horizon of black holes, the presence of these objects in the universe must be inferred by indirect observations of the gravitational effects that black holes have on their surrounding environment.

Astronomers have found evidence for black holes in two different mass ranges. Black

holes in the lower mass range can form from the collapse of a single star at the end of its lifetime. In this formation scenario, black holes have masses a few to several tens of times the mass of our Sun and are thus known as stellar mass black holes. Black holes in the higher mass range instead have masses that are millions to billions of times the mass of our Sun and are known as supermassive black holes (SMBHs); these black holes are the subject of my thesis. SMBHs are found in the centers of galaxies and it is now believed that most, if not all, galaxies host a SMBH at their center (e.g., Magorrian et al., 1998; Kormendy, 2004). It is unclear exactly how these SMBHs formed in the early universe, but it has been shown that their mass correlates with properties of their host galaxy, such as the mass and luminosity of the bulge (see Kormendy & Ho, 2013, for a review). These host galaxy properties are measured on much larger scales than the region that is under the gravitational influence of the SMBHs (known as the sphere of influence) by a factor of $\sim$1000 (see Fig. 1.1), so the observed correlations suggest that the growth of the SMBH and the galaxy across cosmic time are tied together in some global way. Understanding how SMBHs influence the surrounding environment of their galaxy and its overall growth is therefore important to understanding galaxy evolution as a whole.

The presence of a SMBH at the center of a galaxy is revealed by the effects the black hole has on its direct environment through its gravity. Material close to a SMBH undergoes extreme tidal and frictional forces and will form an accretion disk of matter orbiting within a few hundred light hours of the black hole. The light emitted by the hot disk of accreting material as well as light produced by other radiation processes can be observed directly at wavelengths ranging from the radio to the X-ray or can excite emission from gas in the surrounding galactic nucleus. These effects of the SMBH cause the galactic nucleus to have observable properties that cannot be explained by normal stellar processes, and these sources are known as active galactic nuclei (AGN).

The SMBHs in AGN exhibit a wide range of luminosities. The most extreme example is quasars, whose highly luminous emission due to high accretion rates and/or high SMBH mass outshines the light from the approximately 100 billion stars in their host galaxies. Quasars were originally thought to be unusual stars within our own galaxy, but their extragalactic

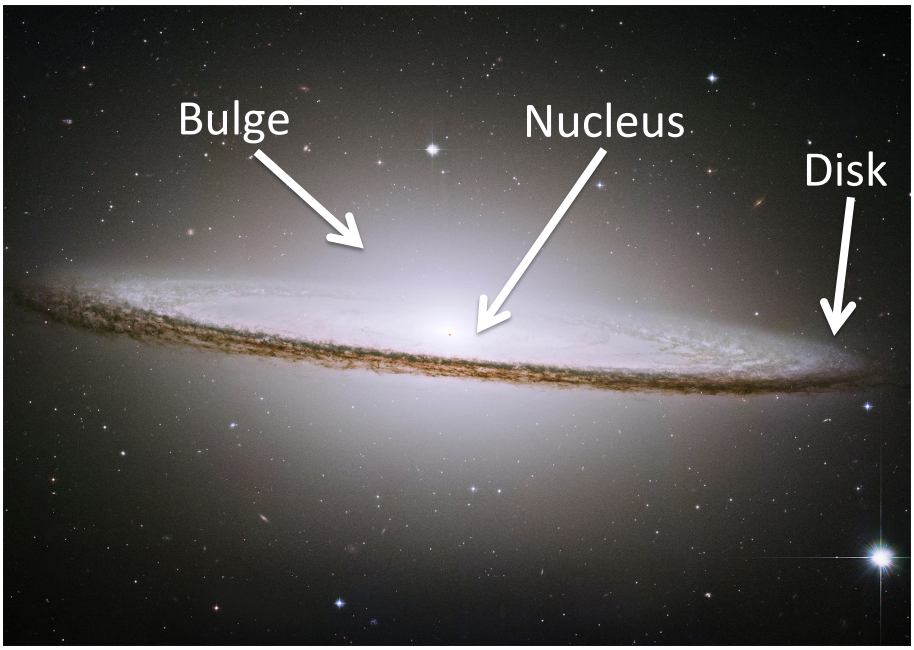


Figure 1.1: Hubble image of the Sombrero galaxy with the galaxy components labeled. The central SMBH of a galaxy is found in its nucleus. The mass of the SMBH correlates with the total mass in the large scale bulge of its host galaxy, but the SMBH's gravitational forces dominant over the stars only out to a few pc, or ∼10 light years, a factor of 1000 smaller than the size of the bulge. This "sphere of influence" is represented by a small red dot in this figure, but note that the dot is still 10 times larger than the actual size of the sphere for display purposes. The correlation between SMBH mass and bulge mass is therefore a sign that the growth of SMBH and the galaxy over cosmic time is somehow tied together. Underlying image credit: NASA/Hubble Heritage Team.

nature was then proposed by Schmidt (1963) after the emission lines in the quasar optical spectra were recognized as hydrogen lines that were redshifted. Later, Salpeter (1964) and Zel'dovich (1964) proposed that the high luminosity of quasars is produced by material accreting onto a central SMBH. These highly energetic phenomena are rare and are more commonly found at earlier ages of the universe about 10 billion years ago than in the present day universe (Schmidt et al., 1995). Based on this fact and the high energy output of quasars, Lynden-Bell (1969) argued that many nearby, present-day galaxies should host "dead" quasars at their centers (i.e., SMBHs no longer accreting as much material as when they were in a quasar state). That work also proposed that accretion onto these SMBHs can explain the emission of Seyfert galaxies, another class of AGN that are less luminous than quasars but more commonly found closer to our own galaxy (Seyfert, 1943). Seyfert galaxies were first identified through their unusual optical spectral properties: they show emission

lines, often from transitions that require a high energy to excite, that sometimes have very large widths, implying that the gas producing these lines is moving at speeds of thousands of km $s^{-1}$. These spectral properties can be explained by the energetic light emitted by SMBH accretion processes, which ionizes atoms in the surrounding gas and excites the emission of the observed lines. AGN can be separated out from galactic nuclei with many young stars, whose hot surfaces emit light that can also excite optical spectral lines, by comparing the strength of lines from high ([OIII]) and low ionized atoms (e.g., [NII]; Baldwin et al., 1981; Veilleux & Osterbrock, 1987). To remove the effects of reddening due to dust, this comparison is often performed by first taking the ratios of these lines and a hydrogen recombination line at a nearby wavelength (H$\beta$ and H$\alpha$). Seyferts have high values of both high and low ionized line ratios compared to star forming galaxies.

Most galaxies in the local/present-day universe fall into a less luminous regime of SMBH activity than quasars or Seyferts (see Ho, 2008, for a review). Optical spectroscopic studies of local galactic nuclei have shown that Seyferts comprise only $\sim$10% of all galaxies within 40 Mc, and that the majority ($\sim$3/4) of AGN and a large fraction ($\sim$1/3) of all galaxies are classified as LINERs, or low ionization nuclear emission line regions (Ho et al., 1997). This least luminous class of AGN, originally identified by Heckman (1980), shows high values of optical line ratios with low ionization species (e.g., [NII]/H$\alpha$) similar to Seyferts, but lower values of line ratios from high ionization species ([OIII]/H$\beta$). The optical line ratios of LINERs cannot be explained by normal stellar processes, so they are typically considered to be AGN along with Seyferts and quasars. Some LINERs show additional evidence at other wavelengths such as radio (Nagar et al., 2005) and X-ray (González-Martín et al., 2006) that they do indeed host SMBHs accreting at a low rate. At the low luminosities of LINERs, however, the accretion onto the central SMBH may not always be the dominant physical process, and in fact the observed optical line ratios can also be explained by excitation of spectral lines by shock waves moving through the gas in the galactic nucleus or even the presence of hot, highly-evolved giant stars (although this has been evoked most often to explain LINER-like emission on galaxy-wide scales; e.g., Stasińska et al., 2008; Singh et al., 2013). Since these lower luminosity galactic nuclei represent the most common state of AGN

activity in the local universe, studying these AGN in detail is important in furthering our understanding of the effect of SMBH accretion in a relatively normal galaxy.

## 1.2 Near-Infrared Adaptive Optics Observations of Nearby Galactic Nuclei

Advances in astronomical telescopes and instrumentation have allowed galactic nuclei to be studied with unprecedented detail and sensitivity. The theoretical angular resolution that can be reached by the largest optical/near-infrared telescopes on Earth (8-10 meters in diameter) is unfortunately limited by the blurring effects of the Earth's atmosphere through which they observe the cosmos. Data taken with telescopes limited by the atmospherical blurring effects are known as seeing-limited data and typically achieve angular resolutions of 0.5 - 1.0 arcsec. Real-time correction of this atmospheric blurring can now be achieved through a technology known as adaptive optics (AO). AO systems measure the distortion of light caused by the turbulence of the atmosphere using a guide star and then apply corrections to the light from a nearby science target by precisely deforming a small mirror that the light hits before reaching the light sensor, or detector, that measures it. These measurements and subsequent corrections are performed hundreds to one thousand times per second. The resulting light can produce images with angular resolutions that are more than 10 times smaller than seeing-limited data. An additional advancement was made with the development of a laser than can excite sodium atoms in an atmospheric layer 90 km above the Earth's surface and thereby create a "laser guide star" anywhere in the sky necessary for astronomical observations. The majority of the data presented in my thesis were taken using the laser guide star AO system at the W. M. Keck Observatory (Fig. 1.2; Wizinowich et al., 2006; van Dam et al., 2006). This AO system uses a deformable mirror with 349 actuators, which adjust the surface of the mirror to correct the incoming science light at a typical rate of 750 kHz for the data presented in this thesis.

With the advent of AO, astronomical instruments must be designed to take full advantage of the high angular resolution delivered by this system. One type of instrument often used

Figure 1.2: Top down view of the W.M. Keck Observatory on the summit of Mauna Kea in Hawaii. This observatory consists of the Keck I and Keck II telescopes. The 10-meter hexagonal mirrors of each telescope are visible inside the telescope domes. Image credit: NASA/JPL.

behind adaptive optics and that is key for my thesis and studies of galactic nuclei in general is called an integral field spectrograph. Unlike traditional spectrographs that use a slit to observe a narrow slice of the sky, an integral field spectrograph (IFS) produces a 3-dimensional cube with two spatial dimensions on the sky and one wavelength dimension, such that every spatial pixel in the cube contains a spectrum (Fig. 1.3). This instrument thereby observes thousands of spectra simultaneously in a contiguous field of view. From another perspective, the data cube produced by an IFS contains 500 - 1500 images, each at a different, closely spaced wavelength of light. The particular integral field spectrograph in my thesis is called OSIRIS (OH-Suppressing Infra-Red Imaging Spectrograph Larkin et al., 2006). The subsequent chapters of my thesis describe both my use of OSIRIS to observe the centers of nearby galaxies (Chapters 2, 4, and 5) and my astronomical instrumentation experience in upgrading the detector in this IFS (Chapter 3). OSIRIS and the AO system at Keck Observatory observe at near-infrared (NIR) wavelengths from 1 to 2.4 $\mu$m, or light that is slightly redder than the human eye can see.

My AO observations using OSIRIS have focused on local galactic nuclei, including our

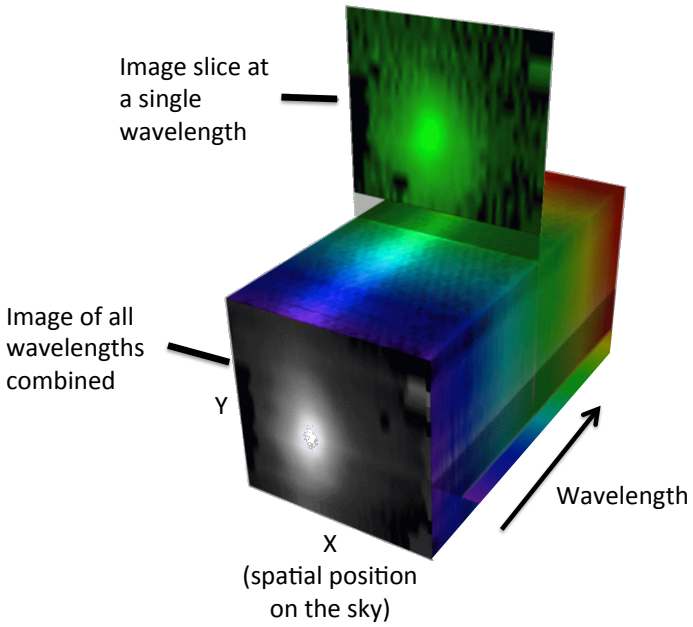


Figure 1.3: Illustration explaining the concept of a data cube. The black and white image in the front of the cube shows the near-infrared light of a galactic nucleus added up across all wavelengths in the data cube. Each spatial pixel of that image on the sky contains a spectrum. The image slice above the cube shows an image at a single wavelength. Underlying image credit: Stephen Todd (ROE) and Douglas Pierce-Price (JAC).

own Milky Way, which are prime targets for AO integral field spectroscopic studies of SMBHs and their effects on the surrounding environment. Studying nearby AGN allows us to access lower luminosity sources, revealing actively accreting SMBHs that are hiding among other physical processes. Additionally, the high spatial resolution accessible in nearby galactic nuclei can be used to disentangle the different physical mechanisms in galactic nuclei. For these sources, diffraction-limited observations made possible from the ground using AO can probe physical scales of 1 - 10 pc, lengths that are 0.1% of the total galaxy diameter and over ten times smaller than the resolution of seeing-limited observations. At the center of our own Galaxy, AO allows individual stars to be resolved and makes it possible to track the motions of these stars as they orbit the Milky Way SMBH, named Sgr A*. Additionally, the NIR wavelengths at which AO and the OSIRIS IFS operate are ideally suited for studying the galactic nuclei of nearby LINERs and the Milky Way. LINERs show unique properties in their NIR spectra, including particularly strong emission from singly ionized iron and molecular hydrogen gas (see Larkin et al., 1998; Riffel et al., 2013). In the Milky Way, the

clouds of dust between Earth and the center of the galaxy require that we observe in the NIR, which is absorbed less by dust compared to optical light.

## 1.3 Outline of Thesis

This thesis consists of 4 parts. Chapter 2 is a version of the Boehle et al. (2016a) paper published in the Astrophysical Journal and describes a study of the orbital motions of short-period stars as they move around the Milky Way's central SMBH. The orbits of two stars in particular, S0-2 and S0-38, are used to constrain the fundamental parameters of the mass and distance of the black hole, called Sgr A*. In addition to performing analyses of near-infrared AO imaging and IFS data, I also developed a new analysis technique that I apply to earlier imaging data sets reduced using an image post-processing technique called speckle holography. By applying this technique to the faint, short-period star S0-38, and simultaneously fitting the orbits of it and S0-2, I improve the errors on the SMBH mass and distance by a factor of $\sim$2.

Chapter 3 is a version of Boehle et al. (2016b) published in the SPIE Ground-based and Airborne Instrumentation for Astronomy Conference Proceedings and discusses the upgrade of the near-infrared detector in the OSIRIS integral field spectrograph. At the first light of OSIRIS in 2005, the IFS was equipped with a Rockwell Hawaii-2 detector. This detector had a lower than expected efficiency of converting incoming near-infrared photons to charge that significantly impacted the sensitivity of OSIRIS, especially at shorter wavelengths (1 - 1.4 $\mu$m). I worked to upgrade the detector to a Teledyne Hawaii-2RG and to add a new detector mount that allows the position of the detector to be accurately adjusted when the instrument is at cryogenic temperatures ($\sim$80 K). This mounting structure reduced the number of thermal cycles of the instrument required to put the detector in focus and adjust its tip/tilt, thereby greatly limiting the time that the instrument was off of the telescope and unavailable for scientific observations.

Chapters 4 and 5 discuss constraints on the physical conditions at the centers of nearby galaxies hosting LINERs. These chapters are based on OSIRIS observations of 11 LINERs at

near-infrared wavelengths, at which these AGN emit spectral lines from molecular hydrogen, singly ionized iron, and recombining hydrogen. I use the near-infrared spectral lines to measure the morphology and kinematics of the molecular and ionized gas, and to put constraints on the physical mechanisms exciting the LINER emission. This project is divided into two chapters: Chapter 4, which focuses on a detailed study of the closest LINER in the sample called NGC 404 and is a version of a paper that has been submitted to the Astrophysical Journal, and Chapter 5, which presents results from the sample as a whole.

Bibliography

Baldwin, J. A., Phillips, M. M., & Terlevich, R. 1981, PASP, 93, 5

Boehle, A., Ghez, A. M., Schödel, R., et al. 2016a, ApJ, 830, 17

Boehle, A., Larkin, J. E., Adkins, S. M., et al. 2016b, Proc. SPIE, 9908, 99082Q

González-Martín, O., Masegosa, J., Márquez, I., Guerrero, M. A., & Dultzin-Hacyan, D. 2006, A&A, 460, 45

Heckman, T. M. 1980, A&A, 87, 152

Ho, L. C. 2008, ARA&A, 46, 475

Ho, L. C., Filippenko, A. V., & Sargent, W. L. W. 1997, ApJ, 487, 568

Kormendy, J. 2004, Coevolution of Black Holes and Galaxies, 1

Kormendy, J., & Ho, L. C. 2013, ARA&A, 51, 511

Larkin, J., Barczys, M., Krabbe, A., et al. 2006, New A Rev., 50, 362

Larkin, J. E., Armus, L., Knop, R. A., Soifer, B. T., & Matthews, K. 1998, ApJS, 114, 59

Lynden-Bell, D. 1969, Nature, 223, 690

Magorrian, J., Tremaine, S., Richstone, D., et al. 1998, AJ, 115, 2285

Nagar, N. M., Falcke, H., & Wilson, A. S. 2005, A&A, 435, 521

Riffel, R., Rodríguez-Ardila, A., Aleman, I., et al. 2013, MNRAS, 430, 2002

Salpeter, E. E. 1964, ApJ, 140, 796

Schmidt, M. 1963, Nature, 197, 1040

Schmidt, M., Schneider, D. P., & Gunn, J. E. 1995, AJ, 110, 68

Schwarzschild, K. 1916, Sitzungsberichte der Königlich Preußischen Akademie der Wissenschaften (Berlin), 1916, Seite 189-196

Seyfert, C. K. 1943, ApJ, 97, 28

Singh, R., van de Ven, G., Jahnke, K., et al. 2013, A&A, 558, A43

Stasińska, G., Vale Asari, N., Cid Fernandes, R., et al. 2008, MNRAS, 391, L29

van Dam, M. A., Bouchez, A. H., Le Mignant, D., et al. 2006, PASP, 118, 310

Veilleux, S., & Osterbrock, D. E. 1987, ApJS, 63, 295

Wizinowich, P. L., Le Mignant, D., Bouchez, A. H., et al. 2006, PASP, 118, 297

Zel'dovich, Ya. B., 1964, Soviet Physics – Doklady, 9, 195

# CHAPTER 2

# An Improved Distance and Mass Estimate for Sgr A* from a Multistar Orbit Analysis

Reproduced by permission of the AAS (Boehle, A., Ghez, A. M., Schödel, R., Meyer, L., Yelda, S., Albers, S., Martinez, G. D., Becklin, E. E., Do, T., Lu, J. R., Matthews, K., Morris, M. R., Sitarski, B., Witzel, G., 2016, ApJ, 830, 17).

## 2.1 Introduction

Following the motions of stars in the center of our Galaxy has given many insights into the properties of the gravitational potential in which they move. The measurement of the high proper motions, and later, accelerations of these stars implies that they move in the gravitational potential of a concentrated dark mass (Eckart & Genzel 1997; Ghez et al. 1998; Ghez et al. 2000; Eckart et al. 2002). With further observations, these stellar motions have provided strong evidence for the presence of a supermassive black hole (SMBH) at the Galactic Center (Sgr A*) with a mass of about $4 \times 10^6$ $M_\odot$. Once the star S0-2 went through closest approach in 2002, it was possible to fit its motion with a Keplerian orbit (Schödel et al. 2002; Ghez et al. 2003). In addition to the mass of the SMBH, stellar orbits with measured radial velocities have been used to determine the distance to the Galactic Center ($R_o$; Ghez et al. 2003; Eisenhauer et al. 2003). With S0-2's short orbital period, this star provides the best constraint on the mass of the central black hole and $R_o$ from stellar orbits to date (e.g., Ghez et al. 2008, Gillessen et al. 2009b). The focus of recent work has been to continue assessing the central black hole's properties as well as exploring the potential for using the measurement of stellar motions to test general relativity.

The mass of Sgr A* ($M_{bh}$) and the distance to the Galactic Center ($R_o$) are both important ways of characterizing this unique region of our Galaxy and putting it in context with other galaxies. Measuring the mass of the central supermassive black hole allows it to be compared to supermassive black holes in the centers of other galaxies. With the mass of Sgr A*, the Milky Way can be added to observed correlations between the mass of the central SMBH and other galactic properties, such as velocity dispersion of stars and bulge luminosity (Ferrarese & Merritt 2000; Tremaine et al. 2002; see Kormendy & Ho 2013 for a review). $R_o$ is a key parameter characterizing our galaxy's size, mass and kinematics. The adopted value of $R_o$ affects estimates of the Milky Way's rotation curve and thereby also measurements of the mass and shape of the dark matter distribution (e.g., Olling & Merrifield 2000). An independent, very accurate measurement of $R_o$ could possibly be used to calibrate stellar distance indicators, such as RR Lyrae and Cepheids, which are important steps on the cosmic distance ladder (see Reid 1993). $R_o$ additionally serves to calibrate the extinction towards the Galactic Center (e.g., Schödel et al. 2010). The mass-to-distance ratio of Sgr A* as derived from stellar orbits is also necessary to determine the predicted size of the black hole shadow that will be observed by the upcoming Event Horizon Telescope, which can be used as a null hypothesis test of general relativity (see Psaltis et al. 2015). Finally, future tests of general relativistic effects on the motion of S0-2 depend on accurate measurements of the gravitational potential due to the SMBH in the Newtonian regime.

Until now, our group has used only S0-2 to constrain $R_o$ and the mass of Sgr A*. This is because S0-2 is unique: it is bright (14.2 in the K band) and has a short orbital period (16.2 years). We therefore have been able to track its motion since Keck observations of the Galactic Center began in 1995 such that our observations now cover more than one full orbit of this star. We would like to also use other short-period stars in the Galactic Center to help determine the gravitational potential, but ideally only those stars with high orbital phase coverage like S0-2. It has been shown for visual binary stars that if less than 40 - 50% of a body's orbit is covered by astrometric observations, the orbital parameters estimated from the data are systematically biased from their true values (Lucy 2014). We therefore only use additional short-period stars to constrain the black hole mass and $R_o$ that conservatively

have at least this minimum orbital phase coverage.

Achieving this minimum orbital coverage for other short-period stars is a challenge because those stars are fainter than S0-2 by more than an order of magnitude, making them difficult to track in the first 10 years of speckle imaging data. In this work, we present a method to increase the orbital phase coverage of these faint stars at the Galactic Center through a complete reanalysis of this data set. In all past analyses of stellar orbital parameters using the speckle data, the data from each observation run has been treated independently. Stars are blindly searched for in the summed image from a given epoch of observation, as if the Galactic Center had never been observed before. No information from other observations is used in this search. In this work, we present a new methodology for analyzing the speckle images that does use information from the much deeper adaptive optics images and the vast improvement that has been made in the knowledge of the central black hole's properties. We use constraints on a star's orbit from the deep adaptive optics data to inform the search for the star in the earlier speckle years.

As a pilot study for this new methodology, we apply this technique to S0-38, one of the three stars at the Galactic Center with an orbital period of less than 20 years (in addition to S0-2 and S0-102; see Meyer et al. 2012), with the ultimate goal of using this star as an additional constraint on the black hole mass and $R_o$. At a magnitude of K=17.0, S0-38 is consistently detected in our deep adaptive optics data taken from 2005 - 2013 but it has not previously been detected in our speckle imaging data taken from 1995 - 2005. S0-38 is an ideal star for the application of this methodology because it is consistently detected in all 21 adaptive optics images and its radial velocity has been measured (Gillessen et al. 2009b and this work), so its orbit is well known even with just over 40% of its orbit covered by AO observations. Our results are also made possible by a new reduction of the speckle data using the more sophisticated reconstruction algorithm called speckle holography (Schödel et al. 2013). This is the first work that includes the speckle holography re-reduction of all Keck Galactic Center speckle data.

The chapter is organized as follows: Section 2.2 describes the data sets used in this work, including the results of the new speckle holography reduction on the full set of Keck Galactic

Center speckle imaging data. Section 2.3 describes the new methodology of analyzing the speckle images as applied to S0-38. Section 2.4 contains the results of the S0-38 orbital analysis, including improved constraints on mass and $R_o$ as well as extended mass.

## 2.2 Data Sets

This chapter is based on three different types of data sets, which are briefly summarized here. The first type is previously reported speckle imaging data that, in this work, are re-reduced with the speckle holography technique (Schödel et al. 2013). The result is a higher-quality, deeper final image for each observation epoch (Section 2.2.1 and Table 2.1). The second is new and previously reported adaptive optics (AO) astrometry data (Section 2.2.2.1). New AO imaging observations (Table 2.2) are analyzed by methods used in prior work by our group to produce star lists of relative astrometric measurements. Initial star lists of relative astrometric measurements from re-analyzed speckle data and star lists from new and existing AO data are transformed to an absolute reference frame using updated measurements for the astrometric standards (see Appendix 2.A). The third data type is new and previously reported AO spectroscopic data. These data are analyzed by standard techniques to extract radial velocity measurements (Section 2.2.2.2), which are combined with radial velocity measurements from the literature. No astrometric measurements from the literature are used due to the difficulty in consistently transforming these measurements to our reference frame. These data and initial data reduction steps allow us to extend the time baseline for S0-38 by a factor of two through analysis steps that are described in Section 2.3.

### 2.2.1 Speckle Imaging

#### 2.2.1.1 Existing Observations

The speckle data sets used for this study provide astrometric measurements of the central $\sim$ 5"x5" of the Milky Way between 1995 and 2005. While the details of these observations can

be found in earlier papers from our group (Ghez et al. 1998; Ghez et al. 2000; Ghez et al. 2005a; Lu et al. 2005; Rafelski et al. 2007), we provide a brief summary. Individual K-band (2.2 $\mu$m) frames were obtained with NIRC (Matthews & Soifer 1994; Matthews et al. 1996) with a pixel scale of 20 milliarcseconds on the W. M. Keck I telescope. During each epoch of observation, between 2,000 and 20,000 frames were obtained using very short exposure times (0.1 sec) to freeze the distorting effects of the Earth's atmosphere. We begin our analysis of these data with individual frames that have had the instrumental effects removed (i.e., sky subtracted, flat fielded, bad pixel corrected, distortion corrected). Table 2.1 provides the dates and number of frames for each of the 27 epochs of observations.

#### 2.2.1.2 New Image Reconstruction and Initial Star Lists

The individual short-exposure frames are combined via post-processing techniques that compensate for the blurring effects of the Earth's atmosphere. The result is a diffraction-limited image whose final Strehl ratio and depth depend on the algorithm used to make the combined image. Originally, our speckle images were reduced using the shift-and-add algorithm (SAA; Ghez et al. 1998; Ghez et al. 2000; Hornstein et al. 2002, Ghez et al. 2005a; Lu et al. 2005; Rafelski et al. 2007). In this technique, the individual frames are shifted so that the brightest pixel of each frame is at the same position before the highest quality frames are averaged together (see Christou 1991). With SAA, only the brightest speckle from each frame contributes to the diffraction-limited core of the final point spread function (PSF) and all other speckles are part of a substantial halo. In the present work, we employ a more sophisticated speckle reconstruction technique called speckle holography (Bates et al. 1973; Primot et al. 1990; Petr et al. 1998), as implemented by Schödel et al. (2013). This technique involves the deconvolution of the observed, distorted images with the instantaneous PSF as measured from a set of reference sources. In this approach, the information from all the speckles contributes to the final diffraction-limited core. In the implementation of speckle holography presented here, the diffraction-limited core of the final PSF contains $\sim 6.5$ times more flux than the case of the SAA PSFs (Strehl ratio in speckle holography $\sim 0.4$ versus

Strehl ratio in SAA $\sim 0.06$)[1] and a much greater fraction of the data obtained is used in the analysis (average fraction of frames used in speckle holography $\sim 92\%$ versus average fraction of frames used in SAA $\sim 17\%$). See Figure 2.1 for a comparison between SAA, speckle holography, and AO images. For each epoch, both a final image and three subset images of similar quality are constructed. An early version of our analysis of these data was reported in our recent work on S0-102 (Meyer et al. 2012). A subset of the epochs presented in that early analysis used a preliminary version of the algorithm described in Schödel et al. (2013), with a smaller field of view and a different treatment of the PSF reference sources. In the present work, the full implementation of the speckle holography algorithm from Schödel et al. (2013) was used. Image quality was further improved by rebinning the speckle frames from the original 20 milliarcsecond pixel scale down to 10 milliarcseconds before applying speckle holography as was done in the original SAA analysis. This is the first complete application of speckle holography to the Galactic Center speckle imaging data set from Keck Observatory.

After the final speckle holography images are constructed for each observation epoch, an initial search for stars in these images is performed. In this preliminary analysis, each observation epoch is treated independently. The positions and fluxes of stars in the field are determined by the PSF fitting program *StarFinder* (Diolaiti et al. 2000). In the running of *StarFinder* to detect sources in both the main and subset images, we choose to set the correlation threshold to 0.8 instead of the value of 0.7 used in Meyer et al. (2012). This more conservative correlation threshold value is chosen to minimize the number of fake sources detected in this preliminary analysis of the images. This correlation threshold is also motivated by the fact that we will later go back and look for sources that this initial analysis missed (see Section 2.3). To further ensure that each detection is robust and to estimate the measurement uncertainties, *StarFinder* is run in the same way on the three subset images. We keep a detection in our initial star list if it was detected in all three of these subset images as well the main image. The astrometry and photometry measurements are taken from the

[1]We note that these Strehl ratios are computed from the post-processed speckle holography and shift-and-add images. These Strehl ratios differ from those of the raw frames, with the SAA ratios being a closer representation.

main image. The error on our astrometric and photometric measurements is taken as the error of the mean (standard deviation divided by $\sqrt{3}$) of the positions and fluxes determined by *StarFinder* in the three subset images.

We use the initial star lists to determine the K-band limiting magnitude for "direct detections" in each speckle holography image. The K limiting magnitude is defined as the magnitude at which the cumulative distribution function of the observed K magnitudes of stars in the initial list reaches 95% of the total sample size. Figure 2.2 shows the K-band limiting magnitude of the SAA and speckle holography images for each observation epoch, as well as the limiting magnitude of the AO images for comparison. In our data, the median SAA K limiting magnitude is 15.7 and the median speckle holography K limiting magnitude is 16.4. For comparison, the median K limiting magnitude of our AO data is 19.4. Table 2.1 summarizes and compares the SAA and speckle holography analyses of the 27 epochs of speckle data used in this work.

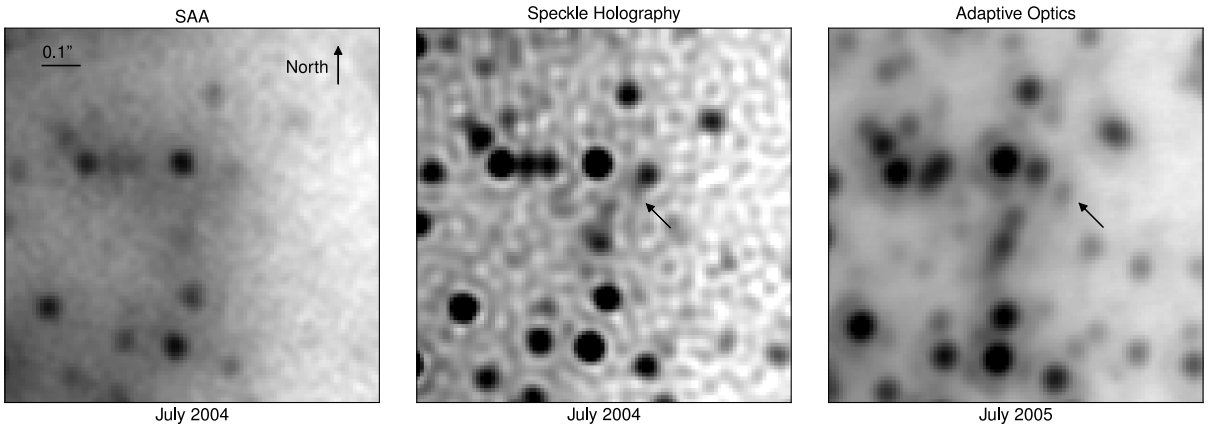


Figure 2.1: Comparison of a speckle shift-and-add final image (*left*), a speckle holography final image (*middle*), and an adaptive optics final image (*right*). The speckle holography and SAA images are made from the same observed frames from July 2004 and the AO image is from July 2005. Note that between these two observations dates the relative positions of the stars are significantly different. Each image is 1 arcsecond on a side. S0-38 is directly detected in both the AO and speckle holography images, but not in the shift-and-add image. Its detected position is shown with the black arrow. With a K-band magnitude of 17.0, S0-38 is easily detected in the deep AO images but it is at the direct detection limit for the speckle holography images.

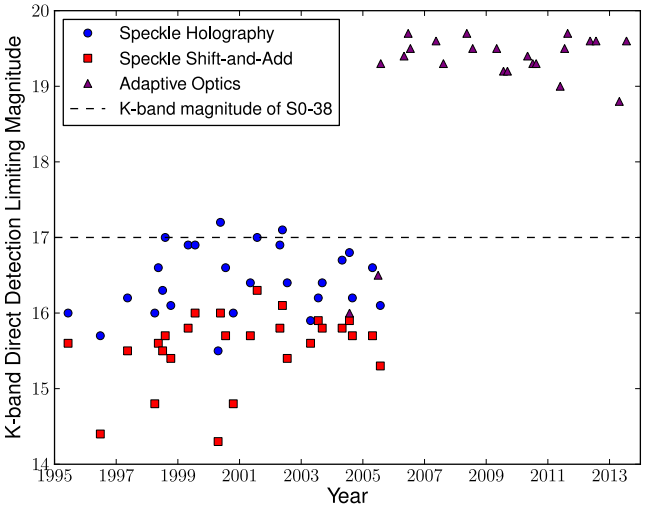


Figure 2.2: The direct detection K-band limiting magnitude of the imaging data used in this work (from Table 2.1). The limiting magnitude is defined as the magnitude at which the cumulative distribution function of the K magnitudes of the directly detected sources reaches 95% of the total sample size. The red squares show this limiting magnitude as derived for the original shift and add reduction of the speckle data and the blue circles show the improved depth that comes from the new speckle holography reduction of the same data. The purple triangles show the direct detection limiting magnitudes of the AO images for comparison. The dashed line shows the average magnitude of S0-38 derived from the AO data. This shows that S0-38 is consistently detected in the deep AO images but is near the limit of direct detection in the speckle holography images. Note that the limiting magnitudes of the first two AO epochs are similar to those of the speckle holography epochs. This is due to the small number of frames going into these AO images (10 frames used versus the typical 100-200 frames). This fact also explains why S0-38 is detected in 21 out of 23 AO epochs.

### 2.2.2 Adaptive Optics

#### 2.2.2.1 Imaging Data and Astrometric Reference Frame

New high-resolution images of the central $\sim 10'' \times 10''$ of our galaxy were taken in 2012 and 2013 using the laser guide star adaptive optics system (Wizinowich et al. 2006; van Dam et al. 2006) on the Keck II telescope. The images were taken with NIRC2 (PI: Keith Matthews) in the K′-band (2.1 $\mu$m) and have a plate scale of 9.952 milliarcseconds per pixel (Yelda et al. 2010). The AO observations of this field from 2004 through 2011 have been previously reported (Ghez et al. 2005b; Ghez et al. 2008; Lu et al. 2009; Yelda et al. 2010; Yelda 2012; Yelda et al. 2014). The new AO observations from the years 2012 and 2013 were collected in the same manner as earlier observations. In this setup, each frame was taken with an

exposure time of 2.8 seconds with 10 coadds (280 times longer than the speckle imaging frames). Astrometry and photometry are extracted using the same techniques reported in our previous work. Uncertainties in these measurements are also determined by running the same analysis on 3 subset images constructed with 1/3 of the frames used in the deep image. Table 2.2 summarizes the results from the new AO observations. Together with existing star lists from earlier Keck AO data, these 3 new star lists bring the total number of epochs of relative AO astrometry available for this study to 23 epochs, from which 21 AO detections of S0-38 are unambiguously made (see Figure 2.1). The average magnitude of S0-38 as derived from these detections is $17.0 \pm 0.1$. S0-38 is well above the direct detection limit of the AO data, but comparable to the direct detection limit of the speckle holography data (see Figure 2.2).

In addition to the central field, we also take observations designed to measure the astrometry in the near infrared (NIR) of a set of 7 SiO masers. We tie the NIR measurements of these masers to astrometric and velocity measurements made in the radio to construct an absolute reference frame with Sgr A* at rest at the origin (see Reid et al. 2007; Ghez et al. 2008; Gillessen et al. 2009b; Yelda et al. 2010; Yelda et al. 2014). Here we repeat the exact procedure detailed in Yelda et al. (2014) to construct the absolute reference frame, adding three new epochs of NIR maser observations from 2011 to 2013. These new maser observations are summarized in Table 2.A.1 in Appendix 2.A. Appendix 2.A also provides the resulting absolute astrometry for the IR secondary standards that are used to combine all the speckle holography and AO star lists of relative positions together into a common absolute reference frame.

#### 2.2.2.2 Spectroscopic Data

New spectroscopic observations for S0-38 were obtained using the integral field spectrograph OSIRIS with the laser guide star AO system on the Keck 1 telescope (Larkin et al. 2006) on 2013 May 11-13. The S0-38 data were taken with the K broadband filter (Kbb; 1.965 - 2.382 $\mu m$) in the 35 milliarcsecond (mas) plate scale. This observational setup is designed to

measure the CO bandheads ($2.3\mu m$) of the short-period, late-type star S0-38. The resulting spectrum has a resolution of $R \sim 3,600$. Thirty four 900-second exposures were taken, each dithered by a small amount ($\sim$ 0.2 arcseconds). In 6 of these frames, the AO correction was such that S0-38 is confused with a neighboring source $\sim$ 100 milliarcseconds away. The remaining 28 frames are used to obtain the spectrum of S0-38, providing a total on-source time of 7 hours. For calibration purposes, we observed skies with the same exposure time (900 s). The AO performance was excellent during these observations, providing a PSF with a full width at half maximum (FWHM) of $\sim$ 70 mas.

The analysis used to extract spectra closely follows previous analyses (Do et al. 2013). For the new Kbb data, we extract S0-38's spectrum using a 35 milliarcsecond aperture. The resulting spectrum is calibrated by subtracting an annulus around the extraction aperture with a width of 70 milliarcseconds. The calibrated and normalized spectrum is shown in Figure 2.3. This spectrum of S0-38 has a signal-to-noise ratio of 10, computed over a small, featureless wavelength range (between 2.212 and 2.218 microns). The radial velocity (RV) of S0-38 is then determined by measuring the cross-correlation of the extracted spectrum and a template spectrum in the wavelength region around the CO bandhead absorption features (from 2.285 to 2.340 $\mu m$). We use the spectrum of the M3II giant HD40239 observed by the SPEX telescope (Rayner et al. 2009) as the template spectrum. Gillessen et al. (2009b) first reported the detection of the CO bandheads in this source, and the RV reported in that paper is also used for our orbital analysis. The observed radial velocity is finally transformed to the local standard of rest reference frame by adding a correction of 27 km $s^{-1}$. The error on the RV measurements is taken as the root mean square of the RV measurements made on three subset spectra that are each made with $\sim$1/3 of the individual frames. From this we obtain an LSR-corrected RV of -111 $\pm$ 25 km $s^{-1}$ for S0-38 in May 2013.

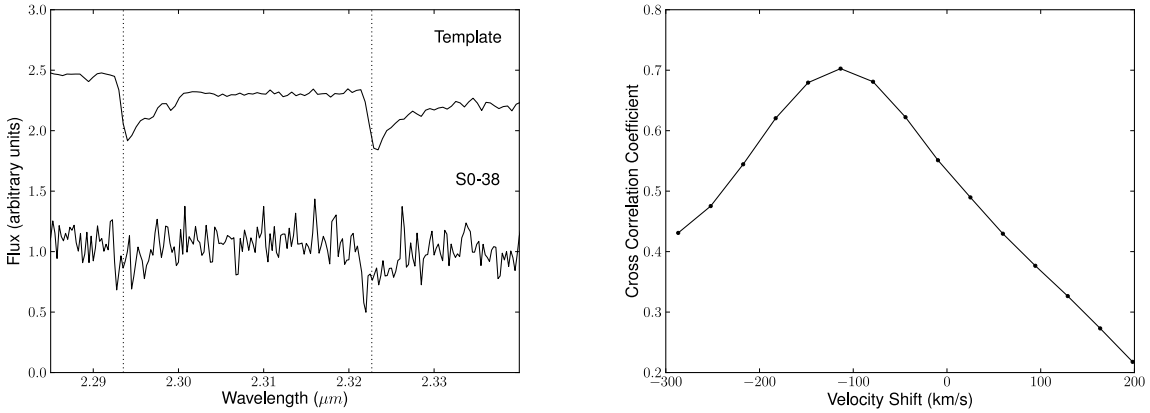


Figure 2.3: *Left*: Observed spectrum of S0-38 as well as the template spectrum (shifted to a radial velocity of 0 km $s^{-1}$; Rayner et al. 2009) used for the cross correlation showing the wavelength range over which this analysis is performed. Dotted vertical lines indicate the rest wavelengths of the CO bandhead absorption features seen in both the template and in S0-38's spectrum. *Right*: The measured cross correlation coefficient between the template spectrum and S0-38's spectrum over a range of radial velocity shifts of S0-38. These velocity shifts are in the local standard of rest reference frame.

Table 2.1. Summary of Speckle Imaging Observations

| Date (UT) | Date (Decimal) | Frames Available | Frames Used Holo | Frames Used SAA | $N_{stars}$ Holo | $N_{stars}$ SAA | Strehl Ratio Holo | Strehl Ratio SAA | $K_{lim}$[a](mag) Holo | $K_{lim}$[a](mag) SAA | $\sigma_{pos}$[b](mas) Holo | $\sigma_{pos}$[b](mas) SAA | Data Source[c] |
|---|---|---|---|---|---|---|---|---|---|---|---|---|---|
| 1995 June 9-12 | 1995.439 | 7532 | 4201 | 1800 | 199 | 151 | 0.23 | 0.06 | 16.0 | 15.6 | 0.5 | 1.1 | (1) |
| 1996 June 26-27 | 1996.485 | 5391 | 4287 | 865 | 136 | 77 | 0.23 | 0.03 | 15.7 | 14.4 | 1.9 | 1.8 | (1) |
| 1997 May 14 | 1997.367 | 3400 | 3400 | 1837 | 229 | 139 | 0.47 | 0.04 | 16.2 | 15.5 | 0.8 | 1.3 | (1) |
| 1998 April 2-3 | 1998.251 | 2744 | 2712 | 1639 | 170 | 83 | 0.31 | 0.04 | 16.0 | 14.8 | 1.3 | 1.5 | (2) |
| 1998 May 14-15 | 1998.366 | 9708 | 9708 | 2102 | 231 | 126 | 0.41 | 0.04 | 16.6 | 15.6 | 0.5 | 1.3 | (2) |
| 1998 July 3-5 | 1998.505 | 2352 | 2352 | 933 | 172 | 127 | 0.46 | 0.06 | 16.3 | 15.5 | 0.5 | 1.2 | (2) |
| 1998 Aug 4-6 | 1998.590 | 19741 | 12061 | 1933 | 235 | 172 | 0.48 | 0.06 | 17.0 | 15.7 | 0.3 | 0.8 | (2) |
| 1998 Oct 9 | 1998.771 | 2548 | 2166 | 1082 | 161 | 120 | 0.58 | 0.07 | 16.1 | 15.4 | 0.5 | 1.5 | (2) |
| 1999 May 2-4 | 1999.333 | 9800 | 9775 | 1857 | 263 | 183 | 0.51 | 0.07 | 16.9 | 15.8 | 0.4 | 1.1 | (2) |
| 1999 July 24-25 | 1999.559 | 5684 | 5684 | 2108 | 273 | 232 | 0.50 | 0.09 | 16.9 | 16.0 | 0.3 | 0.9 | (2) |
| 2000 April 21 | 2000.305 | 2940 | 2940 | 805 | 122 | 63 | 0.18 | 0.04 | 15.5 | 14.3 | 1.4 | 2.1 | (3) |
| 2000 May 19-20 | 2000.381 | 15680 | 15680 | 2492 | 293 | 242 | 0.47 | 0.08 | 17.2 | 16.0 | 0.3 | 0.7 | (3) |
| 2000 July 19-20 | 2000.548 | 11172 | 10637 | 1581 | 269 | 194 | 0.34 | 0.07 | 16.6 | 15.7 | 0.7 | 1.1 | (3) |
| 2000 Oct 18 | 2000.797 | 2352 | 2352 | 1517 | 140 | 77 | 0.39 | 0.04 | 16.0 | 14.8 | 1.1 | 1.3 | (3) |
| 2001 May 7-9 | 2001.351 | 7306 | 7306 | 1994 | 225 | 175 | 0.39 | 0.07 | 16.4 | 15.7 | 0.5 | 1.0 | (3) |
| 2001 July 28-29 | 2001.572 | 6860 | 6565 | 1695 | 290 | 239 | 0.54 | 0.11 | 17.0 | 16.3 | 0.3 | 0.8 | (3) |
| 2002 April 23-24 | 2002.309 | 13620 | 13501 | 1958 | 267 | 183 | 0.41 | 0.05 | 16.9 | 15.8 | 0.4 | 1.2 | (3) |
| 2002 May 23-24 | 2002.391 | 18052 | 11800 | 1443 | 290 | 252 | 0.53 | 0.08 | 17.1 | 16.1 | 0.3 | 0.9 | (3) |
| 2002 July 19-20 | 2002.547 | 8081 | 5518 | 1118 | 208 | 125 | 0.36 | 0.06 | 16.4 | 15.4 | 0.9 | 1.4 | (3) |
| 2003 April 21-22 | 2003.303 | 9392 | 9392 | 1841 | 144 | 121 | 0.36 | 0.04 | 15.9 | 15.6 | 0.6 | 1.1 | (3) |
| 2003 July 22-23 | 2003.554 | 5028 | 5028 | 1703 | 190 | 180 | 0.58 | 0.07 | 16.2 | 15.9 | 0.6 | 1.2 | (3) |
| 2003 Sept 7-8 | 2003.682 | 6270 | 6228 | 1723 | 233 | 182 | 0.35 | 0.07 | 16.4 | 15.8 | 0.6 | 1.2 | (3) |
| 2004 April 29-30 | 2004.327 | 9289 | 9289 | 1423 | 236 | 185 | 0.46 | 0.08 | 16.7 | 15.8 | 0.4 | 0.8 | (4) |
| 2004 July 25-26 | 2004.564 | 13110 | 12920 | 2161 | 293 | 200 | 0.43 | 0.08 | 16.8 | 15.9 | 0.4 | 0.9 | (4) |

Table 2.1 (cont'd)

| Date (UT) | (Decimal) | Frames Available | Frames Used Holo | Frames Used SAA | $N_{stars}$ Holo | $N_{stars}$ SAA | Strehl Ratio Holo | Strehl Ratio SAA | $K_{lim}$[a](mag) Holo | $K_{lim}$[a](mag) SAA | $\sigma_{pos}$[b](mas) Holo | $\sigma_{pos}$[b](mas) SAA | Data Source[c] |
|---|---|---|---|---|---|---|---|---|---|---|---|---|---|
| 2004 Aug 29 | 2004.660 | 2850 | 2850 | 1301 | 203 | 167 | 0.31 | 0.08 | 16.2 | 15.7 | 0.5 | 1.3 | (4) |
| 2005 April 24-25 | 2005.312 | 10553 | 10553 | 1679 | 226 | 162 | 0.37 | 0.06 | 16.6 | 15.7 | 0.4 | 1.0 | (5) |
| 2005 July 26-27 | 2005.566 | 6080 | 5683 | 1331 | 171 | 111 | 0.32 | 0.05 | 16.1 | 15.3 | 0.5 | 1.2 | (5) |

[a] $K_{lim}$ is the magnitude at which the cumulative distribution function of the observed K magnitudes reaches 95% of the total sample size.

[b] Positional error taken as error on the mean from the three sub-images in each epoch and includes stars with $K < 15$.

[c] Data originally reported in (1) Ghez et al. (1998), (2) Ghez et al. (2000), (3) Ghez et al. (2005a), (4) Lu et al. (2005), and (5) Rafelski et al. (2007)

Table 2.2. Summary of New AO Imaging Observations

| Date (UT) | Date (Decimal) | Frames Obtained | Frames Used | FWHM (mas) | Strehl | $N_{stars}$ | $K_{lim}$[a] (mag) | $\sigma_{pos}$[b] (mas) |
|---|---|---|---|---|---|---|---|---|
| 2012 July 24 | 2012.562 | 224 | 162 | 58 | 0.29 | 2344 | 19.6 | 0.06 |
| 2013 April 25-26 | 2013.318 | 268 | 140 | 67 | 0.17 | 1432 | 18.8 | 0.11 |
| 2013 July 20 | 2013.550 | 239 | 193 | 58 | 0.29 | 2492 | 19.6 | 0.08 |

[a]$K_{lim}$ is the magnitude at which the cumulative distribution function of the observed K magnitudes reaches 95% of the total sample size.

[b]Positional error taken as error on the mean from the three sub-images in each epoch and includes stars with $K < 15$ and with an average distance $< 4$ arseconds from the black hole.

## 2.3 Data Analysis

The goal of the work presented here is to increase the time baseline of observations of S0-38 so that more than ∼40% of its orbit is covered and its information can be combined with that of S0-2 to get further constraints on the gravitational potential in the Galactic Center. While the procedure described in Section 2 results in unambiguous detections of S0-38 in all epochs of deep AO data (2005-2013), the same is not true for all epochs of speckle holography data (1995-2005). We refer to the AO and speckle holography detections from Section 2 as "direct detections." In order to add more speckle holography detections of S0-38, we use a new methodology that takes advantage of the knowledge of (1) the black hole properties from S0-2 and (2) S0-38's orbital motion from the AO epochs to search for S0-38 in the speckle holography maps. We refer to the detections that result from this procedure as "prior-assisted detections," in contrast to the "direct detections."

The data analysis associated with establishing and using the prior-assisted detections of S0-38 is described in the following four sections. In Section 2.3.1, we discuss why S0-38 is chosen as the first star to which the new methodology is applied. In Section 2.3.2, we identify stars that are similar in magnitude to S0-38 and that may have overlapped with S0-38 on the plane of the sky between 1995 and 2005. By tracking these stars along with S0-38, we can better determine to which star any new speckle holography detections should be assigned. In Section 2.3.3, we create positional predictions for S0-38, in addition to the stars in the sample, based on existing knowledge of the orbital parameters, and use these

predictions to search for S0-38 in the speckle epochs. In Section 2.3.4, all the AO and speckle holography astrometry along with the RV measured for S0-38 are simultaneously fit with S0-2's measurements to further constrain the gravitational potential through which these stars move.

### 2.3.1 Selecting First Star to Apply New Methodology

In this work, we chose a single star as a pilot test for our new methodology of searching for new detections in speckle holography data. We limit the possible stars to those for which full orbital phase coverage may be acheived, including both turning points, by adding the 11-year speckle holography time baseline to the 9-year AO time baseline. This puts an upper limit of 20 years on the orbital period of candidate stars. The goal of this orbital period criteria is to select a star that would give the most information about the central gravitational potential once new speckle holography detections are included in its orbital fit. There are two stars not consistently directly detected in the speckle holography images that meet this constraint: S0-38 ($P = 19$ years) and S0-102 ($P = 11.5$ years; Meyer et al. 2012). We chose to apply the new methodology to S0-38 for the following reasons. First, S0-38 is consistently detected in every one of our deep adaptive optics data sets (23 astrometric measurements) while S0-102 is detected in just over half (14 astrometric measurements). The reason that S0-102 is often lost in the adaptive optics data is that its orbit moves through areas that are very crowded by other stars and by the NIR component of Sgr A* itself. S0-38 also moves through a similar area on the plane of the sky as it goes through closest approach, but it spends the majority of its orbit away from the very central area in which S0-102 moves, thanks to its longer orbital period/semi-major axis and its projection on the plane of the sky. In the speckle years specifically, S0-38 is predicted overall to be in a less crowded region of the sky than S0-102, which makes finding additional prior-assisted speckle holography detections more feasible. Additionally, the radial velocity of S0-38 has been successfully measured (this work and Gillessen et al. 2009b), whereas the radial velocity of S0-102 has not. This is largely thanks to the CO band heads present in S0-38's late-type star spectrum. The distinct shape and depth of these features make them easier to detect

than the Br-$\gamma$ line present in the spectra of early-type stars. In the specific case of the K broadband spectroscopic data used to measure S0-38's RV in this work (Section 2.2.2.2), we are not able to measure the spectrum of S0-102 because it is confused with nearby sources in most frames. S0-38 was near furthest approach and in a more isolated region at the time of its spectroscopic measurement, making the extraction of its spectrum possible. We therefore choose to apply the new methodology to S0-38.

### 2.3.2 Identifying Sources Potentially Confused with S0-38

We construct a sample of stars that may have overlapped with S0-38 on the plane of the sky between 1995 and 2005. The orbits of these stars are tracked along with that of S0-38 to avoid mismatching a star with any new speckle holography detection. An initial sample set of possibly confusing sources is identified through a radius and magnitude cut, where the radius used here is with respect to Sgr A*. The radius is set by how far away a star could be in the AO epochs from 2005 - 2013 and still have traveled into the central 0.″3 (0.012 pc for $R_o = 8$ kpc), where S0-38's orbit lies, during the 1995-2005 speckle epochs. In order to set a radius cut, we assume a representative velocity for the other stars in this central region. We make a conservative estimate of this velocity by taking 3 times the measured velocity dispersion at the projected distance of 0.″3 from the central black hole ($\sigma$ = 400 km/s; Do et al. 2013). While this assumed velocity is not an exact calculation of the velocities of stars in this region, it is a conservative value for the velocities of possibly confusing stars.

We then assume that the star is constantly moving at this velocity and that this velocity is fully in the plane of the sky in order to calculate the maximum radius of possible confusing stars. The maximum radius is then:

$$r_{max} = 3 \times \sigma(\text{at } 0.''3) \times 10\ yrs + 0.''3 = 0.''62 \tag{2.1}$$

This equation says that a star starting at a distance $r_{max}$ from Sgr A* and moving at a constant velocity of $3 \times \sigma(0.''3)$ towards the black hole on the plane of the sky would be at a distance of 0.″3 from Sgr A* after 10 years. Any star that is within $r_{max}$ at some point

in the AO epochs could have been inside the 0.″3-radius circle in which S0-38 is orbiting at some point in the speckle epochs.

From the stars within this radius, we then eliminate those sources whose magnitude is not consistent with S0-38's within 3 sigma ($K_{mag} = 17.00 \pm 0.24$). Finally, we also remove sources whose velocities are not within 90° of pointing to Sgr A* on the plane of the sky. The final set of possible confusing sources is: S0-104, S0-102, S0-103, S0-37, S0-40, S0-42, S0-45, S0-49, and S0-23.

### 2.3.3 Extending S0-38's Astrometric Orbital Phase Coverage using Orbital Priors

We apply a new methodology of analyzing the speckle holography data to find sources not detected in the initial, blind analysis. Our technique uses the information in the adaptive optics astrometric and radial velocity measurements of S0-38 as a starting point of where to look for this star in the speckle holography images. The orbits of the sample of possibly confusing stars described in Section 2.3.2 are tracked along with that of S0-38 so that any new speckle holography detection is not misidentified. The basic steps of this new methodology as applied to S0-38 are as follows:

1. Perform an orbital fit of S0-2's direct astrometric detections from AO and speckle holography epochs and radial velocities, with all 6 orbital parameters and all 7 gravitational potential parameters left free.

2. Perform an orbital fit of the direct astrometric detections and radial velocity measurements (if available) of S0-38 and the possibly confusing stars (Section 2.3.3.1). In these fits, the gravitational potential is fixed to the best-fit solution from S0-2's orbital fit. For the sample stars, both speckle holography and AO direct detections are included in this fit. For S0-38, only AO direct detections are included.

3. From the probability distributions of the orbital parameters found in each orbital fit, determine the probability distribution of the (X, Y) (on-the-sky) position of each star

in the next earlier speckle holography epoch relative to those epochs included in S0-38's orbital fit (i.e., start with the most recent speckle holography epoch and move backwards in time in subsequent steps).

4. Search for a speckle holography detection of S0-38 in the image from this epoch. We first check whether S0-38 is detected in the initial analysis of the image. If it is not in the initial star list, then apply the newly-developed *StarFinder* Force 1 algorithm to the image (Section 2.3.3.2). This algorithm takes as input the predicted pixel position of the star from the probability distribution of X and Y and searches the speckle holography image for a point source around that position that had not previously been detected in the initial star list.

5. If a new detection is found that meets a minimum correlation (0.3) and signal-to-noise threshold ($3\sigma$) and it is not blended with another known star, add that point to the list of detections of S0-38 and refit the orbit with that point (Section 2.3.3.1). If no detection is found (i.e., the PSF fit in *Starfinder* Force 1 does not converge), then search again in the next earlier speckle holography epoch. Note that the potentially confusing stars are not searched for in the speckle holography images and their orbital fits are therefore not updated. The majority of these stars are typically directly detected in the speckle holography images because their orbital periods are longer than S0-38's and they move through less crowded regions on the sky.

6. Repeat steps 3 - 5 until all speckle holography images are searched for S0-38.

7. After all new prior-assisted detections are identified, the black hole parameter probability distributions are determined by a simultaneous fit with S0-2 (Section 2.3.4).

#### 2.3.3.1 6-Dimensional Orbital Fits and Positional Priors

Orbital fits are carried out several times in our analysis. The initial task in the new analysis is to fit the orbits of all stars in the sample. For each new speckle holography detection, the orbit of S0-38 is also fit again to improve the prediction for earlier speckle epochs. All

the orbital fits performed in steps 2 - 5 assume that the star moves in the gravitational potential of a single point mass that is the central supermassive black hole (BH), Sgr A*. In all orbital fits used to inform the search for the star in speckle holography images, we use the information from S0-2 to determine the probability distributions of the 7 parameters that describe the gravitational potential: the black hole's mass ($M_{bh}$), position on the sky ($x_o$, $y_o$), 3D velocity ($V_x$, $V_y$, $V_z$), and the line of sight distance ($R_o$). The details of how S0-2 is used to determine the BH parameter probability distributions as well as our new S0-2 measurements are presented in Appendix 2.B. We then use the measurements of the star's position and radial velocity along with the constraints from S0-2 on the black hole parameters to determine probability distributions of the star's 6 Keplerian orbital parameters: orbital period ($P$), time of closest approach ($T_o$), eccentricity ($e$), inclination ($i$), argument of periapse ($\omega$), and angle to the ascending node ($\Omega$).

Our approach of using externally constrained black hole parameters speeds up the process of determining positional priors for S0-38 and the other sample stars by a factor of $\sim 5$, allowing these orbits to be fit in a few hours instead of 1 day. The external constraints are implemented by stepping through a grid in the 7D BH parameter space with 5 steps in each dimension, placed at -1, -0.5, 0, 0.5, and 1 sigma from the mean in that dimension.[2] Each of the $5^7 = 78,125$ points in this 7D grid is a single combination of values of the 7 BH parameters. These combinations are assigned weights based on the probability of those values as determined by S0-2 [3]. The weights of these combinations are very unevenly distributed because some sets of BH parameters are highly correlated. In order to not include combinations of BH parameter values that have a very low probability due to these correlations, we keep only the combinations that together make up 95% of the total cumulative weight. This weight cut reduces the number of individual combinations by a factor of $\sim$14 to 5,500.

We then perform a series of individual fits to the star's detections in astrometry and radial velocity, one for each BH parameter value combination that made it past the weight

[2]We choose to use a 1 sigma range in this grid spacing to make the fitting process computationally feasible.

[3]The 7D joint probability distribution of the BH parameters as determined by S0-2 is approximated by a multivariate gaussian. This approximation represents the distribution well (see Figure2.8)

cut. In each of these individual fits to the star's data, the 7 BH parameters are fixed to the values in each combination and the 6 orbital parameters are left free. Each individual fit then results in a set of samples of the posterior distribution of the star's 6 orbital parameters. These individual fits are performed using the Bayesian multimodal nested sampling algorithm MultiNest (Feroz & Hobson 2008; Feroz et al. 2009), which was implemented in our code by Leo Meyer. This algorithm samples the posterior distribution more efficiently than traditional Markov chain Monte Carlo (MCMC) sampling schemes, especially when the distribution is multimodal. The MultiNest algorithm has the advantage over our previous orbit-fitting method (see Ghez et al. 2008) in that the best-fit orbital parameters and their probability distributions are found simultaneously and with much less total computing time. When the MultiNest is run, uniform priors are applied to every free parameter, with ranges chosen such that the full range of the posterior distribution is probed. The results of the individual fits are then combined in order to get the final probability distributions for the orbital parameters of the star. This is achieved by combining the sets of samples of the posterior distributions found in each individual fit with the weight assigned to that fit's unique BH parameter value combination. Finally, the probability distributions of the individual orbital parameters are determined by constructing histograms of the weighted posterior samples.

The result is a probability distribution for each of the 6 orbital parameters determined by the star's detections, with the BH parameter information determined only by S0-2's detections. From the final probability distributions of all the BH and orbital parameters we can then derive the probability distribution of the (X, Y) position on the sky of the star in the speckle holography observation epochs. These probability distributions of X and Y constitute our prior knowledge about the position of this star in all earlier epochs and are used as inputs into the *StarFinder* Force 1 algorithm (Section 2.3.3.2).

Although orbital fits are performed for all the stars in the sample, there are only two that came close enough to be potentially confused with S0-38: S0-104 (in 2002) and S0-49 (in 1998). Figure 2.4 shows the probability distributions of X and Y for S0-38 and these confusing sources in one of the epochs in which these stars are close on the plane of the sky (July 2002), as well as a more typical epoch where S0-38 is isolated from the possibly

confusing sources (September 2003). Any new detection that is found in the images from these observation epochs is only used in the fit of S0-38 if both S0-38 and the nearby source are separately detected.

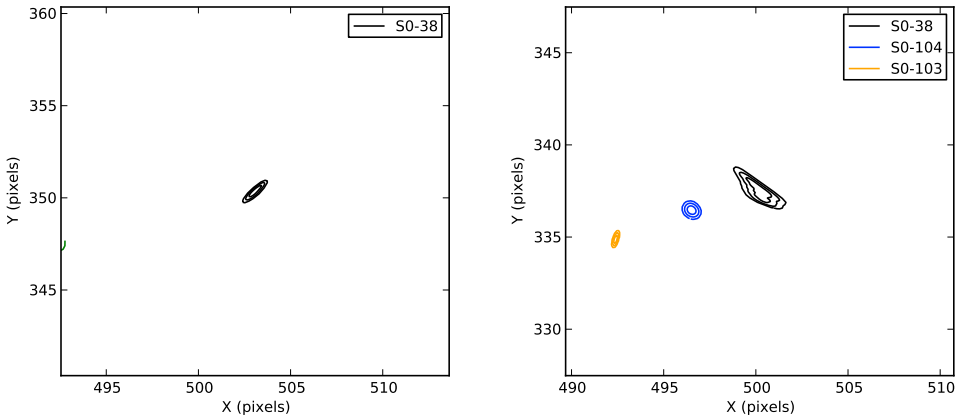


Figure 2.4: Probability distributions of X and Y for S0-38 and nearby sample stars in two example epochs: September 2003 (*left*) and July 2002 (*right*). The pixel position is shown on the image, which has a plate scale of 10 milliarcseconds per pixel. In September 2003, the prediction of the (X, Y) position of S0-38 is well-isolated from predicted positions of all the other stars in the sample. This level of isolation is typical throughout the speckle epochs. In July 2002, however, S0-38 is predicted to be within 70 milliarcseconds of S0-104. These two sources are not separately detected in the 2002 speckle epochs due to their close proximity, so no new detection is assigned to S0-38 in these epochs.

The initial orbital fit of S0-38 includes only the AO direct astrometric detections and radial velocity measurements, while the orbital fits of the possibly confusing stars include both AO and speckle holography direct detections. S0-38 moved so quickly in the speckle years compared to other stars in the sample that its direct speckle holography detections are generally too far away to associate with S0-38 by eye. An initial fit of S0-38's orbit with the gravitational potential fixed to S0-2's best-fit solution gives a reduced chi-squared of 12.2, implying that the AO errors determined by the 3 subset image method are underestimated. In order to correct this, we add in quadrature to the 3 subset image errors an additive error term constant for all AO epochs so that the reduced chi-squared of the AO-only fit equaled 1.0. This additive term is set to 1.7 mas, compared to an average 3 subset image error of 2.9 mas for S0-38's AO direct detections. This same procedure is not required for S0-2 because the reduced chi-squared of the orbital fit of its AO and speckle holography direct detections is already $\sim 1$.

#### 2.3.3.2 *StarFinder* Force 1 Algorithm

We can now use the probability distributions of S0-38's position on the sky in a given speckle epoch to inform our search for the star in that image, while also tracking the orbits of the potentially confusing stars included in our sample. We first check whether there is a direct detection in the initial star list for that epoch that coincides within uncertainties with the predicted position of S0-38. If a detection is not found in the initial analysis, then the newly-developed *StarFinder* Force 1 algorithm is applied.

The *StarFinder* Force 1 algorithm is designed to search for any additional point source that is not in the initial star list. The main inputs to the algorithm are the best guess whole pixel position of the source (Xo, Yo), the size of the search box over which to initially look for the source, and the positions and fluxes of the stars in the initial list for that epoch. (Xo, Yo) and the search box size are chosen so that the initial search is done over the whole 3 sigma range of the probability distribution of X and Y, but in the end new detections are allowed to be found outside the search box.

*StarFinder* Force 1 uses many of the sub-routines of the original *StarFinder* code and follows the same basic steps, outlined here:

1. First, the code takes a subset of the main image centered on the input position (Xo, Yo). The size of this subset depends on the full width at half maximum (FWHM) of the point spread function (PSF). For a typical PSF FWHM, the size of the subset image in this correlation step is 5 pixels on a side. It then finds the position at which the correlation between this small subset image and the inputted PSF is maximized. The search box input parameter sets the offsets over which the PSF and the subset image are cross correlated.

2. Next, the code takes a larger subset of the image (for a typical PSF FWHM, this subset image is 9 pixels on a side) and performs the initial fit of that subset image. The free parameters of this fit are the positions and fluxes of all stars within the subset image (including any sources found in the initial star list plus the additional source).

The initial guess for the position of the additional source is the position of maximum correlation found in the previous step. The position of the additional point source is allowed to move away from this initial guess during the fit and is not constrained by the inputted search box or the previously predicted (X,Y) position. Any contributions of flux in the subset image from stars with positions outside the subset image are considered fixed and are subtracted from the subset image before the fit is performed.

3. Finally, a series of 2 iterative fits is performed over a slightly larger subset image (for a typical PSF FWHM, this is 11 pixels on a side). If these iterative fits converge, then the best-fit position and flux of the newly-detected source are returned. To assign this new detection to S0-38, we require that the new detection (1) has a correlation above 0.3, (2) has a flux more than $3\sigma$ above the noise, and that (3) S0-38 is not confused with any other source in the image.

We generally cannot assign errors to the points detected with *StarFinder* Force 1 using the three subset image method that is used in the construction of the initial star lists. Since the magnitude of S0-38 is close to the detection limit in the deep speckle holography images of each epoch, it is not consistently detected in the three subset images that use only 1/3 of the frames. We therefore assign the error of each *StarFinder* Force 1 astrometric point so that the reduced chi-squared of the orbital fit with the additional point is approximately 1. This is done on an epoch-by-epoch basis, so the errors of each new point are set independently. In this way, an updated orbital fit with the new detection can be done before the search for the star in the next earlier speckle holography epoch is performed. If S0-38 is detected in the initial analysis of that holography epoch (and therefore is already detected in all three subset images), then the errors determined by the three subset image method are used in the subsequent orbital fit.

### 2.3.4 Orbital Fits That Use S0-38 to Constrain the Gravitational Potential

The result of applying the method outlined above to all speckle holography images is a final set of astrometric measurements of S0-38, including both the direct detections and the

prior-assisted detections. With a higher orbital phase coverage that covers both closest and furthest approach, we now use S0-38 to constrain the gravitational potential.

Before performing these orbital fits, we reassign the errors of S0-38's direct and prior-assisted speckle holography detections to a single value for all epochs. The single value is chosen so that the reduced chi-squared of an orbital fit of S0-38 with the black hole potential fixed to the best-fit solution from S0-2 equals 1. This reassignment is done so that the errors on the position of S0-38 are not underestimated in the epochs of the direct detections, whose errors were originally assigned by the three subset image method. The errors determined by the error of the mean of the measurements on three subset images are expected to be on-average slightly underestimated and are also a noisy estimator of the true error of the main map measurement. The reassignment therefore ensures that the errors on S0-38's positions, as well as the resulting errors on the black hole parameters, are not underestimated. This issue of underestimated error bars is already addressed in the AO epochs by the inclusion of an additive error term so that the AO-only orbital fit gives a reduced chi-squared of 1. Additionally, with this reassignment the errors of the direct and prior-assisted detections are treated consistently in that both are set by requiring the reduced chi-squared to equal 1.0.

Once S0-38's speckle holography errors have been reassigned, we perform two Keplerian orbital fits in which S0-38 is used to constrain the gravitational potential parameters: (1) a 13-dimensional fit of only the orbit of S0-38 and (2) a 19-dimensional fit of the orbits of both S0-2 and S0-38. The 13 free parameters in the first fit are the 7 black hole potential parameters and the 6 Keplerian orbital parameters that describe the motion of S0-38. This fit is used to compare the gravitational potential solutions determined by S0-38 alone with those determined by S0-2 alone. The 19 free parameters in the second fit are the 7 black hole potential parameters and a set of 6 Keplerian orbital parameters for each star. This simultaneous fit of the orbits of S0-2 and S0-38 is used to determine the final best-fit values and errors of the black hole potential parameters. Both the 13- and 19-dimensional fits are performed using MultiNest.

We finally perform a simultaneous fit of the orbits of S0-2 and S0-38 that includes deviations from a pure Keplerian orbit due to a distribution of extended dark mass. From this

fit, we find an upper limit for the amount of extended mass within the orbits of these stars. Following Ghez et al. (2008), we set the extended mass distribution to follow a power-law density profile such that the total enclosed mass is given by:

$$M(< r) = M_{bh} + M_{ext}(< r_o) \left( \frac{r}{r_o} \right)^{3-\gamma} \tag{2.2}$$

The power law slope, $\gamma$, is fixed to 1.5 in the orbital fits presented here, though Ghez et al. (2008) showed that the extended mass upper limit within the small radius enclosed by stellar orbits did not depend strongly on the value chosen for $\gamma$ in the range from 0.5 to 3. We set the outer radius cutoff of the extended mass distribution to 3.4 $\times 10^{11}$ km = 0.011 pc, such that it encloses the apoapse distances of S0-2 and S0-38 within uncertainties. Our data are not sensitive to the mass outside of the orbits of these stars. For this fit, we also set the characteristic radius in the equation above, $r_o$, to the same value of 0.011 pc. We then use the extended mass parameters to find the extended dark mass within the apoapse of S0-2's orbit (0.01 pc), to compare with results from previous works. This orbital fit is performed using MultiNest and has 20 free parameters: 7 black hole potential parameters, a set of 6 Keplerian orbital parameters for each star, and the total extended dark mass within $r_o$ ($M_{ext}(< r_o)$). We also perform an extended mass fit of the orbit of S0-2 alone for comparison purposes, which is discussed in Appendix 2.B.

As the final part of these analyses, we explore the additional uncertainties and biases arising from the construction of the absolute reference frame. In Appendix 2.C, we describe the details of a jack knife analysis performed on the 7 SiO masers used to tie our NIR observations to the absolute reference frame. The results of this jack knife analysis are used to correct the statistical bias (which is small compared to the orbital fitting uncertainties for $M_{bh}$ and $R_o$) and add an additional source of error for all the black hole potential parameters. These bias shift and the additional errors are only significant for the parameters describing the position and velocity of Sgr A* on the plane of the sky.

### 2.3.5 Simulations to Investigate Statistical and Systematic Errors

To confirm that the errors on the black hole parameters resulting from the simultaneous fit of S0-2 and S0-38 are reasonable given our measurement uncertainties, we simulate mock S0-2 and S0-38 data. We then fit these mock data and compare the widths of the resulting $M_{bh}$ and $R_o$ probability distributions to the results from the real data.

For every speckle holography, AO, and RV observation epoch, a simulated measurement is created by drawing from a gaussian distribution. This gaussian distribution has an average equal to the best-fit model from the combined S0-2 and S0-38 orbital fit and a standard deviation equal to that epoch's measurement error. The mock data are then fit using MultiNest, in the same way as the real S0-2 and S0-38 data. The widths of the resulting $M_{bh}$ and $R_o$ probability distributions are quantified as the standard deviation of the posterior samples generated by the MultiNest fit. One hundred mock data sets are created and fit in order to sample the possible widths of the $M_{bh}$ and $R_o$ distributions well while not requiring large amounts of computation time.

## 2.4 Results

### 2.4.1 New Speckle Holography Detections of S0-38

The application of the new methodology of analyzing speckle holography images on S0-38 results in 12 new astrometric detections of this star. These new detections go back to May 1997, spanning nearly the entirety of our time baseline for speckle holography. Of these 12 new speckle holography detections, 6 are direct detections found in the initial analysis of the speckle holography data and 6 are prior-assisted detections found using the force method. The 6 direct detections are in the 6 deepest epochs in which S0-38 was not confused with another source. All the prior-assisted detections have K magnitudes that are consistent with S0-38's average AO magnitude within $\pm 0.5$, are 3 - 20 sigma above the noise, and have correlations ranging from 0.7 - 0.85 (well above the 0.3 minimum value). Adding these new speckle holography detections to the 21 adaptive optics detections of S0-38 brings the total

number of astrometric measurements to 33 and almost doubles the time baseline that these measurements cover. Table 2.3 lists all the astrometry and radial velocity measurements of S0-38 used in this study. Appendix 2.B lists the measurements of S0-2 used in the orbital modeling. With the new speckle holography detections, S0-38 has now been observed for over 80% of its 19-year orbit (see Figure 2.5).

S0-38 is not detected in the other 15 speckle epochs for a variety of reasons. S0-38 is confused with another star in 7 speckle epochs, either with a star of similar brightness (with S0-104 in April and May 2002 and with S0-49 in July 1998) or with a much brighter star (with S0-1, K = 14.7, in October 2000 and with S0-20, K = 15.8, in July 2005 and May and July 1999). S0-38 was not detected in 6 other speckle epochs because the PSF fit performed by *Starfinder* Force 1 did not converge (April 2005, September 2003, July 2002, May 2001, April 2000, and April 1998). Finally, only 2 detections were rejected because they did not meet either the correlation or signal-to-noise threshold: June 1996 (signal-to-noise = 1.7) and June 1995 (correlation = 0.04).

Table 2.3. S0-38 Astrometric and Radial Velocity Measurements

| Date (Decimal) | $K'$ (mag) | ΔR.A. (arcsec) | ΔDec. (arcsec) | ΔR.A. Error (arcsec) | ΔDec. Error (arcsec) | $V_z$[b] (km s$^{-1}$) | $V_z$ Error (km s$^{-1}$) | Reference[a] | Detection Method |
|---|---|---|---|---|---|---|---|---|---|
| 1997.367 | 16.9 | -0.229 | -0.076 | 0.012 | 0.012 | - | - | (1) | Speckle (prior) |
| 1998.366 | 16.8 | -0.188 | -0.088 | 0.012 | 0.012 | - | - | (1) | Speckle (prior) |
| 1998.590 | 17.9 | -0.188 | -0.088 | 0.012 | 0.012 | - | - | (1) | Speckle (direct) |
| 1998.771 | 17.0 | -0.164 | -0.079 | 0.012 | 0.012 | - | - | (1) | Speckle (prior) |
| 2000.381 | 17.3 | -0.125 | -0.100 | 0.012 | 0.012 | - | - | (1) | Speckle (direct) |
| 2000.548 | 16.5 | -0.113 | -0.102 | 0.012 | 0.012 | - | - | (1) | Speckle (direct) |
| 2001.572 | 17.0 | -0.068 | -0.083 | 0.012 | 0.012 | - | - | (1) | Speckle (direct) |
| 2003.303 | 17.0 | -0.007 | 0.018 | 0.012 | 0.012 | - | - | (1) | Speckle (prior) |
| 2003.554 | 16.8 | -0.002 | 0.029 | 0.012 | 0.012 | - | - | (1) | Speckle (prior) |
| 2004.327 | 17.0 | -0.067 | 0.060 | 0.012 | 0.012 | - | - | (1) | Speckle (direct) |
| 2004.564 | 17.0 | -0.074 | 0.064 | 0.012 | 0.012 | - | - | (1) | Speckle (direct) |
| 2004.660 | 16.6 | -0.075 | 0.086 | 0.012 | 0.012 | - | - | (1) | Speckle (prior) |
| 2005.580 | 17.1 | -0.1285 | 0.0622 | 0.0045 | 0.0023 | - | - | (1) | AO |
| 2006.336 | 16.9 | -0.1596 | 0.0616 | 0.0017 | 0.0017 | - | - | (1) | AO |
| 2006.470 | 17.0 | -0.1647 | 0.0599 | 0.0020 | 0.0025 | - | - | (1) | AO |
| 2006.541 | 16.9 | -0.1668 | 0.0593 | 0.0017 | 0.0017 | - | - | (1) | AO |
| 2007.374 | 17.2 | -0.1933 | 0.0467 | 0.0017 | 0.0018 | - | - | (1) | AO |
| 2007.612 | 16.9 | -0.1990 | 0.0437 | 0.0018 | 0.0017 | - | - | (1) | AO |
| 2008.260 | - | - | - | - | - | -185 | 70 | (2) | AO |
| 2008.371 | 16.9 | -0.2140 | 0.0322 | 0.0019 | 0.0018 | - | - | (1) | AO |
| 2008.562 | 16.9 | -0.2161 | 0.0311 | 0.0022 | 0.0017 | - | - | (1) | AO |
| 2009.340 | 17.1 | -0.2361 | 0.0225 | 0.0020 | 0.0019 | - | - | (1) | AO |
| 2009.561 | 17.1 | -0.2389 | 0.0185 | 0.0018 | 0.0018 | - | - | (1) | AO |

Table 2.3 (cont'd)

| Date (Decimal) | $K'$ (mag) | ΔR.A. (arcsec) | ΔDec. (arcsec) | ΔR.A. Error (arcsec) | ΔDec. Error (arcsec) | $V_z$ [b] (km s$^{-1}$) | $V_z$ Error (km s$^{-1}$) | Reference[a] | Detection Method |
|---|---|---|---|---|---|---|---|---|---|
| 2009.689 | 17.1 | -0.2426 | 0.0156 | 0.0019 | 0.0021 | - | - | (1) | AO |
| 2010.342 | 17.0 | -0.2473 | 0.0090 | 0.0017 | 0.0017 | - | - | (1) | AO |
| 2010.511 | 16.9 | -0.2461 | 0.0056 | 0.0024 | 0.0022 | - | - | (1) | AO |
| 2010.620 | 17.1 | -0.2495 | 0.0045 | 0.0019 | 0.0019 | - | - | (1) | AO |
| 2011.401 | 17.0 | -0.2585 | -0.0119 | 0.0022 | 0.0018 | - | - | (1) | AO |
| 2011.543 | 16.9 | -0.2576 | -0.0127 | 0.0017 | 0.0017 | - | - | (1) | AO |
| 2011.642 | 17.0 | -0.2558 | -0.0136 | 0.0018 | 0.0018 | - | - | (1) | AO |
| 2012.371 | 17.0 | -0.2545 | -0.0260 | 0.0028 | 0.0020 | - | - | (1) | AO |
| 2012.562 | 17.0 | -0.2570 | -0.0285 | 0.0018 | 0.0017 | - | - | (1) | AO |
| 2013.318 | 16.7 | -0.2523 | -0.0391 | 0.0033 | 0.0020 | - | - | (1) | AO |
| 2013.360 | - | - | - | - | - | -111 | 25 | (1) | AO |
| 2013.550 | 16.8 | -0.2555 | -0.0413 | 0.0021 | 0.0020 | - | - | (1) | AO |

[a]Measurement originally reported in (1) this work and (2) Gillessen et al. (2009b).

[b]$V_z$ values listed here are in the local standard of rest reference frame.

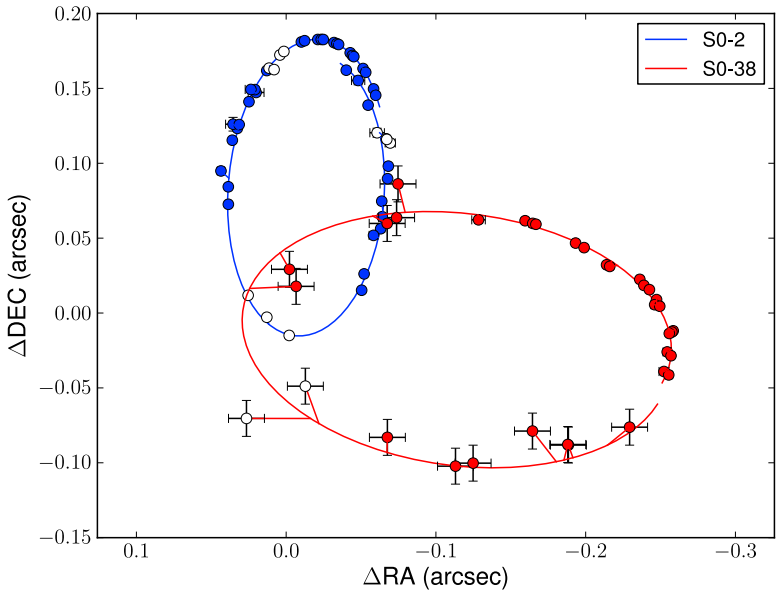


Figure 2.5: The best-fit orbit for S0-2 (blue line) and for S0-38 (red line) on the plane of the sky. These model orbit lines show the positions of these stars from 1995 to 2014. Both stars orbit clockwise on the plane of the sky. Closed circles indicate astrometric detections that were used in the orbital fits. Open circles indicate points that were not used in the fits because these astrometric detections are biased due to the proximity of other known sources on the plane of the sky. For S0-38, this consists of the two epochs of May and June 2002 in which the position of S0-38 shows a bias because it is blended with S0-104; in all other confusion epochs *Starfinder* Force 1 can only recover a position close to the neighboring source and S0-38 is undetected. Note in particular the paucity of detections around the point of closest approach at the bottom of S0-2's orbit. The implication of the absence of useable detections in this part of S0-2's orbit is that S0-2 constrains the horizontal position of Sgr A* in our reference frame ($x_o$) better than its vertical position ($y_o$). S0-38's orbit on the plane of the sky is perpendicular to that of S0-2, so it can provide additional constraints on $y_o$.

### 2.4.2 Gravitational Potential Parameters

#### 2.4.2.1 Values Derived from the Orbital Fit of S0-38 Alone

We fit the orbit of S0-38 alone, leaving the orbital parameters as well as the black hole parameters free, to compare with the fit of S0-2's orbit alone (discussed in Appendix 2.B). The motion of S0-38 alone is well fit by a Keplerian orbital model. Comparisons of the best-fit model from the fit S0-38's data alone are shown in Figure 2.6 (middle and bottom rows). Similarly, the best fit to S0-2's data alone is displayed in Figure 2.7.

The orbital model fit of S0-38's motion alone provides independent estimates the black hole potential parameters $x_o$, $y_o$, $V_x$, and $V_y$ (see Figure 2.8 and Table 2.4). The other black hole parameters ($V_z$, $R_o$, $M_{bh}$) rely on radial velocity measurement and are not well determined. This is because S0-38 has only two radial velocity measurements and these RV values are close to 0 km s$^{-1}$. These three parameters are still left free in this orbital fit of S0-38, but the uniform priors applied to these parameters are set to ranges that fully encompass at least the $\pm 4\sigma$ uncertainties derived from the fit of S0-2 alone (see Table 2.4). Those that are independently well fit are those that only require astrometric measurements ($x_o$, $y_o$, $V_x$, $V_y$; see Figure 2.9). The value for these parameters preferred by S0-38 agree with the values given by S0-2 within 1 sigma, except for the $V_y$ parameter which differs by 2 sigma. Note that reference frame uncetainties are a significant additional error source for $x_o$, $y_o$, $V_x$, and $V_y$ (see Figure 2.9), but are negligible for $M_{bh}$ and $R_o$ (see Appendix 2.C).

#### 2.4.2.2 Values Derived from the Simultaneous Orbital Fit of S0-38 and S0-2

We fit the orbits of S0-38 and S0-2 simultaneously to constrain the gravitational potential. Using the information from both of these stars gives the final values of $M_{bh}$ and $R_o$. Figure 2.6 and Figure 2.7 (top and bottom rows) show the resulting best-fit model orbits for S0-38 and S0-2 respectively in $\Delta$R.A., $\Delta$Decl., and radial velocity versus time. The astrometric data are shown in an absolute reference frame that defines Sgr A*-radio to be at rest at the origin. These figures also give the residuals of these data from the model. The residuals show that orbital models fit the data well within the uncertainties, with a reduced chi-squared of 1.3. Table 2.4 shows the best fit and errors on the black hole and orbital parameters of S0-2 and S0-38 as determined by the simultaneous fit of these stars.

The best-fit black hole parameters presented in Table 2.4 from the fits of S0-2 alone, S0-38 alone, and S0-2 and S0-38 simultaneously are taken as the weighted average of the MultiNest samples for each parameter. The fitting error is then taken as the weighted standard deviation of the MultiNest samples. The best-fit values are then shifted by the bias determined by a jack knife analysis on the 7 SiO masers used to construct the absolute

Table 2.4. Best-Fit Black Hole and Orbital Parameters as Derived From the Fit of S0-2 alone, S0-38 alone, and the Simultaneous Fit of S0-2 and S0-38

| Model Parameter (units) | Best-Fit Parameter Values from Orbital Fits[a] S0-2 only | S0-38 only | S0-2 and S0-38 |
|---|---|---|---|
| Black Hole Properties: | | | |
| Distance (kpc) | $8.02 \pm 0.36 \pm 0.04$ | $[6.5, 9.5]$[b] | $7.86 \pm 0.14 \pm 0.04$ |
| Mass ($10^6 M_\odot$) | $4.12 \pm 0.31 \pm 0.04$ | $[2.5, 5.5]$[b] | $4.02 \pm 0.16 \pm 0.04$ |
| $X$ Position of Sgr A* (mas) | $2.52 \pm 0.56 \pm 1.90$ | $-5.25 \pm 9.41 \pm 1.90$ | $2.74 \pm 0.50 \pm 1.90$ |
| $Y$ Position of Sgr A* (mas) | $-4.37 \pm 1.34 \pm 1.23$ | $-6.85 \pm 5.00 \pm 1.23$ | $-5.06 \pm 0.60 \pm 1.23$ |
| $X$ Velocity (mas/yr) | $-0.02 \pm 0.03 \pm 0.13$ | $-0.40 \pm 0.70 \pm 0.13$ | $-0.04 \pm 0.03 \pm 0.13$ |
| $Y$ Velocity (mas/yr) | $0.55 \pm 0.07 \pm 0.22$ | $-0.48 \pm 0.43 \pm 0.22$ | $0.51 \pm 0.06 \pm 0.22$ |
| $Z$ Velocity (km/sec) | $-15 \pm 10 \pm 4$ | $[-80, 40]$[b] | $-15.48 \pm 8.36 \pm 4.28$ |
| S0-2 Properties: | | | |
| Period (yr) | $15.90 \pm 0.04$ | | $15.92 \pm 0.04$ |
| Time of Closest Approach (yr) | $2002.343 \pm 0.008$ | | $2002.347 \pm 0.003$ |
| Eccentricity | $0.890 \pm 0.005$ | | $0.892 \pm 0.002$ |
| Inclination (deg) | $134.7 \pm 0.9$ | | $134.2 \pm 0.3$ |
| Argument of Periapse (deg) | $66.5 \pm 0.9$ | | $66.8 \pm 0.5$ |
| Angle to the ascending node (deg) | $227.9 \pm 0.8$ | | $228.0 \pm 0.5$ |
| S0-38 Properties: | | | |
| Period (yr) | | $19.1 \pm 0.6$ | $19.2 \pm 0.2$ |
| Time of Closest Approach (yr) | | $2003.1 \pm 0.1$ | $2003.19 \pm 0.04$ |
| Eccentricity | | $0.80 \pm 0.02$ | $0.810 \pm 0.004$ |
| Inclination (deg) | | $170 \pm 4$ | $170 \pm 3$ |
| Argument of Periapse (deg) | | $20 \pm 30$ | $12 \pm 21$ |
| Angle to the ascending node (deg) | | $110 \pm 30$ | $95 \pm 20$ |
| Reduced Chi-Squared | 1.5 | 0.9 | 1.3 |

[a]All best-fit values are shifted by the bias determined by the jack knife analysis of the reference frame (see Appendix 2.C). The first error term for each best fit value corresponds to the error determined by the orbital fit. For the black hole parameters, the second error term corresponds to jack knife uncertainty from the reference frame.

[b]These parameters are not well-determined by S0-38 alone, so instead of a best fit the uniform prior ranges that were used in the fit are reported.

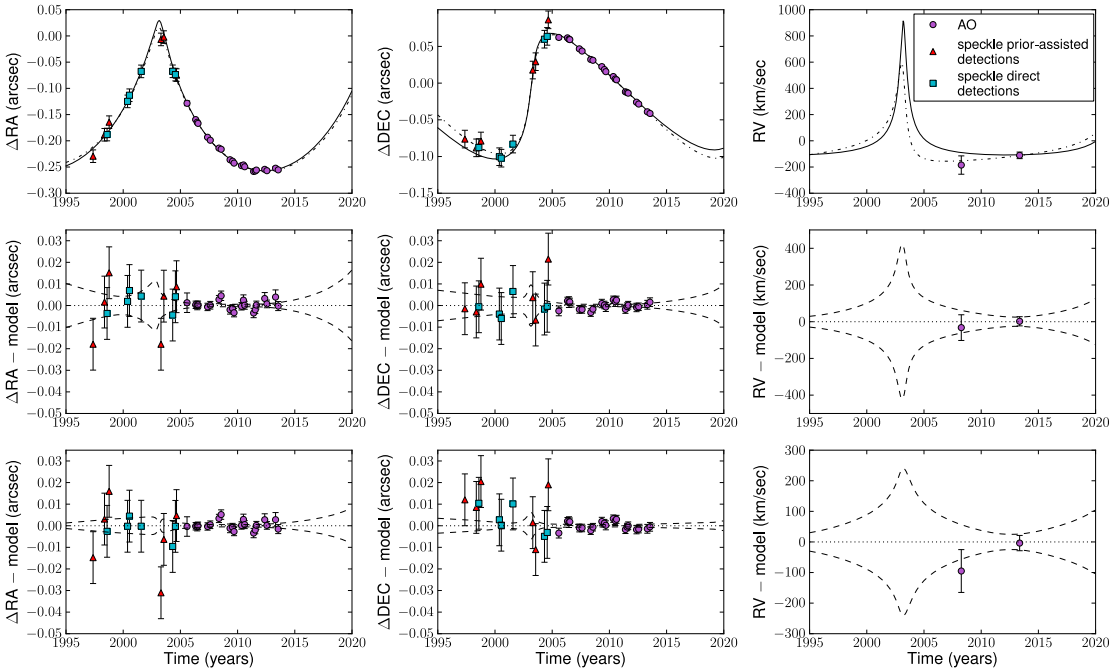


Figure 2.6: Orbital fits of all speckle holography and AO astrometry and radial velocity measurements of the short-period star S0-38. The top row shows the measurements of S0-38's position and radial velocity along with the best-fit models of S0-38's orbit as determined by the fit of S0-38 alone (dash-dotted line) and the simultaneous fit of S0-38 and S0-2 (solid line). The middle and bottom rows show the residuals of the position and radial velocity measurements from the best-fit models. The middle row shows the residuals from the fit of S0-38 alone and the bottom rows shows the residuals from the simultaneous fit of S0-2 and S0-38. The dashed lines in these rows indicate the 1-sigma uncertainties in the best fit models. In all plots, the detections of S0-38 are shown in different colors and shapes depending on the method in which they were detected: AO detections are purple circles, direct detections from the speckle holography images are teal squares, and prior-assisted detections from the speckle holography images are red triangles. The astrometry of S0-38 is plotted as the offset from the position of Sgr A*-radio, which is defined as the origin of our absolute reference frame.

reference frame (see Appendix 2.C for details). The error in this bias shift is also presented as a second error term in Table 2.4. All probability distributions of the 7 black hole parameters presented in this work include the bias shift. Note that the jack knife uncertainties due to the absolute reference construction are small compared to the fitting errors for $M_{bh}$ and $R_o$, so systematics in the reference frame do not greatly affect the values of these two key black hole parameters (see Figure 2.8). Additionally, the black hole position and velocity on the sky ($x_o$, $y_o$, $V_x$, and $V_y$) as determined by the fit of S0-2 and S0-38 are offset from 0.0, but they become consistent with 0.0 when the reference frame errors are included (see Figure

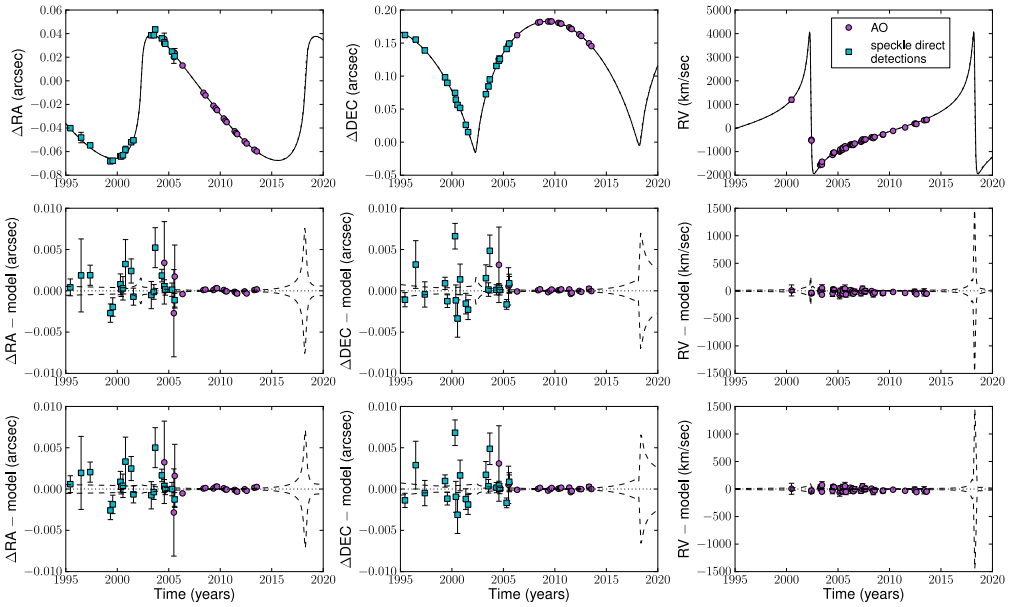


Figure 2.7: Orbital fits of all speckle holography and AO astrometry and radial velocity measurements of the short-period star S0-2. The top row shows the measurements of S0-2's position and radial velocity along with the best-fit model of S0-2's orbit as determined by the fit of S0-2 alone (dash-dotted line) and the simultaneous fit of S0-38 and S0-2 (solid line). Note that these two best-fit models are very similar on the scale of the plots shown here. The middle and bottom rows show the residuals of the position and radial velocity measurements from the best-fit models. The middle row shows the residuals from the fit of S0-2 alone and the bottom rows shows the residuals from the simultaneous fit of S0-2 and S0-38. In all plots, the detections of S0-2 are shown in different colors and shapes depending on the method in which they were detected: AO detections are purple circles and direct detections from the speckle holography images are teal squares. The astrometry of S0-2 is plotted as the offset from the position of Sgr A*-radio, which is defined as the origin of our absolute reference frame. Note that the uncertainty in the prediction of the radial velocity of S0-2 around its next time of closest approach in 2018 exceeds the limits of the y axis of the lower right plot. The uncertainty in the RV at this time ranges between $\pm 1400$ km s$^{-1}$ relative to the best-fit model.

2.9).

The addition of S0-38 leads to a better constraint of the black hole parameters compared to using the information from S0-2 alone. The best-fit black hole parameters and the errors on these values for the simultaneous fit of S0-2 and S0-38 as well as the fit of S0-2 alone are shown in Table 2.4. The errors on the mass of Sgr A* and the distance to the Galactic Center decrease by a factor of $\sim$2 and 2.5 respectively. The best fit values of $M_{bh}$ and $R_o$ as determined from the combined S0-2 and S0-38 orbital fit are: $M_{bh} = 4.02 \pm 0.16 \pm 0.04$

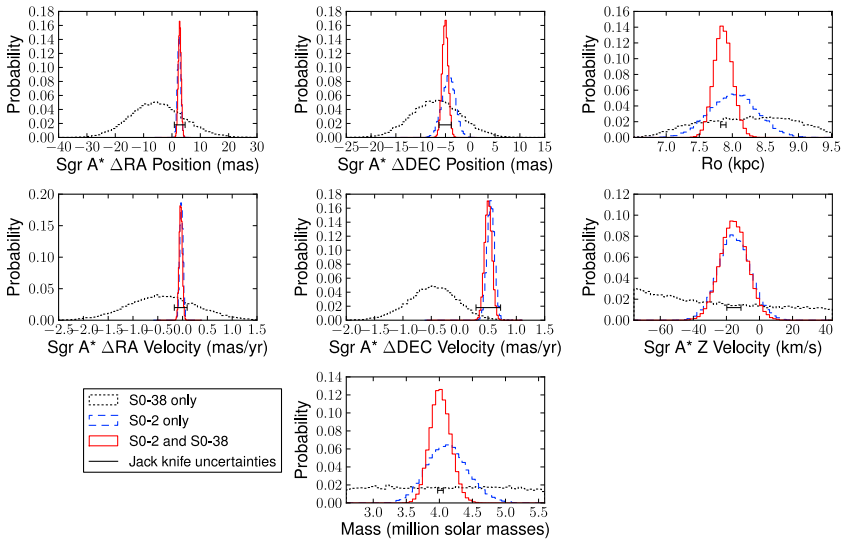


Figure 2.8: Probability distributions of the 7 black hole parameters as determined by an orbital fit of S0-2 alone (blue dashed lines), a fit of S0-38 alone (black dotted lines), and a combined orbital fit of S0-2 and S0-38 (red solid lines). All three probability distributions in each panel are shifted by the bias determined in the jack knife analysis on the construction of the absolute reference frame (see Appendix 2.C). This shift is also applied in all subsequent probability distribution plots. The black, horizontal error bars show the uncertainties in this bias shift. The addition of S0-38 to the orbital fit increases the constraints on the black hole parameters, most notably the $R_o$ and the mass of Sgr A*.

$\times 10^6 M_\odot$ and $7.86 \pm 0.14 \pm 0.04$ kpc. Figure 2.10 shows the joint probability distributions of $M_{bh}$ and $R_o$ as determined by S0-2 alone, S0-38 alone, and by S0-2 and S0-38 together.

To confirm that the estimated uncertainties on $M_{bh}$ and $R_o$ from the simultaneous fit of S0-2 and S0-38 are reasonable given the measurement uncertainties, we compare our estimated uncertainties to the distributions of the uncertainties on $M_{bh}$ and $R_o$ derived from the 100 mock data sets. These mock data sets are simulated assuming the measurement uncertainties are only statistical. The estimated uncertainties on $M_{bh}$ and $R_o$ from the real data are well within the distributions of uncertainties derived from the simulated data sets, with values smaller on average than the widths resulting from the mock data by only 1- and 0.7-sigma respectively. In addition, the $R_o$ uncertainty derived from the real data falls in the most likely bin of the simulated uncertainties. We therefore conclude that the estimated uncertainties on $M_{bh}$ and $R_o$ are reasonable given the measurement uncertainties.

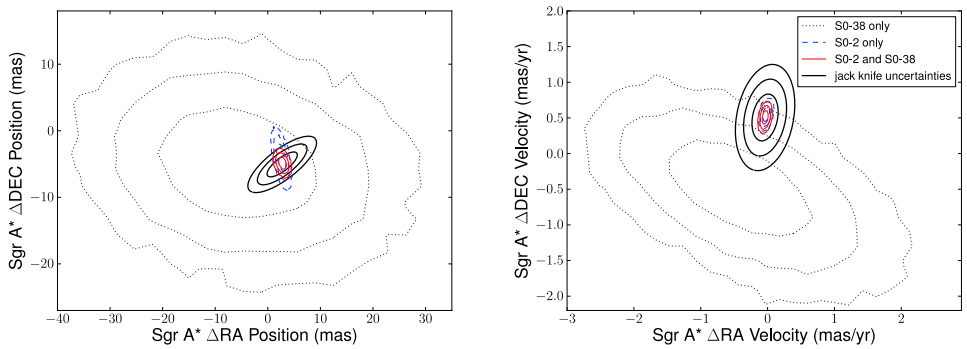


Figure 2.9: Joint probability distribution of $x_o$ and $y_o$ (*left*), the position of Sgr A* on the plane of the sky, and the joint probability of $V_x$ and $V_y$, the velocity of Sgr A* on the plane of the sky (*right*). The joint probability distributions as determined by three orbit fits are shown: S0-2 alone (blue, dashed line), S0-38 alone (black, dotted line), and S0-2 and S0-38 together (red, solid line). All the probability distributions are shifted by the bias determined in the jack knife analysis (see Appendix 2.C). The black, solid lines show the 1, 2, and 3-sigma uncertainties in this bias shift.

The mass-to-distance ratio of Sgr A*, $M_{bh}/R_o$ sets the apparent size of the black hole's gravitational radius at the distance of $R_o$ to Sgr A*: $r_g = GM_{bh}/c^2R_o$. The probability distribution of this value as determined by the orbital fit of S0-2 and S0-38 is shown in Figure 2.12. We find that the best fit angular size of the gravitational radius of Sgr A* is $5.20 \pm 0.12 \pm 0.06$, where the second error term is the estimated uncertainty in the reference frame, jack knife bias shifts of $M_{bh}$ and $R_o$ propagated to the gravitational radius.

The additional information found in S0-38's orbital motion also gives increased constraints on extended dark mass within the apoapse distances of its and S0-2's orbits. In addition to the central supermassive black hole, a central cluster of stellar mass black holes and/or other compact objects has been predicted and theoretically explored (e.g., Morris 1993; Miralda-Escudé & Gould 2000; Freitag et al. 2006; Merritt 2010). The amount of extended dark mass within the orbits of S0-2 and S0-38 influences their orbital motion. Figure 2.13 shows the probability distribution of the extended mass contained within this radius for a fit of S0-2 alone and a simultaneous fit of S0-2 and S0-38. The resulting 68.3% confidence ($1\sigma$) upper limits on the $M_{ext}$ within 0.011 pc are 0.06 $\times 10^6 M_\odot$ for the S0-2 only fit and 0.05 $\times 10^6 M_\odot$ for the simultaneous S0-2 and S0-38 fit. The 99.7% confidence ($3\sigma$) upper limits for these fits are 0.16 and 0.15 $\times 10^6 M_\odot$ respectively.

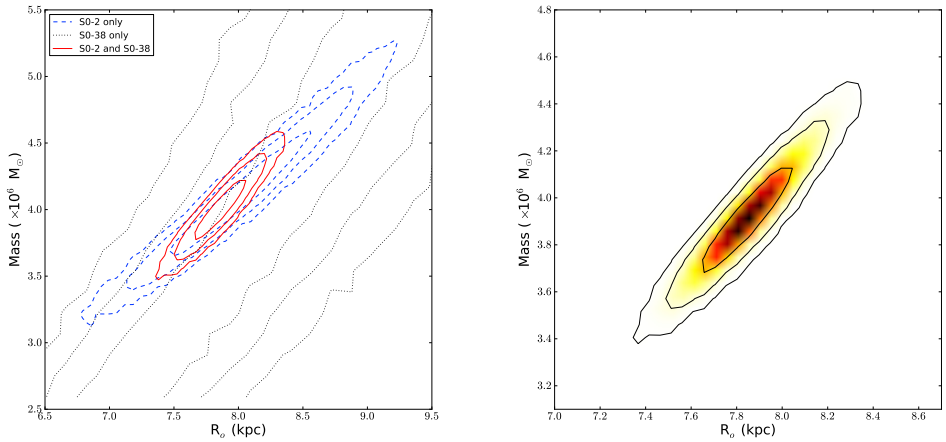


Figure 2.10: *Left*: 2D joint probability distribution with 1-, 2-, and 3-sigma contours of $M_{bh}$ and $R_o$ as derived by the orbital fit of S0-2 alone (blue dashed lines), S0-38 alone (black dotted line), and a simultaneous fit of S0-2 and S0-38, with the new speckle holography detections of S0-38 included (red solid lines). The orientation of S0-38's orbit on the plane of the sky leads to a different correlation of $M_{bh}$ and $R_o$, resulting in small errors on these parameters when S0-2 and S0-38 are fit simultaneously. The precision of our measurements of $M_{bh}$ and $R_o$ has increased by a factor of $\sim$2 and 2.5 respectively compared to S0-2 alone. Note that the $y_o$ parameter (not visualized here) is also highly correlated with $M_{bh}$ and $R_o$ (see Section 2.5.1). *Right*: Final joint probability distribution of $M_{bh}$ and $R_o$ as derived by the simultaneous fit of S0-2 and S0-38.

## 2.5 Discussion

### 2.5.1 Improvements with the Additional Information from S0-38

We have demonstrated the power of our new methodology of searching for speckle holography detections of S0-38 using the information in the AO detections by applying it to S0-38. The combination of S0-2 and S0-38 leads to a significant improvement in our knowledge of $R_o$ and the mass of Sgr A* compared to using the information from S0-2 alone. The reasons why the addition of S0-38 improves the constraints on $M_{bh}$ and $R_o$ so much are described here.

The results of fitting S0-38 alone show that S0-38 primarily gives information about the position and velocity of Sgr A* on the plane of the sky ($x_o$, $y_o$, $V_x$, and $V_y$). Figure 2.14 shows the joint probability distributions of these four parameters with $M_{bh}$ and $R_o$ from the fit of S0-2 alone and in the simultaneous fit of S0-2 and S0-38. In the fit of S0-2 alone, $M_{bh}$ and $R_o$ are both correlated with $y_o$, demonstrating that a better constraint on $y_o$ would lead

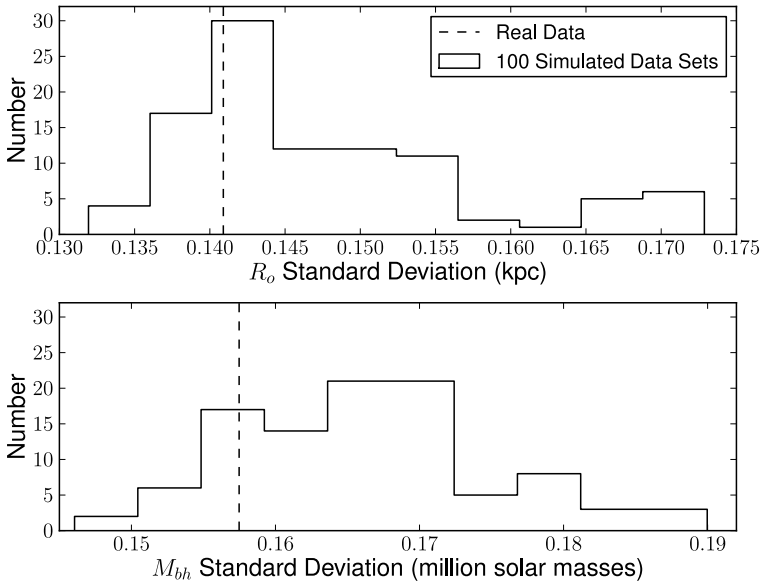


Figure 2.11: Histogram of standard deviation of posterior samples of $M_{bh}$ and $R_o$ generated by the MultiNest fit of 100 fake sets of S0-2 and S0-38 data. The standard deviation quantifies the width of the $M_{bh}$ and $R_o$ probability distributions. The 100 data sets were created by assuming only statistical measurement uncertainties. The vertical dashed lines show standard deviations of $M_{bh}$ and $R_o$ samples generated by the fit of the real S0-2 and S0-38 data, which are smaller on average than the simulated standard deviations by 1- and 0.7-sigma respectively.

to a better constraint on $M_{bh}$ and $R_o$. In the simultaneous fit, the errors on $y_o$ and thereby $M_{bh}$ and $R_o$ are significantly reduced. So it is specifically through improved knowledge of $y_o$ that S0-38 decreases the errors on $M_{bh}$ and $R_o$ when simultaneously fit with S0-2. The fact that $M_{bh}$ and $R_o$ are not correlated with $V_y$ in Figure 2.14 additionally shows that the difference in values of this parameter from the separate fits of S0-2 and S0-38 does not affect the $M_{bh}$ and $R_o$ results from the simultaneous fit.

The reason that the addition of S0-38 gives such an improved constraint on $y_o$ is the orientation of this star's orbit on the plane of the sky. Due to S0-2's orientation on the plane of the sky and the fact that we must omit the detections of S0-2 around its periapse position because of confusion with the NIR counterpart of Sgr A*, S0-2 gives a better constraint on $x_o$ than $y_o$. Figure 2.5 shows the current set of astrometric measurements for S0-2, including those points left out of the fit due to confusion with Sgr A* and other known

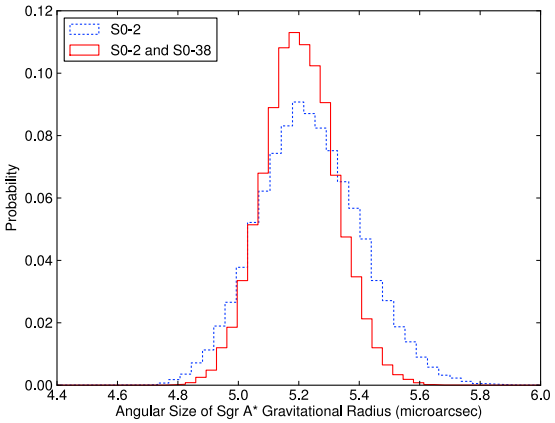


Figure 2.12: Probability distribution of the angular size of the gravitational radius of Sgr A*: $GM_{bh}/c^2R_o$. The distribution is calculated from the $M_{bh}$ and $R_o$ distributions that are shifted by the negligible bias determined in the jack knife analysis (see Appendix 2.C).

sources (indicated by open circles), leaving very few unbiased points in the lower third of the ellipse of S0-2's orbit. S0-38 is fortunately on an orbit that is nearly perpendicular on the plane of the sky to that of S0-2, also shown in Figure 2.5. Therefore, this star can further constrain the $y_o$ position of Sgr A* and in turn the values of $M_{bh}$ and $R_o$. The best-fit solutions of $M_{bh}$ and $R_o$ for each case agree well within 1 sigma. With the addition of the information provided by S0-38, the errors on these parameters decrease by a factor of $\sim$2 and 2.5 respectively.

The joint probability distribution of $M_{bh}$ and $R_o$ (Figure 2.10) also shows that S0-38 contains different information than S0-2 about these parameters. $M_{bh}$ and $R_o$ are not individually constrained by the orbital fit of S0-38 alone, but their correlation is constrained. The correlation as determined by S0-38 alone has a different slope than the correlation determined by S0-2 alone. This different slope leads to the additional constraints on $M_{bh}$ and $R_o$ when information from S0-38 is added. In the future, the addition of more stars with high orbital phase coverage and orbits perpendicular to S0-2 will lead to even smaller errors on $M_{bh}$ and $R_o$.

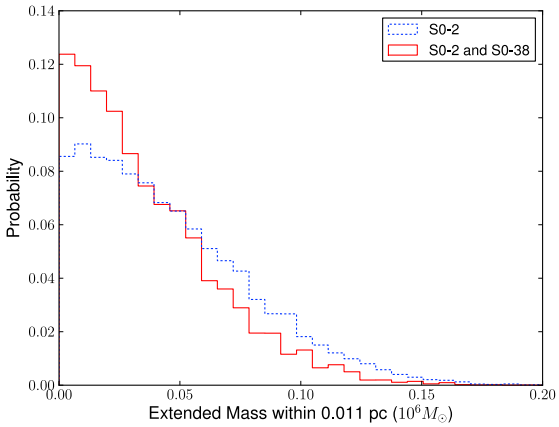


Figure 2.13: The probability distribution of the extended dark mass within 0.011 pc of the supermassive black hole, as determined by the fit of S0-2 alone (blue dotted line) and by the simultaneous fit of S0-2 and S0-38 (red solid line). The 99.7% confidence upper limit of the extended mass component decreases by ∼10% when the information contained in S0-38's orbital motion is added.

### 2.5.2 Scientific Implications of New Constraints on $M_{bh}$ and $R_o$

The values of $M_{bh}$ and $R_o$ presented here agree within uncertainties with previous measurements made using stellar orbits. The most recent previous measurements from Keck and VLT data respectively are $4.1 \pm 0.4$ (Meyer et al. 2012) and $4.30 \pm 0.36$ (Genzel et al. 2010) million solar masses for the mass of the black hole and $7.7 \pm 0.4$ (Meyer et al. 2012) and $8.2 \pm 0.34$ (Gillessen et al. 2013) kpc for $R_o$. The uncertainties derived from the orbital fit of S0-2 alone are slightly smaller than the uncertainties of these previous measurements due to the increased orbital phase coverage of this star, but the primary improvement in this work is the added information from the orbit of S0-38.

The method of using multiple stars' orbits to determine $M_{bh}$ and $R_o$ was also used in Gillessen et al. (2009b). In that work, the orbits of 5 stars in addition to S0-2 were simultaneously fit to determine the gravitational potential parameters. These 5 stars had orbital phase coverages ranging from 12 - 35% and three of the stars had multiple radial velocity measurements. S0-38 was not included in this set of stars, since it had only been observed from 2005 through 2008 at the time. With our observations now covering over 80% of S0-38's orbit, just including this one star in addition to S0-2 has significantly decreased

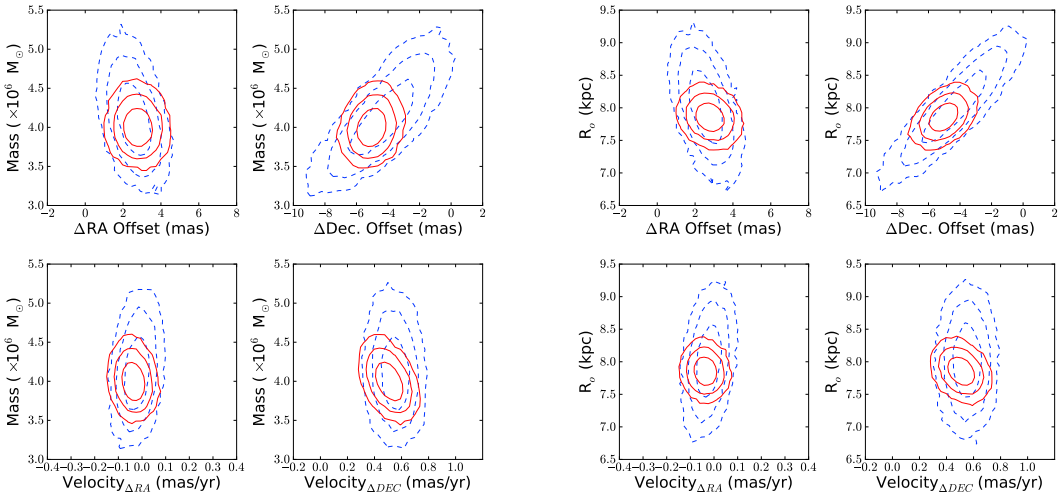


Figure 2.14: Joint probability distributions of $M_{bh}$ (*left* panels) and $R_o$ (*right* panels) and $x_o$, $y_o$, $V_x$, and $V_y$ as determined by the orbital fit of S0-2 alone (blue dotted line) and by the simultaneous orbital fit of S0-2 and S0-38, with all new speckle holography detections included (red solid line). These probability distributions are shifted by the bias determined in the jack knife analysis (see Appendix 2.C). The correlation between these sets of parameters in the case of S0-2 alone shows that our knowledge of $M_{bh}$ and $R_o$ is limited by how well S0-2 constrains $y_o$. With the addition of the measurements of S0-38's position and RV, $y_o$, and therefore also $M_{bh}$ and $R_o$, are much better determined. The errors in $M_{bh}$ and $R_o$ in the combined S0-2 and S0-38 fit are $\sim$2 and $\sim$2.5 times smaller than in the S0-2-only fit respectively.

the errors on $M_{bh}$ and $R_o$. From the arguments presented in the previous section, this seems to mainly be due to S0-38's orientation on the sky, as well as the more than 80% orbital phase coverage. Of the 5 other stars used in Gillessen et al. (2009b), two of them have orientations $\sim$ 45 degrees away from S0-2's vertical orientation, but none has the perpendicular orientation of S0-38.

The $R_o$ value presented in this work also agrees with other, recent direct measurements of the distance to the center of our galaxy within $\sim$ 2 sigma. VLBI measurements of the trigonometric parallax of $H_2O$ masers in the star forming region Sgr B2 give a value of $7.9 \pm 0.8$ kpc (Reid et al. 2009), while dynamical modeling of the nuclear star cluster gives a statistical parallax distance to the Galactic Center of $8.27 \pm 0.13$ kpc (Chatzopoulos et al. 2015). Another recent indirect measurement, using VLBI parallaxes and proper motions of over 100 masers to model the motion and structure of the Milky Way, gives a comparable

value and uncertainty in $R_o$ to that of the statistical parallax method: $8.34 \pm 0.16$ kpc (Reid et al. 2014). The direct statistical parallax method and indirect modeling method have similar uncertainties in $R_o$, but a value of $\sim 2$ sigma higher than presented in this work. It remains to be seen whether continued orbital monitoring and further improvement of $R_o$ constraints from the orbits of S0-2 and S0-38 will maintain this mild disagreement.

The direct measurement of $R_o$ presented here has implications for constraints on the structure and kinematics of our galaxy. Reid & Brunthaler (2004) measured the apparent proper motion of Sgr A*, which is due only to the galactic orbit of the sun if the supermassive black hole is assumed to be at the center of the galaxy. This measurement gave a ratio of the circular rotation speed at the radius of the Sun ($\Theta_o$) and $R_o$ of $29.45 \pm 0.15$ km s$^{-1}$ kpc$^{-1}$. Combining this ratio with the $R_o$ measured in this work gives $\Theta_o = 231$ $\pm 4.3$ km s$^{-1}$. This value of $\Theta_o$ agrees well with the independently measured value found by Reid et al. 2014 of $240 \pm 8$ km s$^{-1}$.

The new mass value presented here does not significantly change the position of the Milky Way in the observed correlations between mass of the central black hole and host galaxy properties, such as stellar velocity dispersion and mass of the bulge (see Kormendy & Ho 2013 for a review). Sgr A*, along with other central black holes in galaxies with pseudobulges, has a lower mass than expected from the tight correlation seen in ellipticals and galaxies with bulges.

The new upper limit on the extended dark mass within the orbits of S0-2 and S0-38 is also improved compared to previous work. To compare the limits presented in Section 2.4 with previous measurements from Ghez et al. (2008) and Gillessen et al. (2009b), we tranform our upper limits to find the extended mass within the apoapse distance of S0-2: 3.1 $\times 10^{11}$ km = 0.01 pc. The 1-sigma (3-sigma) upper limits within this radius are 0.05 (0.14) $\times 10^6 M_\odot$ for the S0-2 only fit and 0.04 (0.13) $\times 10^6 M_\odot$ for the simultaneous S0-2 and S0-38 fit. Ghez et al. (2008) and Gillessen et al. (2009b) found 1-sigma upper limits of 0.12 and 0.17 $\times 10^6 M_\odot$ respectively; therefore our new upper limits are a factor of 3-4 lower than previous measurements. S0-38 does improve the limit compared to S0-2 alone, but the main reason for the lower limit compared to earlier work is due to increased time coverage of the

orbit of S0-2. Our new limit is still over an order of magnitude more than the ∼500 - 1000 $M_\odot$ of stellar remnants predicted to be within 0.01 pc (e.g., Freitag et al. 2006), and other models predict even less mass within 0.01 pc (Merritt 2010). As observations of the orbits of S0-2 and S0-38 continue, the limits on the extended dark mass within 0.01 pc will continue to decrease.

The improved constraints on the gravitational potential that come with the addition of S0-38 also impacts future tests of general relativity in the Galactic Center. General relativistic deviations from pure Keplerian motion are expected to be detectable when S0-2 goes though its time of closest approach to the black hole in 2018. The deviations will be observable as the shift of the measured velocity of S0-2 due to the gravitational redshift. Measuring the deviations from S0-2's Keplerian orbit require as much knowledge of S0-2's Keplerian orbit and the gravitational potential as possible, so the additional constraints from S0-38 are important to this future probe of general relativity. Another observable deviation from a Keplerian orbit is the precession of the point of periapse. This general relativistic precession is confounded by the Newtonian precession due to extended dark mass within stellar orbits. Measuring the general relativistic precession therefore requires the measurement of precession in at least two stars. Additionally, the measurement of the ratio of $M_{bh}$ and $R_o$ from stellar orbits is required to compare the size of the black hole shadow as measured by the upcoming Event Horizon Telescope to theoretical predictions (Psaltis et al. 2015). The theoretical half-opening angle of the shadow of Sgr A* as observed from Earth is predicted to be $(5 \pm 0.2)GM_{bh}/R_oc^2$, regardless of the spin of the black hole. With the addition of S0-38 and an increased time baseline of observations, the gravitational radius is now known within $\sim$ 3%, which is less than $\pm$4% range in the theoretically predicted sizes of the black hole shadow assuming no knowledge of the spin of Sgr A*. In the future, our knowledge of the gravitational potential in the Galactic Center will increase with more observations of S0-2 and S0-38 as well as with the addition of other short-period stars, thereby also increasing the possibility of measuring the effects of general relativity in this extreme environment.

APPENDIX

## 2.A Astrometry of Secondary Standards

The astrometric absolute reference frame is updated using the methods described in Yelda et al. (2014) with the addition of new observations of the masers, which are summarized in Table 2.A.1. The results of this analysis, carried out by Sylvana Yelda, are the updated astrometry measurements for the IR secondary astrometric standards, shown in Table 2.A.2.

## 2.B S0-2 Data and Orbital Analysis

Here we report new astrometric and spectroscopic observations of the star S0-2. New AO astrometric measurements were obtained in the same way as described in Section 2.2.2.1 for new observation epochs. Table 2.B.1 lists the astrometric measurements of S0-2 used in this work. The speckle holography detections used in the fit of S0-2 are all from the set of direct detections discussed in Section 2.2.1; i.e., S0-2 was detected in all three subset images as well as the main image. Speckle holography direct detections in which S0-2 was confused with another known source are not used in the orbital fit, as in Ghez et al. (2008). This is the first paper in which we fit S0-2's orbit with the speckle holography astrometric data. These data supercede the shift-and-add speckle data reported in previous works. Table 2.B.1 lists

Table 2.A.1. Summary of New Maser Mosaic Observations

| Date (UT) | Date (Decimal) | Frames Obtained | Frames Used | FWHM (mas) | Strehl | $N_{stars}$ | $K_{lim}$[a] (mag) | $\sigma_{pos}$[b] mas |
|---|---|---|---|---|---|---|---|---|
| 2011 July 20 | 2011.549 | 65 | 64 | 62 | 0.23 | 2103 | 15.8 | 1.87 |
| 2012 May 16 | 2012.373 | 54 | 54 | 58 | 0.24 | 2040 | 15.7 | 1.82 |
| 2013 July 1 | 2013.501 | 175 | 173 | 59 | 0.24 | 2685 | 16.4 | 1.63 |

[a] $K_{lim}$ is the magnitude at which the cumulative distribution function of the observed K magnitudes reaches 90% of the total sample size.

[b] Positional error taken as error on the mean from the three sub-images in each epoch and is derived from stars with $K < 15$. These positional errors also include distortion error.

Table 2.A.2. Galactic Center Secondary IR Astrometric Standards

| Name | K' (mag) | $T_{0,IR}$ (year) | Radius (arcsec) | Δ R.A. (arcsec) | $\sigma_{R.A.}$[a] (mas) | Δ Dec. (arcsec) | $\sigma_{Dec}$[a] (mas) | $v_{RA}$[b] (mas yr$^{-1}$) | $v_{Dec}$[b] (mas yr$^{-1}$) |
|---|---|---|---|---|---|---|---|---|---|
| S0-6 | 14.2 | 2010.11 | 0.36 | 0.0200 | 1.1 | -0.3558 | 1.1 | -5.2 ± 0.1 | 3.5 ± 0.2 |
| S0-11 | 15.4 | 2010.42 | 0.50 | 0.4934 | 1.1 | -0.0607 | 1.2 | -3.8 ± 0.2 | -2.4 ± 0.3 |
| S0-7 | 15.4 | 2010.08 | 0.52 | 0.5145 | 1.1 | 0.1013 | 1.2 | 5.8 ± 0.2 | 1.0 ± 0.3 |

Note. — Table 2.A.2 is published in its entirety in the electronic version of Boehle et al. (2016).

[a]Positional errors include centroiding, alignment, and residual distortion (1 mas) errors, but do not include error in position of Sgr A* (2.0 mas, 1.4 mas in RA and Dec, respectively).

[b]Velocity errors do not include error in velocity of Sgr A* (0.13 mas yr$^{-1}$, 0.23 mas yr$^{-1}$ in RA and Dec, respectively).

the astrometric measurements of S0-2 used in this work.

New spectroscopic measurements of S0-2 were obtained with OSIRIS on the Keck 1 and Keck 2 telescopes using the Kn3 filter that is centered on the Br-$\gamma$ line at 2.1661$\mu m$. The previously unreported measurements as well as the derived LSR-corrected radial velocities of S0-2 are summarized in Table 2.B.2. Orbital fits of S0-2 performed in this work used these new radial velocities as well as previously reported radial velocities from both Keck and VLT (originally published in Ghez et al. 2008 and Gillessen et al. 2009b; also see Gillessen et al. 2009a in which both data sets are presented together).

In order to perform the orbital fits of stars in our sample (as detailed in Section 2.3.3.1), S0-2's data must first be fit alone in order to determine the probability distribution of the 7 BH parameters (in addition to S0-2's 6 own Keplerian orbital parameters). This 13-dimensional orbital fit was done using the Bayesian multimodal nested sampling algorithm called MultiNest (see Feroz & Hobson 2008 and Feroz et al. 2009). We also use the results of this orbital fit of S0-2 alone to compare with the results of fitting S0-38 alone and S0-2 and S0-38 simultaneously (Section 2.3.4). In addition to a purely Keplerian orbital fit, we also fit S0-2's orbit alone with an additional free parameter describing the amount of extended dark mass within a characteristic radius. This orbital fit also serves as a comparison to the results from fitting S0-2 and S0-38 simultaneously.

Table 2.B.1. S0-2 Astrometric Measurements

| Date (Decimal) | ΔR.A. (arcsec) | ΔDec. (arcsec) | ΔR.A. Error (arcsec) | ΔDec. Error (arcsec) |
|---|---|---|---|---|
| 1995.439 | -0.0401 | 0.16216 | 0.0010 | 0.00086 |
| 1996.485 | -0.0481 | 0.1553 | 0.0044 | 0.0029 |
| 1997.367 | -0.0547 | 0.1388 | 0.0012 | 0.0015 |
| 1999.333 | -0.0682 | 0.09808 | 0.0011 | 0.00074 |
| 1999.559 | -0.0677 | 0.08971 | 0.0011 | 0.00077 |
| 2000.305 | -0.0638 | 0.0747 | 0.0013 | 0.0016 |
| 2000.381 | -0.06411 | 0.0643 | 0.00087 | 0.0019 |
| 2000.548 | -0.0631 | 0.0563 | 0.0014 | 0.0023 |
| 2000.797 | -0.0584 | 0.0519 | 0.0030 | 0.0019 |
| 2001.351 | -0.0520 | 0.0261 | 0.0015 | 0.0013 |
| 2001.572 | -0.0504 | 0.0152 | 0.0010 | 0.0012 |
| 2003.303 | 0.0386 | 0.0726 | 0.0017 | 0.0016 |
| 2003.554 | 0.03863 | 0.08430 | 0.00089 | 0.00082 |
| 2003.682 | 0.0435 | 0.0949 | 0.0024 | 0.0019 |
| 2004.327 | 0.03595 | 0.11539 | 0.00076 | 0.00062 |
| 2004.564 | 0.03261 | 0.12328 | 0.00079 | 0.00053 |
| 2004.567 | 0.0355 | 0.1261 | 0.0050 | 0.0046 |
| 2004.660 | 0.03137 | 0.12584 | 0.00069 | 0.00060 |
| 2005.312 | 0.02483 | 0.14110 | 0.00081 | 0.00059 |
| 2005.495 | 0.0201 | 0.1473 | 0.0053 | 0.0023 |
| 2005.566 | 0.02084 | 0.1492 | 0.00083 | 0.0011 |
| 2005.580 | 0.0235 | 0.1493 | 0.0038 | 0.0010 |
| 2006.336 | 0.01296 | 0.16191 | 0.00015 | 0.00016 |
| 2008.371 | -0.01016 | 0.18101 | 0.00013 | 0.00014 |
| 2008.562 | -0.01232 | 0.18184 | 0.00016 | 0.00016 |
| 2009.340 | -0.02114 | 0.18266 | 0.00011 | 0.00011 |
| 2009.561 | -0.02343 | 0.18269 | 0.00013 | 0.00020 |
| 2009.689 | -0.02478 | 0.18265 | 0.00018 | 0.00014 |
| 2010.342 | -0.03194 | 0.18059 | 0.00012 | 0.00012 |
| 2010.511 | -0.03382 | 0.17984 | 0.00013 | 0.00012 |
| 2010.620 | -0.03501 | 0.17931 | 0.00016 | 0.00013 |
| 2011.401 | -0.04277 | 0.17377 | 0.00022 | 0.00017 |
| 2011.543 | -0.04423 | 0.17196 | 0.00014 | 0.00014 |
| 2011.642 | -0.04517 | 0.17121 | 0.00025 | 0.00025 |

Table 2.B.1 (cont'd)

| Date (Decimal) | ΔR.A. (arcsec) | ΔDec. (arcsec) | ΔR.A. Error (arcsec) | ΔDec. Error (arcsec) |
|---|---|---|---|---|
| 2012.371 | -0.05136 | 0.16326 | 0.00013 | 0.00017 |
| 2012.562 | -0.05312 | 0.16074 | 0.00014 | 0.00020 |
| 2013.318 | -0.05837 | 0.14965 | 0.00021 | 0.00026 |
| 2013.550 | -0.05979 | 0.14541 | 0.00014 | 0.00021 |

Table 2.B.2. Summary of New Spectroscopic Observations and Radial Velocities of S0-2

| Date (UT) | (Decimal) | $N_{frames} \times t_{int}$ | FWHM[a] (mas) | $V_z$[b] (km s$^{-1}$) | $V_z$ Error (km s$^{-1}$) | $V_{LSR}$[c] (km s$^{-1}$) |
|---|---|---|---|---|---|---|
| 2008 May 16 | 2008.373 | 11 × 900 sec | 75 | -417 | 32 | 26 |
| 2008 July 25 | 2008.564 | 10 × 900 sec | 84 | -380 | 43 | -7 |
| 2009 May 5 & 6 | 2009.344 | 24 × 900 sec | 74 | -285 | 32 | 30 |
| 2010 May 5 & 8 | 2010.349 | 16× 900 sec | 69 | -123 | 22 | 30 |
| 2011 July 10 | 2011.521 | 12× 900 sec | 86 | 23.5 | 22 | -11 |
| 2012 June 8 - 11 | 2012.441 | 10 × 900 sec | 72 | 183 | 49 | 14 |
| 2012 July 21 & 22 | 2012.556 | 11 × 900 sec | 102 | 187 | 33 | -5 |
| 2012 August 12 & 13 | 2012.616 | 26 × 900 sec | 61 | 167 | 25 | -13 |
| 2013 May 14 & 16 | 2013.369 | 18 × 900 sec | 67 | 328 | 66 | 27 |
| 2013 July 25 - 27 | 2013.566 | 26 × 900 sec | 84 | 339 | 23 | -18 |
| 2013 August 10 - 13 | 2013.612 | 31 × 900 sec | 78 | 349 | 16 | -13 |

[a]Average FWHM of S0-2 in the mosaic made of all frames, measured by fitting a two-dimensional Gaussian to the source.

[b]All radial velocities are corrected for the local standard of rest velocity.

[c]The local standard of rest velocity used to convert the observed velocities to the local standard of rest.

## 2.C Jack Knife Approximation to Reference Frame Uncertainties

We expect systematic errors in the orbital analysis of stars at the Galactic Center to be dominated by inaccuracies in our distortion solution and unaccounted errors in the construction of the absolute reference frame. While the former is potentially a significant source of uncertainty, currently its exact contribution is unclear and thus is the subject of future research. We also expect non-propagated statistical uncertainty in the reference frame to be a source of significant error. Such issues may arise from rigid model assumptions or improper propagation of error correlations. In this case, this issue is the general of several hundred secondary astrometric standards that have been treated as if their uncertainties are uncorrelated. This assumption is incorrect as the secondary standards are derived based on only 7 primary astrometric standards. If these correlated uncertainties are not incorporated into the full Bayesian orbital analysis, then the underlying statistical variance could produce a systematic bias in the resultant posterior distributions of the black hole parameters.

We can gain some insight into the effect and magnitude of this bias through various resampling methodologies. We use a jack knife resampling methodology to infer, to first order, the random statistical bias of an unbiased estimator by utilizing subsets of the full set of SiO maser positions that are used in the construction of the absolute reference frame (see Yelda et al. 2014 for details on the reference frame). Seven subsets were made by systematically excluding one maser position at a time. These subsets were then used to construct seven new reference frames and a full orbital analysis of S0-2 was performed.[4] The S0-2 astrometric measurements in each reference frame are presented in Table 2.C.1. The results of the orbital fits performed in the seven subset reference frames are then used to infer the statistical bias of some estimator $x$ by (Gottlieb, 2001)

$$x_{\text{bias}} \approx (n-1)(\bar{x}_{n-1} - x_n) \tag{2.3}$$

[4]Note that the orbital analysis of S0-2 was performed on the speckle shift-and-add astrometry of S0-2 and not the new speckle holography astrometry. We do not expect this to affect the results of the maser jack knife analysis, since the absolute reference frame construction is the same in the jack knife analysis and in the speckle holography analysis presented in this work.

with a variance of

$$\sigma^2(x_n) \leq \frac{n-1}{n} \sum_{i=1}^{n} \left(x_{n-1,i} - \bar{x}_{n-1}\right)^2 \tag{2.4}$$

where $n$ is the sample size (in this case 7), $x_n$ is the estimator derived using the full sample, $x_{n-1,i}$ is the estimator derived by the exclusion of the $i$-th maser, and $\bar{x}_{n-1}$ is the average of these subsets. Table 2.C.2 lists this bias and the square root of its variance ($\sigma$) on the inferred average value of the 7 black hole parameters considered in this work. In the black hole parameter probability distribution figures presented in Sections 2.4 and 2.5 we overlay 68%, 95%, and 99% contours over their respective posteriors. For the joint posteriors we infer the correlations through a multidimensional form of Equation 2.4:

$$\sigma^2(x_n, y_n) \leq \frac{n-1}{n} \sum_{i=1,j=1}^{n} \left(x_{n-1,i} - \bar{x}_{n-1}\right)\left(y_{n-1,j} - \bar{y}_{n-1}\right) \tag{2.5}$$

As noted in Section 2.4.2.2, the deviations of the $x_o$, $y_o$, $V_x$, $V_y$ posteriors appear to be explained by previously unaccounted for reference frame uncertainties, while the $M_{bh}$ and $R_o$ posteriors are not affected by these systematics.

We emphasize that the bias estimated by this analysis is only relevant assuming that these uncertainties are not already incorporated into our Bayesian analysis. The bias defined in Equation 2.3 is interpreted as, to first order, the difference between a statistic inferred from a hypothetical set of infinite masers and the same statistic inferred from our set of seven masers. Ideally, an uncertainty of this type would be inherently incorporated into any robust statistical methodology. If, contrary to our assumption, the uncertainties presented in this chapter do indeed account for reference frame construction uncertainties, then direct incorporation of the jack knife results would overestimate the uncertainties and thereby hide additional systematic effects. Thus, here we present our Bayesian uncertainties and jack knife result *separately* in Table 2.4.

If our assumption holds and if the Bayesian posteriors are parameterized in the sufficient statistic of $x_n$, then we may directly derive the resultant 'total' probability of a parameter $x$

as:

$$\mathscr{P}(x|x_{\rm bias},\sigma^2(x_n)) = \int d\hat{x}_{\rm bias}\mathscr{P}(x|x_n+\hat{x}_{\rm bias})\mathscr{P}(\hat{x}_{\rm bias}|x_{\rm bias},\sigma^2(x_n)) \tag{2.6}$$

where $\mathscr{P}(x|x_n+\hat{x}_{\rm bias})$ is the posterior parameterized in $x_n$ and $\mathscr{P}(\hat{x}_{\rm bias}|x_{\rm bias},\sigma^2(x_n))$ is a normal distribution whose parameterization is determined by Equations 2.3 and 2.4. In the limit of asymptotic normality, the net effect of incorporating this uncertainty is to shift the posterior by $x_{\rm bias}$ and adding the variance $\sigma(x_n)$ in quadrature with the derived Bayesian uncertainty. All posteriors plotted with the 68%, 95%, and 99% contours in Sections 2.4 and 2.5 are therefore shifted by the bias presented in Table 2.C.2. The best-fit values of the black hole parameters presented in Table 2.4 are also shifted by this bias and include the standard deviation of the bias as an additional uncertainty term. The most significant effect of the bias shifts and the corresponding additional uncertainties is in the black hole's position and velocity on the plane of the sky ($x_o$, $y_o$, $V_x$, and $V_y$).

Table 2.C.1. S0-2 Shift-and-Add Astrometric Measurements Used in Jack Knife Analysis

| Date (Decimal) | ΔR.A. (arcsec) | ΔDec. (arcsec) | ΔR.A. Error (arcsec) | ΔDec. Error (arcsec) |
|---|---|---|---|---|
| All 7 Masers: | | | | |
| 1995.439 | -0.0418 | 0.1637 | 0.0011 | 0.0014 |
| 1996.485 | -0.0520 | 0.1557 | 0.0046 | 0.0035 |
| 1997.367 | -0.0556 | 0.1384 | 0.0012 | 0.0025 |
| 1999.333 | -0.0648 | 0.0923 | 0.0011 | 0.0015 |
| 1999.559 | -0.0659 | 0.08949 | 0.0014 | 0.00093 |
| 2000.381 | -0.06306 | 0.06357 | 0.00097 | 0.00081 |
| 2000.548 | -0.0626 | 0.0591 | 0.0012 | 0.0012 |
| 2000.797 | -0.0615 | 0.0487 | 0.0024 | 0.0032 |
| 2001.351 | -0.0534 | 0.0258 | 0.0015 | 0.0016 |
| 2001.572 | -0.0492 | 0.0142 | 0.0012 | 0.0017 |
| 2003.303 | 0.0397 | 0.0703 | 0.0015 | 0.0021 |
| 2003.554 | 0.0410 | 0.08209 | 0.0013 | 0.00067 |
| 2003.682 | 0.0393 | 0.08902 | 0.0018 | 0.00084 |
| 2004.327 | 0.03691 | 0.1140 | 0.00081 | 0.0012 |
| 2004.564 | 0.0333 | 0.12245 | 0.0011 | 0.00093 |
| 2004.567 | 0.0352 | 0.1265 | 0.0050 | 0.0046 |
| 2004.660 | 0.03083 | 0.1255 | 0.00098 | 0.0020 |
| 2005.312 | 0.02412 | 0.1430 | 0.00081 | 0.0011 |
| 2005.495 | 0.0199 | 0.1477 | 0.0053 | 0.0023 |
| 2005.566 | 0.0216 | 0.1493 | 0.0021 | 0.0012 |
| 2005.580 | 0.0233 | 0.1497 | 0.0038 | 0.0010 |
| 2006.336 | 0.01280 | 0.16237 | 0.00013 | 0.00013 |
| 2008.371 | -0.01039 | 0.18146 | 0.00015 | 0.00015 |
| 2008.562 | -0.01247 | 0.18227 | 0.00017 | 0.00017 |
| 2009.340 | -0.02141 | 0.18308 | 0.00016 | 0.00016 |
| 2009.561 | -0.02368 | 0.18315 | 0.00016 | 0.00022 |
| 2009.689 | -0.02491 | 0.18311 | 0.00018 | 0.00018 |
| 2010.342 | -0.03216 | 0.18103 | 0.00015 | 0.00018 |
| 2010.511 | -0.03415 | 0.18025 | 0.00021 | 0.00020 |
| 2010.620 | -0.03527 | 0.17972 | 0.00019 | 0.00018 |
| 2011.401 | -0.04295 | 0.17417 | 0.00024 | 0.00022 |
| 2011.543 | -0.04441 | 0.17241 | 0.00017 | 0.00022 |
| 2011.642 | -0.04519 | 0.17152 | 0.00026 | 0.00023 |
| 2012.371 | -0.05162 | 0.16365 | 0.00016 | 0.00026 |

Table 2.C.1 (cont'd)

| Date (Decimal) | ΔR.A. (arcsec) | ΔDec. (arcsec) | ΔR.A. Error (arcsec) | ΔDec. Error (arcsec) |
|---|---|---|---|---|
| 2012.562 | -0.05335 | 0.16112 | 0.00018 | 0.00029 |
| 2013.318 | -0.05847 | 0.15042 | 0.00024 | 0.00041 |
| 2013.550 | -0.05995 | 0.14586 | 0.00018 | 0.00032 |
| | | | | |
| No IRS 10EE: | | | | |
| 1995.439 | -0.0424 | 0.1639 | 0.0013 | 0.0014 |
| 1996.485 | -0.0526 | 0.1558 | 0.0047 | 0.0035 |
| 1997.367 | -0.0561 | 0.1385 | 0.0011 | 0.0026 |
| 1999.333 | -0.0653 | 0.0925 | 0.0013 | 0.0015 |
| 1999.559 | -0.0663 | 0.08967 | 0.0014 | 0.00099 |
| 2000.381 | -0.06335 | 0.06360 | 0.00090 | 0.00084 |
| 2000.548 | -0.0629 | 0.0594 | 0.0011 | 0.0013 |
| 2000.797 | -0.0618 | 0.0489 | 0.0024 | 0.0033 |
| 2001.351 | -0.0536 | 0.0261 | 0.0014 | 0.0016 |
| 2001.572 | -0.0495 | 0.0145 | 0.0012 | 0.0018 |
| 2003.303 | 0.0395 | 0.0705 | 0.0015 | 0.0022 |
| 2003.554 | 0.0408 | 0.08232 | 0.0013 | 0.00071 |
| 2003.682 | 0.0392 | 0.08920 | 0.0018 | 0.00084 |
| 2004.327 | 0.03679 | 0.1142 | 0.00086 | 0.0011 |
| 2004.564 | 0.0332 | 0.12270 | 0.0011 | 0.00089 |
| 2004.567 | 0.0352 | 0.1268 | 0.0050 | 0.0046 |
| 2004.660 | 0.03072 | 0.1258 | 0.00099 | 0.0020 |
| 2005.312 | 0.02406 | 0.1433 | 0.00083 | 0.0012 |
| 2005.495 | 0.0198 | 0.1480 | 0.0053 | 0.0023 |
| 2005.566 | 0.0215 | 0.1495 | 0.0022 | 0.0012 |
| 2005.580 | 0.0231 | 0.1501 | 0.0038 | 0.0010 |
| 2006.336 | 0.01280 | 0.16265 | 0.00013 | 0.00012 |
| 2008.371 | -0.01028 | 0.18174 | 0.00015 | 0.00015 |
| 2008.562 | -0.01235 | 0.18255 | 0.00017 | 0.00017 |
| 2009.340 | -0.02125 | 0.18337 | 0.00016 | 0.00016 |
| 2009.561 | -0.02351 | 0.18342 | 0.00015 | 0.00021 |
| 2009.689 | -0.02473 | 0.18340 | 0.00018 | 0.00016 |
| 2010.342 | -0.03195 | 0.18130 | 0.00014 | 0.00016 |
| 2010.511 | -0.03393 | 0.18053 | 0.00020 | 0.00017 |
| 2010.620 | -0.03504 | 0.18004 | 0.00019 | 0.00018 |

Table 2.C.1 (cont'd)

| Date (Decimal) | ΔR.A. (arcsec) | ΔDec. (arcsec) | ΔR.A. Error (arcsec) | ΔDec. Error (arcsec) |
|---|---|---|---|---|
| 2011.401 | -0.04267 | 0.17447 | 0.00024 | 0.00022 |
| 2011.543 | -0.04413 | 0.17276 | 0.00017 | 0.00021 |
| 2011.642 | -0.04492 | 0.17183 | 0.00025 | 0.00023 |
| 2012.371 | -0.05128 | 0.16391 | 0.00015 | 0.00025 |
| 2012.562 | -0.05301 | 0.16143 | 0.00017 | 0.00027 |
| 2013.318 | -0.05811 | 0.15079 | 0.00023 | 0.00039 |
| 2013.550 | -0.05958 | 0.14618 | 0.00017 | 0.00030 |
| | | | | |
| No IRS 12N: | | | | |
| 1995.439 | -0.0426 | 0.1612 | 0.0017 | 0.0017 |
| 1996.485 | -0.0544 | 0.1538 | 0.0049 | 0.0041 |
| 1997.367 | -0.0579 | 0.1367 | 0.0017 | 0.0030 |
| 1999.333 | -0.0655 | 0.0904 | 0.0012 | 0.0018 |
| 1999.559 | -0.0669 | 0.0880 | 0.0014 | 0.0018 |
| 2000.381 | -0.0651 | 0.0617 | 0.0012 | 0.0019 |
| 2000.548 | -0.0640 | 0.0584 | 0.0014 | 0.0015 |
| 2000.797 | -0.0639 | 0.0486 | 0.0026 | 0.0041 |
| 2001.351 | -0.0552 | 0.0249 | 0.0017 | 0.0020 |
| 2001.572 | -0.0505 | 0.0145 | 0.0020 | 0.0021 |
| 2003.303 | 0.0385 | 0.0702 | 0.0016 | 0.0023 |
| 2003.554 | 0.0391 | 0.0812 | 0.0014 | 0.0013 |
| 2003.682 | 0.0385 | 0.0880 | 0.0012 | 0.0010 |
| 2004.327 | 0.03550 | 0.1135 | 0.00074 | 0.0012 |
| 2004.564 | 0.0320 | 0.1217 | 0.0012 | 0.0011 |
| 2004.567 | 0.0340 | 0.1261 | 0.0050 | 0.0046 |
| 2004.660 | 0.0308 | 0.1251 | 0.0014 | 0.0023 |
| 2005.312 | 0.0227 | 0.1425 | 0.0012 | 0.0015 |
| 2005.495 | 0.0185 | 0.1473 | 0.0053 | 0.0023 |
| 2005.566 | 0.0198 | 0.1488 | 0.0022 | 0.0020 |
| 2005.580 | 0.0218 | 0.1493 | 0.0039 | 0.0011 |
| 2006.336 | 0.01160 | 0.16187 | 0.00013 | 0.00013 |
| 2008.371 | -0.01139 | 0.18136 | 0.00015 | 0.00016 |
| 2008.562 | -0.01355 | 0.18213 | 0.00016 | 0.00017 |
| 2009.340 | -0.02251 | 0.18318 | 0.00016 | 0.00019 |
| 2009.561 | -0.02491 | 0.18320 | 0.00021 | 0.00026 |

Table 2.C.1 (cont'd)

| Date (Decimal) | ΔR.A. (arcsec) | ΔDec. (arcsec) | ΔR.A. Error (arcsec) | ΔDec. Error (arcsec) |
|---|---|---|---|---|
| 2009.689 | -0.02618 | 0.18310 | 0.00020 | 0.00021 |
| 2010.342 | -0.03339 | 0.18122 | 0.00018 | 0.00023 |
| 2010.511 | -0.03514 | 0.18023 | 0.00022 | 0.00028 |
| 2010.620 | -0.03637 | 0.17981 | 0.00021 | 0.00020 |
| 2011.401 | -0.04404 | 0.17436 | 0.00027 | 0.00030 |
| 2011.543 | -0.04541 | 0.17245 | 0.00021 | 0.00030 |
| 2011.642 | -0.04616 | 0.17169 | 0.00034 | 0.00029 |
| 2012.371 | -0.05271 | 0.16394 | 0.00021 | 0.00029 |
| 2012.562 | -0.05437 | 0.16143 | 0.00022 | 0.00030 |
| 2013.318 | -0.05946 | 0.15118 | 0.00027 | 0.00053 |
| 2013.550 | -0.06103 | 0.14638 | 0.00022 | 0.00038 |
| | | | | |
| No IRS 15NE: | | | | |
| 1995.439 | -0.0407 | 0.1636 | 0.0012 | 0.0014 |
| 1996.485 | -0.0509 | 0.1557 | 0.0047 | 0.0035 |
| 1997.367 | -0.0546 | 0.1384 | 0.0012 | 0.0025 |
| 1999.333 | -0.0641 | 0.0926 | 0.0012 | 0.0015 |
| 1999.559 | -0.0652 | 0.08971 | 0.0014 | 0.00091 |
| 2000.381 | -0.06237 | 0.06384 | 0.00092 | 0.00083 |
| 2000.548 | -0.0619 | 0.0596 | 0.0012 | 0.0012 |
| 2000.797 | -0.0608 | 0.0492 | 0.0024 | 0.0032 |
| 2001.351 | -0.0527 | 0.0264 | 0.0015 | 0.0016 |
| 2001.572 | -0.0487 | 0.0148 | 0.0013 | 0.0017 |
| 2003.303 | 0.0401 | 0.0709 | 0.0015 | 0.0021 |
| 2003.554 | 0.0415 | 0.08275 | 0.0014 | 0.00082 |
| 2003.682 | 0.0397 | 0.08961 | 0.0018 | 0.00088 |
| 2004.327 | 0.03729 | 0.1147 | 0.00081 | 0.0012 |
| 2004.564 | 0.0336 | 0.12320 | 0.0011 | 0.00095 |
| 2004.567 | 0.0356 | 0.1272 | 0.0050 | 0.0046 |
| 2004.660 | 0.03120 | 0.1263 | 0.00096 | 0.0020 |
| 2005.312 | 0.02439 | 0.1439 | 0.00086 | 0.0011 |
| 2005.495 | 0.0202 | 0.1486 | 0.0053 | 0.0023 |
| 2005.566 | 0.0219 | 0.1501 | 0.0022 | 0.0012 |
| 2005.580 | 0.0235 | 0.1506 | 0.0038 | 0.0010 |
| 2006.336 | 0.01304 | 0.16336 | 0.00012 | 0.00013 |

Table 2.C.1 (cont'd)

| Date (Decimal) | ΔR.A. (arcsec) | ΔDec. (arcsec) | ΔR.A. Error (arcsec) | ΔDec. Error (arcsec) |
|---|---|---|---|---|
| 2008.371 | -0.01032 | 0.18266 | 0.00014 | 0.00015 |
| 2008.562 | -0.01240 | 0.18346 | 0.00017 | 0.00017 |
| 2009.340 | -0.02143 | 0.18436 | 0.00016 | 0.00016 |
| 2009.561 | -0.02369 | 0.18449 | 0.00015 | 0.00021 |
| 2009.689 | -0.02495 | 0.18445 | 0.00018 | 0.00016 |
| 2010.342 | -0.03224 | 0.18243 | 0.00014 | 0.00016 |
| 2010.511 | -0.03424 | 0.18167 | 0.00019 | 0.00016 |
| 2010.620 | -0.03542 | 0.18119 | 0.00019 | 0.00018 |
| 2011.401 | -0.04312 | 0.17567 | 0.00023 | 0.00022 |
| 2011.543 | -0.04465 | 0.17396 | 0.00016 | 0.00020 |
| 2011.642 | -0.04542 | 0.17307 | 0.00025 | 0.00024 |
| 2012.371 | -0.05186 | 0.16529 | 0.00015 | 0.00023 |
| 2012.562 | -0.05365 | 0.16282 | 0.00016 | 0.00025 |
| 2013.318 | -0.05887 | 0.15217 | 0.00024 | 0.00037 |
| 2013.550 | -0.06035 | 0.14767 | 0.00017 | 0.00029 |
| | | | | |
| No IRS 17: | | | | |
| 1995.439 | -0.0414 | 0.1643 | 0.0012 | 0.0014 |
| 1996.485 | -0.0516 | 0.1562 | 0.0048 | 0.0035 |
| 1997.367 | -0.0553 | 0.1388 | 0.0012 | 0.0025 |
| 1999.333 | -0.0647 | 0.0927 | 0.0010 | 0.0014 |
| 1999.559 | -0.0657 | 0.08990 | 0.0014 | 0.00095 |
| 2000.381 | -0.06292 | 0.06384 | 0.00093 | 0.00081 |
| 2000.548 | -0.0624 | 0.0595 | 0.0012 | 0.0012 |
| 2000.797 | -0.0614 | 0.0491 | 0.0025 | 0.0034 |
| 2001.351 | -0.0532 | 0.0262 | 0.0015 | 0.0016 |
| 2001.572 | -0.0491 | 0.0146 | 0.0011 | 0.0017 |
| 2003.303 | 0.0397 | 0.0705 | 0.0014 | 0.0021 |
| 2003.554 | 0.0410 | 0.08229 | 0.0014 | 0.00068 |
| 2003.682 | 0.0394 | 0.08915 | 0.0018 | 0.00082 |
| 2004.327 | 0.03696 | 0.1142 | 0.00079 | 0.0011 |
| 2004.564 | 0.0333 | 0.12264 | 0.0011 | 0.00092 |
| 2004.567 | 0.0353 | 0.1267 | 0.0050 | 0.0046 |
| 2004.660 | 0.0309 | 0.1257 | 0.0010 | 0.0020 |
| 2005.312 | 0.02412 | 0.1432 | 0.00083 | 0.0011 |

Table 2.C.1 (cont'd)

| Date (Decimal) | ΔR.A. (arcsec) | ΔDec. (arcsec) | ΔR.A. Error (arcsec) | ΔDec. Error (arcsec) |
|---|---|---|---|---|
| 2005.495 | 0.0199 | 0.1479 | 0.0053 | 0.0023 |
| 2005.566 | 0.0216 | 0.1494 | 0.0021 | 0.0011 |
| 2005.580 | 0.0233 | 0.1500 | 0.0038 | 0.0010 |
| 2006.336 | 0.01275 | 0.16250 | 0.00013 | 0.00013 |
| 2008.371 | -0.01054 | 0.18153 | 0.00014 | 0.00015 |
| 2008.562 | -0.01263 | 0.18232 | 0.00017 | 0.00017 |
| 2009.340 | -0.02161 | 0.18309 | 0.00016 | 0.00016 |
| 2009.561 | -0.02389 | 0.18315 | 0.00014 | 0.00022 |
| 2009.689 | -0.02513 | 0.18311 | 0.00018 | 0.00016 |
| 2010.342 | -0.03243 | 0.18099 | 0.00014 | 0.00017 |
| 2010.511 | -0.03441 | 0.18022 | 0.00019 | 0.00018 |
| 2010.620 | -0.03555 | 0.17970 | 0.00019 | 0.00018 |
| 2011.401 | -0.04326 | 0.17409 | 0.00023 | 0.00023 |
| 2011.543 | -0.04474 | 0.17235 | 0.00016 | 0.00020 |
| 2011.642 | -0.04551 | 0.17144 | 0.00026 | 0.00023 |
| 2012.371 | -0.05199 | 0.16352 | 0.00015 | 0.00024 |
| 2012.562 | -0.05373 | 0.16100 | 0.00016 | 0.00026 |
| 2013.318 | -0.05886 | 0.15030 | 0.00023 | 0.00038 |
| 2013.550 | -0.06038 | 0.14573 | 0.00017 | 0.00030 |
| | | | | |
| No IRS 28: | | | | |
| 1995.439 | -0.0413 | 0.1646 | 0.0014 | 0.0014 |
| 1996.485 | -0.0516 | 0.1565 | 0.0047 | 0.0035 |
| 1997.367 | -0.0552 | 0.1391 | 0.0012 | 0.0024 |
| 1999.333 | -0.0645 | 0.0930 | 0.0012 | 0.0014 |
| 1999.559 | -0.0656 | 0.09016 | 0.0015 | 0.00091 |
| 2000.381 | -0.06277 | 0.06402 | 0.00093 | 0.00078 |
| 2000.548 | -0.0623 | 0.0598 | 0.0012 | 0.0012 |
| 2000.797 | -0.0613 | 0.0493 | 0.0024 | 0.0034 |
| 2001.351 | -0.0531 | 0.0265 | 0.0015 | 0.0016 |
| 2001.572 | -0.0490 | 0.0148 | 0.0012 | 0.0017 |
| 2003.303 | 0.0398 | 0.0707 | 0.0014 | 0.0021 |
| 2003.554 | 0.0411 | 0.08252 | 0.0013 | 0.00075 |
| 2003.682 | 0.0394 | 0.08940 | 0.0018 | 0.00084 |
| 2004.327 | 0.03703 | 0.1144 | 0.00081 | 0.0011 |

Table 2.C.1 (cont'd)

| Date (Decimal) | ΔR.A. (arcsec) | ΔDec. (arcsec) | ΔR.A. Error (arcsec) | ΔDec. Error (arcsec) |
|---|---|---|---|---|
| 2004.564 | 0.0334 | 0.12284 | 0.0011 | 0.00092 |
| 2004.567 | 0.0354 | 0.1269 | 0.0050 | 0.0046 |
| 2004.660 | 0.0309 | 0.1259 | 0.0010 | 0.0020 |
| 2005.312 | 0.02422 | 0.1434 | 0.00079 | 0.0011 |
| 2005.495 | 0.0200 | 0.1481 | 0.0053 | 0.0023 |
| 2005.566 | 0.0217 | 0.1496 | 0.0021 | 0.0013 |
| 2005.580 | 0.0233 | 0.1502 | 0.0038 | 0.0010 |
| 2006.336 | 0.01286 | 0.16268 | 0.00012 | 0.00013 |
| 2008.371 | -0.01040 | 0.18163 | 0.00015 | 0.00015 |
| 2008.562 | -0.01249 | 0.18243 | 0.00017 | 0.00017 |
| 2009.340 | -0.02147 | 0.18318 | 0.00016 | 0.00016 |
| 2009.561 | -0.02374 | 0.18325 | 0.00015 | 0.00021 |
| 2009.689 | -0.02496 | 0.18321 | 0.00018 | 0.00016 |
| 2010.342 | -0.03224 | 0.18109 | 0.00014 | 0.00017 |
| 2010.511 | -0.03423 | 0.18030 | 0.00021 | 0.00018 |
| 2010.620 | -0.03540 | 0.17974 | 0.00019 | 0.00018 |
| 2011.401 | -0.04307 | 0.17419 | 0.00023 | 0.00021 |
| 2011.543 | -0.04455 | 0.17244 | 0.00017 | 0.00023 |
| 2011.642 | -0.04532 | 0.17151 | 0.00026 | 0.00023 |
| 2012.371 | -0.05177 | 0.16357 | 0.00016 | 0.00024 |
| 2012.562 | -0.05350 | 0.16107 | 0.00018 | 0.00028 |
| 2013.318 | -0.05867 | 0.15029 | 0.00024 | 0.00039 |
| 2013.550 | -0.06016 | 0.14575 | 0.00018 | 0.00031 |
| | | | | |
| No IRS 7: | | | | |
| 1995.439 | -0.0399 | 0.1631 | 0.0017 | 0.0021 |
| 1996.485 | -0.0498 | 0.1561 | 0.0055 | 0.0044 |
| 1997.367 | -0.0545 | 0.1386 | 0.0013 | 0.0028 |
| 1999.333 | -0.0634 | 0.0920 | 0.0012 | 0.0016 |
| 1999.559 | -0.0644 | 0.0892 | 0.0017 | 0.0012 |
| 2000.381 | -0.0619 | 0.06333 | 0.0012 | 0.00089 |
| 2000.548 | -0.0617 | 0.0587 | 0.0012 | 0.0013 |
| 2000.797 | -0.0621 | 0.0483 | 0.0033 | 0.0044 |
| 2001.351 | -0.0526 | 0.0254 | 0.0015 | 0.0016 |
| 2001.572 | -0.0482 | 0.0140 | 0.0012 | 0.0018 |

Table 2.C.1 (cont'd)

| Date (Decimal) | ΔR.A. (arcsec) | ΔDec. (arcsec) | ΔR.A. Error (arcsec) | ΔDec. Error (arcsec) |
|---|---|---|---|---|
| 2003.303 | 0.0414 | 0.0694 | 0.0016 | 0.0021 |
| 2003.554 | 0.0420 | 0.0812 | 0.0015 | 0.0010 |
| 2003.682 | 0.0411 | 0.08802 | 0.0020 | 0.00086 |
| 2004.327 | 0.03773 | 0.1133 | 0.00086 | 0.0013 |
| 2004.564 | 0.0341 | 0.1213 | 0.0012 | 0.0010 |
| 2004.567 | 0.0363 | 0.1255 | 0.0050 | 0.0046 |
| 2004.660 | 0.0322 | 0.1248 | 0.0014 | 0.0020 |
| 2005.312 | 0.0253 | 0.1419 | 0.0010 | 0.0012 |
| 2005.495 | 0.0209 | 0.1465 | 0.0053 | 0.0023 |
| 2005.566 | 0.0230 | 0.1483 | 0.0022 | 0.0013 |
| 2005.580 | 0.0240 | 0.1485 | 0.0038 | 0.0010 |
| 2006.336 | 0.01372 | 0.16106 | 0.00013 | 0.00013 |
| 2008.371 | -0.00944 | 0.17984 | 0.00016 | 0.00015 |
| 2008.562 | -0.01155 | 0.18067 | 0.00017 | 0.00017 |
| 2009.340 | -0.02057 | 0.18139 | 0.00018 | 0.00016 |
| 2009.561 | -0.02281 | 0.18135 | 0.00017 | 0.00021 |
| 2009.689 | -0.02406 | 0.18129 | 0.00018 | 0.00016 |
| 2010.342 | -0.03134 | 0.17919 | 0.00016 | 0.00018 |
| 2010.511 | -0.03339 | 0.17839 | 0.00023 | 0.00018 |
| 2010.620 | -0.03447 | 0.17777 | 0.00022 | 0.00018 |
| 2011.401 | -0.04205 | 0.17215 | 0.00023 | 0.00023 |
| 2011.543 | -0.04357 | 0.17041 | 0.00017 | 0.00020 |
| 2011.642 | -0.04430 | 0.16950 | 0.00031 | 0.00028 |
| 2012.371 | -0.05081 | 0.16147 | 0.00016 | 0.00028 |
| 2012.562 | -0.05254 | 0.15899 | 0.00016 | 0.00029 |
| 2013.318 | -0.05768 | 0.14818 | 0.00026 | 0.00046 |
| 2013.550 | -0.05916 | 0.14347 | 0.00019 | 0.00034 |
| | | | | |
| No IRS 9: | | | | |
| 1995.439 | -0.0426 | 0.1637 | 0.0013 | 0.0014 |
| 1996.485 | -0.0527 | 0.1556 | 0.0047 | 0.0036 |
| 1997.367 | -0.0563 | 0.1383 | 0.0013 | 0.0026 |
| 1999.333 | -0.0655 | 0.0923 | 0.0013 | 0.0015 |
| 1999.559 | -0.0664 | 0.08948 | 0.0015 | 0.00095 |
| 2000.381 | -0.06354 | 0.06341 | 0.00095 | 0.00086 |

Table 2.C.1 (cont'd)

| Date (Decimal) | ΔR.A. (arcsec) | ΔDec. (arcsec) | ΔR.A. Error (arcsec) | ΔDec. Error (arcsec) |
|---|---|---|---|---|
| 2000.548 | -0.0631 | 0.0592 | 0.0012 | 0.0012 |
| 2000.797 | -0.0620 | 0.0488 | 0.0024 | 0.0032 |
| 2001.351 | -0.0538 | 0.0260 | 0.0015 | 0.0016 |
| 2001.572 | -0.0498 | 0.0144 | 0.0013 | 0.0017 |
| 2003.303 | 0.0393 | 0.0703 | 0.0014 | 0.0021 |
| 2003.554 | 0.0406 | 0.08216 | 0.0014 | 0.00071 |
| 2003.682 | 0.0390 | 0.08905 | 0.0018 | 0.00082 |
| 2004.327 | 0.03666 | 0.1141 | 0.00083 | 0.0012 |
| 2004.564 | 0.0330 | 0.12256 | 0.0011 | 0.00090 |
| 2004.567 | 0.0350 | 0.1266 | 0.0050 | 0.0046 |
| 2004.660 | 0.03062 | 0.1256 | 0.00096 | 0.0020 |
| 2005.312 | 0.02396 | 0.1431 | 0.00078 | 0.0011 |
| 2005.495 | 0.0197 | 0.1478 | 0.0053 | 0.0023 |
| 2005.566 | 0.0214 | 0.1494 | 0.0021 | 0.0012 |
| 2005.580 | 0.02302 | 0.14978 | 0.0038 | 0.00099 |
| 2006.336 | 0.01269 | 0.16255 | 0.00013 | 0.00013 |
| 2008.371 | -0.01037 | 0.18165 | 0.00015 | 0.00015 |
| 2008.562 | -0.01245 | 0.18246 | 0.00017 | 0.00017 |
| 2009.340 | -0.02135 | 0.18327 | 0.00016 | 0.00015 |
| 2009.561 | -0.02359 | 0.18336 | 0.00014 | 0.00021 |
| 2009.689 | -0.02482 | 0.18333 | 0.00018 | 0.00016 |
| 2010.342 | -0.03202 | 0.18127 | 0.00014 | 0.00016 |
| 2010.511 | -0.03401 | 0.18048 | 0.00020 | 0.00017 |
| 2010.620 | -0.03515 | 0.17995 | 0.00020 | 0.00018 |
| 2011.401 | -0.04275 | 0.17444 | 0.00023 | 0.00021 |
| 2011.543 | -0.04422 | 0.17271 | 0.00016 | 0.00021 |
| 2011.642 | -0.04499 | 0.17179 | 0.00025 | 0.00022 |
| 2012.371 | -0.05135 | 0.16390 | 0.00015 | 0.00024 |
| 2012.562 | -0.05306 | 0.16143 | 0.00017 | 0.00025 |
| 2013.318 | -0.05818 | 0.15075 | 0.00023 | 0.00038 |
| 2013.550 | -0.05963 | 0.14620 | 0.00018 | 0.00028 |

Table 2.C.2. Jack Knife Bias and Variance

| Black Hole Parameter (units) | Bias | Standard Deviation of Bias ($\sigma$) |
|---|---|---|
| Distance (kpc) | 0.01 | 0.04 |
| Mass ($10^6 M_\odot$) | 0.09 | 0.04 |
| $X$ Position of Sgr A* (mas) | -0.50 | 1.90 |
| $Y$ Position of Sgr A* (mas) | -0.73 | 1.23 |
| $X$ Velocity (mas/yr) | -0.08 | 0.13 |
| $Y$ Velocity (mas/yr) | -0.17 | 0.22 |
| $Z$ Velocity (km/sec) | 4.07 | 4.28 |

Bibliography

Bates, R. H. T., Gough, P. T., & Napier, P. J. 1973, A&A, 22, 319

Boehle, A., Ghez, A. M., Schödel, R., et al. 2016, ApJ, 830, 17

Chatzopoulos, S., Fritz, T. K., Gerhard, O., et al. 2015, MNRAS, 447, 948

Christou, J. C. 1991, PASP, 103, 1040

Diolaiti, E., Bendinelli, O., Bonaccini, D., et al. 2000, in Presented at the Society of Photo-Optical Instrumentation Engineers (SPIE) Conference, Vol. 4007, Proc. SPIE Vol. 4007, p. 879-888, Adaptive Optical Systems Technology, Peter L. Wizinowich; Ed., ed. P. L. Wizinowich, 879–888

Do, T., Lu, J. R., Ghez, A. M., et al. 2013, ApJ, 764, 154

Eckart, A., & Genzel, R. 1997, MNRAS, 284, 576

Eckart, A., Genzel, R., Ott, T., & Schödel, R. 2002, MNRAS, 331, 917

Eisenhauer, F., Schödel, R., Genzel, R., et al. 2003, ApJ, 597, L121

Feroz, F., & Hobson, M. P. 2008, MNRAS, 384, 449

Feroz, F., Hobson, M. P., & Bridges, M. 2009, MNRAS, 398, 1601

Ferrarese, L., & Merritt, D. 2000, ApJ, 539, L9

Freitag, M., Amaro-Seoane, P., & Kalogera, V. 2006, ApJ, 649, 91

Genzel, R., Eisenhauer, F., & Gillessen, S. 2010, Reviews of Modern Physics, 82, 3121

Ghez, A. M., Klein, B. L., Morris, M., & Becklin, E. E. 1998, ApJ, 509, 678

Ghez, A. M., Morris, M., Becklin, E. E., Tanner, A., & Kremenek, T. 2000, Nature, 407, 349

Ghez, A. M., Salim, S., Hornstein, S. D., et al. 2005a, ApJ, 620, 744

Ghez, A. M., Duchêne, G., Matthews, K., et al. 2003, ApJ, 586, L127

Ghez, A. M., Hornstein, S. D., Lu, J. R., et al. 2005b, ApJ, 635, 1087

Ghez, A. M., Salim, S., Weinberg, N. N., et al. 2008, ApJ, 689, 1044

Gillessen, S., Eisenhauer, F., Fritz, T. K., et al. 2009a, ApJ, 707, L114

Gillessen, S., Eisenhauer, F., Fritz, T. K., et al. 2013, in IAU Symposium, Vol. 289, IAU Symposium, ed. R. de Grijs, 29–35

Gillessen, S., Eisenhauer, F., Trippe, S., et al. 2009b, ApJ, 692, 1075

Gottlieb, A. D. 2001, ArXiv Mathematics e-prints, math/0109002

Hornstein, S. D., Ghez, A. M., Tanner, A., et al. 2002, ApJ, 577, L9

Kormendy, J., & Ho, L. C. 2013, ARA&A, 51, 511

Larkin, J., Barczys, M., Krabbe, A., et al. 2006, in Society of Photo-Optical Instrumentation Engineers (SPIE) Conference Series, Vol. 6269, Society of Photo-Optical Instrumentation Engineers (SPIE) Conference Series

Lu, J. R., Ghez, A. M., Hornstein, S. D., Morris, M., & Becklin, E. E. 2005, ApJ, 625, L51

Lu, J. R., Ghez, A. M., Hornstein, S. D., et al. 2009, ApJ, 690, 1463

Lucy, L. B. 2014, A&A, 563, A126

Matthews, K., Ghez, A. M., Weinberger, A. J., & Neugebauer, G. 1996, PASP, 108, 615

Matthews, K., & Soifer, B. T. 1994, Experimental Astronomy, 3, 77

Merritt, D. 2010, ApJ, 718, 739

Meyer, L., Ghez, A. M., Schödel, R., et al. 2012, Science, 338, 84

Miralda-Escudé, J., & Gould, A. 2000, ApJ, 545, 847

Morris, M. 1993, ApJ, 408, 496

Olling, R. P., & Merrifield, M. R. 2000, MNRAS, 311, 361

Petr, M. G., Coudé du Foresto, V., Beckwith, S. V. W., Richichi, A., & McCaughrean, M. J. 1998, ApJ, 500, 825

Primot, J., Rousset, G., & Fontanella, J. C. 1990, Journal of the Optical Society of America A, 7, 1598

Psaltis, D., Özel, F., Chan, C.-K., & Marrone, D. P. 2015, ApJ, 814, 115

Rafelski, M., Ghez, A. M., Hornstein, S. D., Lu, J. R., & Morris, M. 2007, ApJ, 659, 1241

Rayner, J. T., Cushing, M. C., & Vacca, W. D. 2009, ApJS, 185, 289

Reid, M. J. 1993, ARA&A, 31, 345

Reid, M. J., & Brunthaler, A. 2004, ApJ, 616, 872

Reid, M. J., Menten, K. M., Trippe, S., Ott, T., & Genzel, R. 2007, ApJ, 659, 378

Reid, M. J., Menten, K. M., Zheng, X. W., Brunthaler, A., & Xu, Y. 2009, ApJ, 705, 1548

Reid, M. J., Menten, K. M., Brunthaler, A., et al. 2014, ApJ, 783, 130

Schödel, R., Najarro, F., Muzic, K., & Eckart, A. 2010, A&A, 511, A18

Schödel, R., Yelda, S., Ghez, A., et al. 2013, MNRAS, 429, 1367

Schödel, R., Ott, T., Genzel, R., et al. 2002, Nature, 419, 694

Tremaine, S., Gebhardt, K., Bender, R., et al. 2002, ApJ, 574, 740

van Dam, M. A., Bouchez, A. H., Le Mignant, D., et al. 2006, PASP, 118, 310

Wizinowich, P. L., Le Mignant, D., Bouchez, A. H., et al. 2006, PASP, 118, 297

Yelda, S. 2012, PhD thesis, University of California, Los Angeles

Yelda, S., Ghez, A. M., Lu, J. R., et al. 2014, ArXiv e-prints, arXiv:1401.7354

Yelda, S., Lu, J. R., Ghez, A. M., et al. 2010, ApJ, 725, 331

# CHAPTER 3

# Upgrade of the Detector in the Integral Field Spectrograph OSIRIS at the W. M. Keck Observatory

Reproduced with permission of SPIE (Boehle, A.; J. E. Larkin; S. M. Adkins; T. Aliado; M. P. Fitzgerald, C. A. Johnson; J. E. Lyke; K. G. Magnone; J. M. Sohn; E. Wang; J. L. Weiss, 2016, Proc. SPIE, 9908, Ground-based and Airborne Instrumentation for Astronomy VI, 99082Q).

## 3.1 Introduction

### 3.1.1 OSIRIS Instrument Overview

OSIRIS is a near-infrared (1 to 2.5 $\mu$m) integral field spectrograph (IFS) currently on the Keck 1, 10-m telescope. This instrument simultaneously produces up to 3,000 spectra with a resolution of $\sim$3,800 across a contiguous, rectangular field of view. It offers 4 plate scales (0.02 - 0.10 arcseconds) and 23 broadband and narrowband filters across z, J, H, and K-band wavelengths for a total of 92 observing modes (Larkin et al., 2006). OSIRIS is fed by the Keck Adaptive Optics (AO) System (Wizinowich et al., 2000), which gives diffraction-limited spatial resolution across the instrument's field of view. OSIRIS has been a key instrument for a wide variety of science programs, including high-resolution mapping of gas emission and kinematics across other galaxies and characterizing the atmospheres of extrasolar planets. The instrument also includes an imager that can be used in parallel with the integral field spectrograph. The OSIRIS imager is in the process of being upgraded to an entirely new design (Fitzgerald et al., 2016).

A diagram of the OSIRIS spectrograph optical layout is shown in Fig. 3.1. Light coming from the AO system enters the spectrograph portion of OSIRIS and first passes through the scale-changing optics and the filters. The light is then imaged onto a lenslet array, which spatially samples the input image. The light sampled by each lenslet is collimated by a three mirror anastigmat (TMA), dispersed by a fixed grating, and re-imaged onto the detector by a second camera TMA. The dispersion axis of the grating is aligned with the horizontal rows of the detector. The lenslet array is rotated with respect to the dispersion axis such that the spectra are interleaved on the detector. Each spectrum is separated from its neighbor by ∼2 pixels in the raw data.

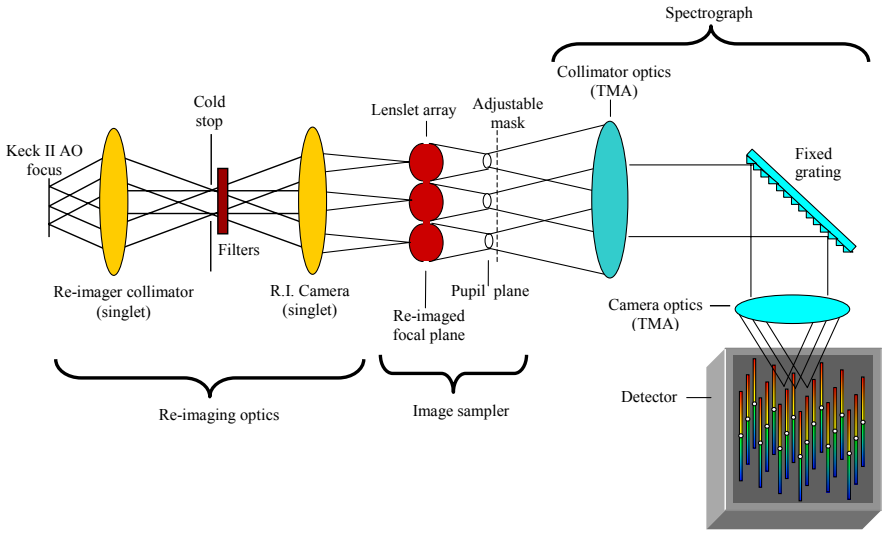


Figure 3.1: A diagram of the optical layout of the spectrograph portion of OSIRIS. The image sampler in this integral field spectrograph is a lenslet array. The light from each lenslet is then dispersed by a fixed grating and re-focused onto the detector. The spectra from the lenslets are interleaved on the detector with spacings of ∼2 pixels in the horizontal/spatial direction.

Due to the dense packing of the spectra, the detector performance and our ability to optimize the detector focus are crucial for OSIRIS's performance. Each of the closely-spaced spectra in the raw data must be extracted and assigned to the appropriate lenslet. The data reduction pipeline delivered with OSIRIS performs this necessary function in addition to basic data reduction steps (e.g., sky subtraction and cosmic ray correction) (Krabbe et al., 2004). The spectral extraction procedure requires knowledge of each lenslet's point spread

function (PSF). The lenslet PSFs are determined for each observing mode by using a white light source to illuminate one column of lenslets at a time. The lenslet spectra in these calibration data are separated by ∼32 pixels, allowing each lenslet's PSF to be mapped out to its wings in the spatial direction. The spectral extraction routine uses the lenslet PSFs to assign the light from each detector pixel to the corresponding lenslet. The resulting data are a three dimensional array consisting of a spectrum for every spatial pixel.

### 3.1.2 Upgrading to the H2RG

The original spectrograph detector delivered with OSIRIS was a Hawaii-2 (H2) from Rockwell Scientific (now Teledyne Sensors). After the grating in OSIRIS was upgraded in 2012 (Mieda et al., 2014), leading to improved throughput across all wavelengths, the H2 detector became the limiting factor in the instrument's sensitivity. The main reason for this is the low quantum efficiency (QE) of the H2 detector, especially at shorter wavelengths. The initial manufacturer estimates of the QE at the J and H bands were over 80%, but on-sky tests of the original OSIRIS detector suggested significantly lower performance.

The H2 detector also suffers from a number of artifacts that are detrimental to the instrument's performance. The 32 readout channels of the H2 have significant bias drifts between them, which lead to artifacts in the final data cube (Fig. 3.2). The H2 lacks reference pixels, so the offsets between channels must be measured from the image itself in order to be corrected. The H2 detector also experiences crosstalk between its readout channels (Fig. 3.3). The crosstalk due to a bright stellar spectrum can cross vertically over spectra from many lenslets. As the pixels are read out, the H2 also occasionally returns spurious bright pixels coordinated across the 32 channels, termed "glitches." The readout channel offsets, crosstalk, and glitches are all corrected by various data reduction pipeline modules, but the corrections are not perfect and therefore act as an additional source of noise in the reduced data.

Frames taken with the H2 detector also include a glow from the shift registers in the read out circuits in each quadrant of the detector (see Fig. 3.2). This glow leads to a higher effective dark current and additional noise. Each non-destructible read contributes to the

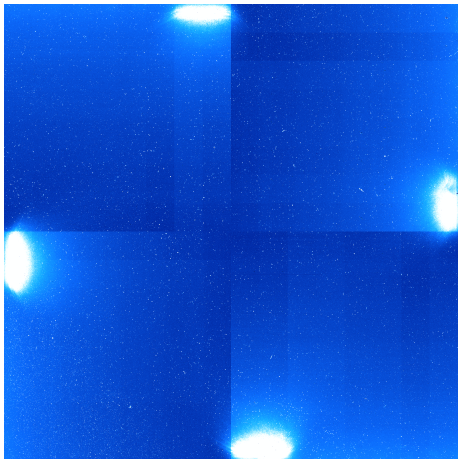

Figure 3.2: An example of a 900-sec dark frame taken with the original OSIRIS H2 detector. The frame is displayed with a log stretch color scheme. The frame shows DC offsets between the 32 readout channels of the detector. This detector artifact must be corrected in the data reduction pipeline by estimating the channel baseline offsets from the image data itself for every science and calibration frame. The example frame also shows the shift register glow in each of the four quadrants of the detector, which contributes to the apparent dark current and the noise in H2 detector frames. This glow limits the total number of reads that can be used in the Up-The-Ramp readout mode.

dark current through the shift register glow, thereby limiting the number of reads that can be used in the Up-The-Ramp (UTR; or Fowler) sampling mode. Additionally, the first two frames of an UTR read out must be discarded due to a "reset anomaly," in which the values read out after a reset decrease on a timescale of $\sim$5 sec (at the operating temperature of the H2 detector). Both the shift register glow and the reset anomaly cannot be corrected and have affected both the efficiency and the sensitivity of the OSIRIS instrument.

Finally, the H2 detector is expected to fail catastrophically via a shattering of the photosensitive HgCdTe layer. This is due to a difference between the coefficients of thermal expansion in the multiple layers of the detector. This eventual failure made the upgrade of the OSIRIS spectrograph detector essential for continued operation of this productive instrument.

The new detector installed in OSIRIS is a Hawaii-2RG (H2RG) HgCdTe focal plane array from Teledyne with a cutoff wavelength of 2.5 $\mu$m. This new detector eliminates many of the issues seen with the original H2 detector. The H2RG has been shown in instruments such as MOSFIRE (McLean et al., 2012) at Keck and the GPI IFS (Larkin et al., 2014) at Gemini

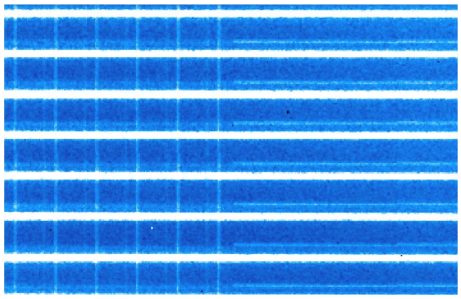

Figure 3.3: A portion of a frame showing the crosstalk between readout channels in the original OSIRIS H2 detector. The bright horizontal lines are spectra from different lenslets and the fainter vertical and horizontal "ghost images" are due to the crosstalk. The direction of the faint crosstalk images depends on the fast readout direction of the channels in that quadrant. This zoomed view of the frame is located at the boundary of the readout quadrants of the detector: on the left quadrant the fast readout direction of the channels is vertical and on the right quadrant the direction is horizontal.

South to have higher QE than the H2, especially at wavelengths below 2 $\mu$m. The H2RG additionally includes reference pixels for each readout channel, removing the need to correct for the offsets from the image data itself. The glow from the shift registers is also shielded in the H2RG and improvements in this detector greatly reduce the crosstalk between channels and eliminate the reset anomaly. Finally, the H2RG used in this upgrade does not suffer from the delamination failure mode.

## 3.2 Summary of Instrument Upgrade

### 3.2.1 H2RG Detector, Electronics, and Software

The new H2RG detector installed in OSIRIS is operated using Teledyne's Sidecar ASIC (Application Specific Integrated Circuit) and the SAM (Sidecar Acquisition Module) card. The ASIC runs at cryogenic temperatures and is mounted to the same structure as the detector. The ASIC and the H2RG are connected by a short flex cable. The SAM is mounted outside the instrument on a newly designed electronics feedthrough plate and in an enclosure designed to shield the SAM from external RF noise sources (see Fig. 3.4). A hermetically potted flex cable passes through the electronics feedthrough plate to connect the SAM to the H2RG/ASIC inside the instrument.

Figure 3.4: Image of the SAM enclosure (bare aluminum) mounted below the original electronics feedthrough box (black anodized aluminum). The spectrograph SAM card mounts to the top plate of the SAM enclosure. The flex cable connecting the SAM to the ASIC is hermetically potted and fed through the top plate of the SAM enclosure. This enclosure is designed to shield the SAM from external, RF noise sources. The front panel of the SAM enclosure provides interfaces for the SAM power, Gigabit ethernet, and USB connectors as well as the motor used to run the detector focus mechanism. The original electronics feedthrough box is kept intact for the OSIRIS imager detector cables. Once the imager detector is upgraded, its new SAM card will also be housed inside the SAM enclosure.

We use the USB 2.0 interface to connect the SAM to a Windows detector control computer. Version 5.0 of Teledyne's HxRG software is run on the control computer and is used to read out the detector. All additional software used to run the H2RG is nearly identical to the MOSFIRE detector software. The SAM, ASIC, and detector are powered by two linear power supplies mounted in the OSIRIS electronics rack (see Fig. 3.5): one for digital power (5.0 V, 1 A) and one for analogue power (5.0 V, 0.2 A). We additionally delivered an alternate digital power supply (5.0 V, 1.5 A) to be used in the future if a Gigabit ethernet interface replaces the USB 2.0.

### 3.2.2 Detector Mount and Focus Mechanism

The H2RG detector was installed in OSIRIS with a completely new mounting structure. A new mounting structure was necessary due to differences between the mechanical interfaces of the H2 and the H2RG. Additionally, the H2RG mounting structure also needed to allow adjustments of the detector position to place it in the focal plane. During the initial commissioning of the instrument, focus was achieved at the detector by adjusting the position and angle of the lenslet array further upstream in the optical path while the detector was kept


Figure 3.5: An image of the electronics rack that contains the new detector control computer and the SAM power supply enclosure. A computer interface panel holds the USB and Gigabit-ethernet mil connectors that connect to the control computer. All of the H2 power and readout electronics have been removed and replaced by the new H2RG components. This electronics rack still contains the original imager detector electronics, which will be replaced in the future as a part of the imager upgrade project.

at a fixed position. When upgrading to the H2RG detector, however, we wanted to avoid adjusting any upstream optics, so this required a new method of focusing the instrument after the new detector was installed.

We therefore mounted the H2RG detector on a focus mechanism that moves the detector along the optical path while the instrument is at cryogenic temperatures. The inclusion of a focus mechanism allows the tip/tilt of the detector relative to the focal plane and which side of the focal plane the detector is on to be determined in a single cool down. This stage greatly reduced the time that the instrument was off of the telescope for the detector upgrade.

Initial designs of the focus mechanism were based on the flexure focus mechanisms used

in the MOSFIRE (McLean et al., 2012) instrument on Keck and the GPI IFS (Larkin et al., 2014) instrument on Gemini South. Although these designs achieved the required precision and repeatability, they only offered half the required range of motion given the uncertainty in the position of best focus for the detector ($\sim$ 1 mm). We therefore changed to a focus mechanism design based on a vacuum, cryogenic linear stage from Physik Instrumente (PI; LS-110). The smallest version of this stage gives a range of motion of 25 mm, well above our requirement, while still fitting in the necessary envelope inside the instrument.

We first tested the LS-110 linear stage at room temperature to confirm its specifications. The stage position was measured by mounting a tooling ball to the stage and using a coordinate measuring machine (CMM) to track the position of the ball. The stage was tested in both unloaded (using only the tooling ball) and loaded configurations (by mounting an additional steel bracket; see Fig. 3.6). We then tested the linear stage inside a vacuum/cryogenic test dewar. After having intermittent issues with moving the stage during these cryogenic tests, we modified the stage by replacing the motor with a high-torque stepper motor from Anaheim Automation (23Y) with its lubrication removed for cryogenic operation. We used an API Controls (now Pac Sci) DM-224i motor controller to run this motor both in the lab and at the telescope. We also removed the cover on the linear stage to expose the lead screw. We further tested this modified stage in the lab under vacuum/cryogenic conditions and found that it ran reliably.

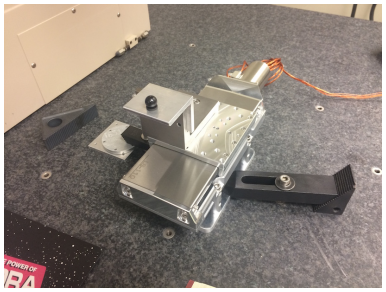

Figure 3.6: Image of the PI LS-110 linear stage in the loaded test configuration. The steel bracket is mounted to the stage to add weight similar to the final detector mounting setup. The position of the tooling ball attached to the bracket is measured by the CMM to track the motion of the linear stage in three dimensions.

We designed interfaces for mounting the linear stage to the optical bench and for mounting

the detector to the linear stage, placing the detector in the best known position of the focal plane. Fig. 3.7 shows images of the focus mechanism and the detector/ASIC mounting setup. The connection interface between L- and S-shaped brackets that form the detector mount includes shim points that can be used to adjust the vertical position of the detector (by placing shims on the lower ledge of the L-bracket) as well as the tip/tilt of the detector (by placing shims behind one or more of the three bolts). The interface plates between the linear stage and the optical bench include places for shim adjustments of the horizontal position of the detector, by shifting the linear stage/detector setup as a whole.

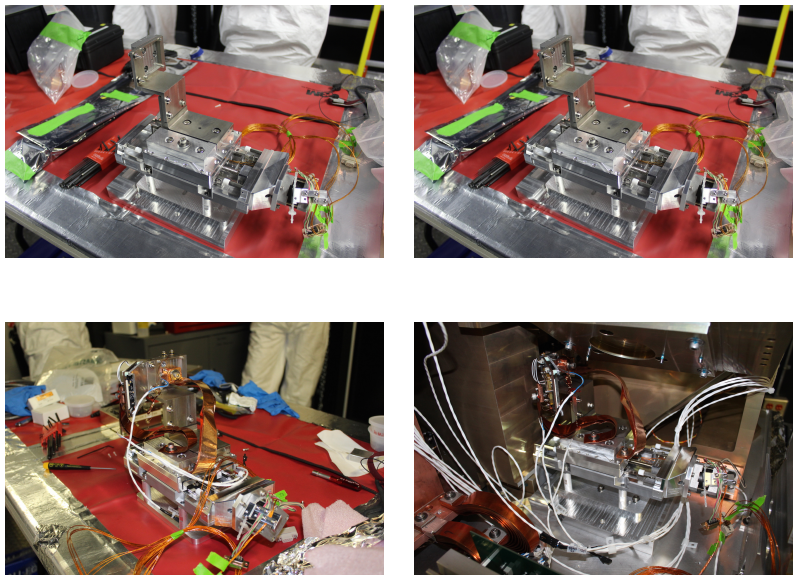

Figure 3.7: Images of the focus mechanism on which the H2RG detector and the ASIC are mounted. The upper left image shows the focus mechanism itself, prior to the detector and ASIC being installed. The upper right and lower left images show the focus mechanism with the H2RG, ASIC, and cold straps attached. The lower right image shows the whole detector and focus mechanism assembly installed inside the OSIRIS dewar. Including a focus mechanism in the upgrade of the OSIRIS spectrograph detector allowed the detector's tip/tilt and direction away from focus to be determined in a single cool down, greatly reducing the time that OSIRIS was off of the telescope.

We found after the initial cool down that there was stray light reaching the detector, likely from light coming around the sides of the detector and reflecting back off of the interior of the TMA enclosure. During the second servicing of OSIRIS, we added a baffling structure that mounts to the TMA enclosure to reduce this stray light. We were able to quickly prototype a baffling structure using the Ultimaker 2 3D printer and a 3D-printed full scale model of the

interior of OSIRIS around the detector position. The baffle was machined out of aluminum and then painted with Aeroglaze to make the material dark at infrared wavelengths. We also added aluminum tape to further improve the baffling of the detector, while still maintaining a range of motion of ∼2 mm for finding the position of optimal focus during the final cool down. Fig. 3.8 shows the baffling setup of the new detector.

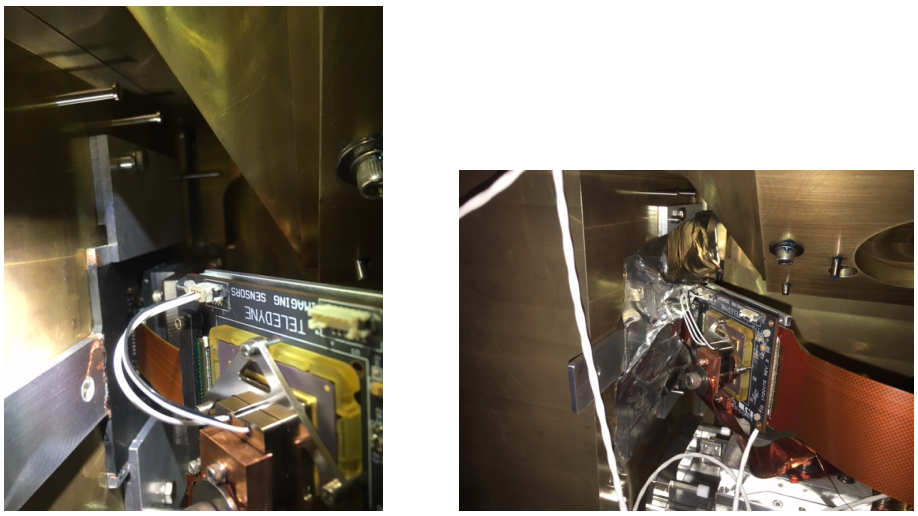


Figure 3.8: Images of the H2RG detector installed in OSIRIS with the baffling that was added during the second servicing of the instrument. The left image shows the baffling structure. The baffle is secured by two clamping pieces connected to the TMA enclosure to the top and bottom of the detector. The baffle is painted with Aeroglaze to make it dark at infrared wavelengths. The right image shows the aluminum tape that completed the baffling of the H2RG detector. The tape was placed such that the linear stage focus mechanism could still move the detector to find the position of best focus.

### 3.2.3 Installation Procedure

OSIRIS was warmed up over the final weeks of December 2015. We opened the instrument in January 2016 for the installation of the new detector. During this initial servicing, the old detector and its electronics were removed from the instrument dewar and the old detector readout electronics and power supply were removed from the external electronics rack. The focus mechanism and mounting structure were then assembled and H2RG detector and ASIC were mounted. This whole setup was then installed in the instrument and the detector was placed at the best-known focus position. The SAM was also mounted to the new electronics interface plate and inside the SAM enclosure. The new detector control computer and the

new power supply for the SAM were installed in the electronics rack.

During the initial cool down, we then moved the detector using the focus mechanism and measured the tip/tilt of the detector and its horizontal/vertical offsets (see Section 3.3.1.2). OSIRIS was then warmed up again and opened in February 2016 to make shim adjustments to the position of the detector and focus mechanism. OSIRIS was then cooled down a final time. Finally, the focus mechanism was used to place the detector at the optimal focus position. The linear stage was then disconnected and is not planned to be used again.

### 3.2.4 Data Reduction Pipeline Updates

OSIRIS was originally delivered with a data reduction pipeline that performs standard data reduction as well as the important step of converting the raw, two-dimensional data into the three-dimensional data cube. This pipeline also was upgraded to work with the new H2RG detector. Data reduction modules that correct for the old H2 detector artifacts, including "Remove Crosstalk," and "Glitch Identification," that are run on data from the new detector no longer perform any corrections to the data. In addition, corrections to offsets between the H2 detector readout channels are no longer applied to H2RG data in the "Adjust Channels," "Subtract Dark," and "Combine Frames" modules. The code that constructs the calibration frames used to extract a spectrum for each lenslet from the raw two-dimensional data was also updated to account for the new positions of the spectra on the detector. A new wavelength solution was also constructed for each lenslet.

## 3.3 Results

### 3.3.1 Off-Sky Results

#### 3.3.1.1 Linear Stage Warm Tests

We measured the position of a tooling ball mounted to the PI LS-110 linear stage using a CMM. The linear stage was positioned on the CMM such that the y-axis of the CMM was

aligned with the horizontal motion of the stage. The x- and z-position of the tooling ball should therefore by constant as the stage moves. We tracked the linear stage position as we moved the stage in one direction across an ∼8 mm portion of its range of motion.

Fig. 3.9 shows the results of these tests in both the unloaded and loaded configurations. The measured values of the x and z position of the stage are plotted in Fig. 3.9 relative to the average value of these measurements. Deviations from the expected linear motion of the stage in the y direction are shown by subtracting the linear best fit to the measured y position of the tooling ball and the nominal stage position. We find that the measured position of the linear stage shows deviations from the expected position at the ±0.050 mm level when the stage is both loaded and unloaded. These deviations cannot be fully explained by the CMM measurement errors.

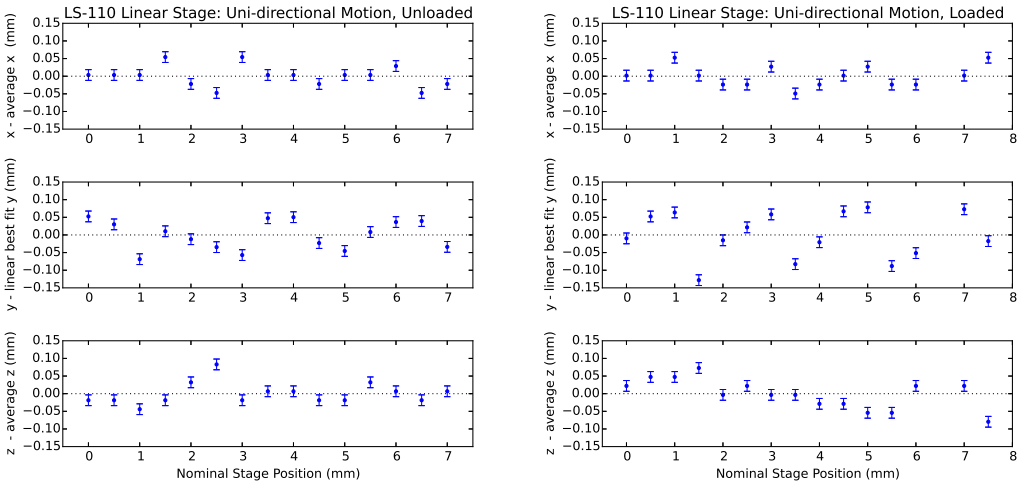


Figure 3.9: The results of warm tests of the PI LS-110 linear stage position, as measured by the CMM, as a function of the nominal position of the stage. The measured x- and z-positions, which should be constant as the linear stage moves, are shown relative to the average value of the measurements. The measured y-positions are plotted by subtracting a linear fit to the data from the measurements. The stage position shows deviations from the expected position at the ±0.050 mm level, which cannot be explained by CMM measurement errors alone.

#### 3.3.1.2 Focus Measurements and Optimization

The focus mechanism on which the detector is mounted allowed us to move the detector along the optical axis to determine the tip/tilt of the detector relative to the focal plane (during the first cool down) and to move the detector to the position of best focus (during the final cool down). The results of both the tip/tilt measurement and the final positioning of the detector are discussed here.

To determine the focus position of the detector, we took images with the Hbb (1.473 - 1.803 $\mu$m) filter and with only the middle column of lenslets illuminated. This setup yields frames with a series of well-separated emission lines across the detector. We then measured the full-width-at-half-maximum (FWHM) by fitting a two-dimensional Gaussian to $\sim$2000 emission lines that were isolated and not saturated in the images. The emission-line data were taken at a range of linear stage positions, such that an X- and Y-FWHM was measured for every emission line at every linear stage position. The linear stage position at which each emission line has a minimum X- and Y-FWHM was then found by fitting a Gaussian to each emission line's X- and Y-FWHM versus linear stage position. This procedure allowed the focal plane to be mapped across the majority of the detector.

During the first cool down, we found that the initial position of the detector had no average tip/tilt across the field. Instead, the data show that the focal plane in OSIRIS is curved, with the position of minimum X-FWHM and Y-FWHM varying across the detector by $\sim$0.3 mm and $\sim$0.5 mm respectively. Fig. 3.10 shows the position of minimum FWHM in the X- and Y-directions, illustrating the curved focal plane. After the second cool down, we repeated the FWHM measurements to find the optimal final position for the detector. We chose a position that minimized the FWHM in the Y (or spatial) direction as opposed to the X (or dispersion) direction. The smaller FWHM in the spatial direction makes sure the spectra are well-separated on the detector, thereby optimizing the spectral extraction process. Fig. 3.11 shows the FWHM of emission lines in X- and Y-directions for the final detector position. In the final position, all emission lines have FWHM's under $\sim$2 pixels, despite the curve of the focal plane. Images taken with the new detector are now in better

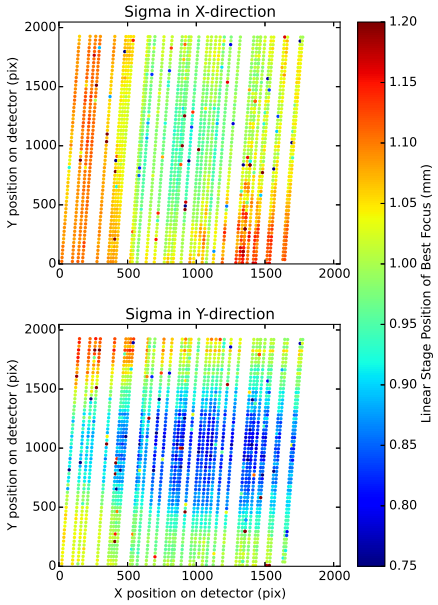


Figure 3.10: A map of the linear stage position at which the FWHM of each emission line is minimized, showing the shape of the focal plane in OSIRIS. These data were used to determine the tip/tilt of the detector during the initial cool down. The top panel plots the position at which the X-direction FWHM is minimized and the bottom panel plots the position at which the Y-direction FWHM is minimized. We conclude that the detector has no average tip/tilt across the array. Instead, differences in the focal plane position at the detector are dominated by the curve of the focal plane. We also find that there are differences in X- and Y-FWHM for a given emission line.

focus than those taken with the original detector, thanks to the ability to finely adjust the H2RG's position with the new focus mechanism.

#### 3.3.1.3 Detector Characterization

Once the H2RG detector was installed in OSIRIS, we performed measurements of the total noise seen in dark frames using various readout modes. These measurements were between frames with 900 second integration times, which is a typical length of science exposures for OSIRIS. We found that the total noise in dark frames with the new OSIRIS H2RG is 7-8 electrons using the Multiple Correlated Double Sampling readout mode with 16 - 128 reads per group. This is comparable to the noise seen in MOSFIRE H2RG dark frames taken with the same setup and is better than the typical $\sim$9 electrons in old OSIRIS H2 frames with

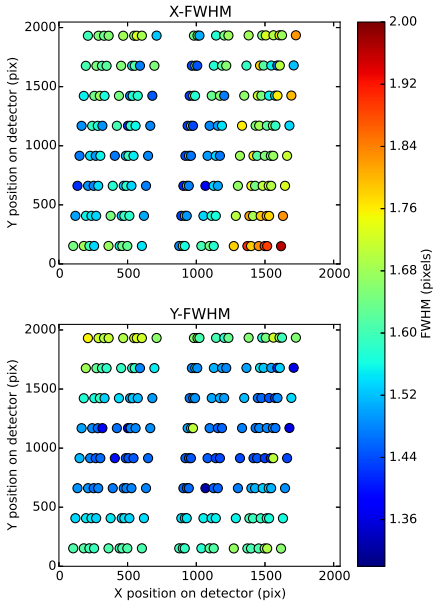


Figure 3.11: The spatially-averaged X- and Y-FWHM of emission lines with the detector at its final position of best focus. The FWHM of each emission line were determined by individual two-dimensional Gaussian fits to the raw image. Sets of 8 emission lines were then averaged to clearly visualize the FWHM changes across the detector. At the final detector position, the emission lines have FWHMs of less than ∼2 pixels across the detector. We chose a final detector position at which the Y (or spatial) direction FWHMs are minimized, to optimize the spectral extraction process.

900 second integration times.

### 3.3.2 On-sky Results

#### 3.3.2.1 Throughput Improvement

One of the main improvements of the new H2RG detector is the increased quantum efficiency compared to the H2, especially at shorter wavelengths. We characterized the resulting throughput improvements on the sky by observing telluric standard stars that had also been observed with the previous detector (after the new grating that was installed in 2012 (Mieda et al., 2014)). These standard stars were observed in the same filter/plate scale setup on both the old and new detectors using only tip/tilt correction from the Keck 1 AO system.

The throughput comparison between the old and new detector was performed on sky-

subtracted raw frames with cosmic rays removed. Only frames in which the star was fully in the field of view were used. The data numbers per second from each star was measured by summing over a large aperture (∼1500 by 1500 pixels) on each raw image taken with the two detectors. This was then converted to electrons per second using the gain of each detector. Comparisons were made in 4 different instrumental modes that used J, H, and K bands and two different plate scales.

The throughput of OSIRIS is improved across all measured wavelengths with the new H2RG detector. The throughput increases by a factor of 2.1 for narrowband J-band filters and by a factor of 1.6 in narrowband H and K-band filters. These measurements match the expectations of a larger increase in throughput at shorter wavelengths. Table 3.1 reports the average ratio of measured electrons per second as measured by the new detector and old detector in each observing setup. Note that part of the large throughput improvements seen in OSIRIS is due to the loss in QE of the H2 detector at temperatures below 77K (Finger et al., 2004). Relative improvements in warmer instruments would be less dramatic.

Table 3.1: Throughput improvements from the installation of the new detector in a variety of OSIRIS observing modes. The throughput improvements were determined by comparing the measured, raw frame flux of the same star observed using the old H2 detector and the new H2RG detector. The measured raw flux in electrons/second is higher with the new detector in all measured modes.

| Filter Name | Central Wavelength ($\mu$m) | Plate Scale (milliarcseconds) | New/Old Detector Raw Flux |
|---|---|---|---|
| Jn1 | 1.20 | 100 | 2.04 |
| Jn2 | 1.26 | 35 | 2.09 |
| Hn2 | 1.57 | 100 | 1.68 |
| Kn3 | 2.17 | 35 | 1.63 |

#### 3.3.2.2 Initial Science Results

As a part of commissioning the new OSIRIS detector, we observed a nearby low-ionization nuclear emission line region, or LINER, galaxy. LINER galaxies are defined by their spectral properties at optical wavelengths. The optical spectra of these galaxies show strong low-

ionization emission lines but lack the high-ionization emission lines that are characteristic of active galaxies that host accreting supermassive black holes. The physical nature of LINERs is still uncertain because their optical emission can be be explained by a number of processes, including the presence of a weakly accreting supermassive black hole or shock waves in molecular or ionized gas.

OSIRIS behind AO can be used to map the morphology and kinematics of gas at the centers of nearby LINER galaxies at high spatial resolutions and thereby constrain the physical processes producing the observed near-infrared emission. At near-infrared wavelengths, we can trace emission from singly-ionized iron ([FeII]), molecular hydrogen ($H_2$), and recombining hydrogen (Pa-$\beta$ and Br-$\gamma$ transitions) in the J and K bands. These measurements are greatly aided by the improved throughput of the new H2RG. Fig. 3.12 shows the emission from molecular hydrogen gas in the LINER galaxy NGC 3627 as observed with the upgraded detector in the Kbb filter (1.965 - 2.381 $\mu$m). The $H_2$ gas in this LINER has a complex structure extending across the central $\sim$100 parsecs of the galaxy. The line emission has a varying morphology as a function of velocity that indicates a rotation of the gas about the center of the galaxy. Comparing this emission with other $H_2$ lines and recombining hydrogen lines will help to constrain the mechanisms exciting the molecular gas emission.

## 3.4 Summary

We have upgraded the spectrograph detector in the integral field spectrograph OSIRIS to a H2RG detector. The new detector has improved the sensitivity of OSIRIS by a factor $\sim$2 at shorter near-infrared wavelengths (J band) and by $\sim$1.6 at longer wavelengths (H and K bands), thanks to its increased quantum efficiency compared to the original H2 detector. Combined with the upgrade of the grating in 2012, the throughput of OSIRIS has now increased by factors of between 2.5 and 3.5 across all wavelengths.

The new H2RG detector also eliminates a number of detector artifacts that affected the efficiency and performance of OSIRIS. In addition to the new detector and readout electronics, this upgrade also included a focus mechanism on which the detector was mounted.

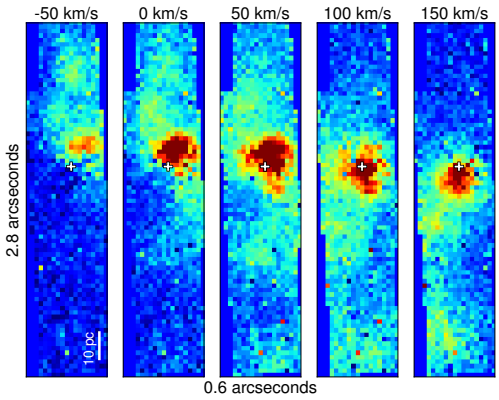


Figure 3.12: Map of molecular hydrogen emission as a function of velocity from the nearby LINER NGC 3627 as observed with the new H2RG in OSIRIS. The $H_2$ emission line shown here falls in the Kbb OSIRIS filter and has a rest wavelength of 2.1218 $\mu$m. The white cross indicates the central position of the galaxy as measured by the continuum emission. The white line indicates a distance of 10 parsecs (33 light years) at the distance of this galaxy. The velocities indicated in the plot are relative to the systemic velocity of the galaxy. The $H_2$ morphology is complex and variable across all velocities and shows rotation in these central regions of the galaxy.

The focus mechanism allowed the new detector to be put in a position of optimal focus, such that images are now in better focus than ever before. Finally, the new H2RG is not in danger of catastrophically failing via delamination.

Bibliography

Finger, G., Dorn, R. J., Meyer, M., et al. 2004, in Proc. SPIE, Vol. 5499, Optical and Infrared Detectors for Astronomy, ed. J. D. Garnett & J. W. Beletic, 47–58

Fitzgerald, M. P., Aliado, T., Arriaga, P., et al. 2016, in Proc. SPIE, Vol. 9908, Ground-based and Airborne Instrumentation for Astronomy VI, Paper 92

Krabbe, A., Gasaway, T., Song, I., et al. 2004, in Proc. SPIE, Vol. 5492, Ground-based Instrumentation for Astronomy, ed. A. F. M. Moorwood & M. Iye, 1403–1410

Larkin, J., Barczys, M., Krabbe, A., et al. 2006, in Proc. SPIE, Vol. 6269, Society of Photo-Optical Instrumentation Engineers (SPIE) Conference Series, 62691A

Larkin, J. E., Chilcote, J. K., Aliado, T., et al. 2014, in Proc. SPIE, Vol. 9147, Ground-based and Airborne Instrumentation for Astronomy V, 91471K

McLean, I. S., Steidel, C. C., Epps, H. W., et al. 2012, in Proc. SPIE, Vol. 8446, Ground-based and Airborne Instrumentation for Astronomy IV, 84460J

Mieda, E., Wright, S. A., Larkin, J. E., et al. 2014, PASP, 126, 250

Wizinowich, P. L., Acton, D. S., Lai, O., et al. 2000, in Proc. SPIE, Vol. 4007, Adaptive Optical Systems Technology, ed. P. L. Wizinowich, 2–13

# CHAPTER 4

# Widespread Shocks in the Nucleus of NGC 404 Revealed by Near Infrared Integral Field Spectroscopy

## 4.1 Introduction

LINER (low ionization nuclear emission line region) galaxies, first defined by Heckman (1980), are the least luminous but most common class of active galactic nucleus (AGN), with $\sim$1/3 of all galaxies within 40 Mpc hosting LINER emission at their centers (Ho et al., 1997b). LINERs are identified by their optical emission line properties and show high values of line ratios with low ionization species (e.g., [NII]/H$\alpha$) similar to Seyferts, but low values of line ratios from high ionization species ([OIII]/H$\beta$). These optical line ratios can be explained by a number of excitation mechanisms, with two dominant models being photoionization from a weakly accreting supermassive black hole (SMBH) or fast shock excitation (Riffel et al., 2013). Although the physical mechanisms exciting optical LINER emission likely vary across the class, studying LINERs in detail can reveal under what circumstances different excitation mechanisms dominate and help us determine the importance of BH accretion, feedback, and other physical processes such as star formation in the nuclei of relatively normal galaxies. The closest LINERs are ideal targets for detailed studies of individual nuclei because diffraction-limited angular resolutions of $\sim$0.1 arcsec can probe physical scales of 5 pc, allowing the excitation mechanisms in a single nucleus to be disentangled at very high spatial resolution.

NGC 404 hosts one of the closest LINERs (Ho et al., 1997a) at a distance of only 3.1 Mpc away and is therefore an ideal source for studying the important physical processes at the centers of these galaxies. There is tentative evidence that NGC 404 hosts an accreting

central black hole (BH) from detections at X-ray (Binder et al., 2011) and radio (e.g., Nyland et al., 2012) wavelengths and variability observed at near-infrared (NIR), optical, and UV wavelengths (Maoz et al., 2005; Nguyen et al., 2017). NIR studies of the molecular gas and stellar dynamics in the nucleus of NGC 404 have placed an upper limit on the mass of this putative central black hole of 1.5 x $10^5$ $M_\odot$, in the mass range of an intermediate mass black hole (Seth et al., 2010; Nguyen et al., 2017). Despite the evidence for the presence of an accreting central BH, it has been unclear whether photoionization from the BH accretion disk or another mechanism such as shock excitation is the dominant physical process in the NGC 404 nucleus driving its LINER emission.

NGC 404, and LINERs in general, also stand out from other emission line galaxies in their NIR spectral properties. NIR spectra of these nuclei in the J (1.1-1.4 $\mu$m) and K bands (2.0-2.4 $\mu$m) often show features from [FeII], $H_2$, and the Pa$\beta$ and Br$\gamma$ hydrogen recombination lines. At seeing-limited spatial resolutions of $\sim$100 pc, LINERs exhibit high ratios of [FeII]/Pa$\beta$ and $H_2$/Br$\gamma$ compared to Seyfert and starburst nuclei (Larkin et al., 1998; Rodríguez-Ardila et al., 2004, 2005; Riffel et al., 2013). NGC 404 in particular shows some of the highest values of these line ratios, with the [FeII]/Pa$\beta$ line ratio of 2.7 being similar to shocked regions of supernova remnants (Larkin et al., 1998). The [FeII]/Pa$\beta$ ratio is sensitive to shock excitation because iron is typically locked in dust grains, and high values of [FeII]/Pa$\beta$ ($> 2.0$) require shocks that can process the dust and convert a sufficient amount of iron to a gaseous state (Blietz et al., 1994; Larkin et al., 1998). With the advent of adaptive optics (AO), the NIR diagnostic spectral features can be probed in LINERs at spatial resolutions 100 times smaller than seeing-limited observations using NIR integral field spectroscopy (IFS). These data consistent of thousands of spectra taken simultaneous and can resolve differences in the [FeII] and $H_2$ emission and kinematics on spatial scales of only 1 pc at the nearby distance of NGC 404. LINERs in general have been included in past NIR IFS studies of nearby galactic nuclei (e.g., Mazzalay et al., 2013; Müller-Sánchez et al., 2013), but these studies have focused on characterizing the molecular gas emission and the stellar absorption features in the K band and have not probed the shock-sensitive [FeII] emission line.

We present results on NIR IFS observations of the nucleus of NGC 404 using the OSIRIS instrument at the W. M. Keck Observatory. These observations are a part of a larger survey of nearby LINER galaxies with the goal of constraining the excitation mechanisms of NIR emission lines at the highest possible spatial scales. We present data at both the J and K bands that measure the emission morphology, kinematics, and physical conditions of the ionized iron and molecular hydrogen gas at spatial scales of 1 pc. This work is the first high spatial resolution study of the shock-sensitive [FeII] line in NGC 404. Sec. 4.2 describes the OSIRIS observations and data reduction procedures. Sec. 4.3 describes the data analysis and the results. Sec. 4.4 discusses the implications of these results on the physical mechanisms exciting the NIR emission in NGC 404.

## 4.2 Observations and Data Reduction

NGC 404 was observed on 2 September 2014 and 8 October 2015 using the OSIRIS instrument (Larkin et al., 2006) on the Keck I telescope (Table 4.1). OSIRIS is an integral field spectrograph coupled to the Keck Adaptive Optics System (Wizinowich et al., 2006; van Dam et al., 2006). This instrument uses an array of small lenses to sample the AO image and produces up to ∼3000 spectra simultaneously across a rectangular, contiguous field of view. The data were taken with the 50 mas (September 2014) and 35 mas (October 2015) plate scale modes using two different filters: Jn2 ($\lambda$ = 1.228 - 1.289 $\mu$m) and Kbb ($\lambda$ = 1.965 - 2.381 $\mu$m). The Jn2 filter covers the [FeII] ($\lambda_0$ = 1.2567 $\mu$m) and Pa$\beta$ ($\lambda_0$ = 1.28216 $\mu$m) emission lines for low redshift galaxies (z < 0.004). The Kbb filter covers a series of $H_2$ emission lines, including the 1-0 S(1) transition ($\lambda_0$ = 2.1218 $\mu$m), as well as the Br$\gamma$ line ($\lambda_0$ = 2.16612 $\mu$m) and stellar absorption features, particularly the CO bandheads ($\lambda_0$ = 2.29 $\mu$m).

The on-source observations of NGC 404 total 0.75 hours in the 50 mas mode on 2 September 2014 and 1.25 hours in the 35 mas mode on 8 October 2015 in each filter, with individual frames having an integration time of 900 sec. The airmass of NGC 404 during the observations ranged from 1.0 - 1.2. The data were taken using the Keck laser guide star AO system

Table 4.1. Summary of OSIRIS Observations of NGC 404

| Date | Filter | Plate Scale (mas) | # of Frames | Integration Time (hours) | FOV (arcsec) Single Frame | Mosaic |
|---|---|---|---|---|---|---|
| 2 September 2014 | Jn2 | 50 | 3 | 0.75 | 2.1 x 3.2 | 2.1 x 3.2 |
| 2 September 2014 | Kbb | 50 | 3 | 0.75 | 0.8 x 3.2 | 0.8 x 3.2 |
| 8 October 2015 | Jn2 | 35 | 5 | 1.25 | 1.47 x 2.24 | 1.65 x 3.29 |
| 8 October 2015 | Kbb | 35 | 5 | 1.25 | 0.56 x 2.24 | 0.70 x 3.33 |

(Wizinowich et al., 2006; van Dam et al., 2006), with the nucleus of the galaxy serving as the tip/tilt reference source. The galaxy was dithered within the field of view such that previous or subsequent on-source frames could be used for sky subtraction, with typical dithers being 1 arcsec. In addition to the on-source frames, one 900-sec pure sky frame offset $\sim$4 arcseconds from the source was taken in each filter and in each plate scale mode.

To correct for atmospheric absorption features, we also observed two telluric standard stars at an airmass similar to the science observations and with the same plate scale/filter setups: an A star (A0 star HD 13869 in 2014 and A1 star HD 217186 in 2015) and a G2 star (HD 12846 in 2014 and HD 217577 in 2015). Both the A and G star spectra were divided by a blackbody spectrum to remove the continuum shape of the stellar photosphere. The spectrum of the A star is used as the telluric spectrum across the majority of both observation bands, with the exception of the regions around the strong hydrogen absorption features of Br$\gamma$ and Pa$\beta$. For these wavelength regions (1.270 - 1.289 $\mu$m in Jn2 and in 2.156 - 2.177 $\mu$m Kbb) the G2 spectrum was used, with the stellar absorption features removed by dividing the G2 spectrum by the solar spectrum. The solar spectrum used to correct the G2 star was created by ESO using National Solar Observatory/Kitt Peak Fourier Transform Spectrograph data produced by NSF/NOAO. Before dividing the OSIRIS G2 spectrum by the solar spectrum, the solar spectrum was shifted to match the radial velocity (RV) of the star and scaled so the width of the hydrogen absorption line matched the G2 spectrum.

All the data were reduced using Version 3.2 of the OSIRIS Data Reduction Pipeline (DRP; Krabbe et al., 2004). Each individual science frame was sky subtracted by both the pure sky and its dithered pair frame (if applicable). The scaled sky DRP routine was also

performed on each frame. This routine scales the intensity of different families of OH lines in intensity to match the sky frame and the science frame and is based on the algorithm developed by R. Davies (Davies, 2007). All sky subtracted frames were visually compared and the frame with the lowest OH line residuals was chosen as the final sky subtracted frame. These sky-subtracted frames were then mosaicked to create the final data cube for each filter. These cubes have a wavelength sampling of 0.00015 $\mu$m in the Jn2 band and 0.00025 $\mu$m in the Kbb band, corresponding to a velocity resolution of $\sim$35 km s$^{-1}$ in both bands. Finally, the spectrum of each spatial pixel, or spaxel, in the mosaicked cube was divided by the telluric spectrum created from the A and G star spectra. All subsequent data analysis was performed on these telluric-corrected data cubes. Fig. 4.1 shows the final Jn2 and Kbb 35 mas data cubes of NGC 404 averaged across all wavelengths in the filter and Fig. 4.2 shows an example spectrum extracted from each of these data cubes. Since the 35 mas data from 8 October 2015 are deeper and have a finer spatial sampling, analyses derived from these data are presented in subsequent sections of this work unless otherwise noted.

## 4.3 Data Analysis and Results

### 4.3.1 Line Emission Morphology

#### 4.3.1.1 Line S/N Estimate

S/N ratios for the [FeII] and 1-0 S(1) $H_2$ emission lines are computed for every spaxel in the mosaicked data cubes for use in subsequent analysis steps. The signal in this calculation is taken as a sum of the continuum-subtracted counts in each wavelength channel within $\pm$150 km s$^{-1}$ of the vacuum wavelength of the emission line shifted to the systemic velocity of the galaxy ($-$48 km s$^{-1}$; from NED[1]). The continuum for this calculation is taken as the average of counts in the wavelength channels from -450 to -300 km s$^{-1}$ and from +300 to +450 km s$^{-1}$ relative to the systemic velocity. The noise is estimated by taking the standard

[1]The NASA/IPAC Extragalactic Database (NED) is operated by the Jet Propulsion Laboratory, California Institute of Technology, under contract with the National Aeronautics and Space Administration.

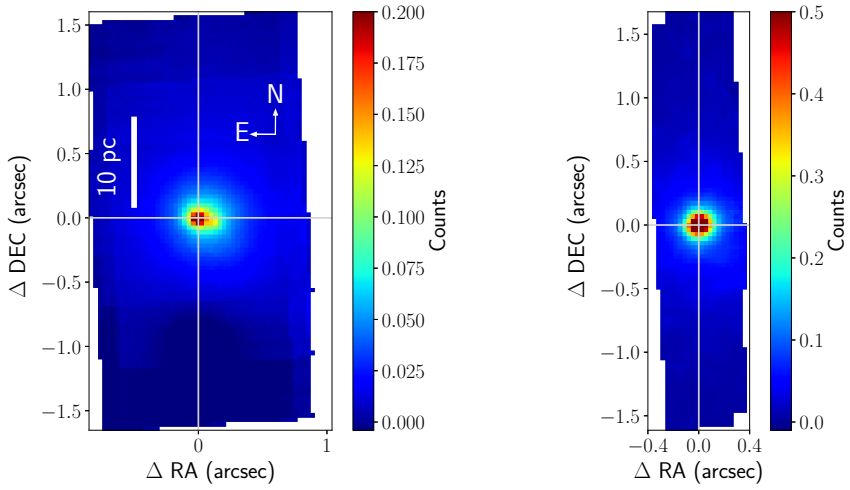


Figure 4.1: The NGC 404 reduced and telluric-corrected data cubes from the Jn2 band (left) and the Kbb band (right) collapsed along the wavelength axis. The displayed maps are made by taking the average value of the spectrum in each spatial pixel (spaxel) across the entire wavelength range in each band and are thus dominated by that band's continuum emission. The origins of these and all subsequent plots are set to the central peak of the Jn2/Kbb continuum emission as determined by a two dimensional Gaussian fit to the emission in each collapsed data cube. We find that the nuclear J and K band continuum emission is compact and point like.

deviation of 10 wavelength channels on either side of the line, starting at $\pm 300$ km s$^{-1}$ and moving outward. Every fifth wavelength channel is used for the noise estimate to avoid the correlated noise present in adjacent wavelength channels. Fig. 4.3 shows an example of this S/N calculation for a single [FeII] emission line with the wavelength channels for the signal, noise, and continuum estimates highlighted.

Signal and noise maps are created for the [FeII] and 1-0 S(1) $H_2$ emission lines by computing the signal and noise for each emission line in each spaxel. Due to the noise present in the signal and noise estimates, the signal and noise maps are then smoothed using a 2D gaussian with a sigma of 3.5 pixels in both the x and y directions. This smoothing is implemented using the `gaussian_filter` function in the `ndimage` module of the SciPy library, a scientific computing library for the Python programming language. The ratio of these smoothed maps is then used as the spatial map of the S/N ratios for each of the [FeII] and 1-0 S(1) $H_2$ emission lines in subsequent analysis steps.

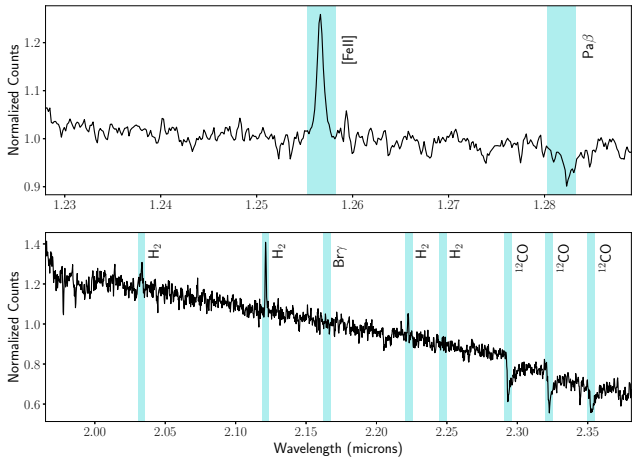


Figure 4.2: Spectrum of the nucleus of NGC 404 in the Jn2 (top) and Kbb (bottom) bands. The vertical bars indicate the wavelengths of the various spectral features at the systemic velocity of NGC 404 (-48 km s$^{-1}$) and span a ±300 km s$^{-1}$ velocity range around the central wavelength. Each spectrum was extracted from the Jn2/Kbb data cubes using an aperture centered on the continuum peak with a radius of 5 spaxels or 2.6 pc. The spectra show emission from the [FeII] line in the Jn2 band and multiple $H_2$ lines in the Kbb band. Stellar absorption features from Pa$\beta$ and the $^{12}$CO bandheads are also visible. Although not detected in this central aperture, Pa$\beta$ and Br$\gamma$ are also seen in emission to the north of the NGC 404 nucleus (see Fig. 4.4).

#### 4.3.1.2 Velocity-Integrated Emission Line Maps

Spatial maps of the continuum-subtracted emission line strengths of the [FeII], Pa$\beta$, 1-0 S(1) $H_2$, and Br$\gamma$ are constructed to compare the morphology of the different lines. The emission line strength in each individual spaxel is found by summing the continuum-subtracted counts in 7 wavelength channels (a velocity range of approximately ±100 km s$^{-1}$) centered on the emission line wavelength. This velocity range was chosen to capture the majority of the line emission while still excluding channels without emission that would only add noise to the line flux measurement. For the [FeII] and 1-0 S(1) $H_2$ emission lines, velocity information is used to determine the emission line wavelength in spectra with an emission line S/N greater than 10 (see Sec. 4.3.1.1). For spaxels with line S/N less than 10, the emission line wavelength is set as the vacuum wavelength of the line shifted to the systemic velocity of the galaxy (−48

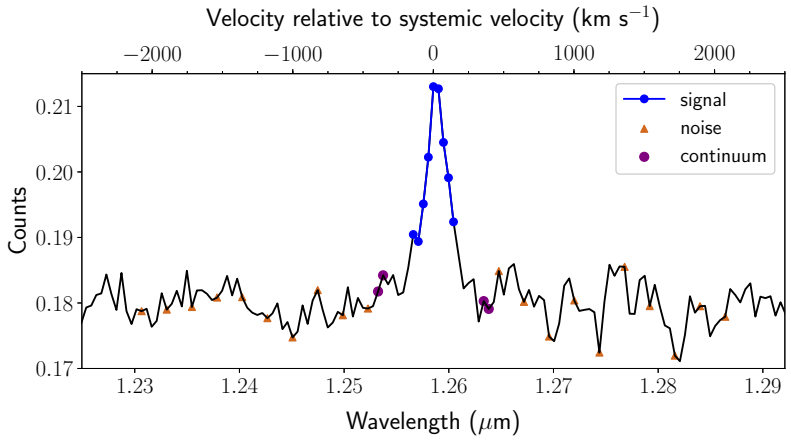


Figure 4.3: Line S/N calculation example for a single [FeII] emission line, with signal, noise, and continuum wavelength channels highlighted. The Jn2 spectrum shown is extracted from an aperture aligned with the continuum center and with a radius of 2 pixels = 0.07 arcsec. The wavelength of each channel is displayed on the bottom x-axis of the plot and the velocity of each channel relative to vacuum wavelength of [FeII] emission line and with the systemic velocity of the galaxy subtracted is displayed on the top x-axis. The wavelength channels used for the signal ($\pm$150 km s$^{-1}$), noise (every fifth channel from $\pm$300 km s$^{-1}$ outward), and continuum (-450 to -300 km s$^{-1}$ and from +300 to +450 km s$^{-1}$) estimates are highlighted.

km s$^{-1}$; taken from NED[2]). For the Pa$\beta$ and Br$\gamma$ emission lines, the systemic velocity of the galaxy is used to determine the emission line wavelength in every spaxel, since these lines are detected with high significance in only a few spatial locations. The continuum around each line is estimated using the average of counts in the wavelength channels from $-450$ to $-300$ km s$^{-1}$ and from +300 to +450 km s$^{-1}$ relative to the systemic velocity of the galaxy.

The resulting emission line maps for 4 emission lines are shown in Fig. 4.4. We find that the morphologies of the [FeII], $H_2$, and Pa$\beta$/Br$\gamma$ vary at the pc spatial scales probed by these data. The [FeII] emission is diffuse and extended out to $\sim$0.5 arcsec (8 pc) from the nucleus of NGC 404, while the $H_2$ is more spatially compact. The majority of the $H_2$ emission is contained in a central peak coincident with the continuum center of the K band emission, with two weaker peaks of $H_2$ emission seen offset to the southeast of the nucleus. Pa$\beta$ and Br$\gamma$ are seen in absorption at the nucleus and in emission $\sim$0.2 arcsec (3 pc) north of the nucleus of NGC 404.

[2]The NASA/IPAC Extragalactic Database (NED) is operated by the Jet Propulsion Laboratory, California Institute of Technology, under contract with the National Aeronautics and Space Administration.

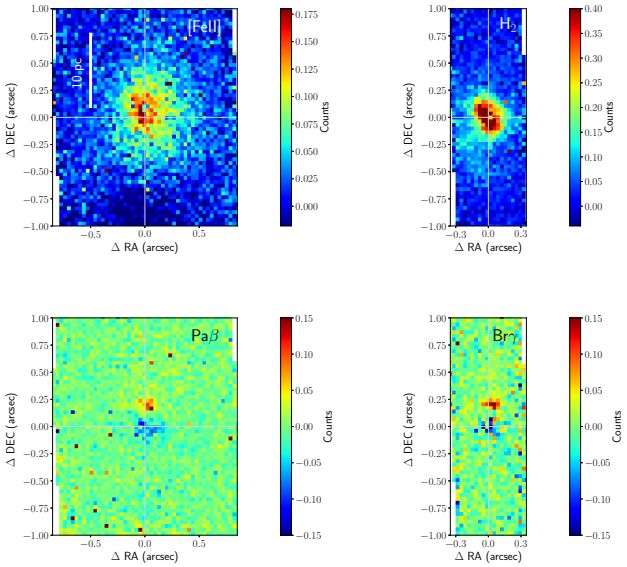


Figure 4.4: Velocity-integrated emission line maps across the central 20 pc of NGC 404 for four emission lines: [FeII] (top left), 1-0 S(1) $H_2$ (top right), Pa$\beta$ (bottom left), and Br$\gamma$ (bottom right). The [FeII] and Pa$\beta$ maps are derived from the Jn2 data and the $H_2$ and Br$\gamma$ maps are derived from the Kbb data. These line maps are the sum of the continuum-subtracted emission in wavelength channels approximately $\pm$100 km s$^{-1}$ around the line relative to the systemic velocity of NGC 404. The displayed maps are subsets of the full field of view of the mosaicked data cubes shown in Fig. 4.1 (1.65 x 3.29 arcsec in the Jn2 band and 0.70 x 3.33 in the Kbb band) and show the regions in which line emission is detected. The [FeII] emission is diffuse and extended out to $\sim$0.5 arcsec (8 pc) from the nucleus of NGC 404. The bulk of the $H_2$ emission is more compact, with additional regions of emission to the bottom left of the nucleus. The Pa$\beta$ and Br$\gamma$ lines are seen in absorption at the nucleus (indicated by the light gray cross hairs) and in emission $\sim$0.2 arcsec north of the nucleus.

#### 4.3.1.3 Velocity-resolved Emission Line Maps

The emission morphology of each line can also be viewed as a function of velocity to reveal morphological structures that only appear at specific velocities. First, continuum-subtracted line cubes for each emission line are created by selecting a subset of wavelength channels around the emission line and then estimating and subtracting a continuum value for every spatial pixel. The continuum value is determined using the same method as for the velocity-integrated line maps, by taking the average of the counts in wavelength channels from $-450$ to $-300$ km s$^{-1}$ and from $+300$ to $+450$ km s$^{-1}$. The wavelength ranges of the line cubes span at least $\pm$300 km s$^{-1}$ around the lines relative to the systemic velocity of the galaxy to fully cover the wings of each emission line. The wavelength channels of each line cube

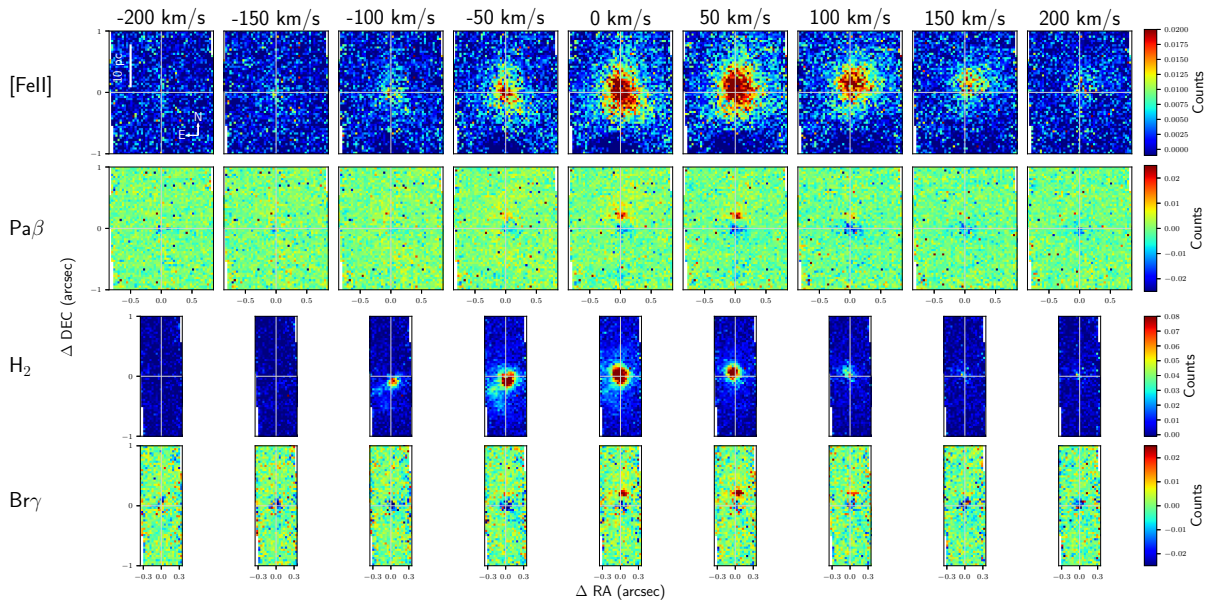


Figure 4.5: Velocity-resolved emission line maps for emission lines: [FeII], Pa$\beta$, 1-0 S(1) $H_2$, and Br$\gamma$. The displayed velocity is relative to the systemic velocity of the galaxy. The cross hairs indicate the continuum center of the galaxy in the Jn2 ([FeII], Pa$\beta$) or Kbb ($H_2$, Br$\gamma$) bands. These maps show that the [FeII] emission is extended and diffuse compared to the compact $H_2$ and Pa$\beta$/Br$\gamma$ emission and spans the largest velocity range of all the emission lines (-150 to +200 km s$^{-1}$). At -50 and 0 km s$^{-1}$, the [FeII] emission is extended to the north and to the southwest of the nucleus and forms an arc-like structure. The central peak of the $H_2$ emission shifts position from the southwest of the continuum center to the northeast with increasing velocity, a signature of rotational motion. Two additional blue-shifted knots of $H_2$ emission to the southeast of the nucleus are visible in the -50 and 0 km s$^{-1}$ maps.

are then resampled to velocities from -250 to 250 km s$^{-1}$ with a spacing of 25 km s$^{-1}$. This resampled spacing is slightly smaller compared to the native wavelength channel spacing of the OSIRIS data cubes ($\sim$35 km s$^{-1}$ in both Jn2 and Kbb bands). The final emission line maps at each velocity are then made by taking the average of the channel at the given velocity and the two channels on either side ($\pm$25 km s$^{-1}$) in the resampled line cubes.

Fig. 4.5 shows the resulting velocity-resolved emission line maps for the [FeII], Pa$\beta$, 1-0 S(1) $H_2$, and Br$\gamma$ emission lines. The [FeII] emission shows a complex velocity structure, with the brightest and most extended emission at 0 and 50 km s$^{-1}$. Low surface brightness [FeII] emission extends out to high velocities from -150 to +200 km s$^{-1}$. At -50 and 0 km s$^{-1}$ the shape of the [FeII] emission forms an arc-like structure extended to the north and southwest of the nucleus. This structure is most apparent at lower surface brightnesses in

the 50 mas data set displayed in Fig. 4.18. The $H_2$ emission is more spatially compact than the [FeII] emission and spans a smaller overall velocity range of $\pm$100 km s$^{-1}$. The emission peaks in the 0 km s$^{-1}$ channel where it aligns with the continuum center of the Kbb emission (indicated by the cross hairs). The $\pm$50 km s$^{-1}$ $H_2$ emission shows offsets from the continuum center to the southwest and northeast respectively, showing that two sides of the central molecular gas emission have different velocities, which is similar to what is expected from a rotating disk with a position angle of about $-45$ km s$^{-1}$ on the plane of the sky. The two knots of $H_2$ emission offset from the continuum center to the southeast are brightest in the -50 km s$^{-1}$ map, revealing their blue-shifted velocity offset from the central region of molecular emission. These blue-shifted $H_2$ structures are not matched in the [FeII], Pa$\beta$, or Br$\gamma$ emission lines. The Pa$\beta$ and Br$\gamma$ maps show similar morphologies to each other across all velocity channels. The knot of emission north of the nucleus seen in these lines spans from -50 to 100 km s$^{-1}$, with the brightest emission found at 0 and 50 km s$^{-1}$. The velocities of the brightest Pa$\beta$/Br$\gamma$ emission match that of the brightest [FeII] emission. Additionally, this bright emission region is spatially located where the [FeII] emission is also very strong. Pa$\beta$ and Br$\gamma$ are also seen in absorption at the center of the NGC 404 nucleus, which can be used to constrain the stellar population in this central region.

### 4.3.2 Kinematics

#### 4.3.2.1 Emission Line Kinematics: [FeII] and $H_2$

The velocity shifts of [FeII] and the 1-0 S(1) $H_2$ emission lines in a given spectrum are estimated using a Gaussian fit to the line profiles. The fits are performed in a wavelength range of $\sim$0.003 $\mu$m around the vacuum wavelength of the emission lines. This wavelength range corresponds to approximately $\pm$350 km s$^{-1}$ in the Jn2 band and $\pm$200 km s$^{-1}$ Kbb band. The model parameters include the central wavelength, the sigma, and the integrated flux of the Gaussian emission line as well as a vertical offset to model the continuum in the region around the line. The central wavelength and the sigma of the best-fit Gaussian are converted into the velocity and the velocity dispersion of the emission line. These fits are

performed on each individual spectrum and on spatially binned spectra in square bins that are 2 spaxels (70 mas) on a side. These binned spectra are created by taking the median of the 4 individual spectra in each bin.

The instrumental dispersion and its variation across the mosaicked field of view is estimated by measuring the widths of OH sky lines in different apertures. The instrumental dispersion is later subtracted in quadrature from the measured velocity dispersion to find the dispersion of the gas due to kinematics in the galactic nucleus. A set of 4 apertures are chosen for each filter to fall in sky regions separated from the continuum emission of the galaxy nucleus. In the Jn2 band, the 4 apertures are offset from the continuum center by $\pm 0.5$ arcsec in the x (east/west) direction and $\pm 0.67$ arcsec in the y (north/south) direction. In the Kbb band, the 4 aperture locations have the same x value as the continuum center and are offset in the y direction by $\pm 1.33$ and $\pm 0.67$ arcsec. The OH line widths in each aperture are estimated by Gaussian fits to 3 emission lines. In the Jn2 band the chosen OH lines are close in wavelength, so their line profiles are fit simultaneously with a model consisting of a sum of 3 Gaussians. The continuum in these spectra is estimated separately by performing a parabolic fit to the majority of the spectrum, with the exact wavelength range adjusted to give a good estimate to the wavelength range of the OH lines on the red side of the bandpass. In the Kbb band, the OH lines are well separated, so the line is fit individually and the continuum is modeled by adding a delta offset to the Gaussian line profile model. The resulting centroid and line width measurements are presented in Fig. 4.6 for each individual OH line and for each aperture spectrum. The median values of the Jn2 and Kbb sigma values for the OH lines are 2.1 and 2.5 $\mu$m respectively. These instrumental line widths are equivalent to velocity dispersions of 50 km $s^{-1}$ in the Jn2 band and 35 km $s^{-1}$ in the Kbb band.

The velocity and velocity dispersion maps for the [FeII] and 1-0 S(1) $H_2$ emission lines are displayed in Fig. 4.7. The velocity is measured for each individual spaxel, while the velocity dispersion is measured from the spatially binned spectra to reduce noise. In the dispersion maps, the instrumental dispersion for each line is subtracted from the measured velocity dispersion to yield the displayed map. For the $\sim$5 bins with measured velocity dispersions less

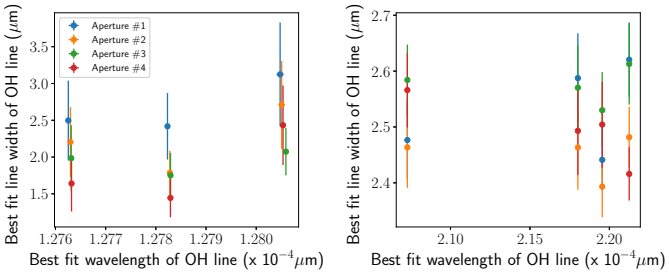


Figure 4.6: Best fit line width and centroid wavelength for OH lines measured in 4 apertures in the dark-subtracted Jn2 and Kbb data cubes. The results of Gaussian fits to three OH lines in each filter are displayed. The measured line width in each aperture is consistent within the fitting errors. The median line width values are 2.1 and 2.5 $\mu$m in the Jn2 and Kbb filters respectively, These instrumental line widths are equivalent to instrumental dispersions of 50 km s$^{-1}$ in the Jn2 band and 35 km s$^{-1}$ in the Kbb band.

than the instrumental dispersion, the dispersion is set to 0 for display purposes. Individual spaxels with a S/N ratio less than 10 in the smoothed S/N maps are masked. Additionally, spaxels whose Gaussian fit did not converge or whose best fit velocity falls outside the wavelength range are also masked. The same mask is applied to both the velocity and the velocity dispersion maps.

The [FeII] and $H_2$ gases show very different velocity structures. The $H_2$ velocity map is consistent with simple rotation centered on the nucleus of NGC 404 with a velocity shift of $\pm$30 km s$^{-1}$ across the central $\sim$15 pc of the galaxy. The two peaks of $H_2$ emission offset to the southeast of the nucleus are found to be blue shifted by $\sim$30 km s$^{-1}$ relative to the systemic velocity of the galaxy. The [FeII] velocity gradient is roughly perpendicular to the gradient of the molecular gas and spans a larger range of velocities, with the northwest region of emission having velocities up to 80 km s$^{-1}$ relative to the systemic velocity of the galaxy. This region with the highest [FeII] velocities also shows higher velocity dispersion with values up to 75 km s$^{-1}$. The $H_2$ gas shows no spatial variation of the velocity dispersion and has generally lower dispersion than the [FeII] gas.

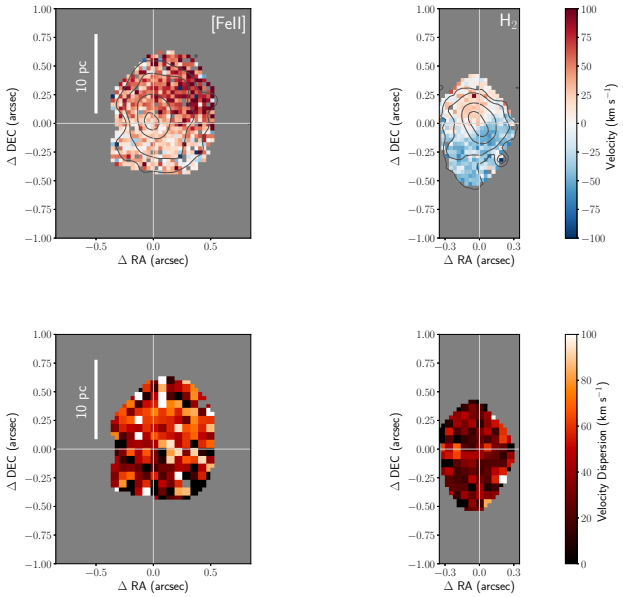


Figure 4.7: Velocity (top row) and velocity dispersion (bottom row) for the [FeII] (left column) and 1-0 S(1) $H_2$ (right column) emission lines. The velocity maps are shown for every individual spaxel and the velocity dispersion maps are shown for spectra in spatial bins measuring 2 by 2 spaxels (70 mas). Contours showing the morphology of the [FeII] and 1-0 S(1) $H_2$ line emission as displayed in Fig. 4.4 are overplotted in dark gray. The velocities are shown relative to the systemic velocity of NGC 404 and with the red colors indicating red shifts and the blue colors indicating blue shifts. The instrumental dispersions are subtracted from the measured velocity dispersions to yield the displayed dispersion map. Individual spaxels with a line S/N of less than 10 are masked. Spaxels whose Gaussian line fit did not converge or whose best fit velocity falls outside the fitting range are also masked. We find that the [FeII] and $H_2$ show different kinematics with velocity gradients that are roughly perpendicular to each other. The [FeII] line reaches high velocities up to 80 km $s^{-1}$ and has a higher dispersion than the molecular gas. The velocities of the central $H_2$ emission are dominated by rotational motion with a velocity gradient of $\pm$30 km $s^{-1}$. The two knots of $H_2$ emission to the southeast of the nucleus are blue shifted by $\sim$30 km $s^{-1}$.

#### 4.3.2.2 Stellar Kinematics: CO bandhead

The kinematics of the stars in the center of NGC 404 are mapped by measuring the velocity shift of the CO bandhead absorption feature observed in the Kbb band. The velocity shift between the spectrum in a single spaxel and a reference spectrum is found by cross correlating the two spectra in the wavelength region containing the CO bandhead features (2.27 - 2.365 $\mu$m). The peak of the resulting cross correlation is then found by fitting a Gaussian to the cross correlation function. We use the spectrum of the spaxel with the brightest Kbb continuum emission as the reference spectrum.

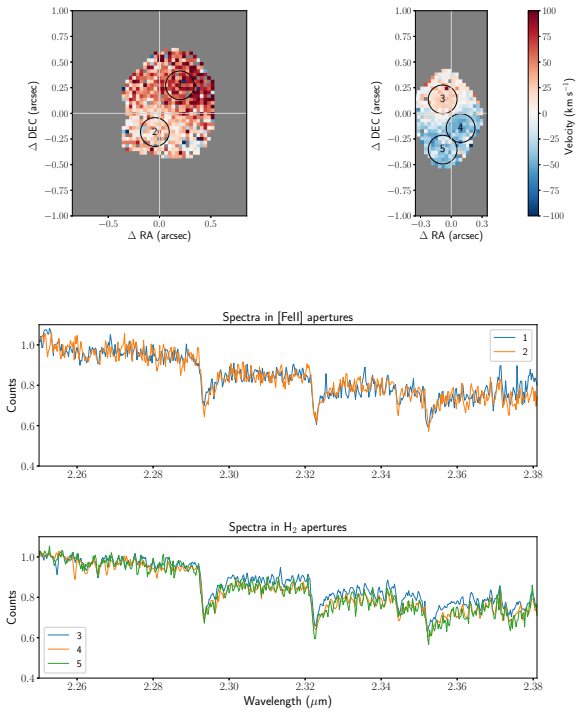


Figure 4.8: Comparison of CO bandhead absorption features in 5 spatial apertures centered on regions of high/low [FeII] or 1-0 S(1) $H_2$ velocities. The 5 circular apertures used are overplotted on the [FeII] and $H_2$ velocity maps in the top two panels. The lower two panels display the 5 spectra extracted from these spatial apertures in the wavelength region around the CO bandhead spectral features. The spectra are separated into two groups: the two apertures centered on regions of high and low [FeII] velocities and the three apertures centered on regions of high and low $H_2$ velocity. No stellar velocity shift is visible within these two groups of spectra, indicating that the stars are not moving in the same velocity field as either the ionized or molecular gas. Additionally, cross correlation measurements between spectra within these groups also give stellar velocity shifts consistent with 0 km $s^{-1}$.

In addition to measuring the stellar velocity for each individual spaxel, we also compare CO bandhead velocity shifts in different spatial locations to regions of large velocity gradients in the ionized or molecular gas. Circular apertures with radii of 4 pixels (2 pc) are placed on 5 locations with high/low [FeII] or 1-0 S(1) $H_2$ velocities. These apertures are overplotted on the [FeII] and 1-0 S(1) velocity maps and the spectra extracted from each aperture are shown in Fig. 4.8. Pairs of spectra with high/low [FeII] or $H_2$ velocities are also cross correlated with each other to check for stellar velocity shifts.

The resulting stellar velocity map is shown in Fig. 4.9. Only spaxels with a continuum S/N greater than 7.0 are displayed, where this S/N is computed using the DER_SNR al-

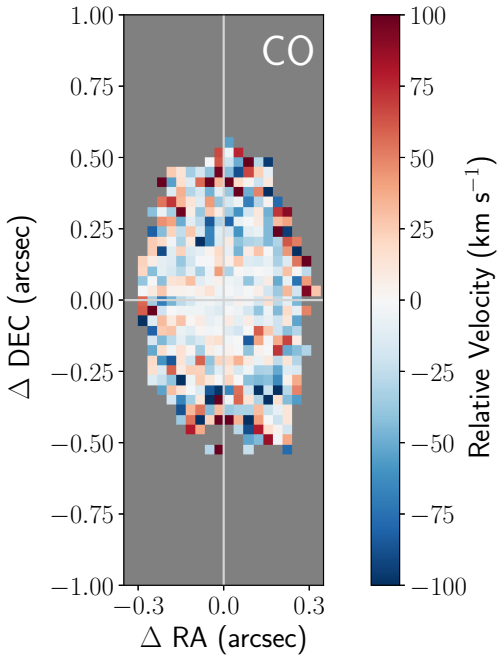


Figure 4.9: Relative stellar velocity map as measured by the CO bandhead absorption feature. The stellar velocities are displayed only for individual spaxels with continuum S/N greater than 7.0. The velocity shifts are measured relative to the spaxel with the highest Kbb continuum emission, which is the spaxel at the origin of this plot. The colorbar used here matches the colorbar used in Fig. 4.7 for the [FeII] and $H_2$ gas kinematics. The CO velocity shows no significant variation across the central ∼15 pc of NGC 404 in contrast with the [FeII] and $H_2$ emission lines, thus revealing that the stars are not moving at the same velocities as the gas.

gorithm (Stoehr et al., 2008). The velocities displayed here are relative to the velocity in the brightest Kbb continuum spaxel. We find no significant variation in the stellar velocity within the central ∼15 pc of NGC 404. In the spatial apertures centered on large gradients in [FeII] and $H_2$ velocity, there is no CO velocity shift visually seen in the extracted spectra. Cross correlations of the CO bandhead spectra in these high/low gas velocity apertures yield stellar velocity shifts consistent with 0 km s$^{-1}$.

### 4.3.3 Stellar Population Constraints: CO and Pa$\beta$ Absorption

The CO stellar absorption feature present in the Kbb data cube can be used to constrain the age of the central stellar population in NGC 404. This absorption feature is sensitive to

intermediate age stellar populations because the CO bandheads are stronger in cooler stars with lower surface gravity (i.e., giant and supergiant stars) than in dwarf stars. The strength of the absorption feature is often characterized by the CO index. We employ the CO index defined by Mármol-Queraltó et al. (2008), $D_{CO}$. That work found the $D_{CO}$ index to be less sensitive to velocity dispersion, radial velocity, and low S/N spectra than previously-defined CO indices. $D_{CO}$ is computed by taking a ratio of the average flux in two continuum bands (2.2460 – 2.2550 $\mu$m and 2.2710 – 2.2770 $\mu$m) over the average flux in one absorption band (2.2880 – 2.3010 $\mu$m), such that a $D_{CO}$ value of $\sim$1 indicates no CO absorption and increasing values indicate a deeper CO absorption depth relative to the continuum. For reference, individual dwarf stars have $D_{CO}$ values ranging from $\sim$1 – 1.1, red supergiants have values of $\sim$1.2 – 1.25, and AGB stars have values up to $\sim$1.3.

The $D_{CO}$ index in the nucleus of NGC 404 is computed for each individual spaxel of the Kbb data cube by first shifting the wavelength ranges of the continuum and absorption bands to the systemic velocity of NGC 404. The resulting map of the $D_{CO}$ index is shown in Fig. 4.10 for spaxels with a continuum S/N greater than 7.0. The CO index has a value of 1.15 - 1.16 at the K band continuum center of NGC 404 and increases to values of $\sim$1.20 (33% more CO absorption) at $\Delta$ DEC = $\pm$0.3 arcsec ($\pm$4.5 pc) from the center.

We also consider the constraints that the Pa$\beta$ absorption feature observed in the central $\sim$4 pc of NGC 404 places on the stellar population. This absorption feature can be affected by contamination of emission unlike the CO bandheads, but it is still interesting to explore the possible stellar population ages consistent with the measurement of this feature's equivalent width (EW). We compare the measured EW in a spatial aperture centered on the nucleus of NGC 404 with a 2 pc radius (aperture #1 in Fig. 4.11 and 4.14) to those measured from the telluric standard spectra of A0V and G2V stars (see Sec. 4.2) and to other dwarf stars ranging from spectral type F to M stars from the IRTF spectral library (Rayner et al., 2009). We find an EW consistent with a single late F/early G star or with a late B star.

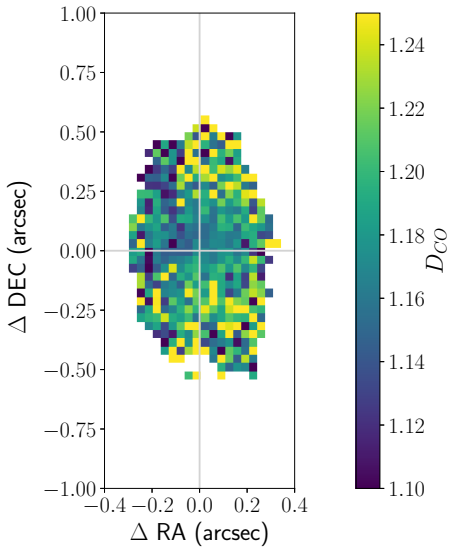


Figure 4.10: Map of the CO index $D_{CO}$ across the central ∼0.5 by 1.0 arcsec (7.5 by 15 pc) of the nucleus of NGC 404. Only the spaxels with a continuum S/N greater than 7.0 are displayed. The origin of the plot is set to the center of the Kbb continuum emission and is highlighted by the horizontal and vertical gray lines. The $D_{CO}$ index in the nucleus of NGC 404 has values of 1.15 - 1.16 at the center and increases to values of ∼1.20, or 33% more CO absorption, at a distance of ±4.5 pc from the center, indicating possible changes in the underlying stellar population.

### 4.3.4 Emission Line Ratios

#### 4.3.4.1 Molecular Hydrogen Excitation Temperatures

We estimate the flux of multiple molecular hydrogen lines within the wavelength range of the K broadband filter. Combinations of these line fluxes can be used to estimate the rotational and vibrational excitation temperature of the $H_2$ and distinguish between different excitation mechanisms of this molecular gas. In addition to the strongest 1-0 S(1) line of $H_2$ in the NGC 404 spectra discussed above, there are 3 detected $H_2$ lines in the Kbb bandpass: 1-0 S(0) ($\lambda_0 = 2.2235$ $\mu$m), 1-0 S(2) ($\lambda_0 = 2.0338$ $\mu$m), and 2-1 S(1) ($\lambda_0 = 2.2477$ $\mu$m). We estimate these 4 line fluxes in 3 different circular apertures with radii of 4 pixels = 0.14 arcsec. These apertures are centered on the different spatial structures observed in the 1-0 S(1) line map: the bright $H_2$ emission centered on the nucleus and the two weaker peaks of $H_2$ emission offset to the southeast of the nucleus. Fig. 4.11 shows the apertures superimposed on this

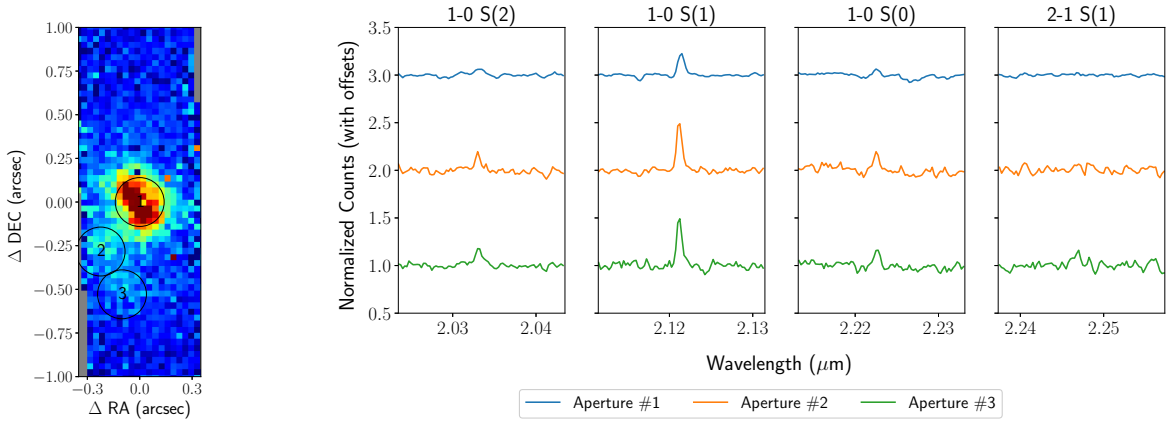


Figure 4.11: Left: 1-0 S(1) $H_2$ emission line map with 3 apertures superimposed. The apertures each have a radius of 4 pixels = 0.14 arcsec and are chosen to align with morphological features in the 1-0 S(1) emission map. Right: Kbb spectra extracted from the three apertures in the wavelength regions around the detected $H_2$ emission lines. These spectra are normalized to have a median of 1.0 and then an offset is applied for display purposes. The wavelength regions around each $H_2$ line are plotted in separate panels. The 1-0 S(2), 1-0 S(1), and the 1-0 S(0) $H_2$ lines are detected in all three apertures and the 2-1 S(1) line is only detected in the aperture #3.

line emission map and the corresponding extracted spectra.

The continuum is estimated globally in each of the three spectra using a line fit to a large subset of the wavelength range: 2.02 - 2.28 $\mu$m. This range excludes regions on the blue side of the spectra that suffer from poor telluric correction and regions on the red side that contain the CO bandhead absorption features while still covering the wavelengths of all 4 $H_2$ lines. Fig. 4.12 shows an example of this continuum fit as applied to the spectrum from the first aperture.

The $H_2$ line fluxes are then estimated from the continuum-subtracted spectra. First, the overall molecular hydrogen velocity in each aperture is estimated using the 1-0 S(1) line, using the same Gaussian fitting method used for the individual spaxel velocity estimate (see Sec. 4.3.2.1). The 1-0 S(1) velocities relative to the systemic velocity of NGC 404 in the apertures from north to south are $-5 \pm 3$, $39 \pm 2$, and $38 \pm 3$ km s$^{-1}$ respectively, where the error bars correspond to the fitting errors given by the curve_fit algorithm from the optimize module of the SciPy library. The flux of each line is then estimated by summing over wavelength channels with velocity in the range of $\pm$ 125 km s$^{-1}$ relative to the 1-0 S(1)

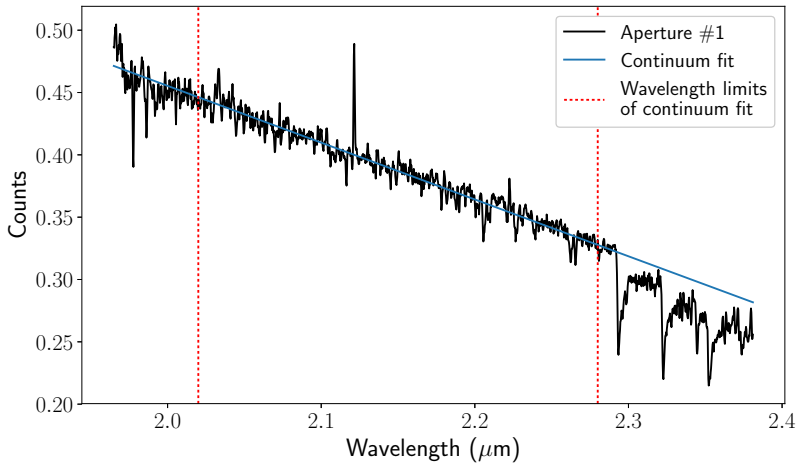


Figure 4.12: Example of the linear fit used to subtract the continuum before measuring the flux of the $H_2$ lines. The spectrum extracted from the first aperture is shown in black with its continuum fit in a dotted blue line. This continuum fit was performed over the wavelength range 2.02 to 2.28 $\mu$m, as indicated by the red dotted vertical lines.

velocity of each aperture. This velocity range was chosen using the 1-0 S(1) line in the central aperture by estimating its flux with a variety of velocity ranges and finding the minimum range that captured all of the line flux. The 1-0 S(1) line flux in the central aperture versus velocity range is shown in Fig. 4.13, with the final velocity range value of 125 km $s^{-1}$ also indicated.

The errors on the line fluxes in each aperture spectrum are estimated by applying the line flux measurement method described above to areas of the spectrum with no line flux. Wavelength values are sampled from a uniform distribution across the continuum fitting range of 2.02 - 2.28 $\mu$m. Various spectral regions within this wavelength range are masked out, including around the 4 $H_2$ lines, the doublet absorption features from NaI (2.206/2.209 $\mu$m) and CaI (2.263/2.266 $\mu$m), and strong OH sky lines. The 675 wavelength values remaining after the mask is applied are then used as the central wavelength for line flux measurements. The standard deviation of these resulting simulated line flux measurements is taken as the error on the measured $H_2$ line fluxes for each spectrum. For $H_2$ lines with fluxes that are less than 3 sigma above the error, a 3-$\sigma$ upper limit on the flux is determined using the method described in Sec. 4.3.4. The velocity dispersion of the Gaussian line profile that sets the

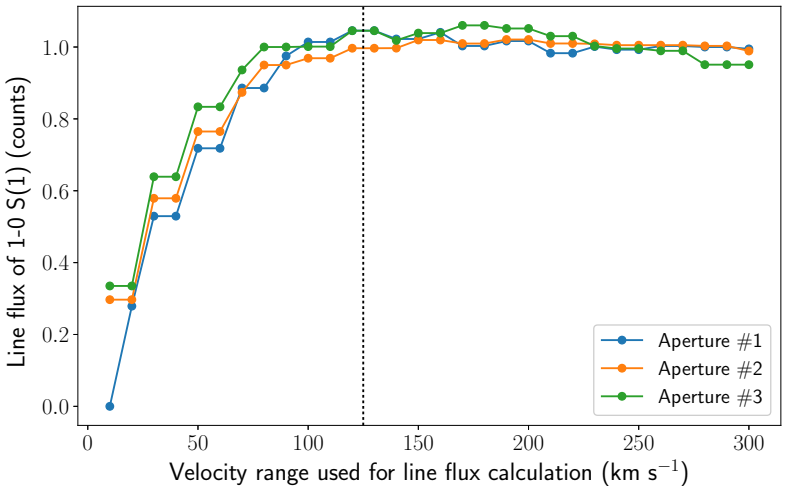


Figure 4.13: Line flux of 1-0 S(1) as a function of different velocity ranges used in the line flux calculation, for each of the three apertures. The chosen velocity range of $\pm$125 km s$^{-1}$ is indicated by the black dotted line. This range was chosen because it is approximately where the curve of the 1-0 S(1) flux begins to flatten and is therefore the minimum velocity range that captures all of the $H_2$ flux for each emission line.

limiting flux is taken as 50 km s$^{-1}$ to match the measured dispersion of the 1-0 S(1) line, which is detected with high significance in all three apertures.

Ratios of the $H_2$ line fluxes 1-0 S(2)/1-0 S(0) and 1-0 S(1)/2-1 S(1) are calculated to constrain the physical mechanism exciting the $H_2$ line emission and to compare to models. These line ratios use fluxes from both ortho (odd $J$) or both para (even $J$) hydrogen molecules, so that a ortho/para ratio does not need to be independently assumed. The line ratios are also converted to the rotational ($T_{rot}$) and vibrational ($T_{vib}$) excitation temperatures of the molecular gas. We apply the equations from Reunanen et al. (2002):

$$T_{rot} = \frac{-1113}{\ln\left(0.323 \times \frac{\text{1-0 S(2)}}{\text{1-0 S(0)}}\right)} \tag{4.1}$$

$$T_{vib} = \frac{5600}{\ln\left(1.355 \times \frac{\text{1-0 S(1)}}{\text{2-1 S(1)}}\right)} \tag{4.2}$$

These equations assume local thermal equilibrium and therefore a thermal distribution for the ro-vibrational level populations.

Table 4.2. $H_2$ Line Fluxes and Excitation Temperatures

| Aperture Number | Line Fluxes (Counts) 1-0 S(2) | 1-0 S(1) | 1-0 S(0) | 2-1 S(1) | Line Flux Error (Counts) | 1-0 S(2)/ 1-0 S(0) | 2-1 S(1)/ 1-0 S(1) | $T_{rot}$ (K) | $T_{vib}$ (K) |
|---|---|---|---|---|---|---|---|---|---|
| #1 | 0.09 | 0.33 | 0.15 | <0.10 | 0.03 | 1.7 ± 0.6 | <0.30 | 1820 | <3610 |
| #2 | 0.029 | 0.089 | 0.042 | <0.020 | 0.007 | 1.5 ± 0.4 | <0.23 | 1470 | <3080 |
| #3 | 0.016 | 0.049 | 0.030 | 0.012 | 0.004 | 1.9 ± 0.5 | 0.25 ± 0.09 | 2290 | 3340 |

The line flux measurements and errors, line ratios, and excitation temperatures for each aperture are presented in Table 4.2. The 2-1 S(1) line was not detected above 3 sigma in apertures #1 and #2, so the upper limits on the line flux, the line ratio, and the $T_{vib}$ are reported. The other emission lines were detected above 3 sigma in all apertures, and with the highest significance in aperture #2, where the lower underlying continuum emission relative to the $H_2$ line emission leads to a lower line flux error. The $T_{rot}$ is measured in all three apertures to be between 1400 and 2300 K. Both the $T_{rot}$ and the 1-0 S(2)/1-0 S(0) line ratio are consistent among the three spatial locations. The 2-1 S(1)/1-0 S(1) line ratio measurement in aperture #3 and upper limits in apertures #1 and #2 are also consistent.

#### 4.3.4.2 [FeII]/Pa$\beta$ and $H_2$/Br$\gamma$ Line Ratios

The line ratios of [FeII]/Pa$\beta$ and 1-0 S(1) $H_2$/Br$\gamma$ are measured to constrain the excitation mechanisms at different physical locations at the center of NGC 404. In general, the S/N of the hydrogen recombination lines is not high enough to estimate their line flux in any but a few spaxels (see Fig. 4.4), so these line ratios are instead measured in various circular apertures placed within the shared Jn2/Kbb FOV with radii ranging from 2 - 4 pixels (1 - 2 pc). We define these apertures by starting with the 3 apertures used for the $H_2$ line ratio meSec. asurements in Sec. 4.3.4.1, which are centered on the NGC 404 nucleus and two other areas of $H_2$ emission. An additional aperture is applied to the location of the Pa$\beta$/Br$\gamma$ emission peak to the north of the nucleus. Other apertures are then added to cover the full spatial extent of the [FeII] line, the most spatially extended emission line. The radii of these apertures are between 2 and 4 pixels depending on the signal to noise. Fig. 4.14 displays the

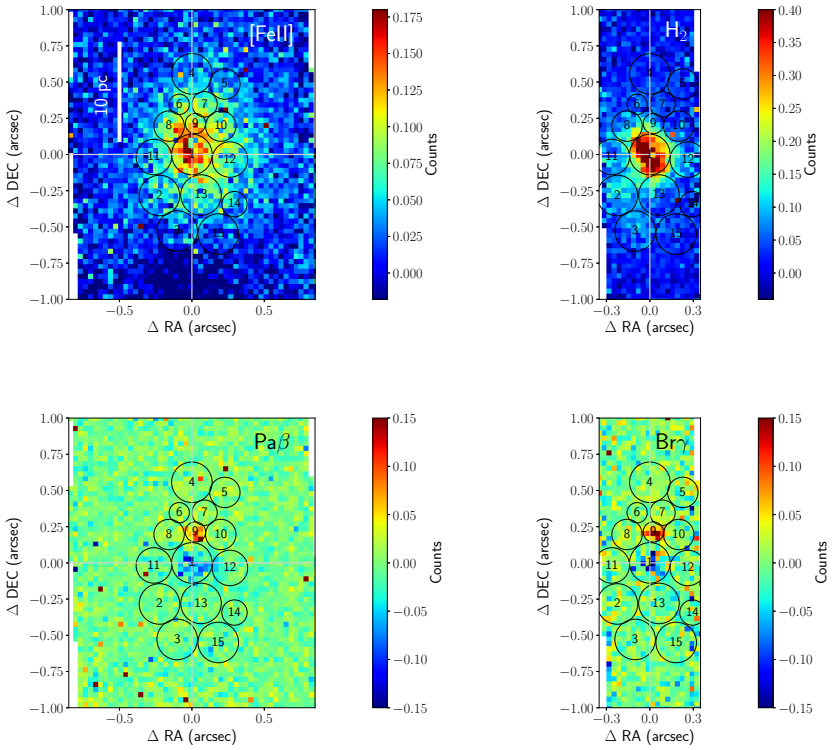


Figure 4.14: Circular apertures in which the [FeII]/Pa$\beta$ and 1-0 S(1) $H_2$/Br$\gamma$ are estimated overplotted on the [FeII], Pa$\beta$, 1-0 S(1) $H_2$, and Br$\gamma$ emission line maps from Fig. 4.4. Apertures #1, 2, and 3 are the same apertures used in the $H_2$ line ratio measurements described in Sec. 4.3.4.1. Aperture #9 was chosen to be centered on the peak of Pa$\beta$/Br$\gamma$ to the north of the NGC 404 nucleus. Other apertures are used to fill in the remaining area of the [FeII] emission, the most spatially extended emission line. The radii of the apertures vary from 2 - 4 pixels (1 - 2 pc).

final set of apertures overplotted on all 4 line emission maps.

In the Jn2 filter, the bandpass is so narrow that a global continuum is difficult to perform consistently for all aperture spectra. Instead, a local continuum around each line is estimated by taking an average of the counts in wavelength channels on either side of the emission line. This method is applied to both the Jn2 and Kbb data to maintain consistency between the bands. The default channels used for the local continuum calculation are -450 to -300 km $s^{-1}$ and +300 to +450 km $s^{-1}$, the same velocity range used for the line S/N estimation described in Sec. 4.3.1.1. The flux of each line is then determined by summing the continuum-subtracted counts in wavelength channels containing the emission line, by default $\pm$250 km

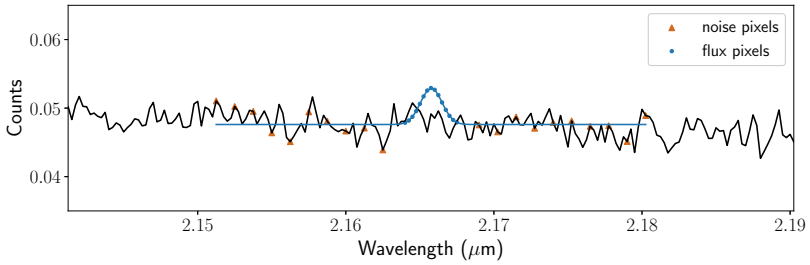


Figure 4.15: Example of upper limit measurement for a Br$\gamma$ emission line. This spectrum was extracted from aperture #6 displayed in Fig. 4.14. The spectrum is plotted as a black line and the wavelength channels used to estimate the noise are plotted as brown triangles. The blue curve shows a Gaussian that sets the upper limit for the Br$\gamma$ flux with a peak that is 3-$\sigma$ above the noise and a velocity dispersion of 100 km sec$^{-1}$. This upper limit Gaussian is centered on the wavelength of Br$\gamma$ at the systemic velocity of the galaxy and is vertically offset to match the average level of counts measured in the noise channels for display purposes. The wavelength channels used for the flux measurement ($\pm$250 km sec$^{-1}$ relative to the systemic velocity of the galaxy) are plotted as blue circles.

s$^{-1}$ relative to the systemic velocity of the galaxy. This velocity range was chosen to cover the wings of all 4 emission lines, including in the case that the lines are doppler shifted with respect to each other or with respect to the systemic velocity. In each aperture, the same continuum and line flux velocity ranges are used for all 4 emission lines so that the [FeII]/Pa$\beta$ and $H_2$/Br$\gamma$ line ratios are calculated using consistently-measured line fluxes and can therefore be compared to each other.

If an emission line is not detected in an aperture, then an upper limit is placed on its line flux. This upper limit is only needed for the hydrogen recombination lines, since these lines are much lower S/N than the [FeII] and 1-0 S(1) $H_2$ lines. An upper limit on the Pa$\beta$ and Br$\gamma$ lines corresponds to a lower limit on the [FeII]/Pa$\beta$ and $H_2$/Br$\gamma$ line ratios. A conservative 3-$\sigma$ upper limit is calculated by taking the flux from a Gaussian emission line with a peak of 3 times the noise estimate described in Sec. 4.3.1.1 and a velocity dispersion of 100 km s$^{-1}$. This dispersion value is on the high end of the observed velocity dispersions of the [FeII] and $H_2$ emission lines (see Fig. 4.7), giving a conservative upper limit for the line flux. The flux of the Gaussian is computed by sampling the Gaussian at wavelength channels within the $\pm$250 km s$^{-1}$ velocity range and taking the sum of these values. Fig. 4.15 gives an example of this upper limit emission line overplotted on a spectrum in which Br$\gamma$ was not detected.

Table 4.3 gives the locations and radii of all 15 apertures, the velocity ranges used for the continuum and line flux estimation, and the resulting line ratio measurements or lower limits. We find that [FeII] and 1-0 S(1) $H_2$ lines are detected in all 15 apertures and Pa$\beta$ and Br$\gamma$ are detected in 9 and 3 apertures respectively. The lowest values of both line ratios ([FeII]/Pa$\beta$ = 2.5 and $H_2$/Br$\gamma$ = 1.2) are found in the aperture centered on the peak of the Pa$\beta$ and Br$\gamma$ emission. Six of the other apertures with Pa$\beta$ detections are located to the north of the nucleus and show [FeII]/Pa$\beta$ ratios between 5.3 and 6.5. Two other apertures to the south of the nucleus also have Pa$\beta$ detections with slightly lower values of 3.8 and 4.3, though these detections have lower S/N than the northern apertures. Two of the northern apertures also have detections of Br$\gamma$ and show $H_2$/Br$\gamma$ ratios of 2.4 and 2.7.

Table 4.3. [FeII]/Pa$\beta$ and 1-0 S(1)/Br$\gamma$ Line Ratio Measurements in NGC 404

| Aperture Number | Aperture Location (arcsec) (Δ RA) | (Δ DEC) | Radius (pixels) | Velocity Ranges (km sec$^{-1}$)[b] Line Flux | Continuum[b] | Line Fluxes ($\times 10^2$ counts) [FeII] | Pa$\beta$ | 1-0 S(1) $H_2$ | Br$\gamma$ | [FeII]/ Pa$\beta$[c] | 1-0 S(1) $H_2$/ Br$\gamma$[c] |
|---|---|---|---|---|---|---|---|---|---|---|---|
| #1 | 0.00 | 0.00 | 4.0 | ±250 | 300-450 | 15 | – | 38 | – | – | – |
| #2 | −0.22 | −0.28 | 4.0 | ±200 | 200-350 | 5.0 | – | 9.9 | – | – | – |
| #3 | −0.10 | −0.53 | 4.0 | ±175 | 175-325 | 2.3 | 0.5 | 5.5 | < 2.2 | 4.3 | > 2.6 |
| #4 | 0.00 | 0.56 | 4.0 | ±250 | 300-450 | 4.4 | 0.8 | 3.6 | 1.3 | 5.7 | 2.7 |
| #5 | 0.23 | 0.49 | 3.0 | ±250 | 300-450 | 4.1 | 0.6 | 4.6 | < 3.4 | 6.4 | > 1.4 |
| #6 | −0.09 | 0.35 | 2.0 | ±250 | 300-450 | 8.4 | 1.4 | 4.2 | < 3.8 | 6.0 | > 1.1 |
| #7 | 0.09 | 0.35 | 2.5 | ±250 | 300-450 | 9.6 | 1.8 | 4.3 | 1.7 | 5.3 | 2.4 |
| #8 | −0.16 | 0.20 | 3.0 | ±250 | 300-450 | 10 | 1.6 | 13 | < 4.5 | 6.5 | > 2.8 |
| #9 | 0.02 | 0.21 | 2.0 | ±250 | 300-450 | 13 | 5.4 | 12 | 11 | 2.5 | 1.2 |
| #10 | 0.20 | 0.20 | 3.0 | ±175 | 175-325 | 7.2 | 1.4 | 4.0 | < 5.1 | 5.3 | > 0.8 |
| #11 | −0.26 | −0.02 | 3.5 | ±250 | 300-450 | 5.9 | – | 8.4 | – | – | – |
| #12 | 0.26 | −0.04 | 3.5 | ±250 | 300-450 | 7.7 | – | 9.2 | – | – | – |
| #13 | 0.06 | −0.28 | 4.0 | ±250 | 300-450 | 8.2 | – | 9.6 | – | – | – |
| #14 | 0.29 | −0.34 | 2.5 | ±200 | 200-350 | 5.1 | – | 3.2 | – | – | – |
| #15 | 0.18 | −0.55 | 4.0 | ±175 | 175-325 | 2.1 | 0.5 | 2.6 | < 3.0 | 3.8 | > 0.9 |

[a]All velocity values are relative to the systemic velocity of the galaxy (-48 km sec$^{-1}$).

[b]The continuum velocity range given here refers to both the red (e.g., +300 to +450 km sec$^{-1}$) and blue (e.g., −450 to −300 km sec$^{-1}$) sides of the emission line. Wavelength channels in these two ranges are used to estimate the continuum.

[c]Line ratio measurements/upper limits are not reported for spectra with measured Pa$\beta$ absorption.

Additionally, there are 6 apertures in which Pa$\beta$ absorption is detected and for these apertures no line ratio measurement or upper limit is reported. The Pa$\beta$ absorption is accompanied by either very weak to no emission (apertures #1 and 12) or by strong emission (apertures #2, 11, 13, and 14). Fig. 4.16 displays 5 representative spectra to show the variation seen within the center of NGC 404. The example spectra are: the aperture centered on the nucleus of NGC 404 showing Pa$\beta$ absorption and no emission (#1), a northern aperture with both Pa$\beta$ and Br$\gamma$ detections (aperture #7), the aperture centered on the Pa$\beta$/Br$\gamma$ emission (#9), an aperture with simultaneous detection Pa$\beta$ absorption and strong emission (#11), and a southern aperture with Pa$\beta$ detected (#15).

## 4.4 Discussion

In this discussion section, we explore the constraints on the excitation mechanisms in the nucleus of NGC 404 given the OSIRIS observations for both the ionized and molecular gas. We also put constraints on the nuclear stellar population of NGC 404 based on measurements of the depth of the CO absorption features. We finally propose a supernova-driven shock excitation scenario that can produce the [FeII] emission and is consistent with constraints on the stellar population.

### 4.4.1 Excitation Mechanisms of [FeII] Gas

Constraints on the physical mechanism that excites the [FeII] emission in NGC 404 can be made using measurements of the [FeII]/Pa$\beta$ ratio (Sec. 4.3.4.2). High values of this ratio (>2.0) are indicative of shock excitation, which can efficiently process dust grains and thereby increase the gas phase abundance of iron, which is typically highly depleted in the interstellar medium (Blietz et al., 1994; Larkin et al., 1998). Fig. 4.17 plots the [FeII]/Pa$\beta$ and $H_2$/Br$\gamma$ line ratios presented in Table 4.3. These measurements, which probe physical scales of 1-2 pc, are compared to values in other objects from the literature and to the overall correlation found in these line ratios from spatially-integrated spectra of starburst, AGN, and LINER galaxies (Larkin et al., 1998; Riffel et al., 2013). The global line ratios for NGC

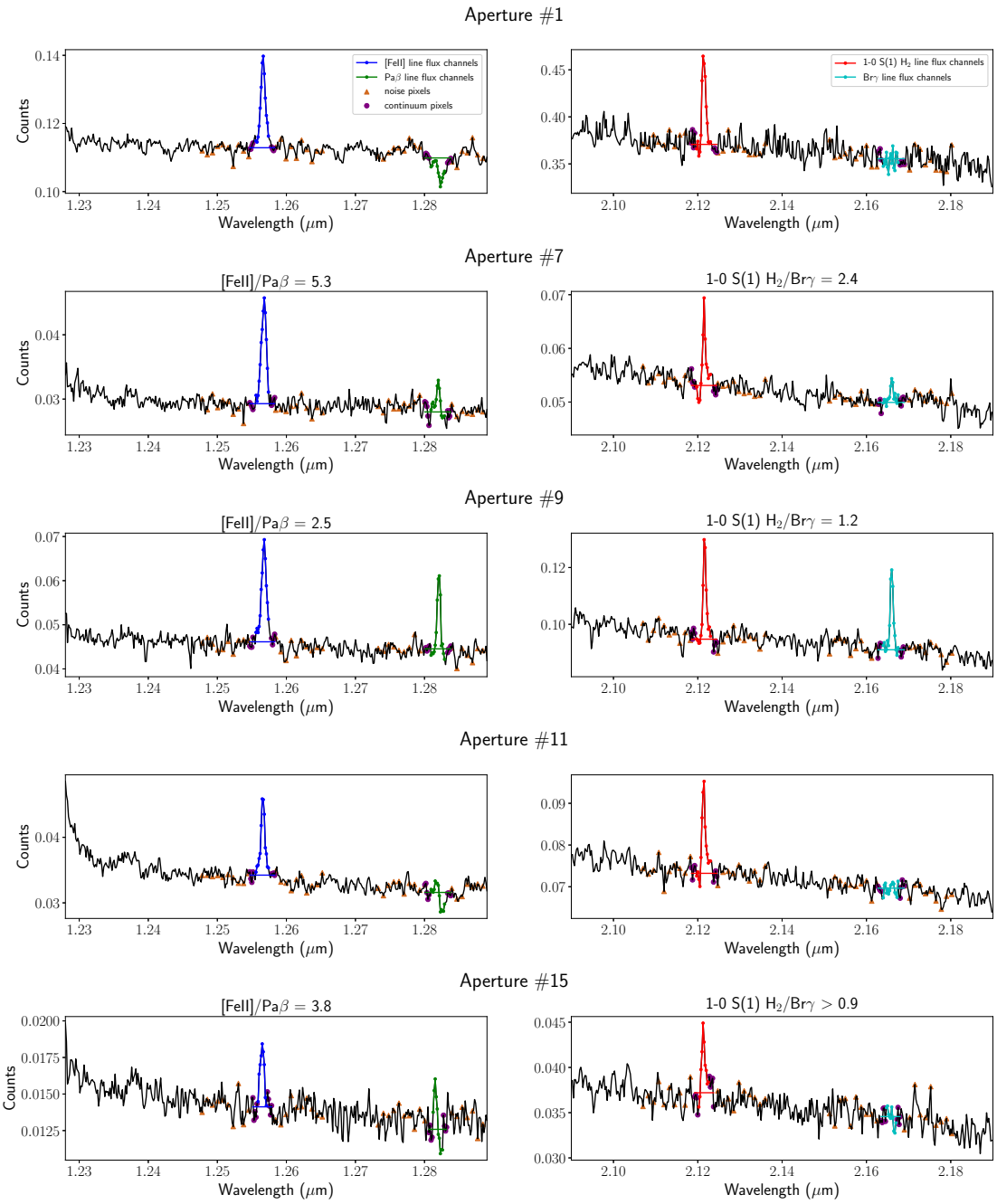


Figure 4.16: Example spectra to represent the variety of emission line morphologies and ratios observed in NGC 404. The overall spectrum is plotted in black and each emission line is plotted in a different color to indicate the wavelength channels used to measure the line flux. The pixels used for both the noise and the continuum estimation are also highlighted as brown triangles and purple circles respectively. The continuum estimation is also plotted as a horizontal line spanning the channels used for both the continuum and line flux measurements. The spectra plotted here show examples of high (#7) and low (#9) [FeII]/Pa$\beta$ and $H_2$/Br$\gamma$ line ratios, a region in which Pa$\beta$ is detected but only a limit can be placed on Br$\gamma$ (#15), and regions of strong (#1) and weak (#11) Pa$\beta$ absorption in which the line ratios are not constrained.

404 derived by Larkin et al. (1998) from slit spectra that cover the central ∼10 by 45 pc are also plotted. We find that the [FeII]/Pa$\beta$ line ratio measured in the small apertures with OSIRIS is generally 1.5 - 2.5 times higher than the global [FeII]/Pa$\beta$ ratio measured by Larkin et al. (1998). The aperture centered on the Pa$\beta$/Br$\gamma$ emission feature (#9) has a [FeII]/Pa$\beta$ line ratio that is lower than the rest of the spatial locations and consistent with the global ratio. The high [FeII]/Pa$\beta$ values ranging from 4 - 6.5 are among the highest measured in extragalactic sources and are similar to those seen in the shocked regions of supernova remnants (SNRs), also plotted on Fig. 4.17. From these high [FeII]/Pa$\beta$ ratios we conclude that the [FeII] emission in NGC 404 is due to shock excitation.

One possible source of the shocks that excite the [FeII] emission is one or more supernova remnants (SNRs). Larkin et al. (1998) previously suggested this scenario for NGC 404's [FeII] emission and found that a few SNRs have enough energy to produce the [FeII] emission seen in the central ∼10 by 45 pc. Pogge et al. (2000) also noted that the extended, bubble-like structure of [NII]+H$\alpha$ emission seen in Hubble Space Telescope optical narrowband imaging is similar to that of a supernova remnant. In comparing the [NII]+H$\alpha$ imaging data to the [FeII] emission at $-50$ km s$^{-1}$, we find that the curvatures and spatial extension of the [FeII] emission to the north and southwest of the nucleus is very similar to the [NII]+H$\alpha$ structure (see Fig. 4.18). The similarity between these morphologies and the high [FeII]/Pa$\beta$ ratios suggest that the [FeII] emission originates from a shock front caused by one or more supernovae which were offset to the west of the nucleus by ∼5 pc (i.e., the location of the center of the [NII]+H$\alpha$ bubble seen in the HST data). As this shock front reaches the denser gas in the nucleus, it can then excite the [FeII] emission and produce the observed [FeII]/Pa$\beta$ ratios. Nyland et al. (2012) explored a supernova remnant caused by a core-collapse supernova as a possible source of the observed radio and hard X-ray (2 - 10 keV; Binder et al., 2011) nuclear emission, but argued that this was statistically unlikely given the current star formation rate (Seth et al., 2010). It is also possible, however, that the supernova causing the observed [FeII]-exciting shocks was instead a type Ia, which would be more consistent with the dominant stellar population age of ∼1 Gyr found in this work (see Sec. 4.4.3) and in previous optical studies of the nucleus of NGC 404 at seeing-limited

(Fernandes et al., 2004; Bouchard et al., 2010) and diffraction-limited angular resolutions (Seth et al., 2010; Nguyen et al., 2017).

### 4.4.2 Excitation Mechanisms of $H_2$ Gas

The dominant excitation mechanism of the $H_2$ molecular gas can be constrained by comparing the $H_2$ line ratios and the rotational/vibration excitation temperatures derived in Sec. 4.3.4.1. In the case of purely thermal (collisional) excitation, the molecular gas is in local thermal equilibrium and the level populations are set by a Boltzmann distribution. The two excitation temperatures are therefore equal to each other and to the kinetic temperature of the gas. For UV fluorescence excitation, upper energy levels of the $H_2$ are over populated compared to the Boltzmann distribution due to the absorption of UV photons, resulting in a higher $T_{vib}$ ratio compared to $T_{rot}$, often by a factor of 10.

We compare the measured line ratios of 2-1 S(1)/1-0 S(1) and 1-0 S(2)/1-0 S(0) and the corresponding excitation temperatures of $T_{vib}$ and $T_{rot}$ in each of the three spatial apertures in NGC 404 in Fig. 4.19 (Mouri, 1994). These measurements are compared to expected values for thermal excitation ($T_{vib} = T_{rot}$) and UV fluorescence excitation ($T_{vib}$ much greater than $T_{rot}$; Black & van Dishoeck, 1987). We measure consistent line ratios and excitation temperatures within the three spatial apertures centered on the central bright $H_2$ emission and the two peaks of emission offset to the southeast of the nucleus. In the 2-1 S(1)/1-0 S(1) versus 1-0 S(2)/1-0 S(0) parameter space in Fig. 4.19, the line ratio measurements and/or upper limits in each aperture fall near the thermal excitation curve of $T_{vib} = T_{rot}$ with an offset towards the UV fluorescence excitation models. We therefore conclude that the $H_2$ excitation mechanism is consistent with thermal excitation at all three spatial locations, with a temperature of 2000-4000 K, plus some contribution of UV fluorescent excitation. Given the kinematic and morphological structure of the $H_2$ emission, we interpret the central peak of emission as a rotating disk of thermally excited molecular gas. Thermally excited disks of $H_2$ gas have been commonly found at the centers of classical Seyferts (e.g., Storchi-Bergmann et al., 2009; Hicks et al., 2009, 2013; Riffel et al., 2015; Hicks et al., 2016) as well as optically-

classified LINERs and low luminosity AGN (e.g., Müller-Sánchez et al., 2013; Mazzalay et al., 2013, 2014). The peaks of offset $H_2$ emission are also dominated by thermal excitation, but it is unclear whether these peaks trace hot spots in a larger scale rotating disk associated with the central emission peak or are physically separate clumps of gas.

Although we can determine that the $H_2$ gas in NGC 404 is dominated by thermal excitation, it is more difficult to constrain the physical mechanism heating the $H_2$ gas from the line ratios alone. One possibility is that the $H_2$ is being heated by the same shock front that is exciting the [FeII] emission as these shocks impinge on the central disk of molecular gas. Other heating sources include UV radiation from young stars or X-ray radiation from X-ray binaries or the central weakly accreting BH. To explore what might be heating the gas, we constrain the mass of the warm $H_2$ gas and its total internal energy. We use the equation presented in Mazzalay et al. (2013) to convert the 1-0 S(1) line flux to the warm $H_2$ gas mass ($M_{H_2}$), which assumes a kinetic gas temperature of 2000 K:

$$M_{H_2} \simeq 5.0875 \times 10^{13} \left(\frac{D}{\mathrm{Mpc}}\right)^2 \left(\frac{\text{1-0 S(1)}}{\mathrm{erg\ s^{-1}\ cm^{-2}}}\right) 10^{0.4 \times A_{2.2}}. \tag{4.3}$$

In this equation, D is the distance to the galaxy (3.1 Mpc for NGC 404) and $A_{2.2}$ is the extinction at 2.2 $\mu$m. We use the 1-0 S(1) $H_2$ line flux presented in Larkin et al. (1998) for the central $\sim$10 by 45 pc of NGC 404 and assume a large value of 1.0 for $A_{2.2}$ (corresponding to a visible extinction $A_V$ of $\sim$ 10.0) to find an upper limit for the $H_2$ gas mass. We find a total mass of only 3 $M_\odot$, showing that the NGC 404 nucleus is not a particularly large reservoir of warm molecular gas. Note that this is only a measurement of the mass of the gas that is warm and emitting the thermally exciting lines; it does not include the cold $H_2$ gas, which is expected to be a factor of $10^5$ to $10^7$ higher than the warm gas mass (see Dale et al., 2005; Müller Sánchez et al., 2006). The warm $H_2$ mass can then be converted to the total internal energy using $U = c_P n T$, where $c_P$ is the specific heat at constant pressure of $H_2$, $n$ is the number of moles of $H_2$, and $T$ is the gas kinetic temperature of 2000 K. Given a value of $c_P$ at 2000 K of 34 J / (K mol) from NIST Standard Reference Database, we find an upper limit for the total internal energy of the $H_2$ gas of $2 \times 10^{45}$ erg. This total energy is quite

small at 6 orders of magnitude lower than the total energy released by a single supernova. This low energy suggests that there are many possible physical mechanisms, including the supernova remnant shock, that could heat the gas and cause the thermal excitation that we observe.

### 4.4.3 Stellar Population

The strength of the CO absorption quantified by the $D_{CO}$ index measured in Sec. 4.3.3 can be interpreted by comparing indices measured on the spectra of a simulated stellar population with the indices measured from the data, thereby constraining the age of the stellar population. Meneses-Goytia et al. (2015) performed single stellar population synthesis modeling in the NIR based on empirical stellar spectra from the IRTF spectral library (Rayner et al., 2009). That work computes a number of spectral indices and tracks their values as a function of age (from 1 - 14 Gyr) and metallicity (-0.70 to +0.20 dex relative to solar) of the stellar population. Note that earlier ages are not modeled due to the lack of high temperature main sequence stars in the IRTF spectral library.

We measure a significant spatial variation of the CO index ($D_{CO}$), with values of 1.15-1.16 at the center of NGC 404 (coincident with the Kbb continuum center) and increasing values of up to $\sim$1.20 moving outward from the center. When comparing to the simulated $D_{CO}$ values (Fig. 11 in Meneses-Goytia et al., 2015), we find that the $D_{CO}$ value at the nucleus of 1.15-1.16 is lower than most of the computed models and can only be produced by a stellar population with an age of 1 - 1.5 Gyr and a high metallicity of +0.2 dex relative to solar. The higher value of 1.20 found at larger radii from the nucleus is reproduced by a larger set of models with ages ranging from 1 to 7 Gyr and with metallicities spanning the full sampled range. A dominant stellar population age of $\sim$1 Gyr in the nucleus of NGC 404 is consistent with previous results using optical spectroscopy (e.g., Seth et al., 2010; Nguyen et al., 2017).

The Pa$\beta$ EW measurements can also be used to constrain the age of the stellar population. We found in Sec. 4.3.3 that the Pa$\beta$ EW in the central aperture is consistent with a late

F/early G star or a late B star. Based on the main sequence lifetimes of these stars, this EW would indicate a component of stars with an age of $< 5 - 8$ Gyr, consistent with our CO bandhead constraints, or a young stellar population with an age of $< 500$ Myr. If the Pa$\beta$ absorption is significantly filled in by Pa$\beta$ emission, then the intrinsic EW would be larger than what we measure, pointing towards the presence of A stars with very strong hydrogen absorption features and suggesting a young component in the stellar population. The previous optical spectroscopic studies mentioned above have also found a component of young stars in this age range in the nucleus of NGC 404, though the preferred model of the most recent work finds that this component is a small fraction of the total mass ($\sim$6%) compared to the 1 Gyr stars (Nguyen et al., 2017). Those authors also point out a region of blue optical colors slightly offset to the west of the nucleus that they attribute to this young stellar population, which coincides with the Pa$\beta$ absorption seen in the velocity-resolved emission maps offset $\sim$1 pc to the west of the nucleus (see 50 and 100 km s$^{-1}$ velocity channels in Fig. 4.5). Another sign of the presence of younger stars in this region is the Pa$\beta$/Br$\gamma$ emission seen 3 pc to the north of the nucleus of NGC 404. This compact clump of hydrogen recombination emission is spatially coincident with bright, extended [FeII] emission (see 50 km s$^{-1}$ channel in Fig. 4.5) and likely originates from a region of star formation.

## 4.5 Summary

We have presented the first spatially-resolved data of J-band [FeII] and Pa$\beta$ emission in the nucleus of NGC 404 and have compared it to the K-band $H_2$ and Br$\gamma$ emission and CO stellar absorption. These high angular resolution data reveal differences in morphology and kinematics of the ionized and molecular gas at pc spatial scales in this LINER nucleus. We find that the [FeII] and $H_2$ emission are both spatially extended and observe spatially separated regions of Pa$\beta$ and Br$\gamma$ emission and absorption. The velocity structure of the $H_2$ reveals a rotating disk of molecular gas centered on the nucleus, while the [FeII] velocity structure is more asymmetric and spans higher velocities. We also quantify the depth of the CO stellar absorption feature using the $D_{CO}$ index and find that the dominant age of the

stellar population is ∼1 Gyr at the center of NGC 404, with a wider range of possible ages from 1 - 7 Gyr at increasing radii. Finally, line ratios measured from multiple $H_2$ lines, [FeII], and the hydrogen recombination lines point to thermal excitation of the central molecular gas with some contribution from UV fluorescence and shock excitation of the ionized iron gas.

We argue that a possible physical source of the [FeII] shock excitation is a supernova remnant. This scenario is supported by both high [FeII]/Pa$\beta$ ratios similar to the shocked regions of supernova remnants (Fig. 4.17) and the morphology of [FeII] and [NII]+H$\alpha$ from HST narrowband imaging (Fig. 4.18; Pogge et al., 2000). We conclude that despite the likely presence of an accreting intermediate mass black hole at the center of NGC 404, black hole processes are not causing the LINER emission observed at optical and NIR wavelengths.

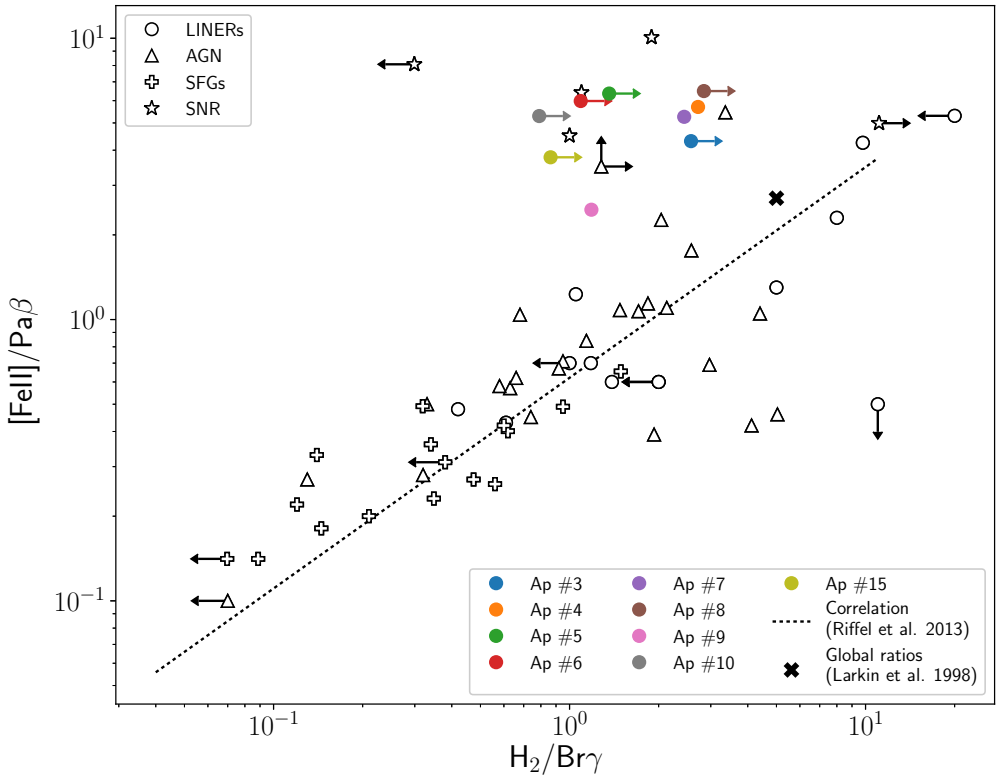


Figure 4.17: Plot of the [FeII]/Pa$\beta$ and 1-0 S(1) $H_2$/Br$\gamma$ emission line ratio measurements and lower limits for different spatial apertures. Apertures in which Pa$\beta$ absorption is detected are not plotted. The correlation between these two line ratios as measured from spatially-integrated slit spectra of AGN, star forming galaxies (SFGs), and LINER galaxies is shown as a black dashed line (Riffel et al., 2013). Values from individual sources in the literature are plotted for LINERs, SFGs, AGN, and supernova remnants (SNRs) (Larkin et al., 1998; Dale et al., 2004; Rodríguez-Ardila et al., 2004, 2005; Riffel et al., 2013). The global line ratios for NGC 404 from Larkin et al. (1998) are plotted as a black cross. We find that the line ratios in NGC 404 measured by OSIRIS are generally 1.5 - 2.5 times higher than the global line ratios measured by Larkin et al. (1998) and fall near the shocked regions of supernova remnants in this parameter space. The aperture centered on the Pa$\beta$/Br$\gamma$ emission (#9) is lower than the other apertures and is consistent with the global line ratios. The high line ratios measured by OSIRIS are evidence that the [FeII] emission in NGC 404 is excited by widespread shocks in the nucleus of this galaxy.

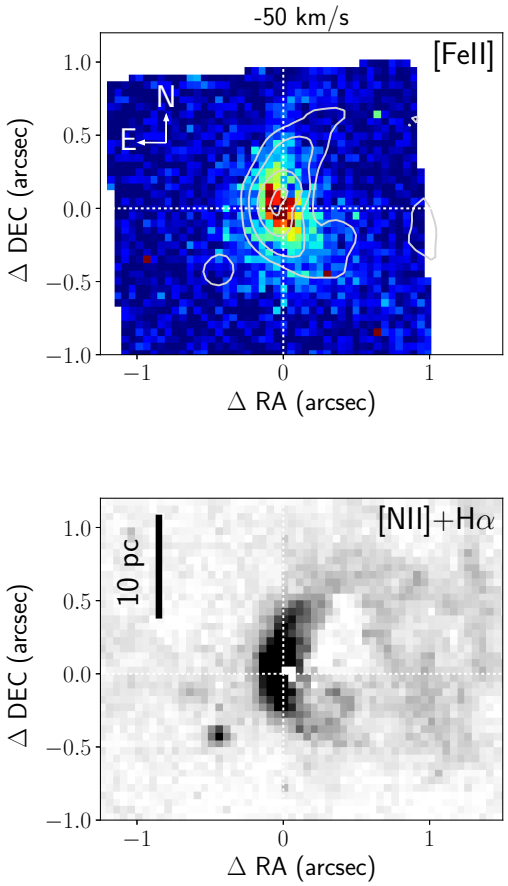


Figure 4.18: Comparison of the [FeII] emission morphology observed at $-50$ km s$^{-1}$ relative to the systemic velocity of the galaxy (this work; see Sec. 4.3.1.3) and the [NII]+H$\alpha$ emission observed using HST narrowband imaging (Pogge et al., 2000). The [FeII] emission map is derived from the OSIRIS data taken in the 50 mas plate scale mode (see Sec. 4.2 for details). Contours of the [NII]+H$\alpha$ image are overplotted on the [FeII] map, highlighting that the curvature and spatial extension of the [FeII] emission at this velocity is similar to the [NII]+H$\alpha$ structure. Based on these similarities and the very high [FeII]/Pa$\beta$ ratios observed in NGC 404, we argue that the [FeII] emission is excited by shocks originating from one or more supernovae that occurred at the center of the [NII]+H$\alpha$ bubble $\sim$5 pc to the west and are now impinging on the central dense gas in the nucleus of NGC 404.

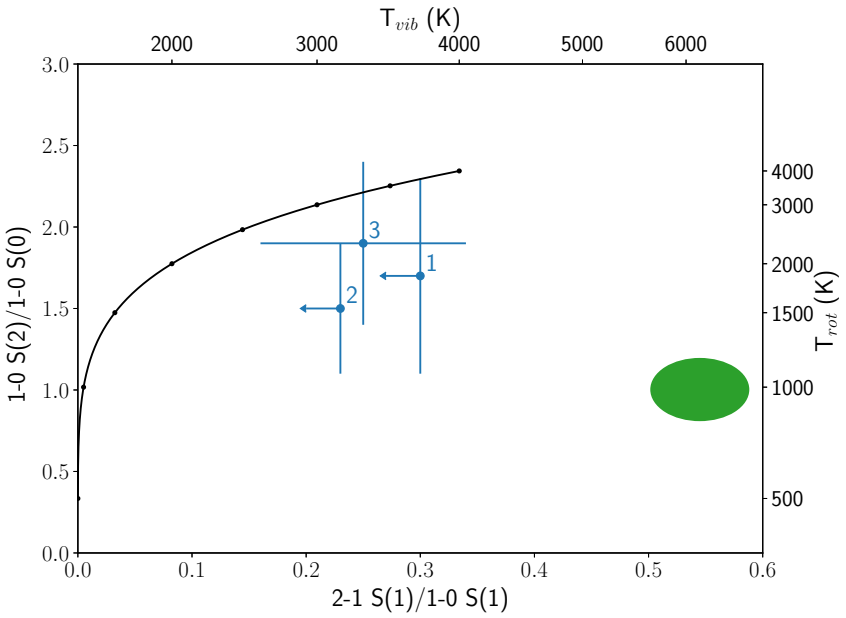


Figure 4.19: 2-1 S(1)/1-0 S(1) versus 1-0 S(2)/1-0 S(0) $H_2$ line ratios for each of the 3 spatial apertures displayed in Fig. 4.11 (Mouri, 1994). The excitation temperatures $T_{rot}$ and $T_{vib}$ calculated from each line ratio are also shown on the top and right axes. The black curve shows the line ratios and temperatures corresponding to thermal excitation ($T_{rot} = T_{vib}$) for gas temperatures ranging 500 to 4000 K, with black points having a spacing of 500 K. The green ellipse covers the range of $H_2$ spectral models from UV fluorescence excitation from Black & van Dishoeck (1987). The line ratios in the three apertures are all consistent with each other and fall near the thermal excitation curve at temperatures of 2000 - 4000 K with a slight shift towards the UV fluorescence models. These results indicate that the $H_2$ gas in NGC 404 is thermally excited with some contribution from UV fluorescence.

Bibliography

Binder, B., Williams, B. F., Eracleous, M., et al. 2011, ApJ, 737, 77

Black, J. H., & van Dishoeck, E. F. 1987, ApJ, 322, 412

Blietz, M., Cameron, M., Drapatz, S., et al. 1994, ApJ, 421, 92

Bouchard, A., Prugniel, P., Koleva, M., & Sharina, M. 2010, A&A, 513, A54

Dale, D. A., Roussel, H., Contursi, A., et al. 2004, ApJ, 601, 813

Dale, D. A., Bendo, G. J., Engelbracht, C. W., et al. 2005, ApJ, 633, 857

Davies, R. I. 2007, MNRAS, 375, 1099

Fernandes, R. C., Delgado, R. M. G., Schmitt, H., et al. 2004, The Astrophysical Journal, 605, 105

Heckman, T. M. 1980, A&A, 87, 152

Hicks, E. K. S., Davies, R. I., Maciejewski, W., et al. 2013, ApJ, 768, 107

Hicks, E. K. S., Davies, R. I., Malkan, M. A., et al. 2009, ApJ, 696, 448

Hicks, E. K. S., Müller-Sánchez, F., Malkan, M. A., & Yu, P.-C. 2016, in IAU Symposium, Vol. 319, Galaxies at High Redshift and Their Evolution Over Cosmic Time, ed. S. Kaviraj, 59–59

Ho, L. C., Filippenko, A. V., & Sargent, W. L. W. 1997a, ApJS, 112, 315

—. 1997b, ApJ, 487, 568

Krabbe, A., Gasaway, T., Song, I., et al. 2004, in Proc. SPIE, Vol. 5492, Ground-based Instrumentation for Astronomy, ed. A. F. M. Moorwood & M. Iye, 1403–1410

Larkin, J., Barczys, M., Krabbe, A., et al. 2006, New A Rev., 50, 362

Larkin, J. E., Armus, L., Knop, R. A., Soifer, B. T., & Matthews, K. 1998, ApJS, 114, 59

Maoz, D., Nagar, N. M., Falcke, H., & Wilson, A. S. 2005, ApJ, 625, 699

Mármol-Queraltó, E., Cardiel, N., Cenarro, A. J., et al. 2008, A&A, 489, 885

Mazzalay, X., Saglia, R. P., Erwin, P., et al. 2013, MNRAS, 428, 2389

Mazzalay, X., Maciejewski, W., Erwin, P., et al. 2014, MNRAS, 438, 2036

Meneses-Goytia, S., Peletier, R. F., Trager, S. C., & Vazdekis, A. 2015, A&A, 582, A97

Mouri, H. 1994, ApJ, 427, 777

Müller Sánchez, F., Davies, R. I., Eisenhauer, F., et al. 2006, A&A, 454, 481

Müller-Sánchez, F., Prieto, M. A., Mezcua, M., et al. 2013, ApJ, 763, L1

Nguyen, D. D., Seth, A. C., den Brok, M., et al. 2017, ApJ, 836, 237

Nyland, K., Marvil, J., Wrobel, J. M., Young, L. M., & Zauderer, B. A. 2012, ApJ, 753, 103

Pogge, R. W., Maoz, D., Ho, L. C., & Eracleous, M. 2000, ApJ, 532, 323

Rayner, J. T., Cushing, M. C., & Vacca, W. D. 2009, ApJS, 185, 289

Reunanen, J., Kotilainen, J. K., & Prieto, M. A. 2002, MNRAS, 331, 154

Riffel, R., Rodríguez-Ardila, A., Aleman, I., et al. 2013, MNRAS, 430, 2002

Riffel, R. A., Storchi-Bergmann, T., & Riffel, R. 2015, MNRAS, 451, 3587

Rodríguez-Ardila, A., Pastoriza, M. G., Viegas, S., Sigut, T. A. A., & Pradhan, A. K. 2004, A&A, 425, 457

Rodríguez-Ardila, A., Riffel, R., & Pastoriza, M. G. 2005, MNRAS, 364, 1041

Seth, A. C., Cappellari, M., Neumayer, N., et al. 2010, ApJ, 714, 713

Stoehr, F., White, R., Smith, M., et al. 2008, in Astronomical Society of the Pacific Conference Series, Vol. 394, Astronomical Data Analysis Software and Systems XVII, ed. R. W. Argyle, P. S. Bunclark, & J. R. Lewis, 505

Storchi-Bergmann, T., McGregor, P. J., Riffel, R. A., et al. 2009, MNRAS, 394, 1148

van Dam, M. A., Bouchez, A. H., Le Mignant, D., et al. 2006, PASP, 118, 310

Wizinowich, P. L., Le Mignant, D., Bouchez, A. H., et al. 2006, PASP, 118, 297

# CHAPTER 5

# A Near-Infrared Integral Field Spectroscopic Survey of Nearby LINERs

## 5.1 Introduction

There is increasing evidence that most, if not all, galactic nuclei host central supermassive black holes (SMBHs; e.g., Magorrian et al., 1998; Kormendy, 2004). These SMBHs exhibit a range of activity, from quasars whose mass accretion generates emission that outshines their host galaxy to the quiescent SMBH in our own Milky Way. The masses of SMBHs span many orders of magnitude and are correlated with properties of their host galaxy, suggesting that the growth of the SMBH and the galaxy are tied together (see Kormendy & Ho, 2013, for a review). Constraining SMBH demographics and activity in the local universe, where the physical conditions of gas and stars can be studied in the greatest detail, is therefore important to understand the evolution of galaxies across cosmic time.

LINER (low ionization nuclear emission line region) galaxies, first defined by Heckman (1980), are the least luminous but most common class of active galactic nucleus (AGN), with $\sim$1/3 of all galaxies within 40 Mpc hosting LINER emission at their centers (Ho et al., 1997b). LINERs are identified by their optical emission line properties using the Baldwin-Philips-Terlevich, or BPT, diagnostic diagram (Baldwin et al., 1981; Veilleux & Osterbrock, 1987). In this parameter space, these active galaxies show high values of line ratios with low ionization species (e.g., [NII]/H$\alpha$) similar to Seyferts, but low values of line ratios from high ionization species ([OIII]/H$\beta$). These optical line ratios can be explained by a number of excitation mechanisms, with two dominate models being photoionization from a weakly accreting SMBH or fast shock excitation (Riffel et al., 2013). Although evidence at other

wavelengths such as X-ray (González-Martín et al., 2006) and radio (Nagar et al., 2005) has revealed the likely presence of a central SMBH in some LINERs, the question still remains whether the LINER emission is always due to a central SMBH or if other physical processes play a more important role. Despite the fact that LINERs are likely a heterogenous class, disentangling the possible excitation mechanisms in LINERs through detailed observations can put constraints on black hole activity in the local or present day universe and help us understand the relative importance of black hole accretion and feedback in relatively normal galaxies.

In addition to their optical line ratios, LINERs and other emission line galaxies also show distinct properties at near-infrared (NIR) wavelengths. NIR spectra of these nuclei in the J (1.1-1.4 $\mu$m) and K bands (2.0-2.4 $\mu$m) often show features from [FeII], $H_2$, and the Pa$\beta$ and Br$\gamma$ hydrogen recombination lines. Larkin et al. (1998) conducted the first infrared survey of nearby LINER galaxies and found that many LINERs were strong emitters of [FeII] and $H_2$ lines and that the ratios of [FeII]/Pa$\beta$ and $H_2$/Br$\gamma$ were good discriminators of LINERs from Seyfert and starburst nuclei. These results were later confirmed in Riffel et al. (2013) using an expanded sample of 67 emission line galaxies presented in that work and in Rodríguez-Ardila et al. (2004, 2005). For the objects with the strongest [FeII] emission in the Larkin et al. (1998), such as NGC 404 discussed in Chapter 4, the ratio of [FeII]/Pa$\beta$ was among the largest seen in extragalactic objects and comparable to shocked regions in supernova remnants. It was hypothesized that the objects with the strongest [FeII] ratios were also shock excited but this requires high shock speeds to destroy dust grains and free the iron.

These NIR measurements, as well as the optical spectroscopic measurements used to define the LINER class, are taken from seeing-limited observations that spatially integrate light across the central $\sim$100 pc of the galaxy. It is not expected, however, that the high values of [FeII]/Pa$\beta$ and $H_2$/Br$\gamma$ are produced by the same parcels of gas, since the shocks or hard X-ray photons required to put enough [FeII] in the gaseous phase (Blietz et al., 1994) would dissociate the $H_2$ gas. NIR integral field spectroscopy (IFS) behind adaptive optics (AO) has the potential to resolve the differences in the [FeII] and $H_2$ emission by taking thousands of spectra simultaneously at spatial scales of a few pc in nearby LINER galaxies.

LINERs have previously been studied using NIR integral field spectroscopy (Mazzalay et al., 2013; Müller-Sánchez et al., 2013, e.g.,), but these studies have focused on characterizing the molecular gas emission and the stellar absorption features in the K band and have not probed the shock-sensitive [FeII] emission line.

We present here initial results from a J and K band survey of 11 nearby LINERs using the OSIRIS integral field spectrograph at the W. M. Keck Observatory with the goal of constraining the excitation mechanisms of NIR emission lines at the highest possible spatial scales. These data measure the emission morphology, kinematics, and physical conditions of the ionized iron and molecular hydrogen gas at 1-10 pc scales. Section 5.2 describe the OSIRIS observations and data reduction. Section 5.3 describes the data analysis methods. Section 5.4 presents the resulting OSIRIS data cubes and nuclear spectra as well as the maps of line emission, velocity, and velocity dispersion for each galaxy in the sample. Finally, section 5.5 discusses the general trends observed in the properties of the LINERs in our sample.

## 5.2 Sample Selection and Observations

The full LINER survey sample is selected from a small subset of optically-classified LINERs that have been previously observed in the NIR. The NIR observations of these LINERs come primarily from Larkin et al. (1998) and Riffel et al. (2013). We also include in our sample 3 LINER galaxies from Mazzalay et al. (2013) that have been observed with the SINFONI integral field spectrograph at the VLT in molecular hydrogen emission, but not in [FeII] emission. That paper reports $H_2$ and Br$\gamma$ (if observed) emission line fluxes, from which we predict [FeII] and Pa$\beta$ line fluxes using the linear correlation of the NIR line ratios and the expected relative strengths of the hydrogen recombination lines given the optical H-$\alpha$/H-$\beta$ ratio (see Larkin et al., 1998). We also require that the nucleus of the LINER galaxy has an r-band magnitude brighter than 17th magnitude within a 1 arcsecond radius, so that it can serve as the tip/tilt star during our laser guide star adaptive optics observations. We obtain a total sample of 11 LINERs with strong [FeII] and $H_2$ emission that we have measured with

OSIRIS (Table 5.1), including NGC 404 that was discussed previously in Chapter 4. The LINERs NGC 4569 and NGC 4826 were also included in the original sample, but have not yet been observed due to poor weather during the spring observing runs. One additional LINER was observed (NGC 660), but its nucleus was too extended to use as the tip/tilt star during observations and so those data are not presented here. Although this sample is small, we believe it represents almost all potential LINERs that are feasible to observe and the sample has a wide range of [FeII]/Pa$\beta$ line ratios, allowing us to probe differences across the LINER class. Table 5.1 summarizes the LINER survey sample, highlighting the range of [FeII]/Pa$\beta$ ratios in these optically classified LINERs (0.3 - 5.3) and the small spatial scales probed using OSIRIS behind AO.

In their optical properties, the galaxies in our sample generally fall in or near the LINER or transition regions of the optical line ratio diagnostic diagrams (Baldwin-Philips-Terlevich, or BPT, diagrams) as defined by Ho et al. (1997a), as shown in Fig. 5.1. Note that those authors identified the transition objects, or objects with [OI] line strengths between those of starburst nuclei and LINERs, as LINERs whose spectra are diluted by neighboring HII regions. As shown in Fig. 5.1, the exact position in the BPT diagram varies among the galaxies in the sample, with some galaxies falling in the starburst region for some of the low-ionization line ratios and others being near the [OIII]/H$\beta$ border dividing the Seyfert nuclei from the LINERs ([OIII]/H$\beta$ = 3.0). There are also 3 luminous infrared galaxies (LIRGs) included in the sample, as noted in Table 5.1.

Table 5.1. LINER Survey Sample

| Galaxy Name | R.A. | Dec. | Distance (Mpc) | Scale (pc/35 mas) | [FeII]/Pa$\beta$ | NIR ref.[a] | Optical ref.[b] | Galaxy Class[c] |
|---|---|---|---|---|---|---|---|---|
| NGC 404 | $01^h09^m27.0^s$ | $+35^h43^m05.3^s$ | 3.1 | 0.5 | 2.7 | (1) | (1) | L2 |
| NGC 1204 | $03^h04^m39.9^s$ | $-12^h20^m29.0^s$ | 61 | 10.4 | 0.4 | (4) | (4) | S2/H(LIRG) |
| NGC 1614 | $04^h33^m59.9^s$ | $-08^h34^m44.0^s$ | 64 | 10.9 | 0.3 | (2) | (3) | H(LIRG) |
| NGC 3627 | $11^h20^m15.0^s$ | $+12^h59^m29.5^s$ | 9.7 | 1.6 | 1.1 | (3) | (1) | T2/S2 |
| NGC 3998 | $11^h57^m56.1^s$ | $+55^h27^m12.9^s$ | 20 | 3.4 | 0.6 | (1) | (1) | L1.9 |
| NGC 4579 | $12^h37^m43.5^s$ | $+11^h49^m05.5^s$ | 19 | 3.3 | 2.2 | (3) | (1) | S1.9/L1.9 |
| NGC 4736 | $12^h50^m53.1^s$ | $+41^h07^m13.7^s$ | 5.2 | 0.9 | 5.3 | (1) | (2) | L2 |
| NGC 5953 | $15^h34^m32.4^s$ | $+15^h11^m37.6^s$ | 27 | 4.6 | 3.5 | (2) | (2) | S2/T2 |
| NGC 7217 | $22^h07^m52.4^s$ | $+31^h21^m33.7^s$ | 19 | 3.3 | 2.3 | (1) | (1) | L2 |
| NGC 7465 | $23^h02^m01.0^s$ | $+15^h57^m53.2^s$ | 27 | 4.6 | 1.2 | (4) | (2) | T2 |
| NGC 7591 | $23^h18^m16.3^s$ | $+06^h35^m08.9^s$ | 64 | 10.8 | 0.7 | (4) | (3) | T2(LIRG) |

[a]NIR references: (1) Larkin et al. (1998); (2) Rodríguez-Ardila et al. (2005); (3) Mazzalay et al. (2013); (4) Riffel et al. (2013).

[b]Optical references: (1) Ho et al. (1997a); (2) Moustakas & Kennicutt (2006); (3) Kim et al. (1995); (4) Corbett et al. (2003).

[c]The classifications listed here are: H = HII nucleus (or starburst galaxy), S = Seyfert nucleus, L = LINER nucleus, T = transition object, as defined by Ho et al. (1997a). If the galaxy is in the Ho et al. (1997a) sample, then the nuclear classification from that work is given here. Otherwise, the AGN class is determined using the critera outlined in Sec. 3 of Ho et al. (1997a) and the line ratios from the optical reference listed in column 8. If more than one classification is consistent with the line ratio measurements then all are listed, with the first entry being the more likely classification. The number 1.9 or 2 indicates the type of the nucleus (1.9 for broad H$\alpha$ and no broad H$\beta$ detected and 2 for only narrow lines detected; e.g., Osterbrock, 1981). It is also noted here if the galaxy is a luminous infrared galaxy (LIRG).

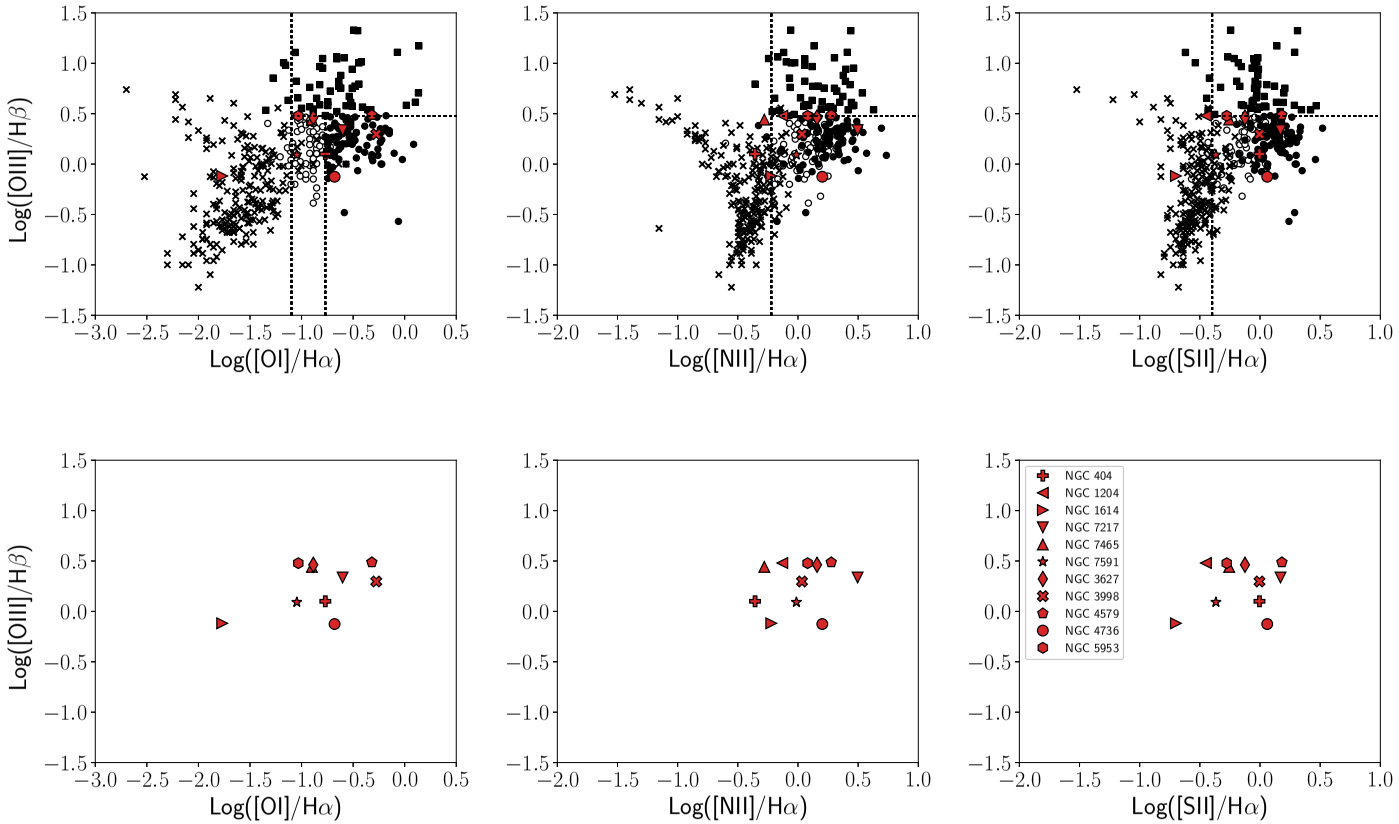


Figure 5.1: Optical diagnostic plots from Ho et al. (1997a) to classify different types of emission line galaxies and optical properties of the LINER survey sample observed with OSIRIS. The black dotted lines in the top row of panels show the line ratios used to classify the galaxies in that paper. Each class of galactic nucleus is shown in black with a different marker shape: starburst (crosses), Seyfert (filled square), transition objects (open circles), and LINERs (filled circles). Note that Ho et al. (1997a) considered transition objects, those with [OI] line strengths between those of starburst nuclei and LINERs, as LINERs whose spectra were diluted by neighboring HII regions. The sample of LINER galaxies observed in this survey are plotted as red circles. The optical emission line ratios for the LINER sample come from the references listed in Table 5.1.

Observations for this survey were carried out between October 2015 and October 2016. Each LINER was observed with the OSIRIS integral field spectrograph on the Keck I telescope (Larkin et al., 2006). This instrument is coupled to the Keck Adaptive Optics (AO) system (Wizinowich et al., 2006; van Dam et al., 2006) and uses an array of small lenses to sample the AO image, producing up to ∼3000 spectra simultaneously across a rectangular, contiguous field of view. Each LINER was observed in both the J band and the K band at the 35 mas plate scale. Depending on the redshift of the galaxy, either a narrowband J filter (Jn2; $\lambda$ = 1.228 - 1.289 $\mu$m) or the broadband J filter (Jbb; $\lambda$ = 1.180 - 1.416 $\mu$m) was used to cover the [FeII] ($\lambda_0$ = 1.2567 $\mu$m) and the Pa$\beta$ ($\lambda_0$ = 1.28216 $\mu$m) spectral lines simultaneously. The broadband K filter (Kbb; $\lambda$ = 1.965 - 2.381 $\mu$m) was used for all galaxies to cover multiple $H_2$ lines (e.g., the 1-0 S(1) transition at $\lambda_0$ = 2.1218 $\mu$m), Br$\gamma$ ($\lambda_0$ = 2.16612 $\mu$m), and stellar absorption features such as the CO bandheads ($\lambda$0 = 2.29 $\mu$m). In January 2016, the detector in the OSIRIS spectrograph was upgraded from the original Rockwell Hawaii-2 to a Teledyne Hawaii-2RG (H2RG), improving the raw throughput of the instrument by a factor of ∼1.6 in K band to ∼2 in J band (Boehle et al., 2016). Data taken after April 2016 were observed with this new detector, or just over half of the total LINER survey data set.

Each LINER was generally observed between 0.5 and 1.25 hours in each filter (see Table 5.2 for details), with each individual frame having an integration time of 900 sec. The field of view of each individual frame is 1.47 by 2.24 arcsec for the Jn2 filter and 0.56 by 2.24 arcsec for both the Kbb and Jbb filters and all galaxies were observed with a PA of 0°. Each galaxy was dithered by ∼1 arcsec within the filter's field of view to allow neighboring frames to be used in sky subtraction. The resulting mosaicked fields of view are given in Table 5.2. In addition to dithered frames on the galaxy, one sky frame offset by 3-7 arcsec from the galaxy nucleus was taken in each filter. All data were taken using Keck laser guide star AO system, with the nucleus of the galaxy serving as the tip/tilt reference source.

In addition to the on-source and pure sky frames, telluric standard stars were observed at similar airmasses to the LINER galaxies to correct for atmospheric absorption features in the galaxy spectrum. In general, both an A0 star and a G2 star were observed for each galaxy. Each stellar spectrum is extracted from the sky-subtracted and mosaicked data cube

and then divided by a blackbody to remove the stellar continuum. The A0 star spectrum is then used for the majority of the telluric correction, with the exception of the region around the strong hydrogen absorption from Pa$\beta$ (1.27 - 1.289 $\mu$m) and Br$\gamma$ (2.156 - 2.177 $\mu$m). For these wavelength regions, the G2 star spectrum is used after being divided by a solar spectrum convolved to the OSIRIS spectral resolution. The solar spectrum used to correct the G2 star was created by ESO using National Solar Observatory/Kitt Peak Fourier Transform Spectrograph data produced by NSF/NOAO. Before the division is performed, the solar spectrum is shifted to the RV of the G2 star and the hydrogen absorption feature is scaled to match the width of the G2 line. For dates in which no G star was observed, the region of hydrogen absorption is instead replaced by an interpolation based on a linear fit to the wavelength region just outside the absorption line.

Data are reduced using Version 3.2 (2015 data; original detector) or Version 4.0 (2016 data; upgraded detector) of the OSIRIS Data Reduction Pipeline (DRP; Krabbe et al., 2004). Version 4.0 of the DRP includes updates to make the pipeline compatible with the new H2RG detector installed in January 2016 (Boehle et al., 2016). Each individual science frame is sky subtracted by a pure sky frame and, where possible, a dithered science frame. The sky subtraction is performed both by a straight subtraction of the science and sky frames and by using the scaled sky DRP routine based on the algorithm developed by R. Davies (Davies, 2007). All sky subtractions for each individual frame are compared and the frame with the least OH sky line residuals is used in the final mosaic. The sky-subtracted science frames in each filter are mosaicked together to produce the final data cube for each galaxy. The resulting data cubes have wavelength sampling of 0.00015 $\mu$m in the Jn2 and Jbb bands and 0.00025 $\mu$m in the Kbb band. Finally, the telluric spectra produced from all nights in the observing run are compared to the galaxy spectrum extracted from the mosaicked data cube. The telluric spectrum that best matches the deepest atmospheric absorption features in the science data is then used to divide out the telluric features in each spectrum of the data cube. The telluric features are generally well-corrected, with the exception of the deep atmospheric absorption in the red end of the Jbb band ($>$ 1.33 $\mu$m). This wavelength region of the Jbb spectrum does not contain the [FeII] or the Pa$\beta$ spectral lines for the redshifts of

Table 5.2. Observations of LINERs Using OSIRIS

| Galaxy Name | Filter | Observation Date | # of Frames | Integration Time (hours) | FOV of Mosaic (arcsec) | Telluric Stars A | Telluric Stars G |
|---|---|---|---|---|---|---|---|
| NGC 1204 | Jbb | 09 Oct 2015 | 3 | 0.75 | $0.67 \times 2.21$ | HD 210501 | – |
| | Kbb | 09 Oct 2015 | 3 | 0.75 | $0.67 \times 2.24$ | HD 210501 | – |
| NGC 1614 | Jbb | 19 Oct 2016 | 5 | 1.25 | $1.65 \times 3.71$ | HD 45137 | HD 33093 |
| | Kbb | 8, 9 Oct 2015 | 7 | 1.75 | $1.65 \times 3.92$ | HD 25792 | HD 31867 |
| NGC 3627 | Jn2 | 21 Apr 2016 | 4 | 1.00 | $1.58 \times 3.29$ | HD 107655 | HD 112257 |
| | Kbb | 21 Apr 2016 | 4 | 1.00 | $0.77 \times 3.22$ | HD 107655 | HD 112257 |
| NGC 3998 | Jn2 | 22 Apr 2016 | 5 | 1.25 | $1.68 \times 3.43$ | HD 118214 | HD 117845 |
| | Kbb | 22 Apr 2016 | 4 | 1.00 | $0.88 \times 3.26$ | HD 118214 | HD 117845 |
| NGC 4579 | Jbb | 21 Apr 2016 | 5 | 1.25 | $0.77 \times 3.22$ | HD 121880 | HD 124019 |
| | Kbb | 21 Apr 2016 | 3 | 0.75 | $0.88 \times 3.26$ | HD 121880 | HD 124019 |
| NGC 4736 | Jn2 | 18 Apr 2016 | 5 | 1.25 | $1.72 \times 3.29$ | HD 118214 | HD 117845 |
| | Kbb | 22 Apr 2016 | 4 | 1.00 | $0.74 \times 3.22$ | HD 107655 | HD 112257 |
| NGC 5953 | Jbb | 22 Apr 2016 | 2 | 0.50 | $0.67 \times 1.75$ | HD 118214 | HD 117845 |
| | Kbb | 22 Apr 2016 | 4 | 1.00 | $0.67 \times 2.24$ | HD 107655 | HD 112257 |
| NGC 7217 | Jn2 | 08 Oct 2015 | 3 | 0.75 | $1.61 \times 2.31$ | HD 217186 | HD 217577 |
| | Kbb | 08 Oct 2015 | 3 | 0.75 | $0.63 \times 2.24$ | HD 217186 | HD 217577 |
| NGC 7465 | Jbb | 19 Oct 2016 | 5 | 1.25 | $0.74 \times 3.22$ | HD 45137 | HD 33093 |
| | Kbb | 19 Oct 2016 | 5 | 1.25 | $0.74 \times 3.22$ | HD 45137 | HD 33093 |
| NGC 7591 | Jbb | 09 Oct 2015 | 4 | 1.00 | $0.67 \times 2.38$ | HD 210501 | – |
| | Kbb | 09 Oct 2015 | 4 | 1.00 | $0.67 \times 2.24$ | HD 210501 | – |

any galaxies in our sample, and so it is not shown in subsequent figures.

## 5.3 Data Analysis

### 5.3.1 Extraction of Nuclear Spectra

A representative nuclear spectrum is extracted from each galaxy's J and K band data cubes to determine which lines are detected in the source and the average systemic velocity of the galaxy and the overall width of the emission lines. This information is then used to tune subsequent analyses to each galaxy in the sample. By default, the nuclear spectrum is extracted from a circular aperture centered on the peak of the continuum emission in each band. There is one galaxy in which the majority of the galaxy's line emission is seen off of the galactic nucleus (NGC 1614), and so a region 0.25 arcsec to the east of the continuum

center is used as the center of the extraction aperture in that case. Each extraction aperture has a radius of 6 spatial pixels (spaxels) or 0.21 arcsec, corresponding to a physical scale of 3 - 65 pc depending on the distance of the galaxy.

In each nuclear spectrum, the S/N of the [FeII], Pa$\beta$, 1-0 S(1) $H_2$, and Br$\gamma$ emission lines is determined to identify the detected emission lines. A nominal systemic velocity for the galaxy is taken from NED[1], which is then updated using measurements from the nuclear spectrum itself. In the S/N calculation, the signal is a sum of the continuum-subtracted counts in each wavelength channel within $\pm$125 km $s^{-1}$ of the emission line, with the continuum being the average of counts in the wavelength channels from -750 to -600 km $s^{-1}$ and from +600 to +750 km $s^{-1}$. The noise is estimated by taking the standard deviation of 10 wavelength channels on either side of the line, starting at $\pm$450 km $s^{-1}$ and moving outward. Every fifth wavelength channel is used for the noise estimate to avoid the correlated noise present in adjacent wavelength channels. These continuum and noise velocity ranges are chosen to be well outside the width of any emission line in the nuclear spectra, while the signal range is chosen to avoid wavelength channels falling outside even the narrow emission lines. All lines with a S/N above 50 are fit with a Gaussian using the wavelength channels $\pm$0.01 $\mu$m around the emission line. A DC offset parameter is included in this fit to account for the continuum emission. The measured velocity shift of each detected line relative to the vacuum wavelength is then averaged to find the systemic velocity of the galactic nucleus. If no lines above the S/N threshold are detected, then the nominal systemic velocity from NED is adopted for this source. This case only applies to one galaxy in the sample (NGC 4736). All subsequent measurements are made assuming these systemic velocities of the galaxies.

### 5.3.2 Line S/N Maps

A line S/N map is created for the [FeII], Pa$\beta$, 1-0 S(1) $H_2$, and Br$\gamma$ emission lines in each galaxy. The goal of these line S/N maps is to identify spatial regions in which velocity information can be extracted from each emission line, which is later used to display the

[1]The NASA/IPAC Extragalactic Database (NED) is operated by the Jet Propulsion Laboratory, California Institute of Technology, under contract with the National Aeronautics and Space Administration.

maps of the line velocity (derived in Sec. 5.3.3) and to make the maps of the line emission (Sec. 5.3.4). To construct the line S/N maps, the line signal and noise measurements described in Sec. 5.3.1 are applied to each emission line in every spaxel. The same velocity ranges for the signal, noise, and continuum estimations are used for these spaxel by spaxel measurements for the majority of galaxies, with these velocities now being relative to the systemic velocity determined in Sec. 5.3.1. A subset of sample galaxies is identified as having large velocity dispersions (with visible line wings out to $\pm$1000 km s$^{-1}$) and in some of their emission lines based on their nuclear spectra: NGC 3998 ([FeII] and Pa$\beta$ lines), NGC 4579 (Pa$\beta$), and NGC 7465 (Pa$\beta$, Br$\gamma$). For these galaxies, the continuum velocity ranges are changed to $-1650$ to $-1500$ km s$^{-1}$ and from $+1500$ to $+1650$ km s$^{-1}$, to avoid using wavelength channels containing the broad line emission in the continuum calculation. The noise estimate is also changed accordingly to start at $\pm$1500 km s$^{-1}$ and move outward. For a consistent comparison among all galaxies, the same signal velocity range of $\pm$125 km s$^{-1}$ is used for both the broad and narrow line sources.

The resulting signal and noise maps for every emission line are quite noisy, so they are then smoothed by a 2-dimensional gaussian with sigma of 3.5 pixels in both the x and y directions. This smoothing is performed so that a minimum line S/N threshold (defined in Sec. 5.3.4) will identify a contiguous spatial region for use in displaying the velocity maps and constructing the line maps. The spatial smoothing is implemented using the `gaussian_filter` function in the `ndimage` module of the SciPy library, a scientific computing library for the Python programming language. The final line S/N map is then computed by taking the ratio of the smoothed signal and noise maps.

### 5.3.3 Emission Line Kinematics

The kinematics of the [FeII], Pa$\beta$, 1-0 S(1) $H_2$, and Br$\gamma$ emission lines are measured using a Gaussian fit to the line profiles. This fit is performed for every spaxel in the J and K band mosaicked data cubes and for each of the 4 emission lines. The Gaussian fits also include a DC offset to account for the continuum emission around each line. For the

narrow emission lines, the Gaussian fits are performed in a wavelength range $\pm 0.0075$ $\mu$m around the wavelength of the emission line shifted to the systemic velocity of the galaxy, corresponding to approximately $\pm 1800$ km s$^{-1}$ in the J band and $\pm 1100$ km s$^{-1}$ in the K band. This wavelength range is expanded to $\pm 0.0125$ $\mu$m for the broad emission lines listed in Sec. 5.3.2 so that some continuum emission is covered by the fitting range. This wider range corresponds to $\pm 3000$ km s$^{-1}$ in the J band and $\pm 1800$ km s$^{-1}$ in the K band. The central wavelength and the sigma of the best fit Gaussian are converted to the velocity and velocity dispersion respectively. The OSIRIS instrumental dispersion determined from the analysis of NGC 404 (Chapter 4; 50 km s$^{-1}$ in J band and 35 km s$^{-1}$ in K band) is then subtracted in quadrature from the measured velocity dispersion to find the intrinsic width of the emission lines.

### 5.3.4 Emission Line Maps

A spatial map of the emission line flux for the [FeII], Pa$\beta$, 1-0 S(1) $H_2$, and Br$\gamma$ lines is created for every galaxy to compare the morphology of the emission. The line flux maps are computed by summing of the continuum-subtracted counts in 7 wavelength channels centered on the wavelength of the emission line. This 7 channel width corresponds to a velocity range of $\pm 100$ km s$^{-1}$ in both the J and K bands.

For spaxels with a high enough line S/N as measured in Sec. 5.3.2, the velocity shift measured from the Gaussian fit to the emission line detailed in Sec. 5.3.3 is used to determine the wavelength of the emission line and thereby the center of the 7 channel range over which the line flux is summed. The S/N threshold is set to 10.0 by default. This S/N cut generally does a good job excluding spatial regions in which line flux is low and therefore the velocity fits produce only noise, but there are some lines in which velocity information is found in spaxels below the default threshold. In these cases a custom S/N threshold is set: S/N $> 3.0$ for the Pa$\beta$ and Br$\gamma$ in NGC 3627 and for $H_2$ in NGC 3998, S/N $> 7.0$ for [FeII] in NGC 4736, and S/N $> 5.0$ for [FeII], Pa$\beta$, and $H_2$ in NGC 5953. For the remaining spaxels with a line S/N below the threshold, the emission line wavelength is determined by the systemic

velocity of the galaxy measured in its nuclear spectrum (Sec. 5.3.1).

The continuum around the line is estimated by taking the average of the wavelength channels from $-600$ to $-450$ km s$^{-1}$ and from $+450$ to $+600$ km s$^{-1}$ relative to the measured velocity shift of the emission line (for spaxels with a line S/N above the threshold) or the systemic velocity of the galaxy (for spaxels with a line S/N below the threshold). This range is expanded to $-1500$ to $-1350$ km s$^{-1}$ and $+1350$ to $+1500$ km s$^{-1}$ for the broad emission lines seen in a subset of the galaxies. Note that these continuum velocity ranges are different from the velocity ranges used for the S/N measurements described in Sec. 5.3.1 and 5.3.2, which were relative to the global systemic velocity of the galaxy for all spaxels.

### 5.3.5 Line Ratio Fits in Nuclear Spectra

The line ratios of [FeII]/Pa$\beta$ and 1-0 S(1) $H_2$/Br$\gamma$ are estimated for the J/K band nuclear spectra of each galaxy from Sec. 5.3.1. The flux of each emission line is taken as the sum of continuum-subtracted wavelength channels around the wavelength of the emission line shifted to the systemic velocity of the galaxy. The default velocity range of the line flux channels is set to $\pm300$ km s$^{-1}$. This range is expanded to $\pm1500$ km s$^{-1}$ for the galaxies that show visibly broad emission lines in their nuclear spectra. The same line flux velocity range is used for each of the 4 emission lines. The continuum around each line is estimated by taking the average of wavelength channels in the same velocity ranges as used in Sec. 5.3.2 to estimate the line S/N: $-750$ to $-600$ km s$^{-1}$ and from $+600$ to $+750$ km s$^{-1}$ for the galaxies without broad lines and $-1650$ to $-1500$ km s$^{-1}$ and $+1500$ to $+1650$ km s$^{-1}$ for the galaxies with broad lines. The noise around the line is simultaneously calculated by taking the standard deviation of the same noise channels used in Sec. 5.3.2. The line flux S/N is then taken as the line flux divided by this noise value. For line fluxes with a S/N $< 15$, an upper limit for the line flux is estimated. A conservative 3-$\sigma$ upper limit is calculated by taking the flux from a Gaussian emission line with a peak of 3 times the noise estimate and a velocity dispersion of 250 km s$^{-1}$ for the galaxies with only narrow emission lines and 500 km s$^{-1}$ for the galaxies with broad emission lines. The limiting line flux is then computed

by sampling the Gaussian at wavelength channels within the velocity range used for the line flux estimate.

## 5.4 Results

This section shows the resulting mosaicked data cubes and nuclear spectra in the J/K bands for each galaxy, as well as the line emission, velocity, and velocity dispersion maps derived for the [FeII], 1-0 S(1) $H_2$, Pa$\beta$, and Br$\gamma$ emission lines. Sec. 5.4.1 presents the overall properties of these analysis products for the whole LINER sample and Sec. 5.4.2 describes the results for each individual galaxy.

### 5.4.1 Overall Properties of Sample

The final OSIRIS mosaicked data cubes for each galaxy are displayed in Fig. 5.2 for both the J and K band. These maps are median collapses of the data cubes along the wavelength direction and thus primarily show the spatial structure of the continuum emission in each band. We find that all galaxies in our sample have continuum emission that is dominated by a compact core. This is likely in part due to our original sample selection, which requires a galaxy to have an optical r-band magnitude of at most 17 in the central 1 arcsec for the purposes of using the nucleus as the tip/tilt star in the AO observations. There are also some galaxies that show spatially extended continuum emission. For example, the compact core of the continuum emission in NGC 1204 and NGC 7591 is elongated to the northeast/southwest and northwest/southeast respectively. NGC 7591 also has an additional arm of continuum emission to the north of the compact core, most visible in J band. NGC 3627 also has diffuse continuum emission to the south and west in both J and K bands, in addition to the compact core of emission.

The nuclear spectra extracted from the region around the continuum centers are shown in Fig. 5.3. For NGC 1614, the region shown is offset to the east from the center by 0.25 arc, since most line emission in this source is off of the nucleus. These are the spectra used to determine the systemic velocity of the galaxies, which are presented in Table 5.3. The nuclear

Table 5.3. Systemic Velocities of LINER Sample

| Galaxy Name | $V_{sys}$ (km s$^{-1}$) | Emission Lines Used |
|---|---|---|
| NGC 1204 | 4534 | [FeII], Pa$\beta$, $H_2$, Br$\gamma$ |
| NGC 1614 | 4748 | [FeII], Pa$\beta$, Br$\gamma$ |
| NGC 3627 | 820 | [FeII], Pa$\beta$, $H_2$ |
| NGC 3998 | 1080 | [FeII] |
| NGC 4579 | 1544 | [FeII], $H_2$ |
| NGC 4736 | 308 | |
| NGC 5953 | 2057 | [FeII], $H_2$ |
| NGC 7217 | 1012 | [FeII], $H_2$ |
| NGC 7465 | 1985 | [FeII], Pa$\beta$, $H_2$ |
| NGC 7591 | 4964 | [FeII], Pa$\beta$, $H_2$, Br$\gamma$ |

spectra show that at least two of the targeted emission lines of [FeII], 1-0 S(1) $H_2$, Pa$\beta$, and Br$\gamma$ are detected in all the sources. 6 out of 10 of the K-band spectra also show multiple $H_2$ lines in addition to the strong 1-0 S(1) transition: NGC 1204, 3627, 4579, 5953, 7217, and 7591. The CO bandhead stellar absorption features are also detected in all K-band spectra. We find a large variation in the relative line strengths in the galaxies in our sample, with some galaxies showing strong [FeII] and/or 1-0 S(1) $H_2$ emission compared to the Pa$\beta$/Br$\gamma$ recombination lines and others showing the opposite. This variation is quantified by the [FeII]/Pa$\beta$ and 1-0 S(1) $H_2$/Br$\gamma$ line ratios measured from the nuclear spectra, which are presented in Table 5.4. As mentioned in Sec. 5.3 and discussed further in Sec. 5.4.2 and 5.5.2, broad line emission is detected in three of the nuclear spectra: NGC 3998 ([FeII] and Pa$\beta$ lines), NGC 4579 (Pa$\beta$), and NGC 7465 (Pa$\beta$, Br$\gamma$).

The emission line maps displayed in Fig. 5.4 show the spatial extent and morphology of the [FeII], 1-0 S(1) $H_2$, Pa$\beta$, and Br$\gamma$ emission lines in each galaxy. For lines with a high enough S/N, the velocity and velocity dispersion information in also displayed. Based on the line maps, we find that [FeII] and 1-0 S(1) $H_2$ emission is detected in all 10 galaxies in the sample. 8 out of 10 galaxies also show Pa$\beta$ emission in the line maps, sometimes accompanied by Br$\gamma$ emission. Only one galaxy, NGC 4736, shows strong Pa$\beta$ absorption. The emission line maps show many examples of spatially extended or off-nuclear emission, with all galaxies having at least 1 line that is extended beyond the compact continuum core. The morphology of the emission lines also often varies between the [FeII], $H_2$, and/or

Table 5.4. [FeII]/Pa$\beta$ and 1-0 S(1)/Br$\gamma$ Line Ratio Measurements in Nuclear Spectra of LINERs

| Galaxy Name | [FeII]/ Pa$\beta$ | 1-0 S(1) $H_2$/ Br$\gamma$ |
|---|---|---|
| NGC 1204 | 0.4 | 0.6 |
| NGC 1614 | 0.3 | $< 1.9$ |
| NGC 3627 | 4.7 | 1.5 |
| NGC 3998 | 2.9 | 0.6 |
| NGC 4579 | 2.3 | $> 1.2$ |
| NGC 5953 | $> 1.8$ | $> 1.2$ |
| NGC 7217 | $> 2.5$ | $> 6.8$ |
| NGC 7465 | 0.4 | 0.6 |
| NGC 7591 | 0.7 | 0.9 |

Note. — Line ratios measurements for NGC 4736 are not reported due to the presence of Pa$\beta$/Br$\gamma$ absorption in its nuclear spectra.

hydrogen recombination emission lines.

The kinematic structures traced by the emission lines typically have velocity gradients consistent with rotational motion. All galaxies have at least one emission line showing rotation, with the exception of NGC 4736. These gradients range from $\pm$30 to $\pm$300 km s$^{-1}$ within the fields of view of the mosaicked OSIRIS frames. For galaxies in which multiple lines have high enough S/N for velocity measurements, we find that different emission lines often show different kinematics. For example, there are 3 galaxies in which the [FeII] shows higher velocity gradients than the other detected emission lines (NGC 1614, 3627, and 7465). The dispersion of the emission lines can also vary with spatial location. This spatial variation is especially clear in some of the broad emission lines, which show dispersions peaking at the continuum centers of the galaxies with values of up 650 km s$^{-1}$ (e.g., NGC 3998 and NGC 7465). Other regions of higher dispersion correspond to regions of high velocity (e.g., [FeII] in NGC 3627 and NGC 5953), large velocity gradients (e.g., $H_2$ in 4579), or enhanced line emission (NGC 7465).

### 5.4.2 Individual Objects

#### 5.4.2.1 NGC 1204

The continuum emission of NGC 1204 is elongated in the northeast and southwest directions, spanning a distance of 50 pc at the distance of this galaxy (Fig. 5.2a). The nuclear spectrum of this source contains emission lines from [FeII], 1-0 S(1) $H_2$, Pa$\beta$, and Br$\gamma$, as well as at least 2 additional $H_2$ lines and the CO stellar absorption features (Fig. 5.3a). The line emission from $H_2$, Pa$\beta$, and Br$\gamma$ is spatially extended across the central 200 pc of the galaxy (Fig. 5.4a). Velocities of these lines show signs of rotational motion, with the velocity gradient oriented along the major axis of the continuum and line emission. The [FeII] emission shows signs of a higher velocity to the northeast of the continuum center compared to the $H_2$ and hydrogen recombination emission, but the velocity measurements for this line are also more noisy than the other lines and so its velocity cannot be mapped over the same spatial area. The velocity dispersions of the lines, especially Pa$\beta$ and Br$\gamma$, show increasing values near the continuum center. This is most clear in the Br$\gamma$ map, which has dispersion values rising from 50 km $s^{-1}$ to 100 km $s^{-1}$ in the center. The $H_2$ gas has a slightly lower dispersion of 80 km $s^{-1}$ at the continuum center.

#### 5.4.2.2 NGC 1614

The J and K band continuum emission in NGC 1614 is very compact (Fig. 5.2a) and its nuclear spectra show weak [FeII] and $H_2$ and strong Pa$\beta$/Br$\gamma$ emission as well as CO stellar absorption (Fig. 5.3a). Although its continuum emission is compact, the line emission in NGC 1614 is primarily found in a ring that starts 50 -100 pc beyond the continuum center (Fig. 5.4b). The ring of line emission is strongest in the hydrogen recombination lines and shows significant substructure, including many knots of emission. In [FeII], Pa$\beta$, and Br$\gamma$ the strongest knot of emission is seen to the east of the nucleus. Although $H_2$ also emits in the same location as this strong emission knot, the strongest $H_2$ emission is instead found to the west of the nucleus. There are additionally some substructures particularly to the west that are visible in the Pa$\beta$ and Br$\gamma$ but do not have corresponding peaks of [FeII] emission,

indicating possible spatial changes in the [FeII]/Pa$\beta$ line ratio.

The velocity maps of all 4 lines show a dominant rotational motion across the central ∼700 pc of the galaxy. The [FeII], Pa$\beta$, and Br$\gamma$ velocity maps also have an S-shaped distortion to the east and west of the continuum center. In these velocity maps, the Although the overall velocity structure of the [FeII] and the hydrogen recombination lines are very similar, the actual velocity of the [FeII] line is higher (redshifted) at all measured spatial locations by ∼80 km s$^{-1}$. The velocity dispersion maps show significant variation across the field of view, with the dispersions in the [FeII] and Pa$\beta$/Br$\gamma$ lines ranging from 20 to 150 km s$^{-1}$. Regions of high dispersions sometimes line up with the fine structures seen in the velocity maps (e.g., the region of highest dispersion to the northwest of the nucleus) or the peaks of line emission (e.g., the region to the south and slightly east). The [FeII] velocity dispersion is also generally higher than the Pa$\beta$/Br$\gamma$ dispersion by about 25 km s$^{-1}$.

#### 5.4.2.3 NGC 3627

The continuum emission of NGC 3627 has a compact component and a diffuse extended component to the south and west of the compact core (Fig. 5.2a). All 4 emission lines are detected in its nuclear spectrum, with the [FeII] and $H_2$ being brighter than the Pa$\beta$ and Br$\gamma$ lines (Fig. 5.3a). Additional $H_2$ lines and the CO bandhead stellar absorption features are also detected. The line emission shows spatial extension in all 4 lines, especially in $H_2$, which shows diffuse emission that covers nearly the full Kbb mosaicked field of view (∼25 by 125 pc; Fig. 5.4c). The velocity maps show motion dominated by rotation, with additional regions in the $H_2$ and Pa$\beta$ maps of blue shifted emission to the south and slightly east of the continuum center. The [FeII] velocity map shows a similar gradient to the other lines but is generally found at a higher velocity, especially to the south and southeast of the continuum center.

Some interesting structures are visible that stand out in their line emission, velocity, and dispersion properties. The [FeII] line map has a knot of bright emission 25 pc to the west and 10 pc to the south of the continuum center that is not matched in the Pa$\beta$

emission, indicating a likely increase in the [FeII]/Pa$\beta$ line ratio. This region also has an increased [FeII] velocity dispersion of 90 km s$^{-1}$ compared to a typical dispersion of 75 km s$^{-1}$. Additionally, the southeast region of increased [FeII] velocity also has a similar increase in velocity dispersion. The Pa$\beta$ and Br$\gamma$ maps both show a clump of emission to the northeast of the continuum center where there is only faint [FeII] emission, indicating a possible decrease of the [FeII]/Pa$\beta$ ratio. The velocity dispersion of the $H_2$ gas also varies, with the central more compact emission having a lower dispersion of 55 km s$^{-1}$ and the surrounding diffuse emission having an increased dispersion of 80 km s$^{-1}$. Finally, the dispersions of the hydrogen recombination lines are generally lower than the [FeII] and $H_2$ lines: these lines are unresolved at the edges of the dispersion map field of view and increase slightly towards the continuum center to values of 60-70 km s$^{-1}$.

#### 5.4.2.4 NGC 3998

NGC 3998 has a compact core in the J and K band emission (Fig. 5.2b) and shows line map detections in all 4 emission lines. The nuclear spectrum of NGC 3998 includes detections of broad emission from [FeII], Pa$\beta$, and Br$\gamma$ with visible line wings spanning $\pm$1000 km s$^{-1}$, as well as detections of the CO bandheads (Fig. 5.3a). The emission from these 3 lines is seen primarily at the continuum center with some additional spatially extended emission (Fig. 5.4d). There is a compact peak of emission seen in [FeII] and Pa$\beta$ to the south and slightly west of the continuum center. The corresponding spaxels in the velocity and dispersion maps show a blue shift in the [FeII] velocity and a slightly enhanced dispersion. The $H_2$ emission has a different morphology from the rest of the lines, with emission primarily in a region $\sim$20 pc to the east of the nucleus as well as diffuse, extended emission around the continuum center.

The [FeII] and Pa$\beta$ velocity maps both have indications of rotational motion and show similar velocity structures that are significantly offset from each other. The [FeII] emission spans $\pm$125 km s$^{-1}$ around the systemic velocity, which is defined only by the velocity shift of the [FeII] line in NGC 3998's nuclear spectrum (see Sec. 5.3.1 and Table 5.3). Pa$\beta$ spans

a larger range of velocities from -30 to -380 km $s^{-1}$ and is blue shifted with respect to [FeII] emission at each spaxel. The dispersions of both the Pa$\beta$ and [FeII] lines peak at the continuum center, with Pa$\beta$ having a larger dispersion ($\sim$700 km $s^{-1}$) compared to [FeII] ($\sim$450 km $s^{-1}$). The $H_2$ emission to the east of the nucleus is blue shifted with respect to the systemic velocity and matches the velocity of the [FeII] in that region. The dispersion of $H_2$ is generally much lower than the [FeII] and Pa$\beta$ lines, ranging from 70 - 90 km $s^{-1}$.

#### 5.4.2.5 NGC 4579

The continuum emission in NGC 4579 is compact (Fig. 5.2b) and its nuclear spectra show strong detections of [FeII] and $H_2$ with some fainter and broader emission from Pa$\beta$ (Fig. 5.3b). The telluric correction is not ideal in this source, but the Kbb spectrum still has signs of the CO bandhead absorption features and multiple $H_2$ lines. The emission line maps show extended emission in [FeII] and $H_2$ with very different morphologies (Fig. 5.4e). The [FeII] is brightest at the continuum center and also has extended emission to the south of the nucleus. The $H_2$ emission is brightest in a region just south of the nucleus and shows elongation in the east/west direction spanning 75 pc. The $H_2$ emission also extends from the horizontal emission region to the north, offset slightly to the west from the continuum center. Pa$\beta$ emission is also detected and is aligned with the J band continuum center.

The velocity and dispersion maps vary greatly among the different emission lines. The [FeII] emission only has a small velocity gradient, with higher (red shifted) velocities of 55 km $s^{-1}$ to the northwest of the continuum center and lower (blue shifted) velocities of -10 km $s^{-1}$ to the southeast. The $H_2$ shows a much larger range of velocities from -140 to 80 km $s^{-1}$ and has a different direction of the velocity gradient than the [FeII], with higher velocities to the north of the continuum center and lower velocities to the south. The dispersion of the [FeII] is also higher and spatially varies, with the highest dispersion of 265 km $s^{-1}$ aligning with the continuum center and slightly to the north. The $H_2$ dispersion peaks to the southwest of the continuum center with a dispersion of 140 km $s^{-1}$, in a region where the velocity gradient is large.

#### 5.4.2.6 NGC 4736

NGC 4736 has compact continuum emission in the J and K bands (Fig. 5.2b) and its nuclear spectrum shows weak emission from [FeII] and $H_2$ as well as strong Pa$\beta$ and CO bandhead absorption (Fig. 5.3b). The line emission morphology differs between the $H_2$ and [FeII] lines, with the $H_2$ emission being compact and centered on the nucleus and the [FeII] emission being more diffuse (Fig. 5.4f). There is also a compact region of [FeII] emission offset from the continuum center by 15 pc to the north and west. This region does not show any visible increase in Pa$\beta$ emission (or decrease in absorption) and therefore may indicate a region of increased [FeII]/Pa$\beta$ line ratio; it is however also possible that any emission present there is being removed by the stellar absorption. The velocity of this region is redshifted by 140 km $s^{-1}$ relative to the systemic velocity and shows a slightly enhanced velocity dispersion of 120 km $s^{-1}$. The $H_2$ line in NGC 4736 has the smallest velocity gradient in the sample ($\pm$ 30 km $s^{-1}$, with higher velocities to the north and east and lower velocities to the southwest) and has a constant dispersion of 60 km $s^{-1}$.

#### 5.4.2.7 NGC 5953

The J and K band continuum emission is compact in NGC 5953 (Fig. 5.2c) and its nuclear spectra show clear detections of [FeII] and 1-0 S(1) $H_2$, as well as the 1-0 S(2) $H_2$ line and the CO stellar absorption features (Fig. 5.3b). The emission line maps show that Pa$\beta$ and Br$\gamma$ are also detected and that much of the emission from all 4 lines comes from regions offset from the continuum center (Fig. 5.4g). The [FeII] emission is especially clumpy with concentrations of emission aligned with the continuum center and to the northeast and southwest. The $H_2$ emission forms a ring whose center is offset to the south of the nucleus by $\sim$10 pc. There may also be [FeII] and $H_2$ emission that extends to the east and west of the continuum center, but this is cut off by the field of view of the broadband J and K mosaicked data cubes. The Pa$\beta$ and Br$\gamma$ emission peaks in a region southwest of the nucleus, which aligns with a region of [FeII] emission. Other clumps of [FeII] emission do not have corresponding regions of Pa$\beta$ emission, indicating that there is spatial variation in

the [FeII]/Pa$\beta$ line ratio.

The [FeII] and $H_2$ emission is generally found at different velocities across the central 150 pc of the galaxy, with the exception of the blue shifted region slightly to the southwest of the continuum center and the spaxels just around the continuum center. The [FeII] reaches higher velocities (up to 200 km $s^{-1}$) and dispersions (up to 300 km $s^{-1}$) than the $H_2$ gas in areas to the south of the continuum center. The Pa$\beta$ emission has a similarly broad dispersion in its emission region to the southwest of the nucleus and is blue shifted by $\sim$50 km $s^{-1}$ relative to the systemic velocity of the galaxy, although the velocity measurements are quite noisy in this region.

#### 5.4.2.8 NGC 7217

NGC 7217 has compact continuum emission (Fig. 5.2c) and has strong detections of [FeII], multiple $H_2$ lines, and the CO bandhead absorption features in its nuclear spectra (Fig. 5.3b). The hydrogen recombination lines are not detected in the nuclear spectra or in the emission line maps. The [FeII] and $H_2$ line emission is aligned with the continuum center, with the [FeII] emission being more diffuse than the $H_2$ emission (Fig. 5.4h). The velocity information in the [FeII] is very noisy, so it is not displayed here; this line would likely benefit from a spatial binning of the data before fitting for the line velocity. The $H_2$ line shows a significant velocity gradient from east (8 km $s^{-1}$) to west (-90 km $s^{-1}$) and is generally blue shifted with respect to the systemic velocity of the galaxy, which is determined by a fit to both the [FeII] and 1-0 S(1) $H_2$ lines in nuclear spectrum (see Sec. 5.3.1 and Table 5.3). The dispersion of this line shows a slight increase from the edge of the velocity map field of view about (0.25 arcsec away from the continuum center) to the continuum center from 60 to 80 km $s^{-1}$.

#### 5.4.2.9 NGC 7465

NGC 7465 shows compact continuum emission in the J and K band (Fig. 5.2c) and its nuclear spectra have strong detections of [FeII] and $H_2$ as well as both broad and narrow components of Pa$\beta$ and Br$\gamma$ emission (Fig. 5.3c). Multiple $H_2$ lines and the CO absorption features are

also detected. The emission line maps all show similar morphology with a dominant compact core of emission plus more emission seen extending up to 75 pc to the north and south of the continuum center (Fig. 5.4i). The [FeII] has an additional peak of emission 15 pc to the north and east of the continuum center, which is not matched in the other emission line maps. This region of [FeII] emission possibly has an enhanced [FeII]/Pa$\beta$ ratio.

The $H_2$, Pa$\beta$, and Br$\gamma$ lines show similar velocity fields, with a gradient to the northeast and the southwest of the nucleus and velocities spanning $\pm$50 km s$^{-1}$. The [FeII] has generally higher velocities than the other lines and is redshifted relative to the systemic velocity, ranging from 0 to 100 km s$^{-1}$. The dispersion in the [FeII] is also generally higher than the $H_2$ and Pa$\beta$/Br$\gamma$ dispersion and varies spatially, with enhanced dispersion seen to the south of the continuum center (110 km s$^{-1}$) and to the northeast (140 km s$^{-1}$), where it aligns with the region of increased [FeII] emission. The $H_2$ dispersion shows no spatial variation and has a value of $\sim$30 km s$^{-1}$.

The Pa$\beta$ and Br$\gamma$ have a significant increase of dispersion at the continuum center, going from being nearly unresolved at the edges of the filed of view to more than 400 km s$^{-1}$ at the nucleus. Note that although both narrow and broad components of Pa$\beta$ and Br$\gamma$ are detected in the nuclear spectra, the velocity and dispersion maps presented here are derived from a single Gaussian fit. The maps therefore represent an average shift/dispersion of the two components, and in particular the dispersion of the broad line component is likely significantly higher than shown here.

#### 5.4.2.10 NGC 7591

The J and K band continuum of NGC 7591 has an extended morphology (Fig. 5.2d). The central region of continuum emission is elongated to the northwest and the southeast and there is also an extended arm of faint emission visible to the north of the highest continuum peak. The nuclear spectrum of NGC 7591 has clear detections from [FeII], Pa$\beta$, 1-0 S(1) $H_2$, and Br$\gamma$, as well as the 1-0 S(2) $H_2$ line and the CO bandhead absorption features (Fig. 5.3c). The line emission maps show a similar elongation like the continuum emission (Fig. 5.4j).

The hydrogen recombination lines have a ring-like morphology with knots of emission seen along the ring to the south and west of the continuum center. The [FeII] seems to follow a similar morphological structure as the Pa$\beta$ and Br$\gamma$ lines, but it is more difficult to identify corresponding knots of [FeII] emission due to the lower S/N in this line. The $H_2$ line emission shows slightly different morphology with some increased emission found to the northwest and southeast of the ring seen in Pa$\beta$/Br$\gamma$. All 4 lines have similar velocity structures spanning up to $\pm$140 km s$^{-1}$. The $H_2$, Pa$\beta$, and Br$\gamma$ lines have increased velocity dispersions near the continuum center, from $\sim$60 km s$^{-1}$ at the outskirts of the dispersion map fields of view to $\sim$100 km s$^{-1}$ at the nucleus. The [FeII] dispersion measurements are quite noisy, but do not show any significant spatial variation and have a value of $\sim$110 km s$^{-1}$.

## 5.5 Discussion

The sample of LINERs presented in this work can be divided into 3 subgroups based on their observed properties: galaxies with broad lines in their OSIRIS nuclear spectra (NGC 3998, 4579, and 7465), galaxies whose far-infrared properties classify them as LIRGs (NGC 1204, 1614, and 7591), and the remaining sample that all show high values of the [FeII]/Pa$\beta$ ratio in their OSIRIS nuclear spectra (NGC 404, 3627, 4736, 5953, and 7217). The nuclear line ratios of the sample as a whole (Sec. 5.5.1) and properties of the sample subgroups in the OSIRIS data set as well as possible physical interpretations (Sec. 5.5.2 – 5.5.4) are discussed below.

### 5.5.1 Nuclear Line Ratios

The [FeII]/Pa$\beta$ and 1-0 S(1) $H_2$/Br$\gamma$ line ratios measured from the nuclear spectra are compared to each other and to other objects from the literature in Fig. 5.5. As discussed in Sec. 5.1, these NIR line ratios in LINERs and other emission line galaxies are found to be correlated from seeing-limited observations (Larkin et al., 1998; Riffel et al., 2013). The 1-0 S(1) $H_2$/Br$\gamma$ versus [FeII]/Pa$\beta$ parameter space serves as a diagnostic diagram for emission line galaxies, with starburst galaxies, Seyferts, and LINERs occupying regions along the

correlation from low to high line ratios. In general, the [FeII]/Pa$\beta$ line ratios from the OSIRIS nuclear spectra agree with the seeing-limited measurements presented in Table 5.1, with a few exceptions noted below. NGC 4736 is not presented here because the line ratios cannot be constrained in its nuclear spectrum due to the strong Pa$\beta$ absorption (Fig. 5.3b).

The ratios measured from the nuclear spectra fall into 2 groups in this diagram: those with high [FeII]/Pa$\beta$ ratios (>1.8) and those with low [FeII]/Pa$\beta$ ratios (<0.8). These groups are similar to those presented in Larkin et al. (1998), but the AO-assisted IFS measurements presented here probe spatial scales that are an order of magnitude smaller than the previous seeing-limited observations. There are 4 galaxies in the low [FeII]/Pa$\beta$ ratio group: the 3 LIRGs (NGC 1204, 1614, and 7591) and NGC 7465, one of the broad line galaxies. These galaxies fall near the correlation line in Fig. 5.5 and around the boundary dividing starburst and Seyfert nuclei, suggesting that either star formation or SMBH accretion processes power their NIR emission.

The galaxies in the high [FeII]/Pa$\beta$ group include 2 sources with broad lines (NGC 3998 and 4579) and the remaining 3 galaxies in the sample (NGC 3627, 5953, and 7217) as well as NGC 404. Note that NGC 4736 also has a very high [FeII]/Pa$\beta$ ratio of 5.3 in its seeing-limited spectrum from Riffel et al. (2013), but as mentioned above the line ratios can not be constrained in its OSIRIS nuclear spectra due to Pa$\beta$ absorption. These galaxies tend to fall above the correlation line, near the parameter space occupied by the shocked regions of supernova remnants. The high values of the [FeII]/Pa$\beta$ ratio suggest that the [FeII] emission in these sources in excited by shocks, which can process dust grains and thereby efficiently convert iron from the solid to the gaseous phase (Blietz et al., 1994; Larkin et al., 1998). Given the spatial variation of relative [FeII] and Pa$\beta$ strength visible in many of the line maps, it is possible that smaller apertures in other sources will also have [FeII]/Pa$\beta$ ratios that are similarly high, as is found in NGC 404 (see Chapter 4). These smaller shocked regions could be caused by either stellar processes, such as supernova remnants (like in NGC 404), or AGN-related processes, such as a jet that is shocking the surrounding medium or an AGN-driven outflow (e.g., Riffel et al., 2015).

### 5.5.2 Galaxies with Broad Lines

Three LINERs in the sample are found to have broad line emission in their NIR nuclear spectra: NGC 3998, NGC 4579, and NGC 7465. NGC 3998 and NGC 4579 both have broad H$\alpha$ emission in their optical spectra as well, being classified as an L1.9 and S1.9/L1.9 respectively. NGC 7465 does not have broad lines detected in its optical spectrum, but its type 1 nature has been previously reported based on seeing-limited NIR spectroscopy (Ramos Almeida et al., 2009). In the OSIRIS data set, the velocity dispersion maps of the broad lines in NGC 3998 ([FeII], Pa$\beta$) and NGC 7465 (Pa$\beta$, Br$\gamma$) reveal that the dispersions of these lines peak at a position aligned with the continuum center and have values between 400 and 700 km s$^{-1}$, corresponding to FWHM between 900 and 1650 km s$^{-1}$. Although the Pa$\beta$ line in NGC 4579 is too faint to measure its velocity and dispersion on a spaxel by spaxel basis, a Gaussian fit to the Pa$\beta$ line in the J band nuclear spectrum finds that this line has a dispersion of 520 km s$^{-1}$, or a FWHM of 1225 km s$^{-1}$. These FWHM correspond to the low end of velocities that are typically associated with AGN broad line regions and therefore may indicate that these nuclei host SMBHs.

As discussed in Sec. 5.5.1, two of the broad line galaxies have a high [FeII]/Pa$\beta$ ratio in their nuclear spectra (2.9 in NGC 3998 and 2.3 in NGC 4579) and one has a low [FeII]/Pa$\beta$ ratio (0.6 in NGC 7465). NGC 3998 in particular has one of the highest nuclear [FeII]/Pa$\beta$ ratios in the sample and falls near the supernova remnant points in the diagram, suggesting that shock excitation is the dominant mechanism causing its LINER emission. Note that this line ratio in NGC 3998 is a factor of $\sim$4.5 larger than the value found in seeing-limited data, showing the power of measuring line ratios on the small spatial scales possible with OSIRIS behind AO. On the other hand, the low [FeII]/Pa$\beta$ ratio found in NGC 7465 may indicate that X-ray emission due to accretion onto the SMBH that it hosts is the dominant excitation mechanism of the [FeII] gas, as Larkin et al. (1998) argued for LINERs with [FeII]/Pa$\beta$ below 2.0 (see also Ramos Almeida et al., 2009; Riffel et al., 2013). The ratio presented here, however, includes all of the broad line Pa$\beta$ flux even though there is no [FeII] emission present at the larger velocities. If only the narrow line Pa$\beta$ component were

included in the [FeII]/Pa$\beta$ ratio, the ratio of NGC 7465 would increase, perhaps up to a factor of 2. This increase would also bring the ratio closer to the value measured from the seeing-limited spectra in Riffel et al. (2013), in which no broad line component was reported, and in Ramos Almeida et al. (2009), in which the ratio was measured using only the narrow Pa$\beta$ component.

It is also interesting to note that while the hydrogen recombination emission is broad in all 3 sources in this group, the [FeII] velocity dispersion varies significantly. At the lowest end, the [FeII] dispersion in NGC 7465 is 110 km s$^{-1}$, a dispersion typical of the other narrow line sources in the sample. At the other extreme, the [FeII] dispersion in NGC 3998 is 450 km s$^{-1}$, a value similar to the Pa$\beta$ widths in the 3 broad line sources. The [FeII] dispersions also differ spatially: the [FeII] dispersions in NGC 3998 and 4579 peak at the continuum center of the galaxy, which is the same location at which the Pa$\beta$ dispersion/emission peaks, while the [FeII] dispersion substructure in NGC 7465 is all found offset from the galaxy nucleus. These differences of [FeII] dispersion combined with the variations of [FeII]/Pa$\beta$ line ratios observed in each galaxy's nuclear spectrum suggest that the physical mechanism exciting the [FeII] emission differs among the broad line nuclei. In the case of NGC 3998, it is possible that the source of the high [FeII] and Pa$\beta$ velocity dispersions is not a classical broad line region, since these lines only have a broad component in the nuclear spectrum and a velocity gradient is measured across the central nuclear region, suggesting that the region of high FWHM emission is spatially resolved. We instead physically interpret the high velocity dispersions, the high [FeII]/Pa$\beta$ ratio, and the velocity offset between Pa$\beta$ and [FeII] emission by $\sim$175 km s$^{-1}$ (see Fig. 5.4d) as the presence of an AGN-driven outflow of material that is causing shock excitation of the [FeII] emission.

### 5.5.3 LIRGs

The LIRGs in the sample (NGC 1204, 1614, and 7591) are separated from the rest of the LINERs because these sources have significantly different far-infrared properties. The large infrared luminosities of these LIRGs of over $10^{10.5}$ $L_{\odot}$ (Kim et al., 1995) indicate that these

galaxies as a whole are undergoing high rates of star formation. The location of all 3 LIRGs in the NIR line ratio diagnostic plot (Fig. 5.5) near the starburst galaxy region of the diagram suggests that their NIR emission lines are also excited by star formation processes. It should also be noted that the 3 LIRGS are all located at significantly further distances compared to the rest of the sample ($\sim$60 Mpc compared to 3 - 30 Mpc), and thus the OSIRIS spatially-resolved emission, velocity, and dispersion maps probe larger physical scales and have wider fields of view.

In the OSIRIS data, two of the LIRGs in particular show similarities in the morphological structures of their line emission. Both NGC 1614 and NGC 7591 have ring structures with knots of line emission along the ring that are especially bright in the Pa$\beta$ and Br$\gamma$ hydrogen recombination lines. As mentioned in Sec. 5.5.1, the brightness of Pa$\beta$ and Br$\gamma$ emission with respect to [FeII] and 1-0 S(1) $H_2$ suggests that the rings and knots are regions of on-going star formation. The projected radii of these rings are $\sim$200 pc in NGC 1614 and $\sim$50 pc in NGC 7591, similar to nuclear star forming rings that have been studied using NIR IFS in other galactic nuclei (e.g., Böker et al., 2008; Riffel et al., 2016). There has been debate about the physical mechanism that induces star formation in these rings: the "pearls on a string" scenario, in which the star formation occurs at the location where new gas enters the ring and then the newly formed star cluster orbits away before a new cluster starts to form (Böker et al., 2008), and the "popcorn" scenario, in which star clusters form at random locations on the ring as those regions become gravitationally unstable and collapse (Elmegreen, 1994). Future work to measure spatially-resolved line ratios, CO stellar absorption strength, and velocity dispersions will be performed to test for possible age gradients among the knots of star formation, thereby putting constraints on these two formation scenarios in NGC 1614 and NGC 7591. This spatially-resolved information may also reveal regions in which the line emission is excited by mechanisms other than photoionization by young stars, such as shock excitation, which may explain why the optical nuclear spectra can classify some LIRGs are LINERs. Future work will also include modeling the kinematics of NGC 1614, which show an S-shaped distortion to the east and west of the continuum center that may suggest that gas is inflowing along a nuclear bar (e.g., Hicks et al., 2013; Davies et al., 2014, and references

therein).

NGC 1204 instead shows a continuous, elongated continuum emission in both J and K band and similarly elongated line emission in all 4 emission lines. The kinematics of the emission lines show rotational motion and have a velocity gradient across the major axis of the continuum and line emission. One possible interpretation of these morphological and kinematic structures is that NGC 1204 has a rotating disk of star formation at its nucleus that we are viewing from an edge on angle. The physical scale of the disk is then ∼100 pc in the long axis and ∼50 pc in height, although the latter dimension may be unresolved. This disk could be feeding material onto a central SMBH, which may explain this galaxy's [OIII]/H$\beta$ optical line ratio that is close to the border between LINER and Seyfert. It seems from the line ratios presented in Sec. 5.5.1 however that the excitation of the NIR emission lines in this source is likely dominated by processes related to star formation.

### 5.5.4 LINERs

As pointed out in Sec. 5.5.1, the galaxies in the last subgroup (NGC 404, 3627, 4736, 5953, and 7217) are all found to have high values of the [FeII]/Pa$\beta$ line ratio in their OSIRIS nuclear spectra ($> 1.8$) or in their seeing-limited spectra in the case of NGC 4736. This subgroup includes all but one of the galaxies whose nuclei are optically classified as pure LINERs (i.e., all 3 optical line ratios fall in the LINER regions of the BPT diagrams; see Fig. 5.1): NGC 404, 4736, and 7217. This subgroup also includes the source with the highest [FeII]/Pa$\beta$: NGC 3627 with a value of 4.7. This value is much higher than the seeing-limited value reported in Table 5.1, but note that the table value is a predicted [FeII]/Pa$\beta$ ratio based on the K band observations from Mazzalay et al. (2013) and the correlation of [FeII]/Pa$\beta$ with $H_2$/Br$\gamma$. In the NIR diagnostic diagram, NGC 3627 falls close to the shocked regions of supernova remnants and to the shocked regions of NGC 404 presented in Chapter 4 that have ratio values ranging from 3.8 - 6.5, suggesting that the LINER emission in NGC 3627 is also excited by shocks. The emission line kinematics in this source are also similar to NGC 404, with the [FeII] velocity being offset from $H_2$ towards higher velocities.

In addition to the nuclear line ratios, the emission line morphologies and kinematics as measured by OSIRIS also show some similar features among the galaxies in this subgroup. Three of the sources (NGC 3627, 4736, and 5953) have knots of [FeII] emission that correspond to enhanced [FeII] velocity dispersion and do not have an associated knot of Pa$\beta$ emission. These [FeII] emission knots may be regions of even higher [FeII]/Pa$\beta$ than measured in the nuclear spectra where a supernova remnant, inflow, outflow, or jet is causing shock-excited [FeII] emission. On a larger spatial scale, the [FeII] emission in this subgroup also tends to be more extended or diffuse than the $H_2$ or hydrogen recombination emission (NGC 404, 4736, 5953, and 7217), suggesting different excitation mechanisms for the ionized and molecular gas in these galactic nuclei.

## 5.6 Summary and Future Outlook

This chapter presents results from a survey of 11 LINERs in the J and K band using the OSIRIS integral field spectrograph behind the Keck AO System. These data measure the strength and kinematics of the [FeII], multiple $H_2$, Pa$\beta$, and Br$\gamma$ emission lines as well as the CO stellar absorption features at the smallest possible spatial scales (1-10 pc). For each galaxy, the nuclear spectra and their line ratios are presented, as well as continuum and line emission, velocity, and velocity dispersion maps for all detected emission lines. These data products reveal variations in the morphology and kinematics of the measured emission lines, both within a given LINER and across the entire sample, that can only be observed using an integral field spectrograph. The range of [FeII]/Pa$\beta$ and $H_2$/Br$\gamma$ line ratios measured in the nuclear spectra, which probe spatial scales an order of magnitude smaller than previous seeing-limited spectra, suggest that a variety of physical mechanisms related to star formation, accretion onto a central SMBH, and shocks are responsible for exciting the NIR emission in these LINERs. For the classical optical LINERs in particular (i.e., those without broad lines and that are not LIRGs), the high line ratios we measure indicate that the NIR emission is excited by shocks.

There is likely even more information that can be gleaned from the large and complex

data set presented here. Next analysis steps include producing line emission maps as a function of velocity to reveal structures that are only present at certain velocities, measuring line ratios in small apertures to search for spatial variations of the excitation mechanism of the NIR lines, and constraining the stellar population age and kinematics through the CO bandhead absorption features and the Pa$\beta$ absorption feature in NGC 4736. This additional information will likely improve our ability to put constraints on the dominant excitation mechanisms in the individual LINERs in this sample, as well as make broader statements about the variety in this class as a whole; however, this further analysis is beyond the scope of this thesis.

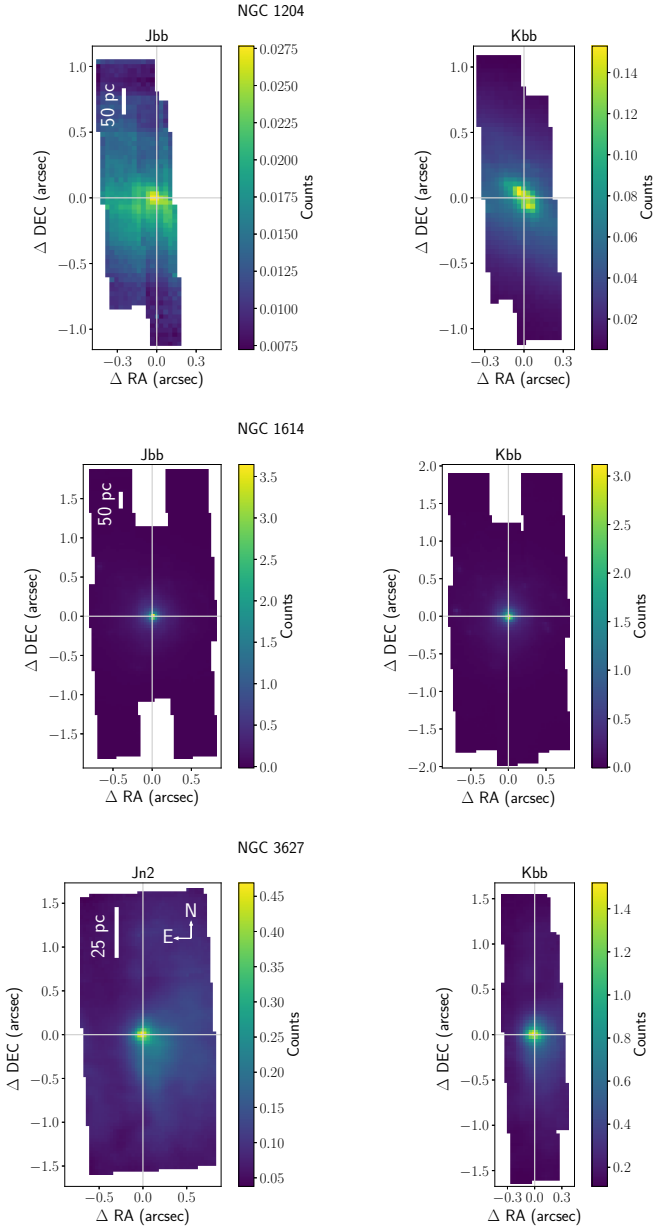


Figure 5.2a: Mosaicked data cubes for NGC 1204, 1614, and 3627 showing the continuum emission of the galaxy nucleus in the J (left column) and K bands (right column). The images are created by taking the median across all wavelength channels in the spectrum of every spatial pixel (or spaxel). Spaxels in which no flux is measured are not displayed. The origin of these and all subsequent plots is placed at the center of the continuum emission as measured from these maps. These plots display the full mosaic fields of view, including regions of negative counts that indicate a dithered science frame was used to subtract the sky emission from one or more on-source frames. Note that these and all maps displayed in this work are at a PA of 0°, with north up and east to the left.

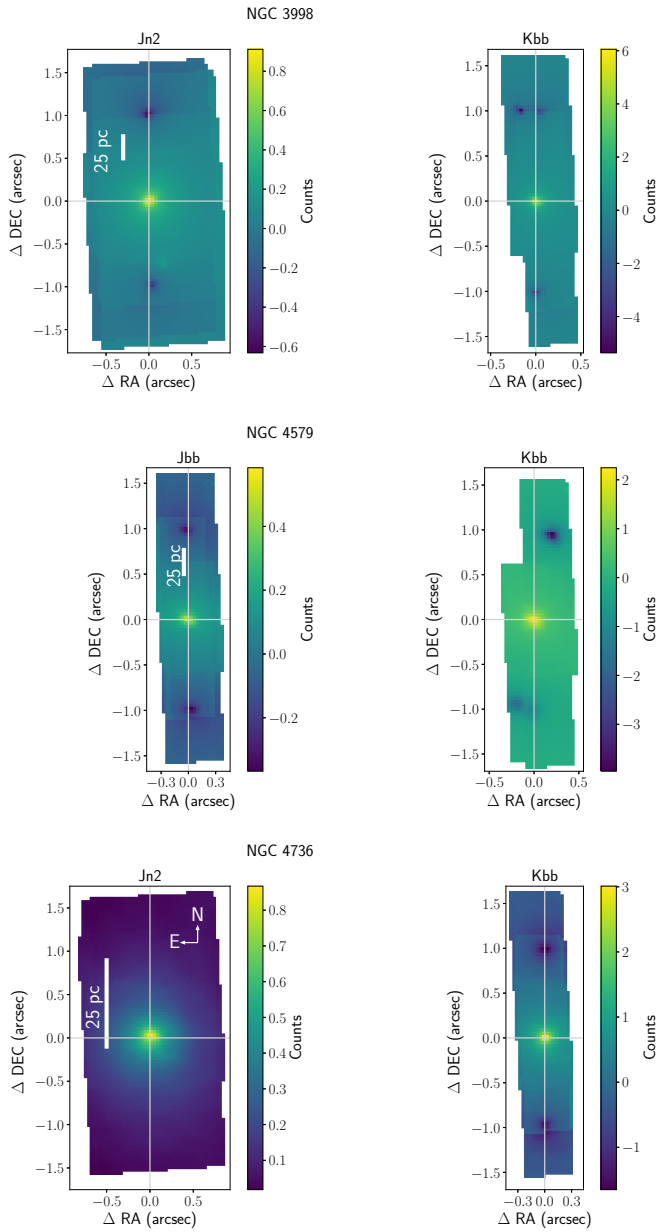


Figure 5.2b: Same as Fig. 5.2a for NGC 3998, 4579, and 4736.

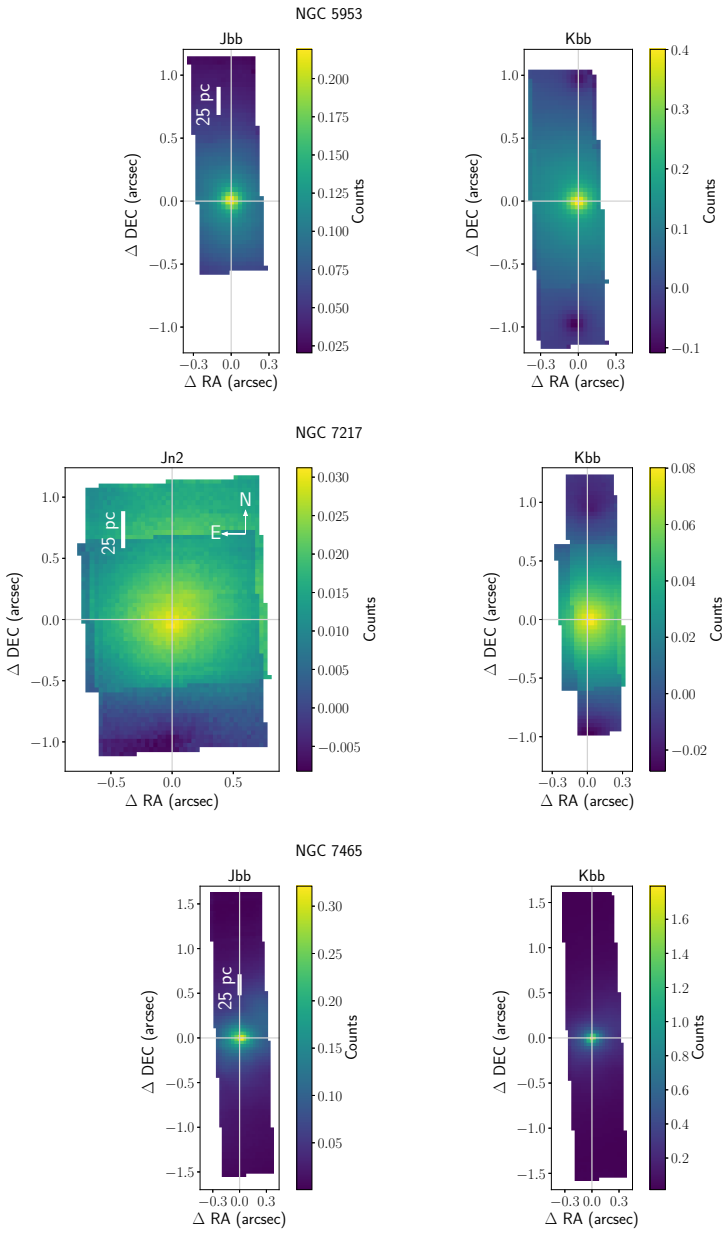


Figure 5.2c: Same as Fig. 5.2a for NGC 5953, 7217, and 7465.

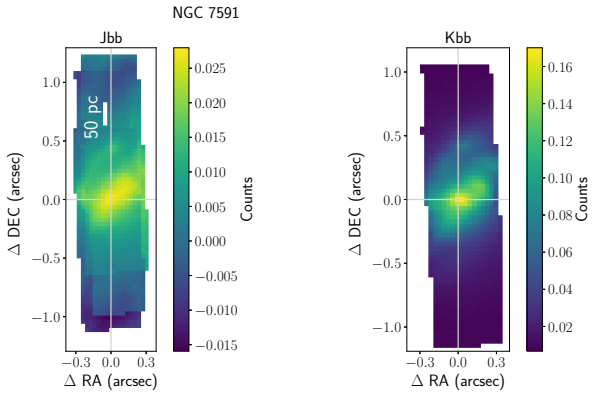


Figure 5.2d: Same as Fig. 5.2a for NGC 7591.

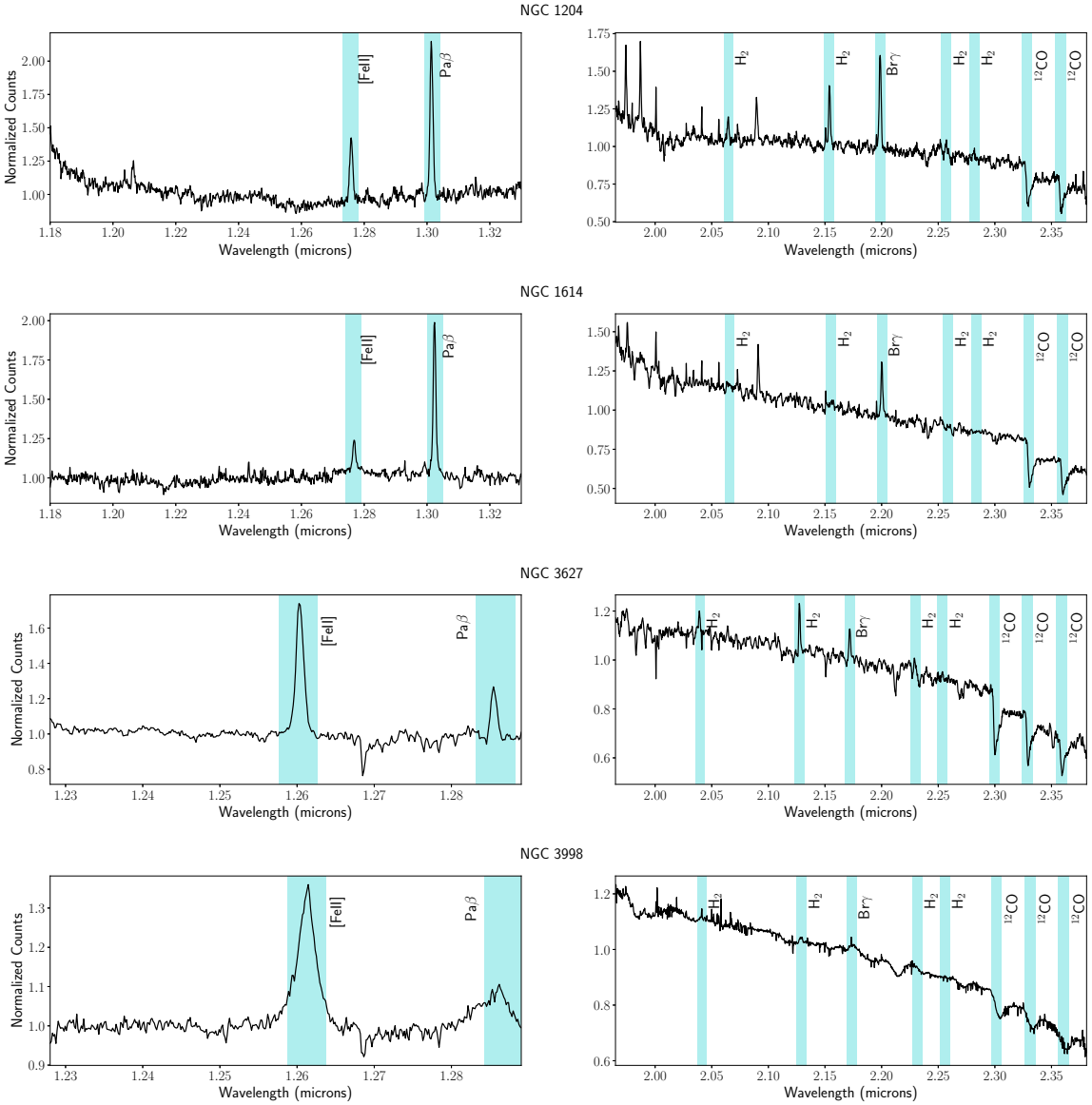


Figure 5.3a: Nuclear spectra in the J (left column) and K band (right column) for NGC 1204, 1614, 3627, and 3998. These spectra are extracted from a circular aperture centered on the continuum peak in each band and with a radius of 6 spaxels or 0.21 arcsec. The angular radius of the aperture corresponds to 3 - 65 pc, depending on the distance of the galaxy. For NGC 1614, the center of the circular aperture is offset by 0.25 arcsec to the east of the continuum center since most of this galaxy's line emission is seen off of the nucleus. Light blue boxes highlight the $\pm 600$ km s$^{-1}$ wavelength range relative to the systemic velocity of the galaxy around the observed spectral features in each bandpass: [FeII] and Pa$\beta$ in J band and $H_2$, Br$\gamma$, and CO in K band. For galaxies observed in the Jbb band, only the wavelengths lower than 1.33 $\mu$m are displayed because the redder wavelengths exhibit extreme telluric absorption and are generally not well corrected.

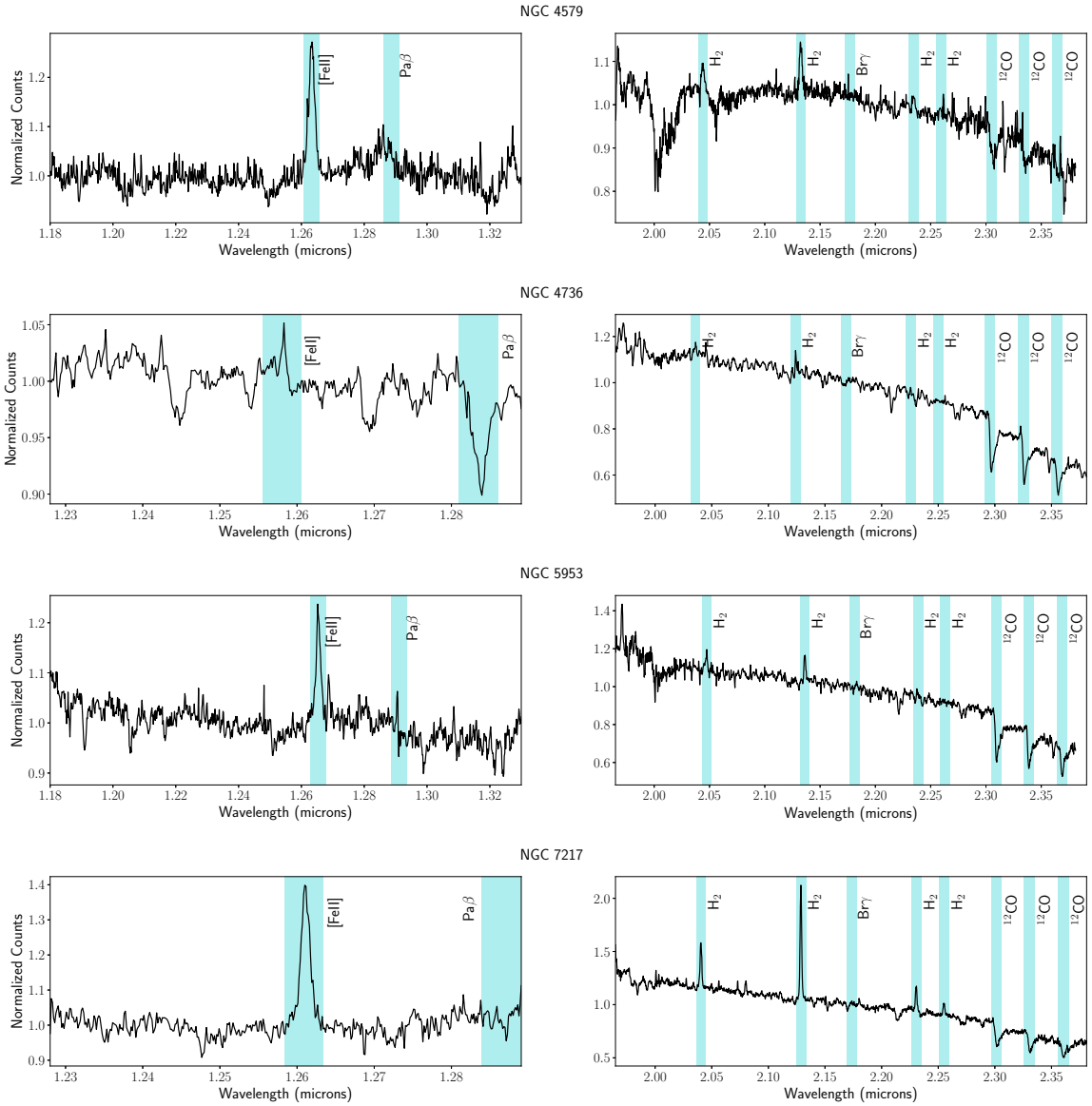


Figure 5.3b: Same as Fig. 5.3a for NGC 4579, 4736, 5953, and 7217.

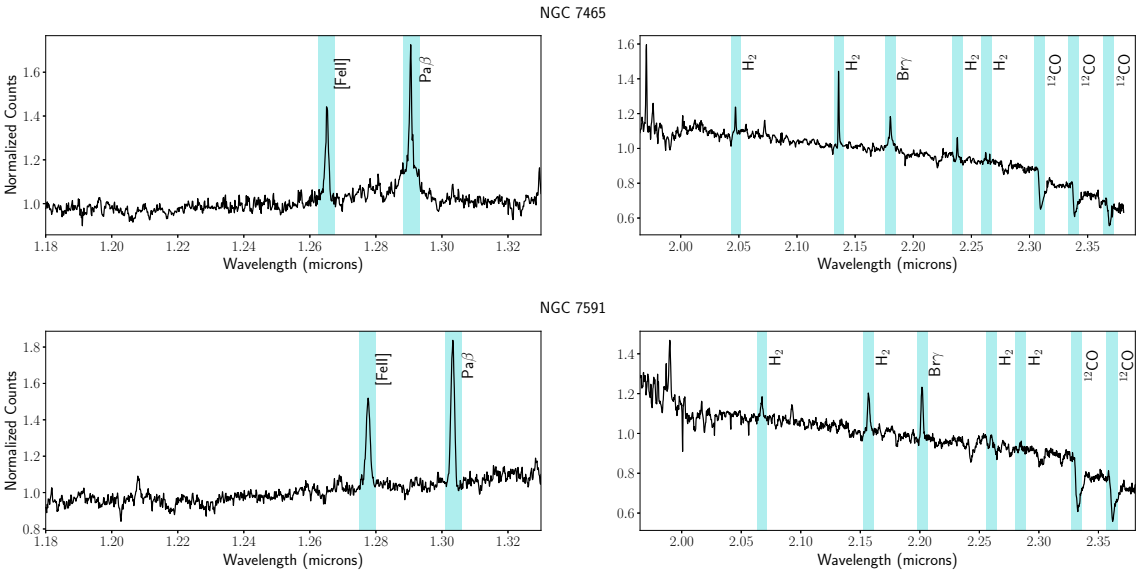


Figure 5.3c: Same as Fig. 5.3a for NGC 7465 and 7591.

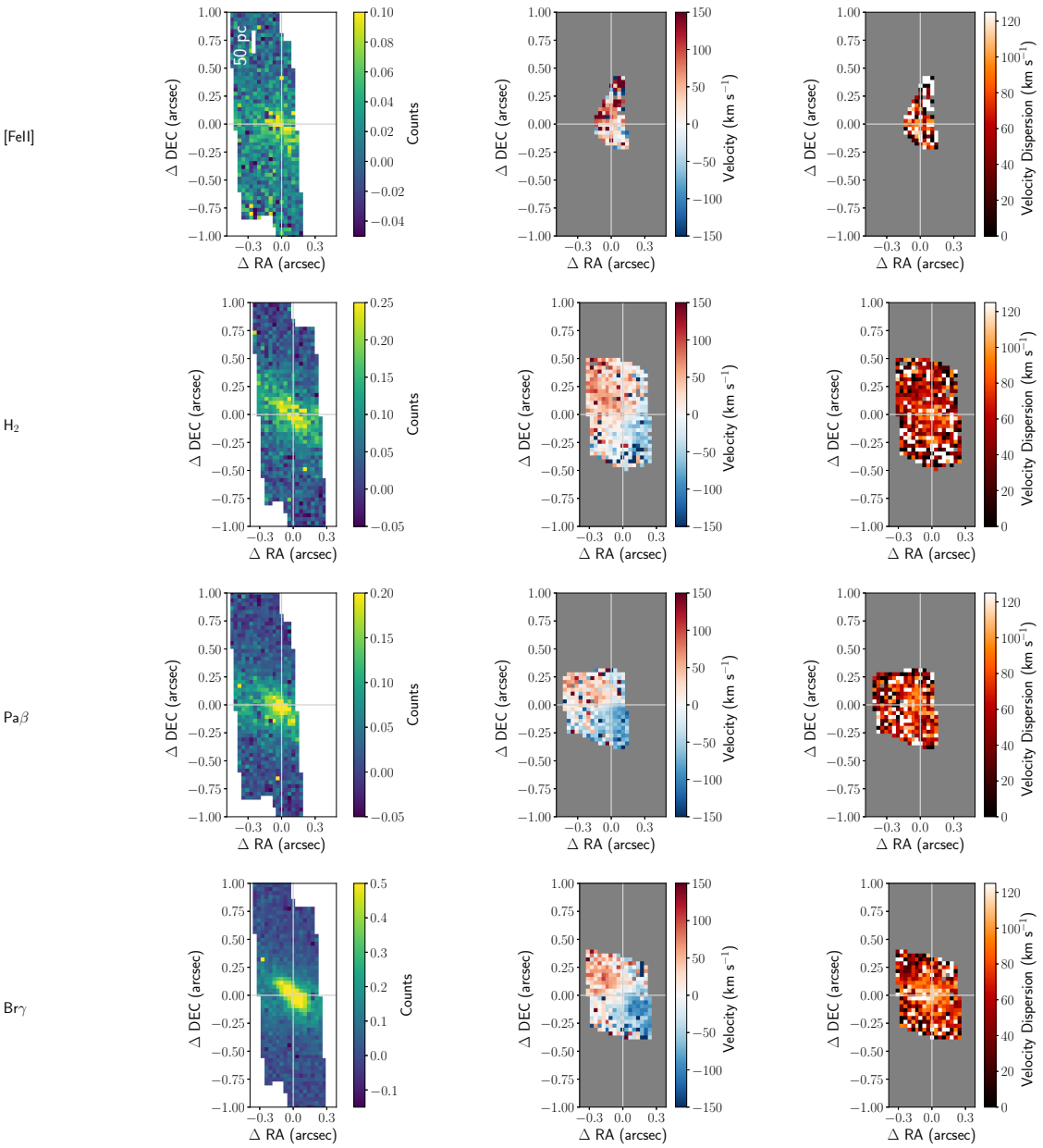


Figure 5.4a: Line emission maps (left column), velocity maps (middle column), and velocity dispersion maps (right column) at the nucleus of NGC 1204 for [FeII], 1-0 S(1) $H_2$, Pa$\beta$, and Br$\gamma$ lines. The line emission maps show the regions within the full mosaicked fields of view that exhibit line emission. The velocity and velocity dispersion maps are shown with the same plotting limits as the line maps. Spaxels that have a line S/N less than the threshold defined in Sec. 5.3.4 are also masked in the velocity and dispersion plots. The OSIRIS instrumental dispersion as determined by the analysis of NGC 404 in Chapter 4 is removed from the displayed velocity dispersion plots. The white cross hairs in all panels indicate the origin of the plots, which is set to the continuum center of the galaxy in the J ([FeII] and Pa$\beta$) or K band ($H_2$ and Br$\gamma$). Note that in some subsequent subfigures (Fig. 5.4d - 5.4h), velocity and velocity dispersion maps are not displayed for lines for which a velocity measurement was not possible due to low line S/N.

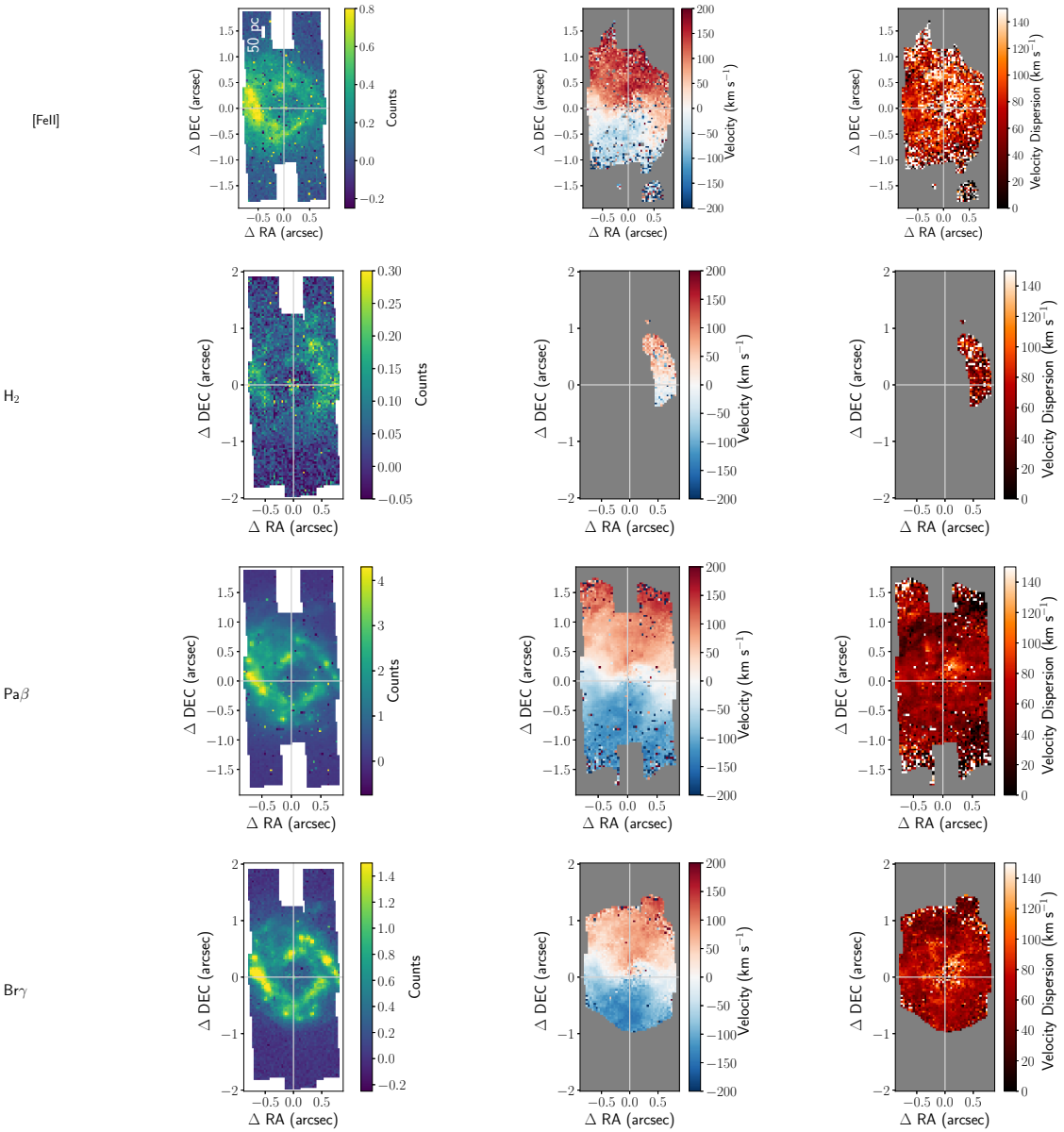


Figure 5.4b: Same as Fig. 5.4a for NGC 1614.

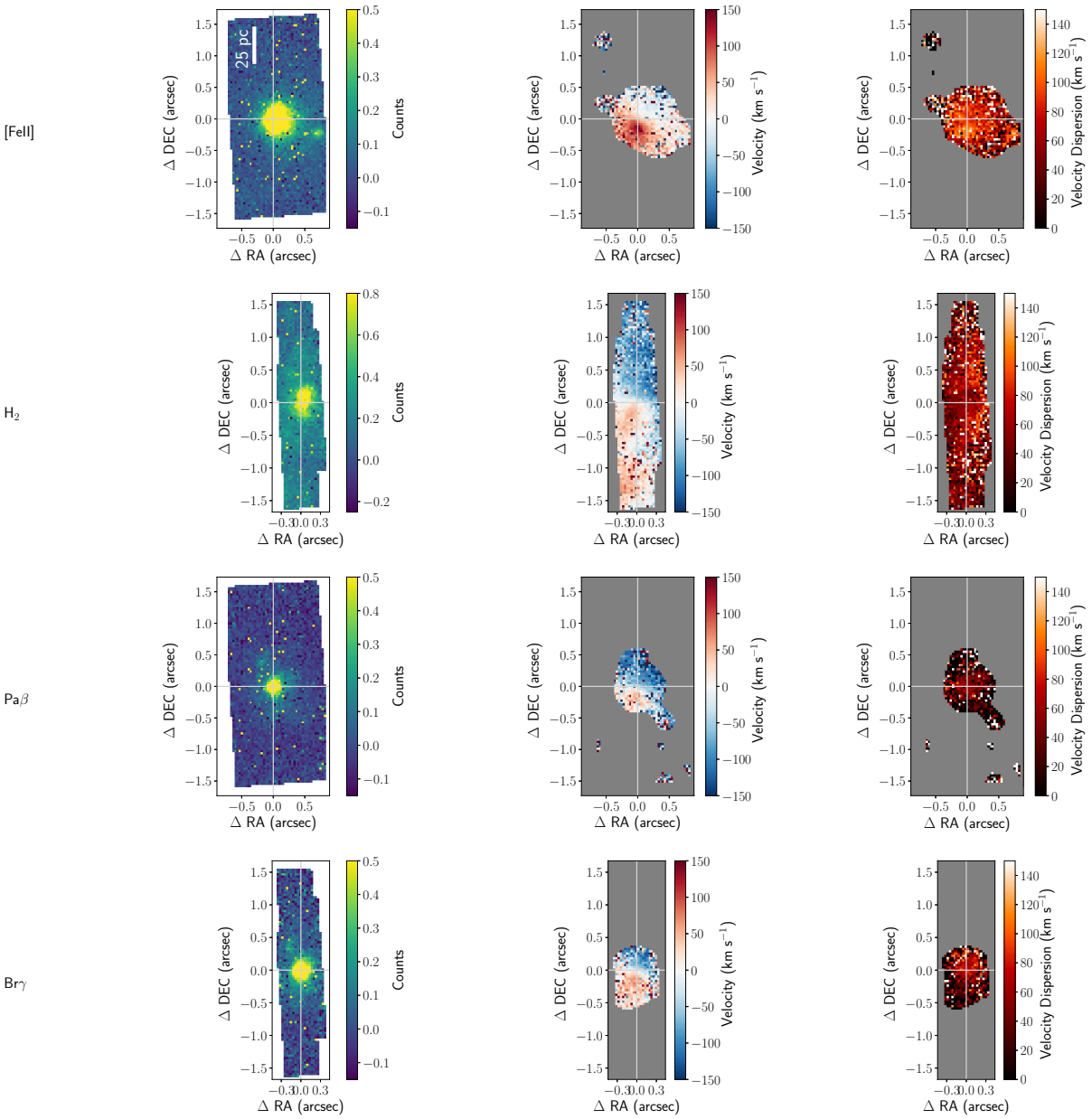


Figure 5.4c: Same as Fig. 5.4a for NGC 3627. Note that for the Pa$\beta$ and Br$\gamma$ lines in this source, the line S/N threshold for masked pixels is 3 instead of the default 10.

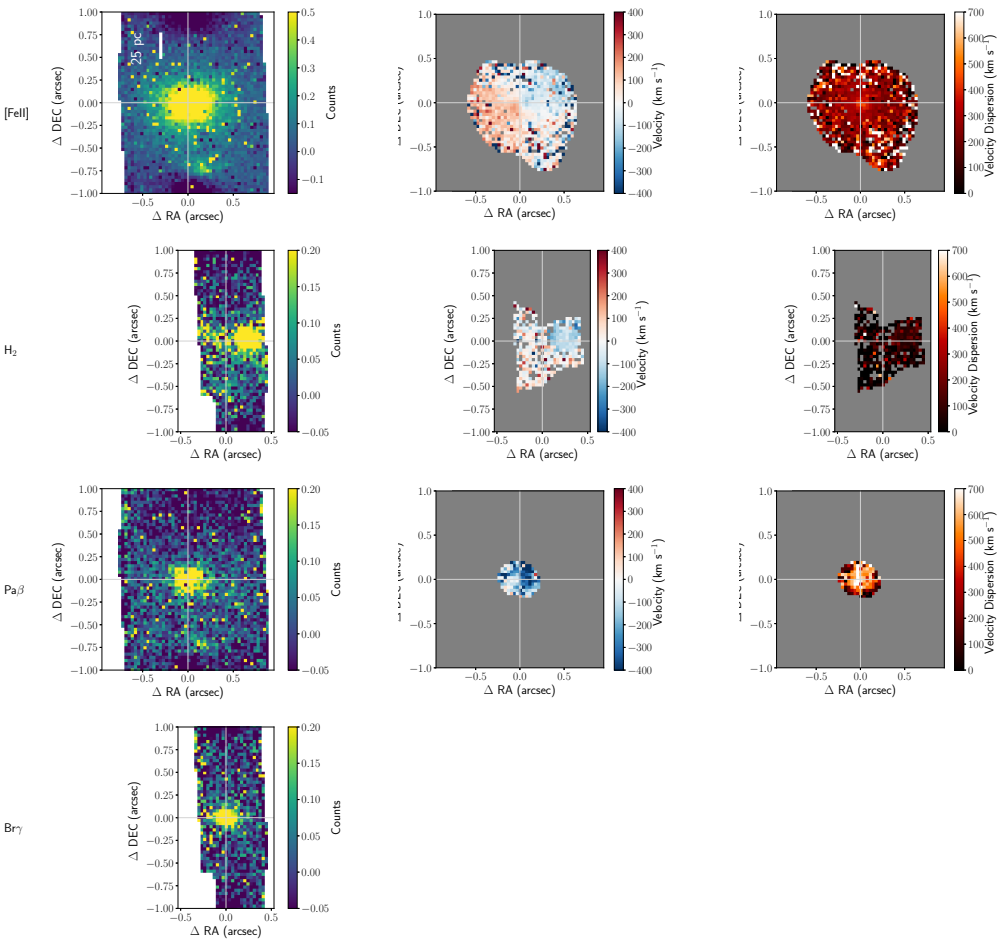


Figure 5.4d: Same as Fig. 5.4a for NGC 3998. Note that for the $H_2$ emission line in this source, the line S/N threshold for masked pixels is 3 instead of the default 10.

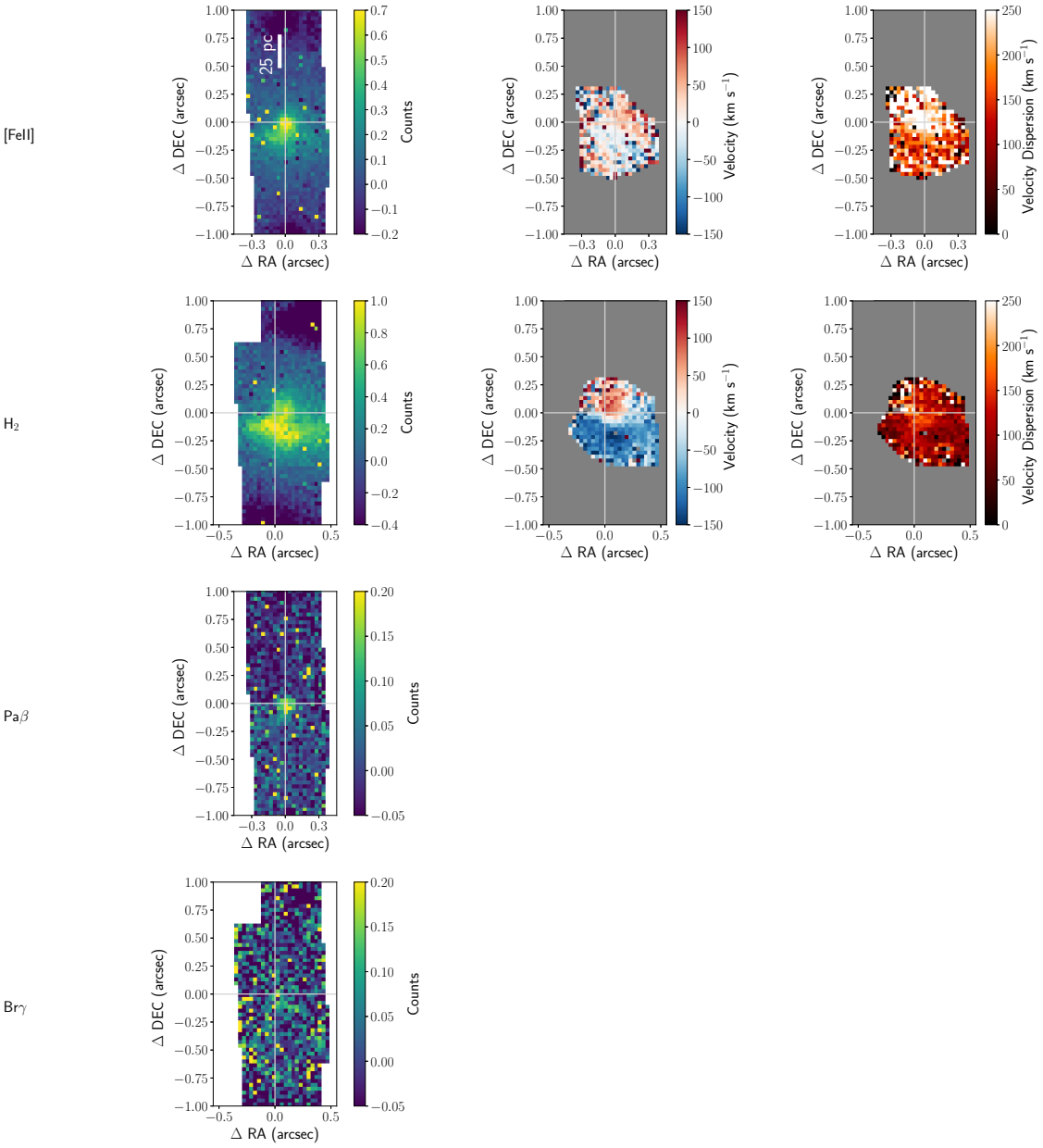


Figure 5.4e: Same as Fig. 5.4a for NGC 4579.

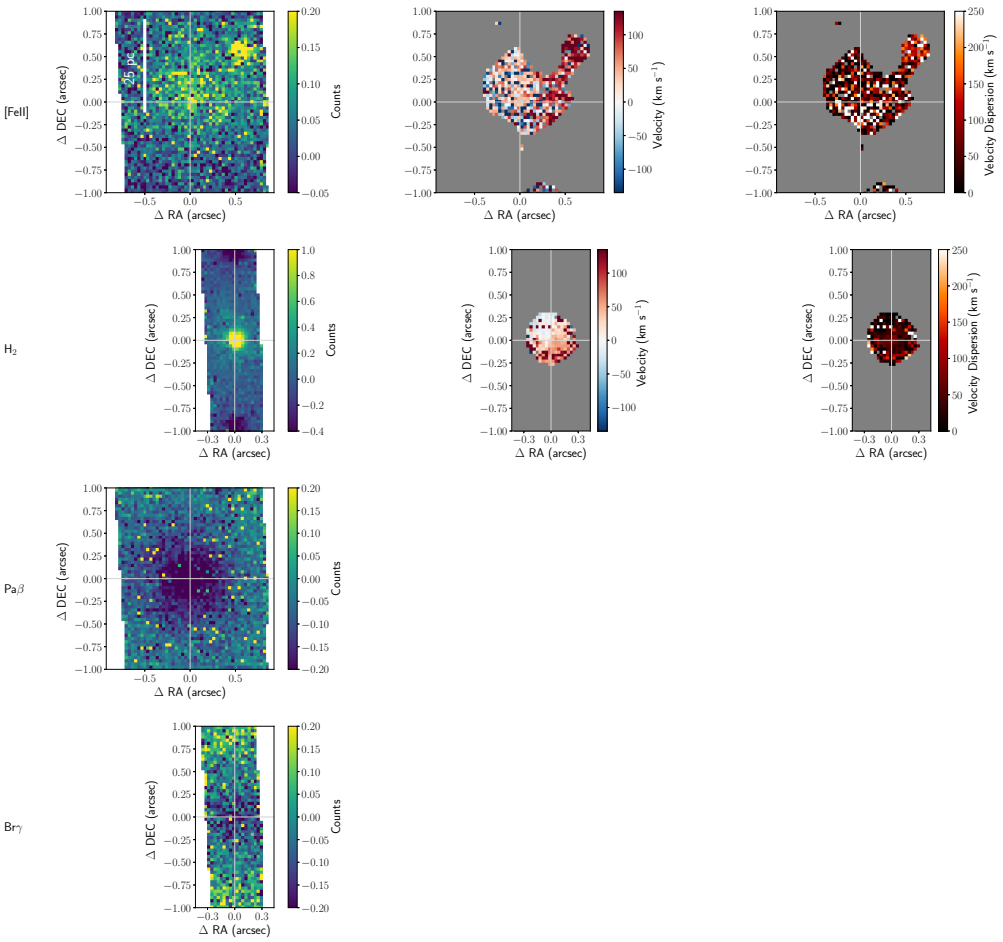


Figure 5.4f: Same as Fig. 5.4a for NGC 4736. Note that for the [FeII] emission line in this source, the line S/N threshold for masked pixels is 7 instead of the default 10.

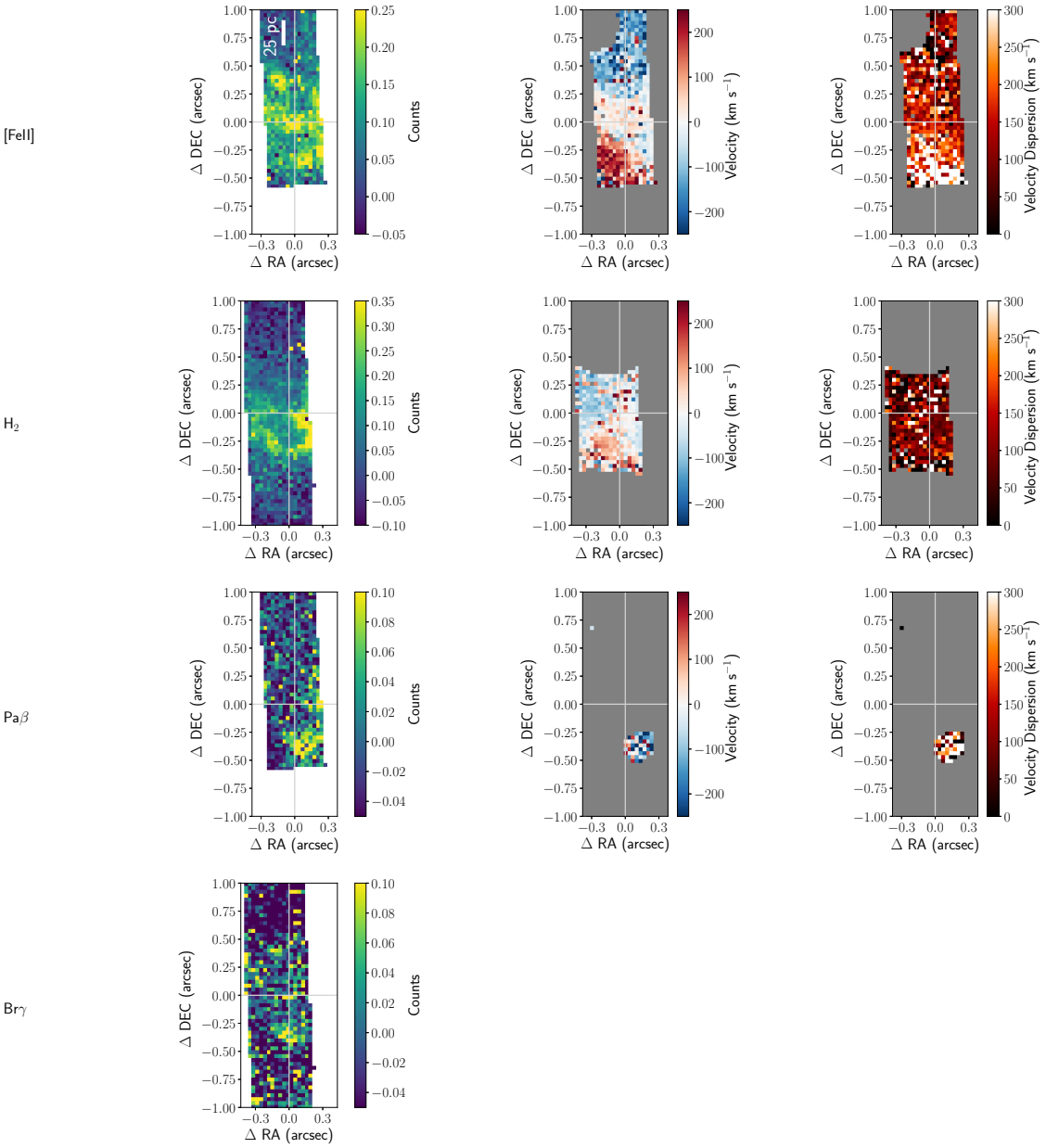


Figure 5.4g: Same as Fig. 5.4a for NGC 5953. Note that for the Pa$\beta$ emission line in this source, the line S/N threshold for masked pixels is 5 instead of the default 10.

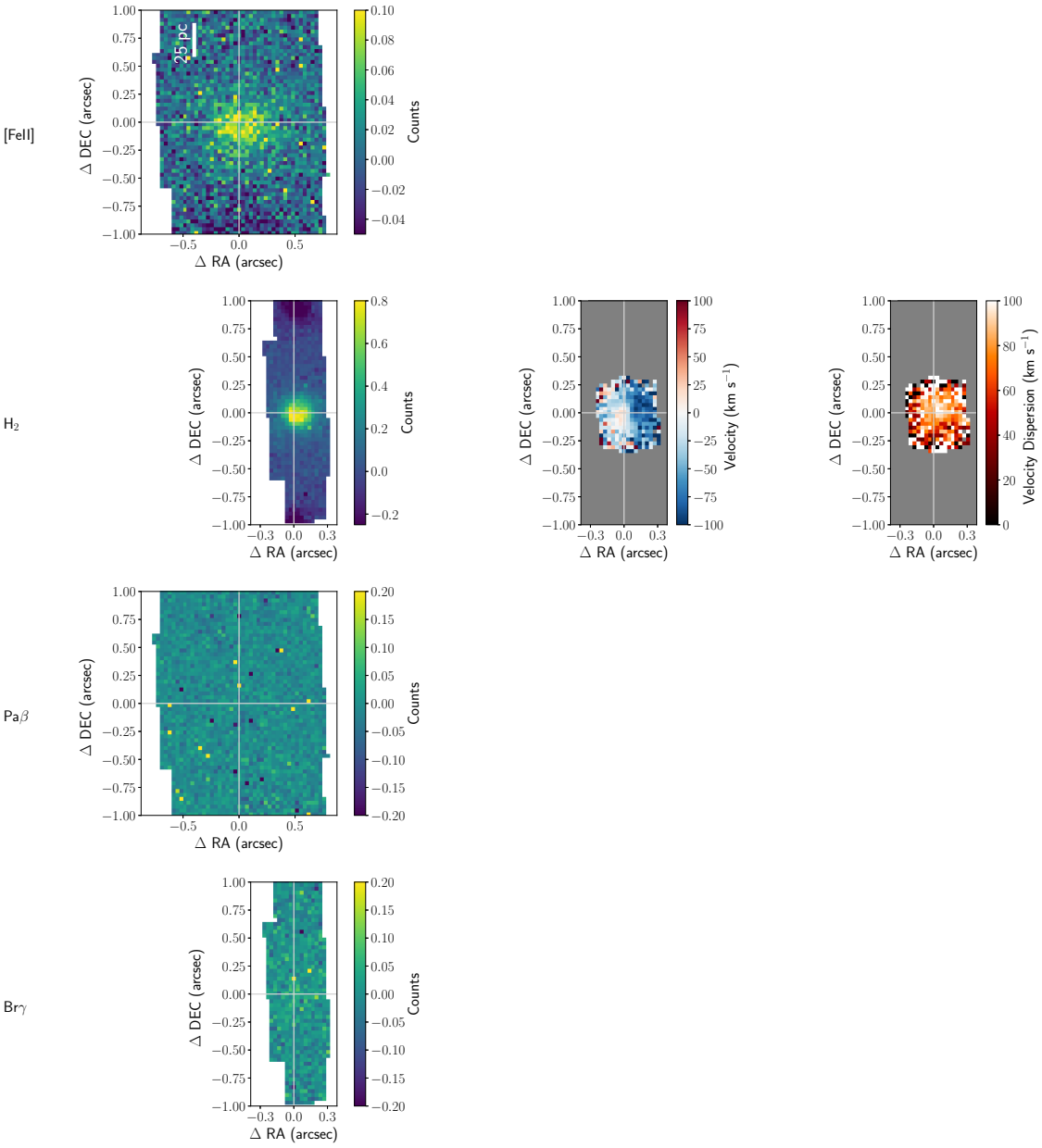


Figure 5.4h: Same as Fig. 5.4a for NGC 7217.

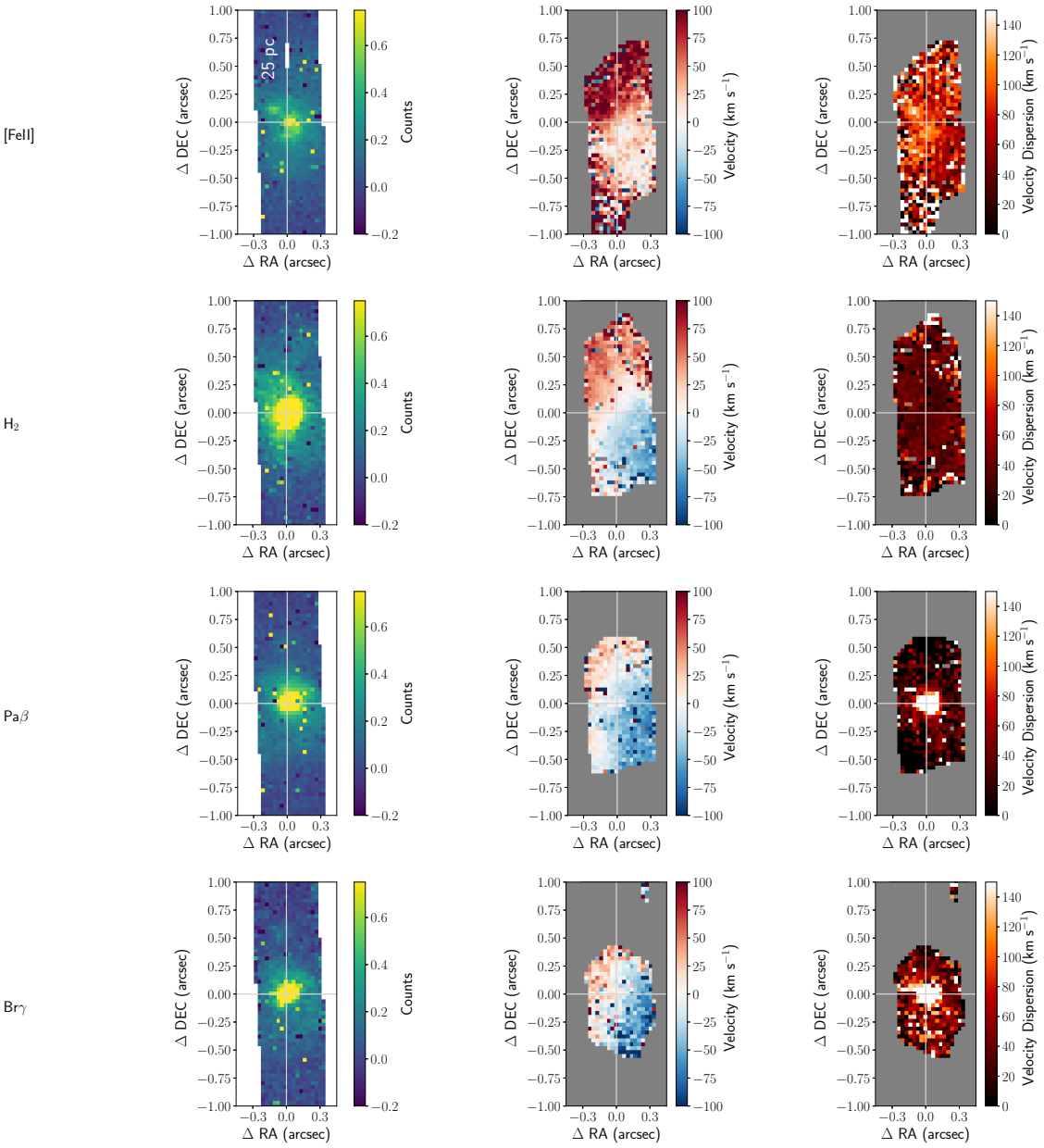


Figure 5.4i: Same as Fig. 5.4a for NGC 7465.

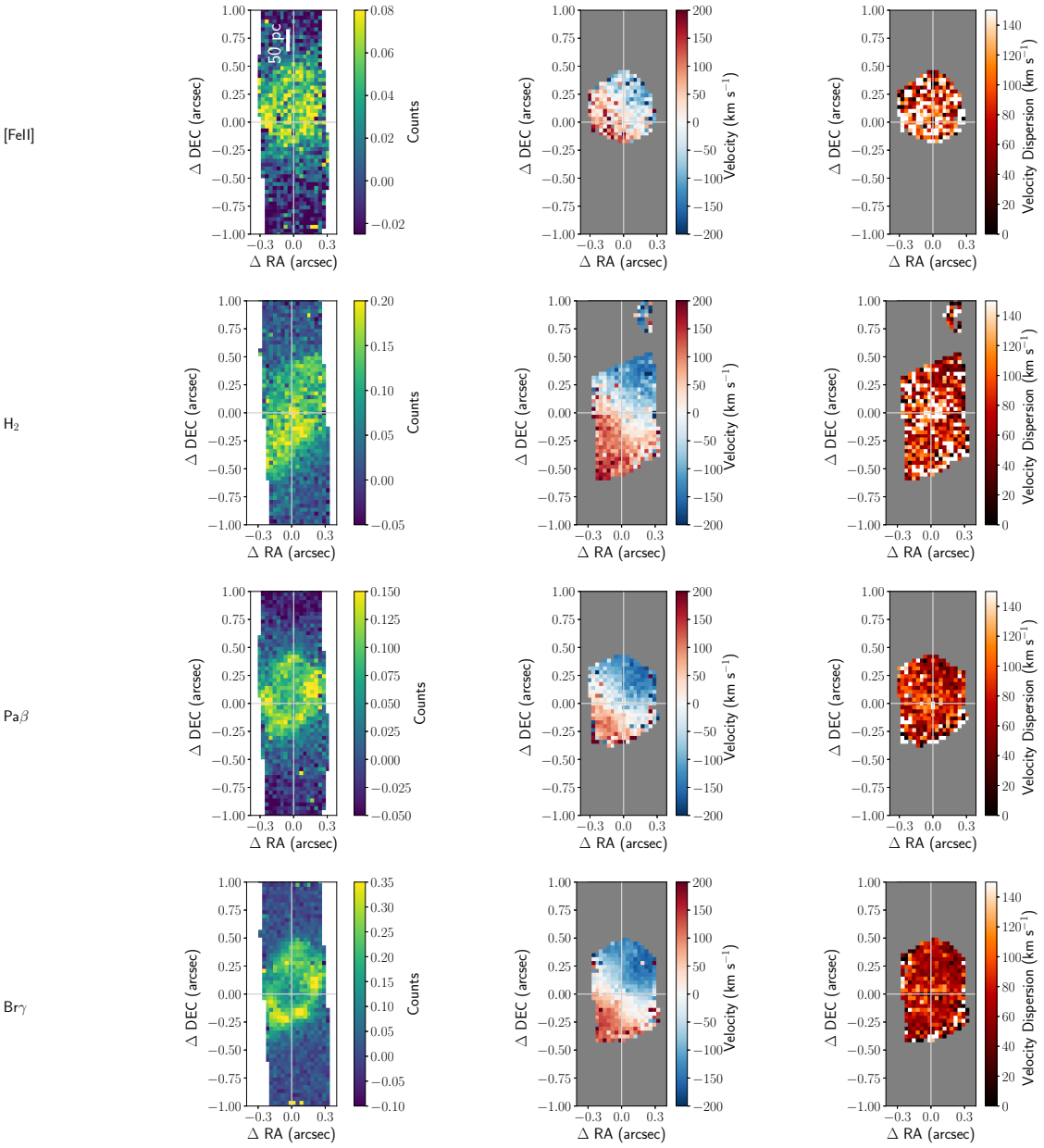


Figure 5.4j: Same as Fig. 5.4a for NGC 7591.

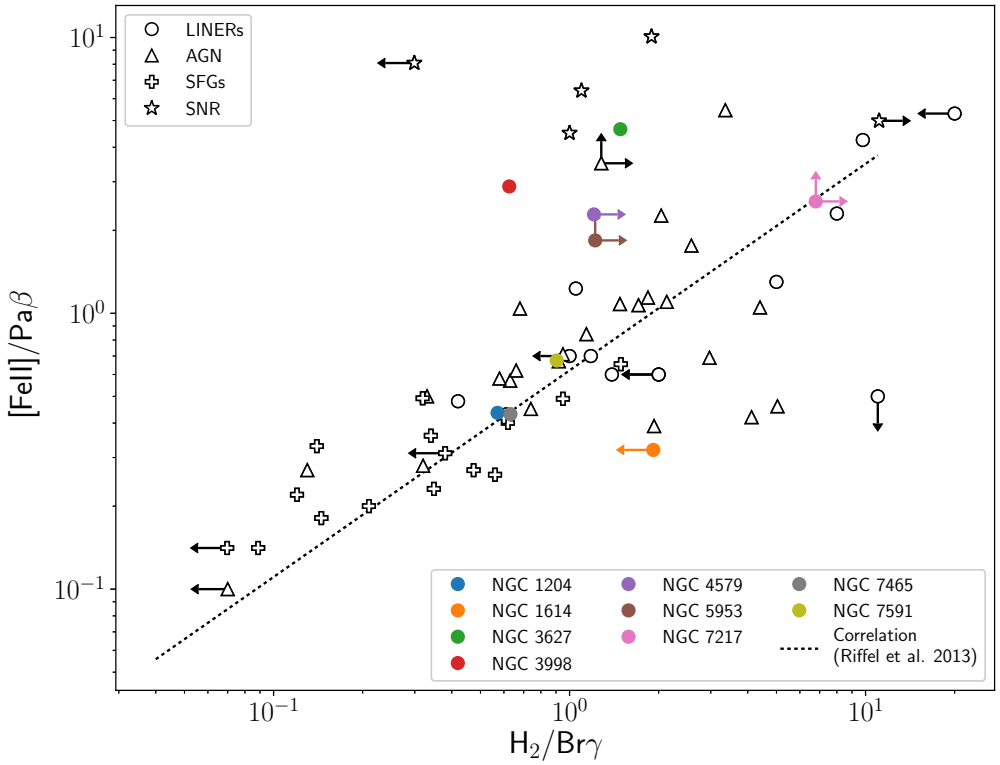


Figure 5.5: Plot of the [FeII]/Pa$\beta$ and 1-0 S(1) $H_2$/Br$\gamma$ emission line ratio measurements derived from the nuclear spectra of LINERs observed with OSIRIS. NGC 4736 is not included because its nuclear spectra contain strong Pa$\beta$/Br$\gamma$ absorption. The correlation between the two NIR line ratios as measured from seeing-limited slit spectra of AGN, star forming galaxies (SFGs), and LINER galaxies is shown as a black dashed line (Riffel et al., 2013). Values from individual sources in the literature are plotted for LINERs, SFGs, AGN, and supernova remnants (SNRs) (Larkin et al., 1998; Dale et al., 2004; Rodríguez-Ardila et al., 2004, 2005; Riffel et al., 2013).

Bibliography

Baldwin, J. A., Phillips, M. M., & Terlevich, R. 1981, PASP, 93, 5

Blietz, M., Cameron, M., Drapatz, S., et al. 1994, ApJ, 421, 92

Boehle, A., Larkin, J. E., Adkins, S. M., et al. 2016b, Proc. SPIE, 9908, 99082Q

Böker, T., Falcón-Barroso, J., Schinnerer, E., Knapen, J. H., & Ryder, S. 2008, AJ, 135, 479

Corbett, E. A., Kewley, L., Appleton, P. N., et al. 2003, ApJ, 583, 670

Dale, D. A., Roussel, H., Contursi, A., et al. 2004, ApJ, 601, 813

Davies, R. I. 2007, MNRAS, 375, 1099

Davies, R. I., Maciejewski, W., Hicks, E. K. S., et al. 2014, ApJ, 792, 101

Elmegreen, B. G. 1994, ApJ, 425, L73

González-Martín, O., Masegosa, J., Márquez, I., Guerrero, M. A., & Dultzin-Hacyan, D. 2006, A&A, 460, 45

Heckman, T. M. 1980, A&A, 87, 152

Hicks, E. K. S., Davies, R. I., Maciejewski, W., et al. 2013, ApJ, 768, 107

Ho, L. C., Filippenko, A. V., & Sargent, W. L. W. 1997a, ApJS, 112, 315

—. 1997b, ApJ, 487, 568

Kim, D.-C., Sanders, D. B., Veilleux, S., Mazzarella, J. M., & Soifer, B. T. 1995, ApJS, 98, 129

Kormendy, J. 2004, Coevolution of Black Holes and Galaxies, 1

Kormendy, J., & Ho, L. C. 2013, ARA&A, 51, 511

Krabbe, A., Gasaway, T., Song, I., et al. 2004, in Proc. SPIE, Vol. 5492, Ground-based Instrumentation for Astronomy, ed. A. F. M. Moorwood & M. Iye, 1403–1410

Larkin, J., Barczys, M., Krabbe, A., et al. 2006, New A Rev., 50, 362

Larkin, J. E., Armus, L., Knop, R. A., Soifer, B. T., & Matthews, K. 1998, ApJS, 114, 59

Magorrian, J., Tremaine, S., Richstone, D., et al. 1998, AJ, 115, 2285

Mazzalay, X., Saglia, R. P., Erwin, P., et al. 2013, MNRAS, 428, 2389

Moustakas, J., & Kennicutt, Jr., R. C. 2006, ApJS, 164, 81

Müller-Sánchez, F., Prieto, M. A., Mezcua, M., et al. 2013, ApJ, 763, L1

Nagar, N. M., Falcke, H., & Wilson, A. S. 2005, A&A, 435, 521

Osterbrock, D. E. 1981, ApJ, 249, 462

Ramos Almeida, C., Pérez García, A. M., & Acosta-Pulido, J. A. 2009, ApJ, 694, 1379

Riffel, R., Rodríguez-Ardila, A., Aleman, I., et al. 2013, MNRAS, 430, 2002

Riffel, R. A., Storchi-Bergmann, T., & Riffel, R. 2015, MNRAS, 451, 3587

Riffel, R. A., Colina, L., Storchi-Bergmann, T., et al. 2016, MNRAS, 461, 4192

Rodríguez-Ardila, A., Pastoriza, M. G., Viegas, S., Sigut, T. A. A., & Pradhan, A. K. 2004, A&A, 425, 457

Rodríguez-Ardila, A., Riffel, R., & Pastoriza, M. G. 2005, MNRAS, 364, 1041

van Dam, M. A., Bouchez, A. H., Le Mignant, D., et al. 2006, PASP, 118, 310

Veilleux, S., & Osterbrock, D. E. 1987, ApJS, 63, 295

Wizinowich, P. L., Le Mignant, D., Bouchez, A. H., et al. 2006, PASP, 118, 297